



Patrícia Tavares Coutinho Borges de Sousa

Mestre em Engenharia Física

Liquid hydrogen thermal energy storage unit for future ESA science missions

Dissertação para obtenção do Grau de Doutora em
Engenharia Física

Orientador: Grégoire Bonfait,
Professor associado com agregação,
Universidade Nova de Lisboa
Co-orientadora: Maria Isabel Simões Catarino,
Professora auxiliar,
Universidade Nova de Lisboa

Júri

Presidente: Prof. Doutor José Paulo Barbosa Mota
Arguentes: Doutor Jean-Marc Duval
Prof. Doutor Srinivas Vanapalli
Vogais: Prof. Doutor António Joaquim Rosa Amorim Barbosa
Prof. Doutor Daniel Cardoso Vaz
Prof. Doutor Grégoire Bonfait
Doutora Patricia de Rango
Prof. Doutor Paulo Jorge Valente Garcia



FACULDADE DE
CIÊNCIAS E TECNOLOGIA
UNIVERSIDADE NOVA DE LISBOA

Abril, 2016

Liquid hydrogen thermal energy storage unit for future ESA science missions

Copyright © Patrícia Tavares Coutinho Borges de Sousa, Faculty of Sciences and Technology, NOVA University of Lisbon.

The Faculdade de Ciências e Tecnologia and the Universidade NOVA de Lisboa have the right, perpetual and without geographical boundaries, to file and publish this dissertation through printed copies reproduced on paper or on digital form, or by any other means known or that may be invented, and to disseminate through scientific repositories and admit its copying and distribution for non-commercial, educational or research purposes, as long as credit is given to the author and editor.

Este documento foi gerado utilizando o processador (pdf) \LaTeX , com base no template “unlthesis” [1] desenvolvido no Dep. Informática da FCT-NOVA [2]. [1] <https://github.com/joaomlorenco/unlthesis> [2] <http://www.di.fct.unl.pt>

Acknowledgements

I would like to sincerely acknowledge a few people that have been absolutely essential during this undertaking, at both professional and personal levels.

Firstly, I would like to thank professors Grégoire Bonfait and Isabel Catarino for their guidance for a period that spans almost 5 years spent working at the Cryogenics Laboratory of FCT/UNL. This was a period of great personal and professional growth and I thank you both for the opportunity to do so: it has been a valuable experience that will accompany me throughout my life. Also to my colleagues in the laboratory, whose help was invaluable and whom I have come to call friends.

I would also like to thank our partners in this project, Active Space Technologies, especially Daniel Martins: he has been a colleague and a friend throughout my years exploring cryogenics: it was a pleasure to be able to work with him once more.

To Martin Linder, the technical officer at ESA in charge for this project: I would like to personally acknowledge his support during the many discussions and setbacks.

To Dr. Patricia de Rango, Dr. Daniel Fruchart and Richard Haettel for their warm welcome during my stay in Grenoble, and for allowing me to participate in some of the processes that led to the full development of the metal hydride canister.

I am grateful to R.C. Bowman for our lengthy discussions on metal hydrides: some of our work was largely inspired on his work on sorption compressors on-board Planck and his input was invaluable.

For his unconditional support, I would like to thank my boyfriend Hugo who has always managed to get me back on my feet when times got tough.

But, most of all, I would like to express my heartfelt thanks to my parents. Throughout this long journey, they were my most enthusiastic supporters, always providing me with the emotional and physical tools needed to see this project through.

Abstract

The X-IFU instrument for X-ray observation on ESA's new ATHENA satellite will employ a complex cryogenic chain for detector cooling down to 50 mK. The existence of heat peaks during the recycling stages of a 300 mK cooler can compromise the stability of the entire chain; this issue can be solved by using large cryogenic liquid reservoirs or by over-dimensioning the system. However, these solutions are either costly or temporary, as cryogenic liquids will eventually run out.

An Energy Storage Unit (ESU) using liquid hydrogen has been developed as a solution for absorbing 400 J of thermal energy in 30 min between 15 K and 16 K by taking advantage of the liquid-to-vapour latent heat of hydrogen in a closed system. The ESU is composed of a low temperature liquid hydrogen reservoir, two intermediate interfaces for gas pre-cooling and a hydrogen storage vessel at room temperature. This vessel can either be a 56-litre expansion volume (for ground testing) or a canister filled with a metal hydride, $\text{LaNi}_{4.8}\text{Sn}_{0.2}$, that chemically absorbs hydrogen in its atomic form. The latter largely reduces the volume of the vessel and enables working at near-constant pressure and temperature.

Two devices have been developed for this project: a Development Model breadboard device used for preliminary testing and the Engineering Model, the final model of the ESU that is to be delivered to ESA and that was subjected to severe mechanical testing in order to comply with strict requirements. Results obtained with both models show that 400 J can be absorbed with a temperature increase of 2 K when a 56-litre expansion volume is used, while results using metal hydrides show that the same heat load can be absorbed between 15 K and 16.5 K, where the cold cell temperature is above 16 K for less than 10 min. Full regeneration of the ESU can be achieved in under 24 h without exceeding the cooling power available at the different temperature stages. Experimental results are discussed and suggestions for further improvement are proposed.

Keywords: Energy Storage Unit, cryogenics, metal hydrides, liquid hydrogen

Resumo

O instrumento X-IFU para observação de raios-X no ATHENA, o novo satélite da ESA, irá utilizar uma complexa cadeia criogénica para arrefecimento dos seus detectores até 50 mK. A libertação de energia térmica durante a fase de reciclagem de um refrigerador a adsorção a 300 mK pode comprometer a estabilidade de todo o sistema; este problema pode ser resolvido através da utilização de banhos criogénicos ou sobre-dimensionando o sistema, mas estas soluções são dispendiosas e/ou temporárias.

Uma *Unidade de Armazenamento de Energia* com hidrogénio líquido foi desenvolvida como solução para a absorção de 400 J de energia térmica entre 15 K e 16 K, tomando partido do calor latente da transição líquido-vapor do hidrogénio num sistema fechado. Este dispositivo é composto por uma célula de hidrogénio líquido a baixa temperatura, duas interfaces para pré-arrefecimento do gás e um reservatório de hidrogénio à temperatura ambiente. Este reservatório pode ser um volume de expansão de 56 litros (para testes em laboratório) ou um *canister* contendo um hidreto metálico, $\text{LaNi}_{4.8}\text{Sn}_{0.2}$, que absorve quimicamente o hidrogénio na sua forma atómica. Esta solução reduz significativamente o volume à temperatura ambiente e permite a operação do sistema a pressão e temperatura quase-constantes.

Dois dispositivos foram desenvolvidos: um *Development Model*, utilizado para testes preliminares, e o *Engineering Model*, o modelo final que será entregue à ESA e que foi sujeito a testes num ambiente mecânico severo. Os resultados obtidos mostram que é possível absorver 400 J com um aumento de temperatura de 2 K usando um volume de expansão de 56 litros, enquanto que a utilização de hidretos metálicos permite a absorção da mesma carga térmica entre 15 K e 16.5 K, em que a célula criogénica excede 16 K durante menos de 10 min. A regeneração completa do ESU é possível em menos de 24 h sem exceder a potência frigorífica disponível nos diferentes estágios. Os resultados experimentais são discutidos e sugestões para melhorias futuras são propostas.

Palavras-chave: Energy storage unit, criogenia, hidretos metálicos, hidrogénio líquido

Contents

List of Figures	xv
List of Tables	xxv
Acronyms	xxix
1 Introduction	1
2 The challenge: working towards Advanced Telescope for High-ENergy Astrophysics (ATHENA)	5
2.1 Cryogenic chain for the X-ray Integral Field Unit (X-IFU) instrument . . .	6
2.2 Commissariat à l'Énergie Atomique et aux énergies alternatives - Service des Basses Températures (CEA/SBT)'s hybrid sorption/Adiabatic Demagnetisation Refrigerator (ADR) cooler	9
2.3 Addressing heat bursts at 15 K	11
2.3.1 Specific heat of solid materials	13
2.3.2 Triple point cells	15
2.3.3 Liquid-to-vapour phase change	18
2.4 The proposal: a liquid hydrogen thermal buffer	21
3 A liquid hydrogen thermal buffer	25
3.1 Molecular forms of hydrogen	25
3.2 Basics of liquid-to-vapour phase change	28
3.3 Thermodynamics of a dual-volume Energy Storage Unit (ESU)	30
3.3.1 Heat absorption phase	31
3.3.2 Regeneration phase	33
3.4 Dimensioning the expansion volume	34
3.5 Finding a compact storage solution	36
3.5.1 Physical adsorption at low temperatures	36
3.5.2 Chemical absorption	38

4	The approach: designing according to specs	43
4.1	System requirements	43
4.2	System outline	45
4.3	Sizing the cold cell	45
4.3.1	Mechanical design	47
4.4	Liquid confinement in micro-g	48
4.5	Intermediate temperature stages	52
4.5.1	Heat load through solid conduction	52
4.5.2	Pressure drop	54
4.6	Heat exchange at the intermediate interfaces	56
4.7	Influence of ortho-to-para conversion	61
4.8	Room temperature storage	62
4.8.1	Sizing the expansion volume	62
4.8.2	Metal hydride storage	63
4.9	Sizing the metal hydride canister	65
4.10	Thermal model for metal hydrides	68
4.10.1	Regeneration phase	69
4.10.2	Heat absorption phase	71
5	System Implementation	75
5.1	Development Model	75
5.1.1	Cold cell	76
5.1.2	Filling capillary	77
5.1.3	Intermediate interface heat exchangers	78
5.1.4	Metal hydride canister design	82
5.1.5	Metal hydride production	85
5.1.6	Filling the canister	86
5.1.7	Thermal environment for the metal hydride canister	89
5.1.8	Cryocooler assembly	91
5.2	Engineering Model	92
5.2.1	Cold cell	92
5.2.2	Filling capillary and Heat exchangers	94
5.2.3	Metal hydride canister	98
5.2.4	Cryocooler assembly	101
6	Results and Discussion	105
6.1	Development Model	105
6.1.1	Preliminary testing	105
6.1.2	Liquid confinement tests	109
6.1.3	Heat Load Profile using a 56-litre volume	111
6.1.4	Condensation using a 56-litre volume	112

6.1.5	Heat Load Profile using metal hydrides	116
6.1.6	Condensation using the metal hydride canister	119
6.1.7	Effects of an additional heat load	121
6.1.8	Discussion and Summary	122
6.2	ESU as a Cold Source	123
6.3	Engineering Model	125
6.3.1	Performance tests with constant heat load	126
6.3.2	Operational cycle tests	129
6.3.3	Discussion and summary of Operational tests	133
6.4	Qualification Tests	135
6.4.1	Proof pressure tests	135
6.4.2	Burst test of cold cell	136
6.4.3	Thermal shock to cold cell	136
6.4.4	Thermal cycling of Room Temperature (RT) canister	137
6.4.5	Thermal vacuum cycling of cold cell	138
6.4.6	Vibrational tests	139
6.5	Functional tests	143
7	Final Remarks	149
	References	153
A	Requirements	159
B	Useful data	165
C	Technical Drawings	169

List of Figures

2.1	Scientific instruments on board ATHENA [13]. The X-IFU provides high spectral resolution, while the Wide Field Imager (WFI) enables a $12\text{ m} \times 12\text{ m}$ wide field view, coupled with high time resolution and a high count rate capability.	6
2.2	Types of coolers used in space: the range for each type is given in terms of cooling power <i>vs.</i> operating temperature. Adapted from [14].	7
2.3	Proposed cryochain for the X-IFU instrument on board ATHENA. It makes use of passive radiators, pulse tube and Joule-Thomson coolers and a hybrid sorption/ADR cooler to cover the whole temperature range down to 50 mK [11].	8
2.4	50 mK hybrid cooler consisting of an ADR and a ^3He sorption stage, developed by CEA/SBT and the reference solution for the last stage cooler of ATHENA [6].	9
2.5	Association of a sorption cooler with an ADR, designed for the International X-ray Observatory (IXO) mission, adapted from [9]. This version of the device features an intercept at 15 K for heat removal during the recycling stage. . .	9
2.6	Heat load dissipated at the 2.5 K and 15 K heat intercepts in a nominal cycle of the system shown in Figure 2.5 [9]. The peak power dissipated at 15 K is $\approx 100\text{ mW}$	10
2.7	One of the possible cryogenic chain configurations for X-IFU on ATHENA, with a hybrid sorption/ADR cooler for the last stage of cooling. An enthalpy reservoir or ESU could be placed between the 15 K cooler and the sorption cooler heat intercept at the same temperature.	11
2.8	Operation of an enthalpy reservoir on an interface with a variable heat load. Adapted from [21].	12
2.9	General scheme of the lead solid-state ESU, coupled to a gas-gap heat switch (Gas Gap Heat Switch (GGHS)), and where a copper platform for the sensor is visible. Adapted from [24].	13
2.10	Drawing of the $\text{Gd}_2\text{O}_2\text{S}$ solid-state ESU. It can be seen that in addition to the $\text{Gd}_2\text{O}_2\text{S}$ spheres, a copper mass was needed to confine them and helium gas was used to promote thermal homogeneity. Adapted from [25].	14

2.11	Specific heat of selected materials in the 14 K to 18 K range, data from [26, 27, 28]. The highlighted zone represents the area of interest for the ESU.	14
2.12	Triple point phase change: a) Pressure-temperature diagram; the phase change occurs at constant temperature and pressure. b) Temperature-Enthalpy diagram. In a triple-point ESU, only the solid-to-liquid enthalpy change is usable.	16
2.13	Thermal Storage Unit using the triple point of hydrogen, developed by CEA/SBT [30]; the diameter of the cell is 30 mm.	17
2.14	Different first-order phase changes of a pure fluid, where 1 is a solid-to-vapour transition, 2 is a solid-to-liquid transition and 3 is a liquid-to-vapour transition. These phase changes are represented in a) a Pressure-temperature diagram and b) a Temperature-Enthalpy diagram, where the relative enthalpy change for each transition can be seen.	18
2.15	Two possible configurations for a cryogenic energy storage unit; adapted from [21].	19
2.16	Cryogenic fluids available in the temperature range; data from Reference Fluid Thermodynamic and Transport Properties Database (REFPROP) [31].	20
2.17	Latent heat of normal hydrogen along the liquid-to-vapour saturation curve; the square symbol indicates the solid-to-liquid latent heat at the triple point. Data from [31, 32].	20
2.18	Possible cryogenic chain configuration for X-IFU on ATHENA, with the liquid hydrogen ESU integrated between the 15 K stage of the chain and the sorption/ADR cooler heat intercept.	22
3.1	Spin isomers of the hydrogen molecule, ortho- and parahydrogen.	26
3.2	Fraction of equilibrium ortho- and para- species in hydrogen as a function of temperature.	27
3.3	Fraction of ortho- and para-hydrogen as a function of time during a conversion process at low temperature (below 20 K).	28
3.4	Temperature <i>vs.</i> enthalpy diagram for a generic pure substance. The red curve represents an isobaric process at pressure P_1 : if the transition occurs from left to right, it is an evaporation; if it goes from right to left, it is a condensation.	29
3.5	Schematic P - T and T - H diagrams for a generic pure substance. The red lines represent an evaporative process that occurs inside a closed system. In a the liquid starts to evaporate; the evaporation from a to b occurs along a pressure/temperature drift until all the liquid is evaporated at b . As there is no more liquid, the system is not in saturation conditions and hydrogen only exists in gas form.	30
3.6	Time evolution of a liquid ESU as a function of the cold part temperature. States a and b are in saturation conditions and represent the minimum and maximum temperatures achieved during ESU operation.	31

3.7	Evolution of a control volume in an evaporative process in an enthalpy reservoir, considering the whole system as a closed one; adapted from [36].	32
3.8	Amount of activated carbon needed to adsorb hydrogen at 100 mbar as a function of the increase in the carbon temperature (green curve). a) and b) represent data for hydrogen adsorption at 25 K and c) and d) for adsorption at 120 K. The right-hand side of the plots depicts the amount of copper (a) and c)) and ice water (b) and d)) needed to absorb the released heat of adsorption at that temperature (orange and blue curves).	37
3.9	Schematic of cascading LN ₂ and LH ₂ vessels with activated carbon for adsorption of the gas at various temperature stages. As hydrogen evaporates, the generated gas is adsorbed by the activated carbon at 77 K, and the released heat of adsorption causes the liquid nitrogen to evaporate; the nitrogen gas is in turn adsorbed by the activated carbon at room temperature, releasing heat at that temperature.	38
3.10	Inter-metallic hydrides. Upon contact, the hydrogen molecule dissociates into two hydrogen atoms that chemically bond with the metallic compound. . . .	39
3.11	Ideal Pressure-Temperature-Composition diagram, with the hydride phases α and β displayed; the length of the pressure plateau AB represents the effective hydrogen storage capacity. Adapted from [43].	40
3.12	LaNi _{4.8} Sn _{0.2} isotherms at various temperatures, as used in the Planck sorption cooler; adapted from [49]. Full symbols represent the desorption process and empty symbols the absorption process.	42
4.1	Overall schematic of the ESU and its three main components: the room temperature gas storage, the intermediate interfaces for gas pre-cooling, and the cold cell where the heat load is absorbed. The available cooling power (cf. European Space Agency (ESA) requirements) is indicated for each of the interfaces.	45
4.2	Schematic of the distribution of volumes inside the cell. The total capacity of the cell is 17.2 cm ³ and the void volume is 90% of that (15.5 cm ³).	47
4.3	Circumferential stresses on a thin-walled cylinder under internal pressure. .	48
4.4	Ground configurations for testing liquid confinement: a) Baseline or normal configuration, where the exhaust is located at the top of the cell, preventing liquid exit; b) Anti-gravity configuration. In this configuration the exhaust is at the bottom of the cell, and liquid needs to be confined or it will be spilled due to the effect of gravity.	49
4.5	Capillary action inside tubes with different diameters.	49
4.6	Wicking or capillary height for hydrogen along the temperature range 14 K to 32 K for different pore sizes. The red dashed line indicates the cell height. . .	50

4.7	Alumina foam KVR 164-242: a) macroscopic appearance of a sample of foam; b) Scanning Electron Microscope (SEM) image of its microscopic structure (scale: $200\text{ }\mu\text{m}$). The equivalent estimated pore size is indicated ($\approx 100\text{ }\mu\text{m}$). .	51
4.8	Vitreous carbon foam: a) macroscopic appearance of a sample of foam; b) Optical microscope image the foam structure (scale: $100\text{ }\mu\text{m}$). The estimated pore size is $\approx 250\text{ }\mu\text{m}$	51
4.9	Schematic drawing of the different interfaces which the capillary tube must cross; L_1 , L_2 and L_3 represent the length of capillary between each interface.	53
4.10	Pressure drop per meter of tube length for the temperature range 15 K to 300 K, given as a function of the heat load applied to the cold cell.	55
4.11	Error in cold cell temperature as computed from pressure measurements in saturation conditions for the temperature range 15 K to 300 K, given as a function of the heat load applied to the cold cell.	56
4.12	Fluid temperature distribution along a tube with uniform wall temperature; adapted from [60].	57
4.13	Reynolds number as a function of the condensation time for interfaces Interface (I/F) 1 and I/F 2.	58
4.14	Heat exchange at intermediate interface I/F 1 (120 K) for condensation of 0.5 mol of hydrogen: a) Temperature of gas as it exits I/F 1 as a function of the condensation time. The orange dashed line represents 120 K; b) Heat load on that interface as a function of the condensation time. The dashed line represents the maximum available heat load, 40 mW.	59
4.15	Heat exchange at intermediate interface I/F 2 (25 K) for condensation of 0.5 mol of hydrogen: a) Temperature of gas as it exits I/F 2 as a function of the condensation time. The orange dashed line represents 25 K; b) Heat load on that interface as a function of the condensation time. The dashed line represents the maximum available heat load, 15 mW.	59
4.16	Heat exchange at the cold interface (15 K) for condensation of 0.5 mol of hydrogen, given as a function of the condensation time; the dashed line represents the maximum available heat load, 15 mW.	60
4.17	Heat exchange at the cold interface (15 K) as a function of the condensation time, considering that all of the hydrogen is converted into $p\text{-H}_2$; the dashed line represents the maximum available heat load, 15 mW.	62
4.18	Expansion volume needed as a function of the temperature increase in the cell. Data given for a total energy absorption of 400 J and for a starting temperature of 15 K.	63
4.19	Heat load on the room temperature canister as a result of hydrogen absorption during the Heat Load Profile (HLP) applied to the cold cell. The dashed line represents the average heat load.	66

4.20	Temperature increase in the metal hydride canister when the heat load is applied to the cold cell for different canister masses using Stainless steel (SS) 316, with no added cooling power. The dashed line represents the 8 K limit on temperature increase.	67
4.21	Temperature increase in the metal hydride canister when the heat load is applied to the cold cell for different canister masses using SS 316, with 10 W constant cooling power. The dashed line represents the 8 K limit on temperature increase.	67
4.22	Sources of error in hydrogen quantity when computed from pressure measurements: a) flat absorption plateaus along the same isotherm; b) hysteresis in the absorption/desorption pair for the same temperature; c) temperature measured outside ($T_{MH} + \Delta T$) is different from the true temperature of the hydride (T_{MH}).	69
4.23	Calculation of the condensation rate when using pressure measurements is not viable: as long as the Qmeters such as Qmeter 3 are calibrated, the heat load at every instant can be related to the changes in enthalpy, which in turn allows for the determination of the flow rate.	70
4.24	Gas gap thermodynamic model for the heat absorption phase in the canister. Δx is the thickness of the hydrogen gas gap.	72
4.25	Evolution of the temperature inside the metal hydride and at the outer walls of the canister when considering a gas gap between the canister and the contents of the canister, during hydrogen absorption due to a heat load.	73
5.1	Overall schematic of the Development Model assembly.	75
5.2	Cold cell as designed for the Development Model: a) Solidworks® rendered image; b) Cell after machining and prior to filling and soldering.	77
5.3	Schema of the cold part of the ESU (shown in the anti-gravity configuration): it features two separate capillary tubes, one for pressure measurements and one that connects to the expansion volume; the three intermediate interfaces with the Qmeters can be seen mounted on the 1st stage and cold finger. . . .	78
5.4	Overall schematic of the Development Model assembly.	79
5.5	Qmeters as built for the Development Model.	80
5.6	Temperature measured at the interface as a function of the applied heat load for I/F 1, I/F 2 and Cold I/F. In the case of I/F 2 and Cold I/F, different cold finger temperatures were tested.	81
5.7	Aluminium foam wafers produced by electro-discharge machining and porous filter.	83
5.8	Development Model metal hydride canister as designed. Some of the external features can be seen such as the flat mounts for the radiator and heater placement, as well as inserts for the thermometers.	84

5.9	Section cut of the canister. The porous filter is mounted at the entrance of the canister and allows for hydrogen to evenly reach the metal hydrides that are embedded in the aluminium foam matrix.	85
5.10	LaNi _{4.8} Sn _{0.2} ingot after annealing: a) ingot right after exiting the oven, still incandescent; b) ingot after natural cooling down to room temperature. . . .	85
5.11	LaNi _{4.8} Sn _{0.2} activation process: a) before activation, where the ingot was broken into 10 mm chunks and is still exposed to air; b) after activation, where the resulting powder can be seen; at this stage the pressure vessel was opened and kept in a controlled atmosphere glove-box.	86
5.12	Canister inside the glove-box ready for the filling process. The filter is visible in the centre of the inner cylinder.	87
5.13	Development Model canister ready for use; resistive kapton heaters can be seen on the side walls, as well as the wiring for the Pt100 thermometers. . .	88
5.14	Pressure-Composition-Temperature measurements for a sample of LaNi _{4.8} Sn _{0.2} powder. The solid curves denote an absorption process whereas the dashed lines represent a desorption process.	88
5.15	Heat exchanger at room temperature for the metal hydride canister immersed in a cooling bath. By controlling the length L the cooling power can be tuned. On the right-hand side, image of the actual system showing the insulation housing and parts of the cooling unit and bath.	89
5.16	Temperatures of the canister and heat exchanger as a function of the applied heat load, for a cooling bath temperature of -34°C	90
5.17	Cold part of the Development Model of the ESU. All three interfaces can be seen, as well as the cold cell and both capillary tubes: one that connects to the room-temperature volume and one for pressure measurements inside the cell free of pressure drop.	91
5.18	Overview of the Engineering Model of the ESU, complete with its mechanical and thermal interfaces. Image courtesy of Active Space Technologies (AST). .	92
5.19	Cold cell of Engineering Model. The copper straps connect to the thermal interfaces and the carbon tubes provide mechanical support from the 25 K stage. Image courtesy of AST.	93
5.20	Cold cell, filling capillary and intermediate interfaces coupled to the capillary tube. The length of each section of tube is identified. Image courtesy of AST.	94
5.21	Qmeters as built for the Engineering Model.	96
5.22	Temperature measured at each interface as a function of the applied heat load for I/F 1, I/F 2 and Cold I/F.	97
5.23	Exploded view of the metal hydride canister for the Engineering Model. Image courtesy of AST.	98

5.24	View of the exterior of the Engineering Model (EM) canister; the flap for structural support and a manifold that includes a pressure sensor are the main additions when compared to the Development Model (DM). Image courtesy of AST.	99
5.25	Pressure-Composition-Temperature measurements for a sample of $\text{LaNi}_{4.8}\text{Sn}_{0.2}$ powder as synthesised for the EM. The solid curves denote an absorption process whereas the dashed lines represent a desorption process.	99
5.26	Engineering Model canister ready for use, where kapton heaters are placed on the side walls and a pressure sensor can be seen mounted on top of the canister. The aluminium flap provides support for the manifold.	100
5.27	Temperatures of the canister and heat exchanger as a function of the applied heat load, for cooling bath temperatures of -18°C and -25°C	100
5.28	Drawing of the Gifford-McMahon (GM) cryocooler assembly, as designed for testing of the Engineering Model.	101
5.29	Cold cell of the Engineering Model as assembled inside the cryocooler. . . .	103
6.1	Configurations used during performance testing of the DM and thermometer placement. P_{50L} and P_{ESU} refer to pressure sensors at room temperature. The colours displayed for the thermometers match those found in the experimental result curves.	106
6.2	Experimental results for a 1 W constant-power heat absorption phase (“ESU mode”); temperatures are to be read on the left-hand side scale, while the liquid filling ratio is displayed on the right.	107
6.3	Liquid confinement experiments using a 6ℓ expansion volume: a) cell in the baseline configuration and heating at the top of the cell (capillary side); b) cell in the anti-gravity configuration, heating at the top of the cell (opposite to capillary side). In both cases, a constant load of 1 W was applied.	109
6.4	Liquid confinement experiments using a 56ℓ expansion volume when a constant load of 1 W is applied. The temperature shown for each case is the temperature inferred from pressure measurements free of pressure drop (T_{gasESU}).	111
6.5	Temperature evolution when the Heat Load Profile is applied to the top of the cold cell in its anti-gravity configuration; the applied power can be read on the right-hand side of the plot. Experiment performed using a 56ℓ expansion volume.	112
6.6	Temperature evolution during a regeneration phase of the ESU, where liquid hydrogen is condensed from the gas stored in a 56ℓ expansion volume over a period of 21 h.	113
6.7	Heat load at each interface as calculated by means of flow rate and using Qmeter calibration. The temperature of the interface can be read on the right-hand side of each plot.	115

6.8	Amount of hydrogen condensed in the cold cell over the 21 hour regeneration phase, using three different methods: calculations using the flow rate inferred from the variation in the pressure and using the calibration of both Qmeters 2 and 3.	115
6.9	Pressure-Composition-Temperature (PCT) curves for the DM canister, and explanation for the total amount of hydrogen inside the canister. Roughly 0.5 mol remain in the canister at all times acting as a buffer, so that the system can operate in the flat part of the pressure plateaus.	116
6.10	Temperature evolution when the Heat Load Profile is applied to the bottom of the cold cell in its anti-gravity configuration; experiment performed using the metal hydride canister for hydrogen gas storage.	117
6.11	Typical preparation period before a heat absorption phase using the metal hydride canister. After condensation, the heating in the canister is cut and it is allowed to cool down, pumping on the liquid hydrogen and decreasing the cold cell temperature.	118
6.12	Condensation phase with the metal hydride canister for hydrogen storage. The temperature evolution of the cold cell and intermediate interfaces, as well as the canister, can be seen. The bottom plot shows the amount of condensed hydrogen, calculated using the flow rate obtained by the Qmeters calibration curves (cf. subsection 6.1.4).	120
6.13	Heat load profile with an extra 10% applied power to the cold cell over 30 min: a) Temperature profile in the cold cell during the “HLP+10%”; b) Comparison of this experiment with one where the regular HLP is applied. For ease of comparison, only the highest temperature (Bottom cell) is displayed in this plot.	121
6.14	ESU as a Cold Source experiment performed at 14.2 K, which was able to provide an average extra cooling power of ≈ 30 mW during 4 h, absorbing a total of 480 J.	124
6.15	Anti-gravity configuration used during performance testing of the EM and thermometer placement. P_{gas} refers to the pressure sensor at room temperature. The colours displayed for the thermometers match those found in the experimental result curves.	125
6.16	PCT curves for the EM canister, and explanation for the total amount of hydrogen inside the canister. Adding an additional amount of hydrogen allows the sorption cycles to be performed in the flat part of the pressure plateaus.	126
6.17	Evolution of system temperatures when a constant heat load of 1 W is applied to the bottom of the cell. Experiment carried out with the Engineering Model using the metal hydride canister for hydrogen storage; the cold finger was kept at 13 K during the experiment.	127

6.18 Evolution of system temperatures when a constant heat load of 0.5 W is applied to the bottom of the cell. Experiment carried out with the Engineering Model using the metal hydride canister for hydrogen storage; the cold finger was kept at 13 K during the experiment.	128
6.19 Evolution of system temperatures when a constant heat load of 100 mW is applied to the bottom of the cell. Experiment carried out with the Engineering Model using the metal hydride canister for hydrogen storage; the cold finger was kept at 13 K during the experiment.	128
6.20 Increasing system pressure in a metal hydride canister with decreasing temperature: because the plateaus are not flat, the global pressure can increase with increased hydrogen absorption even as the metal hydride temperature decreases.	129
6.21 Cycling tests with the Engineering Model. The temperature evolution of the cold cell, interfaces and canister are shown as a function of time for a period of 96 h that encompasses 5 complete regeneration and heat absorption cycles.	130
6.22 Evolution of cold cell and canister temperatures when the HLP is applied to the bottom of the cell; results shown for the 5 HLP cycles performed continuously during a 96 h period.	131
6.23 Heat load at each of the three interfaces during the condensation phase for each of the 5 cycles. During this experiment, an artificial heat load of 7 mW was being constantly applied to I/F 2 and of 35 mW to I/F 1.	132
6.24 Illustration of the manifold used for helium purification and proof pressure tests.	135
6.25 Dedicated model of the cold cell for the burst test: a) after machining, before the tests; b) after the burst test.	136
6.26 Thermal shock tests: a) cold part being dipped in liquid nitrogen; b) cold part immediately after the tests before thawing back to room temperature.	137
6.27 Dedicated Carbon Fibre Reinforced Plastic (CFRP) tube dummy for thermal shock tests.	137
6.28 Measurements of the hydrogen pressure inside the canister as a function of temperature, for a content of 1 mol of hydrogen.	138
6.29 Thermal vacuum tests performed in the cold part of the system.	138
6.30 Last half of the thermal vacuum tests performed in the cold part of the system where a leak test was performed simultaneously.	139
6.31 ESU ready for the vibrational tests, assembled in the shaker unit at AST: a) Cold part; b) RT canister.	140
6.32 Leak test in the cold part of the ESU, using helium as tracer gas; the right-hand side of the plot shows the cell temperature (orange dashed line) during the leak test.	142
6.33 Leak test in the room temperature canister using helium as tracer gas; the test was performed at room temperature.	142

6.34	Functional test performed after the qualification test campaign using a 6 ℓ expansion volume, with an applied heat load of 0.5 W.	143
6.35	EM cold cell after preliminary functional tests: a) exhaust capillary was cut and alumina powder can be seen exiting the cell; b) open cell, where what is left of the alumina foam can be seen as powder.	144
6.36	SEM images of alumina foam KVR 174-402; its structure can be seen as well as the mean “pore” size; a) scale: 200 μm; b) scale: 50 μm.	144
6.37	Post-shaker experiment with 0.5 W constant heat load applied, using the EM cold cell with new alumina foam and a 6 ℓ expansion volume.	145
6.38	Post-shaker experiment with the HLP applied to the cold cell, using the EM cold cell with new alumina foam and the metal hydride canister.	146
B.1	Phase diagram of hydrogen near the triple point; data obtained using REFPROP [31].	165
B.2	Surface tension of liquid hydrogen at saturation conditions as a function of temperature; data obtained using REFPROP [31].	166
B.3	Density of liquid and vapour hydrogen under saturation conditions as a function of temperature; data obtained using REFPROP [31].	166
B.4	Specific heat of stainless steel 316 as a function of temperature; data obtained from National Institute of Standards and Technology (NIST) [58].	167
B.5	Specific heat of copper as a function of temperature; data obtained from NIST [58].	167
B.6	Specific heat of ice water as a function of temperature; data taken from [67].	168
B.7	Thermal conductivity of carbon fibre composite M 40 A [68].	168

List of Tables

2.1	ATHENA mission summary; adapted from [10].	5
2.2	Sensible heat materials and their properties for 400 J of thermal energy storage between 15 K and 17 K. Density of alloys was estimated to be between 8 g/cm ³ and 12 g/cm ³ for mass calculations.	15
2.3	Triple point temperature and pressure of cryogenic fluids below 80 K. Data was calculated using REFPROP [31].	17
2.4	Expansion volume characteristics needed at different temperature interfaces for the cold cell to be able to store 400 J between 15 K and 17 K using the liquid-to-vapour phase change of hydrogen. Computed using the model described in [33] and summarised in section 3.4.	21
2.5	Summary of the different solutions proposed for an ESU operating between 15 K and 17 K. Note that the masses and volumes considered are only those of the active heat absorbing material; no housing was considered for any of the options.	22
3.1	Physical constants of normal hydrogen and parahydrogen, calculated using REFPROP [31].	26
3.2	Ortho-para hydrogen data (adapted from [32]): equilibrium composition of hydrogen and heat of conversion from <i>o</i> -H ₂ to <i>p</i> -H ₂	27
3.3	Energy that needs to be removed from 0.44 mol of hydrogen gas to pre-cool it from 300 K down to 15 K and condense it in the cold cell, and evaluation of the cooling power needed if spread out during a 24 h condensation period; comparison with the requirements given in Interface Requirements (IR) 1 of Appendix A. Data calculated using REFPROP [31].	34
3.4	Expansion volume requirements for different temperature drifts in the hydrogen cold cell. Data for expansion volumes at room temperature, and for an energy storage in the cold cell of 400 J, computed using the model described in [33].	35

3.5	Parameters for operation of a cascading LN ₂ and LH ₂ system with activated carbon for adsorption of hydrogen gas at 77 K and adsorption of the nitrogen gas at room temperature (273 K).	38
3.6	Main properties of the LaNi _{4.8} Sn _{0.2} metal hydride [50].	42
4.1	Main requirements for the design and performance of the ESU. Adapted from [51].	44
4.2	Properties of the selected porous materials used for liquid confinement testing.	51
4.3	Maximum allowed parasitic heat load through conduction between each stage of the system.	53
4.4	Required length for the different segments L_1 , L_2 and L_3 of capillary tube using stainless steel 304.	54
4.5	Parameters used for determination of the Reynolds number and outlet temperature of the gas at I/F 1 and I/F 2.	58
4.6	Data for calculation of the heat load at the Cold I/F.	60
4.7	Data for calculation of the heat load at the Cold I/F considering ortho-to-para conversion.	61
4.8	Amount of LaNi _{4.8} Sn _{0.2} needed to absorb 0.5 mol of hydrogen.	64
4.9	Total mass and volume of LaNi _{4.8} Sn _{0.2} needed considering safety factors.	64
5.1	Specifications to be considered for the design of cold cell of the Development Model.	76
5.2	Parameters for calculation of the heat leaks at the three interfaces.	79
5.3	Solutions adopted for the heat leaks or Qmeters at each interface.	80
5.4	Specifications to be considered for the design of the room temperature metal hydride canister.	82
5.5	Properties of the 8% nominal density Duocel [®] aluminium foam matrix used inside the metal hydride canister.	83
5.6	Effective amount of LaNi _{4.8} Sn _{0.2} inside the DM canister.	87
5.7	Dimensions of the room temperature canister heat exchanger.	90
5.8	Heat load along the CFRP tubes from 25 K to 15 K.	94
5.9	Heat load across the filling capillary.	95
5.10	Parameters for calculation of the heat leaks at the three interfaces.	95
5.11	Dimensions of the Qmeter links in the Engineering Model: in every case, the material used was Cu Residual Resistivity Ratio (RRR) 100.	95
5.12	Effective amount of LaNi _{4.8} Sn _{0.2} inside the EM canister.	99
5.13	Estimation of the collapsing pressure for a vacuum vessel of $L = 400$ mm, $t = 1$ mm and $D_o = 159$ mm.	102
5.14	Properties of the components designed and built for the cryocooler assembly.	102
6.1	Conditions of each liquid confinement experiment using the 56 ℓ volume. In all cases, a heat load of 1 W was applied.	110

6.2	Checklist for ESA requirements and achieved results.	134
6.3	Vibrational test results for the cold part: Sine qualification tests.	140
6.4	Vibrational test results for the cold part: Random vibration tests.	140
6.5	Vibrational test results for the canister: Sine qualification tests.	141
6.6	Vibrational test results for the canister: random vibration tests.	141
A.1	Functional & Performance Requirements.	160
A.2	Interface Requirements.	161
A.3	Environmental Requirements.	161
A.4	Physical & Resource Requirements.	162
A.5	Operational Requirements.	162
A.6	Design Requirements.	163

Acronyms

ADR Adiabatic Demagnetisation Refrigerator

ASME American Society of Mechanical Engineers

AST Active Space Technologies

ATHENA Advanced Telescope for High-ENergy Astrophysics

CEA/SBT Commissariat à l'Énergie Atomique et aux énergies alternatives - Service des Basses Températures

CFRP Carbon Fibre Reinforced Plastic

CNRS Centre National de la Recherche Cientifique

DM Development Model

DR Design Requirements

EACS ESU as a Cold Source

EDM Electrical Discharge Machining

EM Engineering Model

ER Environmental Requirements

ESA European Space Agency

ESU Energy Storage Unit

FCT/UNL Faculdade de Ciências e Tecnologia - Universidade Nova de Lisboa

FPR Functional & Performance Requirements

GGHS Gas Gap Heat Switch

GM Gifford-McMahon

ACRONYMS

HLP Heat Load Profile

I/F Interface

IR Interface Requirements

ISO International Organization for Standardisation

IXO International X-ray Observatory

JT Joule-Thomson

LT Low Temperature

MH Metal Hydride

NASA National Aeronautics and Space Administration

NIST National Institute of Standards and Technology

OFHC Oxygen-Free High Conductivity

OR Operational Requirements

PCT Pressure-Composition-Temperature

PRR Physical & Resource Requirements

QM Qmeter

RC Resistor-Capacitor

REFPROP Reference Fluid Thermodynamic and Transport Properties Database

RRR Residual Resistivity Ratio

RT Room Temperature

SAFARI SpicA FAR-infra-red Instrument

SEM Scanning Electron Microscope

SPICA SPace Infra-red telescope for Cosmology and Astrophysics

SS Stainless steel

TIG Tungsten Inert Gas

TRL Technology Readiness Level

TRP Technological Research Program

WFI Wide Field Imager

X-IFU X-ray Integral Field Unit

1 Introduction

Cryogenics is a field of technology in which man has largely surpassed nature [1]: while the lowest temperature observable in the universe is 2.7 K, temperatures obtained in a laboratory environment have reached 6 mK for large-scale objects such as a 1 m³ copper vessel [2] and as low as 100 pK [3] for a small rhodium sample. In a nutshell, cryogenics has produced temperatures 12 orders of magnitude lower than the lowest temperature in nature. This means that even in space, there is the need for man-made cooling devices for reaching extremely low temperatures.

Space cryogenics has suffered a remarkable evolution over the past two decades; in fact, it has been an essential technology for virtually as long as there has been a space program. Ever since Robert Goddard first used liquid oxygen as a much more efficient oxidiser in the 1920's, cryogenic fuels have been the backbone of space-borne launchers [4]. Then came the idea of sending scientific instruments into space, since it allowed for an unobstructed view of many phenomena. With the advent of scientific missions, more advanced detectors and instruments have been developed that are more efficient, through better sensitivity and reduced thermal background noise when cooled down to cryogenic temperatures.

Cryogenic detectors on board satellites are now major drivers for cryogenics in space: their requirements determine the architecture of the payload system and parameters such as the system's operating temperature and stability [5]. Indeed, cryogenics has established itself as a core mission enabling technology, allowing the use of new types of detectors that provide better energy resolution and higher sensitivity across the electromagnetic spectrum. It has been called a "necessary evil" [6]: while it enables the use of a whole range of detector technology, it highly increases the complexity of a system.

For most of its history, cryogenics in space meant stored cryogenics; however, increased mission durations and volume/mass restrictions have started to render this solution unusable for the next generation of science missions; fortunately, new developments in mechanical cryocoolers allow for new, cryogen-free solutions. The new objective of achieving cryogen-free cooling chains for scientific instruments would mean longer mission lifetimes, less risks associated with cryogenic fluids, and would allow for open architecture

satellites such as the James Webb Space Telescope, since the satellite can be launched warm and be cooled down once in position in the vacuum of space: the reduction in complexity from removing a vacuum shroud alone is remarkable. But cryogen-free cooling systems are not without their own handicaps. The increased mechanical complexity calls for redundancy in case of failure or wear, and there is often the need to over-dimension the cooling chain to account for unforeseen heat loads, as power may not be as readily available as it was in a stored cryogen system. In the deep end of the cryogenic chain, sub-Kelvin coolers are often one-shot systems that need to be thermally recycled from time to time, calling for either a redundant system or for ways to manage the thermal load due to the recycling phase. This is one of the drawbacks of using mechanical cryocoolers instead of cryogenic fluids: stored cryogens have a certain cooling capacity, and there is usually no real constraint on the rate at which heat can be absorbed — only the lifespan of the cryogen supply will change [7]. Mechanical cryocoolers, however, are designed to have a determined maximum cooling power: this means that for an application in which the heat load changes significantly with time (such as in systems that have one-shot components that need to be recycled) the cryocoolers will either not be able to cope with the extra heat load, or are over-dimensioned to fit those sporadic events. Even so, the advantages of using mechanical cryocoolers instead of cryogenic fluids for space applications outweighs their disadvantages.

One of the European Space Agency's next large-class scientific mission, [ATHENA](#) [8], is due to be launched in 2028. One of the characteristics of this mission is that it integrates a fully cryogen-free cooling chain, all the way from room temperature down to temperatures that will reach as low as 50 mK. One of the components under study for the lowest stage of the chain is a hybrid sorption/[ADR](#) cooler [9] developed by [CEA/SBT](#) in Grenoble. Being composed of one-shot coolers, this architecture inherently needs to be thermally recycled. This recycling process releases heat to the upper stages of the cooling chain, resulting in an increased heat load to the system over a short period of time: roughly 400 J in 30 min on a daily basis, which can compromise the stability of the upper stages of the chain, namely the pre-cooling stage of a Joule-Thomson cooler. There are two main ways to cope with this issue: either we oversize the upper stages of the chain in order to account for the heat coming from the recycling phase, or we find a way to temporarily store this heat load, and then releasing it gradually over a longer period of time. While the first solution means an overall increase in mass and volume due to more powerful cryocoolers whose extra cooling power would only be used during recycling of the sorption/[ADR](#) stage, the latter enables the heat load to be redistributed over time, resulting in a small increase in the average heat load instead of a large heat burst.

An enthalpy reservoir could be used to absorb this heat load released from the sorption/[ADR](#) stage without a significant temperature increase. This can be achieved either by using the sensible heat of selected materials or by taking advantage of the first order phase change of cryogenic fluids, be it at the triple point or somewhere along a saturation curve. This enthalpy reservoir or thermal Energy Storage Unit ([ESU](#)) can in turn be regenerated

after depletion but doing so during over a long period of time, effectively distributing the impact of the heat burst from the sorption/ADR into a much more manageable average heat load.

The present work consists in the development of a liquid hydrogen Energy Storage Unit operating between 15 K and 17 K, that is able to absorb a 400 J heat load coming from the sorption/ADR module over 30 minutes, with peaks that reach up to 1 W; these specifications are a result of data taken from other parts of the chain and were imposed by ESA. The ESU absorbs energy by taking advantage of the latent heat of evaporation of liquid hydrogen along the liquid-to-vapour saturation curve; this energy is then dumped over a period of 20 h to 24 h when the ESU is recycled, resulting in an average heat load lower than 15 mW at the 15 K stage instead of the much higher heat load released directly by the sorption/ADR stage.

Carried out in the framework of an ESA contract to develop a solution for absorbing a particular heat load at 15 K, this work deals with quite a few challenges that arise from working on space instrumentation, such as strict mass/volume budgets, limited cooling power, and liquid confinement in a micro-gravity environment. The project has had two phases: preliminary technology development and testing which resulted in the Development Model (DM) of the ESU, followed by a more carefully designed and built Engineering Model (EM). The objective was to experiment with the DM, and fine-tune its design and performance for an EM that could undergo severe environmental and operational tests. According to the ISO standard 16290 used by ESA (Space Systems - Definition of the Technology Readiness Levels (TRLs) and their criteria assessment [10]) this project aims to achieve a TRL 5, meaning that the components and their critical function have been validated in a relevant environment. As such, the EM underwent a series of functional, thermal and mechanical tests to assess not only its ability to withstand the harsh environment of a launch to space but also its capacity to perform as intended, with no changes when compared to its operation before launch.

This dissertation is divided into six chapters.

Chapter 1 is the present chapter and presents an introduction to this dissertation.

Chapter 2 establishes the relevance of the project within the framework of ESA's new large-class science mission, ATHENA. It gives an overview of ATHENA, the satellite in which the ESU is to be integrated and briefly describes the options considered for its cryogenic chain. It presents the challenge at hand and the trade-off that lead to the decision of developing a liquid hydrogen ESU. The various studied solutions are presented and discussed, eventually concluding why a liquid-to-vapour ESU was considered the best solution.

Chapter 3 describes the principle of operation of a liquid-to-vapour Energy Storage Unit, and provides the theoretical background needed to describe the operation of this device. It deals with the thermodynamics of using a dual-volume ESU and with the multiple hydrogen storage options at the various temperature stages.

Chapter 4 deals with the detailed sizing of the ESU according to the specifications

given by [ESA](#).

[Chapter 5](#) provides a description of how the sizing described in [Chapter 4](#) was implemented in the ground set-up and what mechanical and design decisions were adopted, both for the Development Model and the Engineering Model.

[Chapter 6](#) presents the most important results for both the Development and Engineering models. In both cases, experiments were carried out with an expansion volume during preliminary testing and with a metal hydride canister during a more advanced stage. The results obtained with both configurations are compared with the specifications given by [ESA](#) in order to assess its ability to perform correctly in a relevant environment.

[Chapter 7](#) summarises the main findings of this work and the lessons learnt from the many challenges faced. Future perspectives on the project and on how to further improve the performance of the ESU are given.

2 The challenge: working towards [ATHENA](#)

The European Space Agency ([ESA](#)) has officially selected [ATHENA](#) (the Advanced Telescope for High-ENERgy Astrophysics) as its second large-class science mission aiming to study “the Hot and Energetic Universe”, the science theme to be pursued by the Cosmic Vision’s programme; the official mission summary is shown in Table 2.1. Since its official selection in June 2014, the mission has moved into a study phase, where issues such as design and mission cost are addressed. It will then be proposed for “adoption” in 2019, and from that point onwards the actual construction of the spacecraft will be carried out; its launch is foreseen to take place in 2028 [8].

Table 2.1: [ATHENA](#) mission summary; adapted from [10].

ATHENA	
Advanced Telescope for High-ENERgy Astrophysics	
Cosmic Vision Themes	The Hot and Energetic Universe
Primary goals	Mapping hot gas structures and determining their physical properties Searching for supermassive black holes
Orbit	Halo orbit around L2, the second Lagrange point of the Sun-Earth system
Launch	2028
Lifetime	Five years, possible five-year extension
Type	L-class mission

[ATHENA](#) is an X-ray observatory with unprecedented capabilities in high resolution spectroscopy and wide field X-ray imaging, whose primary goals are the mapping of hot gas structures and determination of their physical properties and the search for supermassive black holes. According to the mission statement, it aims to answer two key questions in astrophysics: How and why does ordinary matter assemble into the galaxies and galactic clusters we see today? and How do black holes grow and influence their surroundings? [8]. Since no other observatory-class X-ray instrument is planned for the same time frame, [ATHENA](#) will be the sole instrument able to fill the gap for observations in this energy range [11] and the single most cryogenics-demanding mission for the next

10 years.

[ATHENA](#) will make use of the innovative silicon pore optics technology in order to achieve its science goals with a 2 m^2 effective collecting area with $5''$ angular resolution. Its science payload will consist of two instruments, the [X-IFU](#) (X-ray Integral Field Unit) and the [WFI](#) (Wide Field Imager) [12]. The [WFI](#) consists of an active pixel sensor camera with a $40' \times 40'$ field of view, high count-rate capability and high time resolution. The [X-IFU](#) is a cryogenic X-ray micro-calorimeter spectrometer that will employ a large array of transition-edge sensors, which need to be cooled down below 50 mK [11]. A depiction of both instruments can be found in Figure 2.1.

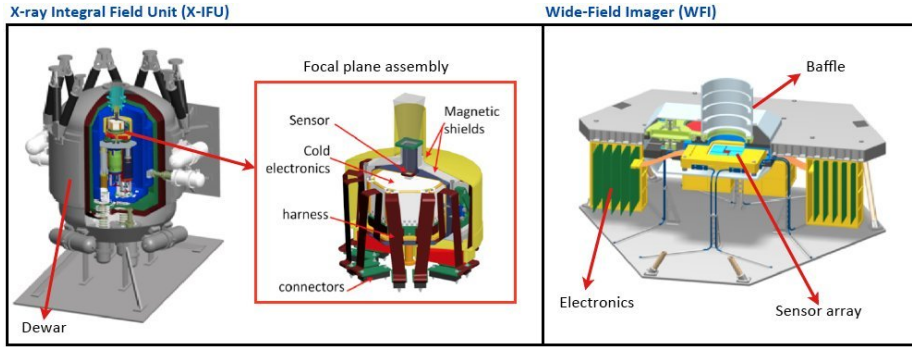


Figure 2.1: Scientific instruments on board [ATHENA](#) [13]. The [X-IFU](#) provides high spectral resolution, while the [WFI](#) enables a $12\text{ m} \times 12\text{ m}$ wide field view, coupled with high time resolution and a high count rate capability.

While previous missions relied on open-loop cryostats or coolers — Herschel for cooling at 1.6 K and Planck for sub-Kelvin cooling — this limited mission lifetime as the spacecraft ran out of cryogenic fluids: both lasted for approximately 4 years due to cryogen supply and not due to instrument failure. The aim for [ATHENA](#) is to take advantage of closed-cycle mechanical cryocoolers down to and at the sub-Kelvin range in order to increase the lifetime of the mission to at least 10 years [6]. Over the course of this chapter, the cryogenic chain for [X-IFU](#) will be presented, especially focussing on the last stage of cooling; solutions for dealing with some aspects of the proposed chain will be addressed and discussed.

2.1 Cryogenic chain for the [X-IFU](#) instrument

Europe has established itself in advanced cryocooler development over the last years, making it not only possible but highly likely to have a fully European cryogenic chain with a high TRL by the end of 2015 [11]. There is a mature heritage on this subject thanks to system studies for [IXO](#) (International X-ray Observatory) and [SPICA](#) (SPace Infra-red telescope for Cosmology and Astrophysics), where various cryogenic chains have been investigated to provide cooling down to the sub-Kelvin range. These studies have been put to good use when designing the cooling chains for both instruments on [ATHENA](#).

The detectors on X-IFU will require a complex cooling chain in order to comply with challenging requirements, such as a temperature of 50 mK with a cooling power higher than 1 μ W. Its cryogenic chain is composed of multiple cryocoolers and several intermediate temperature stages that can be divided into two parts: the upper cooling chain that is responsible for providing cooling power down to 2 K and the last stage cooler, which will cover the 2 K to 50 mK range. Figure 2.2 shows the most important types of coolers used for space applications depending on the temperature range and the achievable cooling power, as well as the cooling power of an ideal Carnot cooler using 100 W at room temperature.

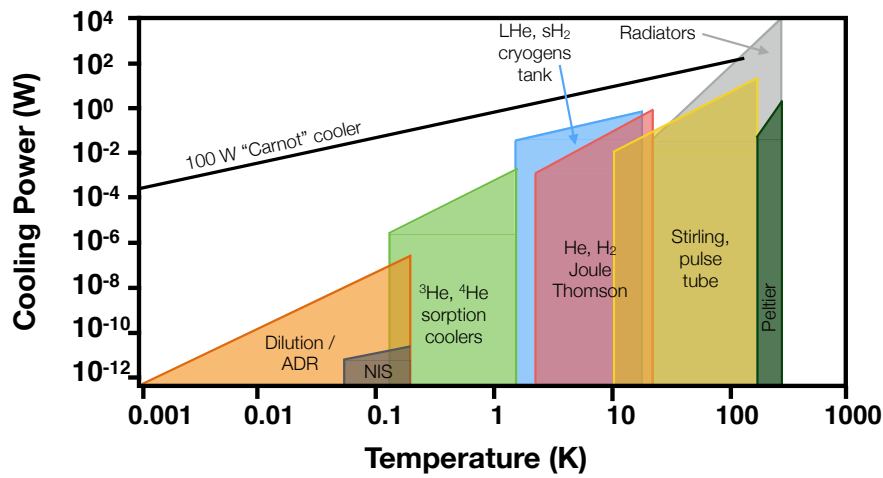


Figure 2.2: Types of coolers used in space: the range for each type is given in terms of cooling power *vs.* operating temperature. Adapted from [14].

Up to now, the proposed cryogenic chain for X-IFU (Figure 2.3) includes passive radiators for the upper stages and pulse tube and Joule-Thomson coolers for the temperature stages down to 2 K.

However, building a complete cooling chain for X-IFU remains an important challenge, and a definitive solution is yet to be defined. At both the 5th and 6th European Space Cryogenics Workshops, held by ESA in 2013 and 2015, multiple solutions were still being discussed and, as of December 2015, a definite cooling chain had not yet been chosen. While there are multiple alternatives for the upper stages of cooling, up to now only three technologies have been developed that are able to provide enough cooling power at sub-Kelvin temperatures and that have been qualified for space applications:

- Dilution refrigerators;
- Adiabatic Demagnetisation Refrigerators (ADR);
- ^3He evaporative cooling using a sorption pump.

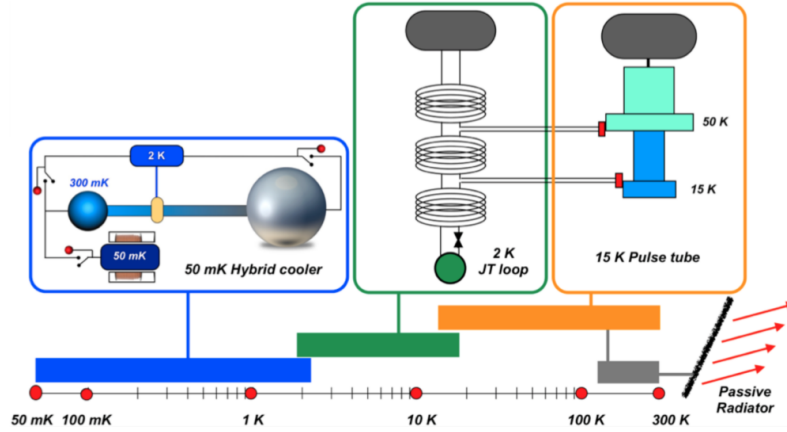


Figure 2.3: Proposed cryochain for the X-IFU instrument on board ATHENA. It makes use of passive radiators, pulse tube and Joule-Thomson coolers and a hybrid sorption/ADR cooler to cover the whole temperature range down to 50 mK [11].

While dilution refrigerators can provide continuous cooling down to 50 mK without recycling, the only version that has been qualified for space thus far is the open-cycle that integrated the cryogenic chain on-board Planck [15] for 4 years; this makes it unsuitable for ATHENA since the objective is to extend mission lifetime with an increased cooling power at a lower temperature, rendering the amount of ^3He isotopes at launch prohibitive. A closed-cycle version of the dilution refrigerator is under study [16], although not at the desired state of development since challenges like dealing with micro-gravity still need to be fully solved and tested.

The adiabatic demagnetisation refrigerator (ADR) is thermodynamically very efficient, providing the needed cooling power and it is unbeatable in terms of lowest achievable temperature. It does so without any moving parts, which is highly desirable for both space and sensitive applications as it eliminates mechanical wear and vibrations. But it comes with its own drawbacks: if used for an increased temperature range its mass and magnetic field intensity can become unmanageable, and it needs recycling since it is a one-shot system.

The ^3He sorption cooler is attractive due to its simplicity and low mass when compared to an ADR, with its main handicaps being an ultimate temperature limit of 200 mK and the need for recycling, since it is also a one-shot system. It also operates without any moving parts, and is a lightweight solution when compared to an ADR stage covering the same temperature range: it has been used successfully on-board Herschel during almost 4 years [17].

The solution that has been proposed for X-IFU's cooling chain is a hybrid one: by combining a sorption cooler with an ADR, continuous cooling can be achieved [6] and the main advantages of each system complement the other one's cons. By using a ^3He sorption cooler to pre-cool the ADR down to 300 mK, the mass and magnetic field of the ADR can be reduced substantially. This hybrid system is currently the baseline solution

for *ATHENA*. Figure 2.4 shows the sorption/ADR stage developed by CEA/STB during the study phase for the *SAFARI* [18] and *IXO* [19] missions. This type of device remains the most likely solution for the lower stages of *X-IFU*'s cooling chain due to its maturity level, obtained performance and overall compliance with requirements.

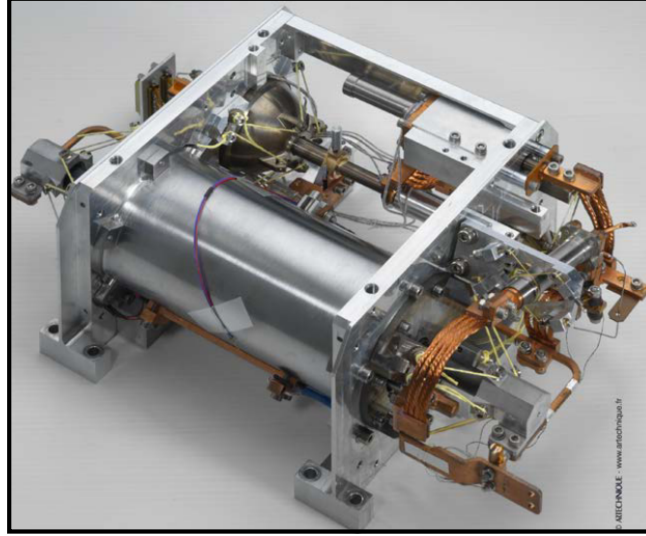


Figure 2.4: 50 mK hybrid cooler consisting of an ADR and a ^3He sorption stage, developed by CEA/STB and the reference solution for the last stage cooler of *ATHENA* [6].

2.2 CEA/STB's hybrid sorption/ADR cooler

In the framework of a Technological Research Program (TRP) funded by ESA, CEA/STB developed and extensively tested the Engineering Model of a hybrid ^3He sorption stage coupled to an ADR intended for either *ATHENA* or *SPICA* [9]. The device and its thermal environment are schematised in Figure 2.5.

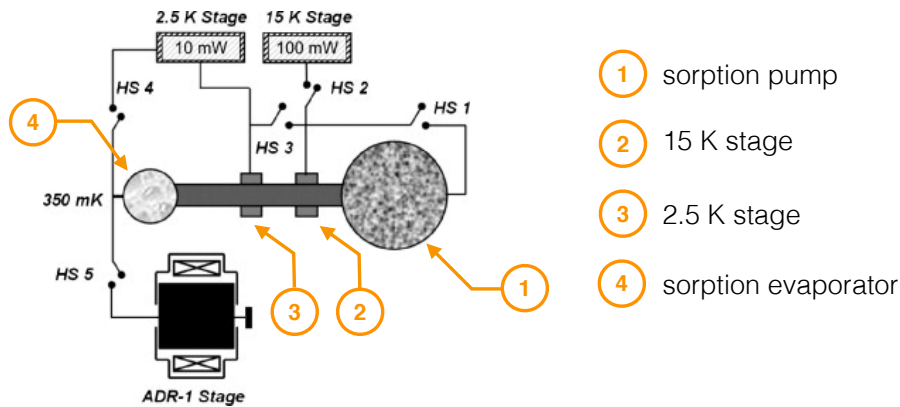


Figure 2.5: Association of a sorption cooler with an ADR, designed for the *IXO* mission, adapted from [9]. This version of the device features an intercept at 15 K for heat removal during the recycling stage.

This device can provide $1\text{ }\mu\text{W}$ at 50 mK and $10\text{ }\mu\text{W}$ at 300 mK and do so continuously for a period of 24 h , after which it needs to be recycled. During the recycling process the sorption pump is first heated to 45 K while ^3He condenses in the evaporator. Then the pump is cooled down to 15 K and then to 2.5 K [20]: its cooling from 45 K down to 15 K generates a heat load of roughly 400 J that needs to be managed. Recycling can be fully achieved in 8 h if 10 mW and 100 mW are available at 2.5 K and 15 K respectively (Figure 2.6). If the recycling phase is performed rapidly, large heat loads of up to 1 W can reach the 15 K stage: mechanical cryocoolers cannot cope with this kind of heat peak even for a short duration, and this heat load needs to be managed differently.

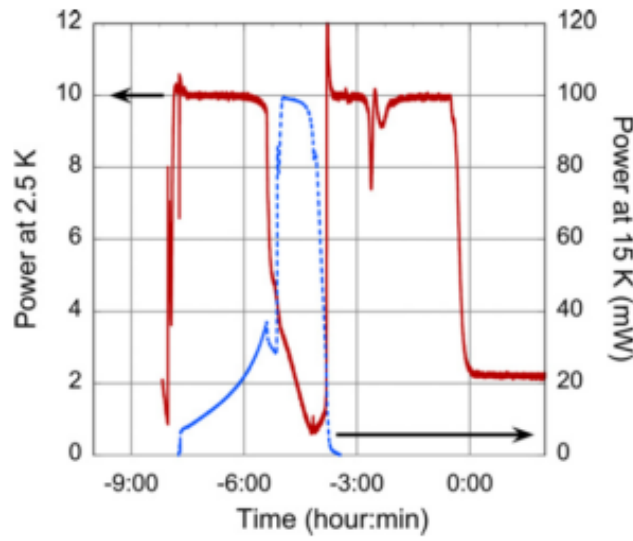


Figure 2.6: Heat load dissipated at the 2.5 K and 15 K heat intercepts in a nominal cycle of the system shown in Figure 2.5 [9]. The peak power dissipated at 15 K is $\approx 100\text{ mW}$.

The heat lift at both the 2.5 K and the 15 K stages is provided by the mechanical cryocoolers that sit higher up in the cryogenic chain. One way of dealing with the recycling phases of one-shot coolers is to oversize these upper stages, sizing them accordingly so that they can cope with the extra heat load generated by the recycling. This, however, means that the upper cooling stages are sized for a heat load that is larger than what is needed for most of the operating time. Moreover, this over-sizing can generate temperature oscillations due to an uneven heat load that can in turn provoke instabilities in the upper stages of the cooling chain.

Another way of dealing with the extra heat load is to distribute this heat load evenly throughout the whole operation time. For a nominal cycle, the recycling stage is 8 h long and the 15 K stage needs to absorb a heat load of up to 100 mW during roughly 1 h . However, if a heat load higher than 100 mW could be intercepted at the 15 K stage, this could decrease the recycling time significantly, increasing the duty cycle of the cooler and consequently increasing the observation time for the instrument.

This is where an enthalpy reservoir or Energy Storage Unit comes into play: it can

store thermal energy from the upper cooling stages during the operational time of the instruments (*i.e.* the operating time of the sub-Kelvin stage) and use that energy to absorb the large heat peak generated from recycling the sorption/ADR module. This makes it possible to design the mechanical coolers only for the average heat loads of the system, which has a significant impact on the cryogenic chain.

2.3 Addressing heat bursts at 15 K

An enthalpy reservoir works as a thermal buffer between the 15 K stage of the sorption cooler and the 15 K heat intercept of one of the foreseen cryogenic chain configurations (Figure 2.7): the sorption stage releases a certain heat load that is absorbed by the enthalpy reservoir without a large temperature increase, and hence not transmitting this heat load directly to the 15 K cooler. This can be done over a longer period of time, when the enthalpy reservoir is itself regenerating in a process that will by design use up a lower cooling power than the one originally needed to directly absorb the heat load from the sorption cooler. A comparison can be made with the process described in Figure 2.8.

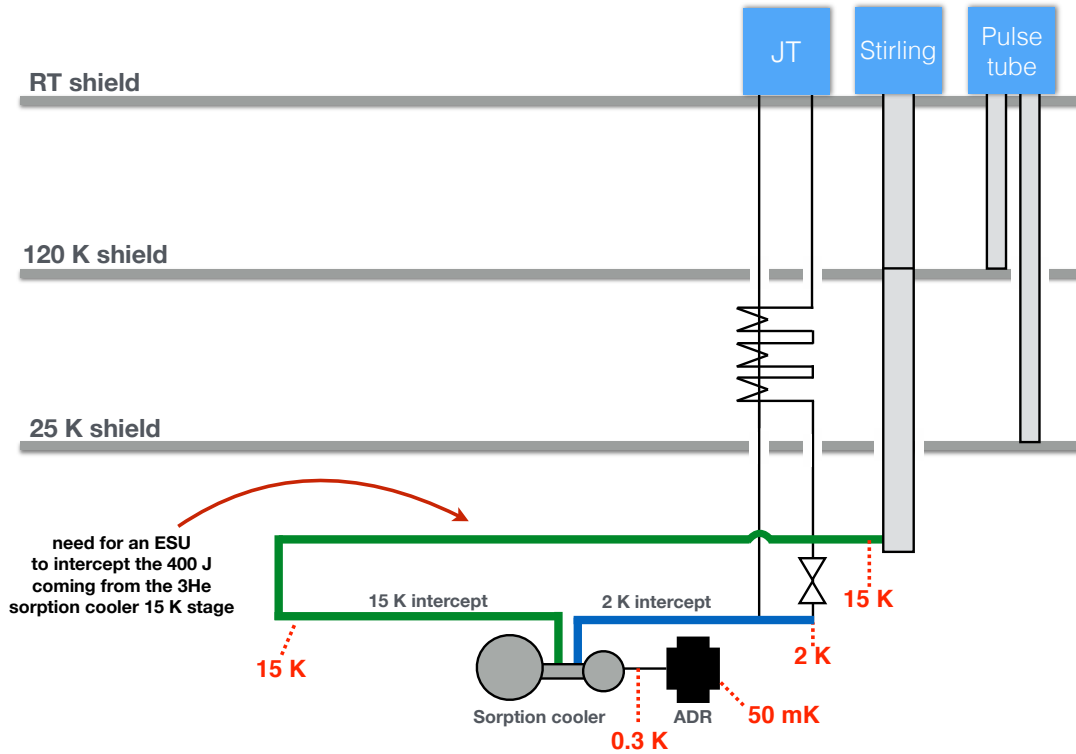


Figure 2.7: One of the possible cryogenic chain configurations for X-IFU on ATHENA, with a hybrid sorption/ADR cooler for the last stage of cooling. An enthalpy reservoir or ESU could be placed between the 15 K cooler and the sorption cooler heat intercept at the same temperature.

Consider a heating profile that has a heat load $\dot{Q}_{HL,max}$ during δt that is higher than the average cooling capacity \dot{Q}_C at that interface, and that is lower than that ($\dot{Q}_{HL,min}$) for

the rest of the time period P . During the period $P - \delta t$, there is excess cooling capacity and the enthalpy reservoir is storing this extra thermal energy E_{stored} . When the heat load becomes higher than the average cooling capacity $\dot{Q}_{cool,avg}$ the energy that was stored by the enthalpy reservoir is used (E_{used}). For the enthalpy reservoir to be efficient, E_{stored} needs to be equal to E_{used} . In the case of the sorption cooler, the recycling phase will produce a heat load $\dot{Q}_{HL,max}$ during a δt of 30 min that will need to be absorbed using the enthalpy reservoir's stored energy, and the system will have an average available cooling power $\dot{Q}_{cool,avg}$ of 15 mW.

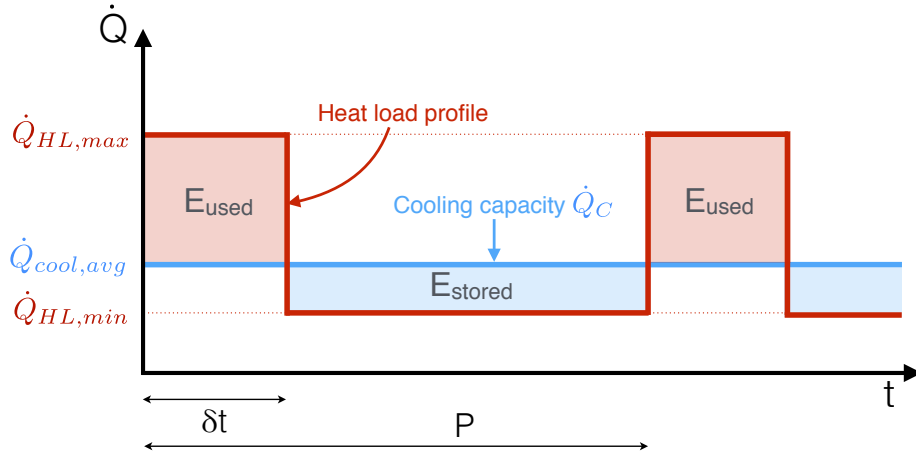


Figure 2.8: Operation of an enthalpy reservoir on an interface with a variable heat load. Adapted from [21].

In the framework of this application, there are three possible solutions to store the required thermal energy in the 15 K to 17 K range (as per FPR 3 of [Appendix A](#)):

- using the specific heat of solid materials;
- using the latent heat of solid-to-liquid phase change at the triple-point transition of a pure substance;
- using the latent heat of liquid-to-vapour phase change of cryogenic substances.

As with most challenges, there is no universal answer to the problem at hand and the solution must be a trade-off between the options available at this temperature range and the restrictions imposed by [ESA](#) requirements: a solution that might seem straightforward might not comply with the mass budget, for example. These three options must be compared in terms of competitiveness according to the given requirements of temperature stability and of the resulting mass and volume of the solution for the amount of energy that needs to be stored.

2.3.1 Specific heat of solid materials

One way of storing thermal energy is using the specific heat of a solid material, which is the quantity of heat required to raise the temperature of a unit quantity of the substance by unit of temperature. By allowing a material with a high heat capacity C to change its temperature (*i.e.* from 15 K to 17 K), a significant amount of energy $Q = C\Delta T$ can be stored even along a small temperature increase. The specific heat of solid materials at low temperature is a function of the Debye temperature θ_D and obeys the relation $c = f(\frac{T}{\theta_D})$, with an extra contribution AT due to electrons in the case of a metallic material; at temperatures below $\theta_D/10$, this specific heat will be proportional to T^3 [22]. One quickly arrives at the conclusion that the specific heat of most materials will be rather low at the temperature range of interest of this project: in the 15 K to 17 K range, only materials with a low Debye temperature θ_D will still be somewhat competitive. This is the case of lead, for which the Debye temperature is 105 K [23]: an ESU using lead has been developed at the Cryogenics Laboratory at FCT/UNL (Figure 2.9) that is able to store 36 J between 11 K and 20 K with a cold mass of only 102 g of lead (9 cm³) [24]. For absorbing 400 J along a temperature increase of 2 K, however, a solution using lead might reveal itself to be too heavy (see Table 2.2).

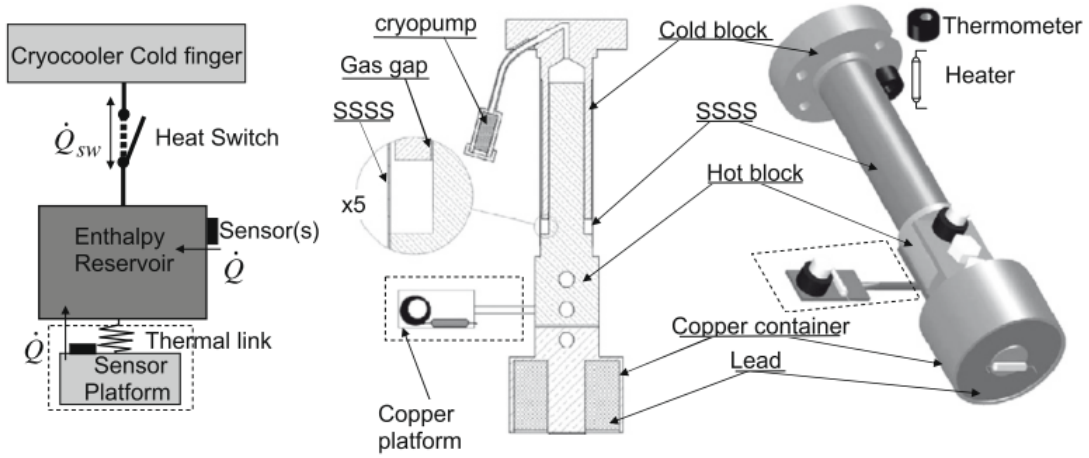


Figure 2.9: General scheme of the lead solid-state ESU, coupled to a gas-gap heat switch (GGHS), and where a copper platform for the sensor is visible. Adapted from [24].

However, if a material undergoes a magnetic change transition it will display a second-order transition with a relatively high associated entropy change, giving rise to a peak in its specific heat. Due to this property, these materials are most often used as regenerator materials in regenerative cryocoolers. An ESU that takes advantage of these kind of materials has been developed at the Cryogenics Laboratory at FCT/UNL [25] where Gd₂O₂S was used to absorb 36 J between 3 K and 6 K: Gd₂O₂S has a specific heat peak at 5.2 K due to a paramagnetic-to-anti-ferromagnetic phase transition. Even though the

153 g of $\text{Gd}_2\text{O}_2\text{S}$ spheres had to be embedded in a copper reservoir filled with helium gas, the cold volume did not exceed 40 cm^3 , making it a rather compact solution as shown in Figure 2.10.

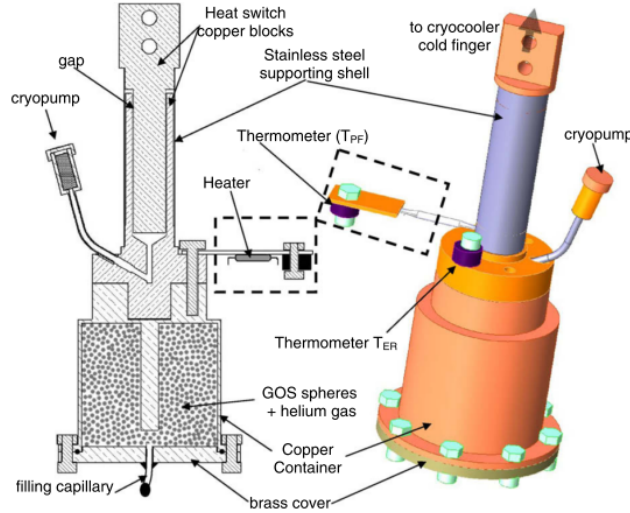


Figure 2.10: Drawing of the $\text{Gd}_2\text{O}_2\text{S}$ solid-state ESU. It can be seen that in addition to the $\text{Gd}_2\text{O}_2\text{S}$ spheres, a copper mass was needed to confine them and helium gas was used to promote thermal homogeneity. Adapted from [25].

Considering the need to work between 15 K and 17 K, Figure 2.11 shows a selection of materials that have a high specific heat around the temperature range of interest, as well as some well-known materials for comparison.

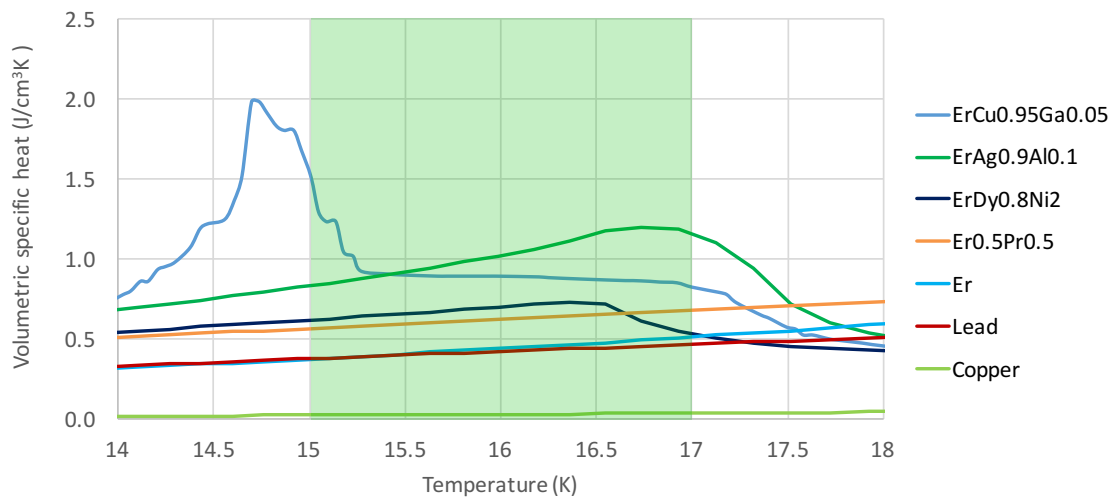


Figure 2.11: Specific heat of selected materials in the 14 K to 18 K range, data from [26, 27, 28]. The highlighted zone represents the area of interest for the ESU.

Although no materials have a specific heat peak between 15 K and 17 K as far as we know, the so-called regenerator materials containing rare earth elements are significantly competitive when compared to copper, for example, and they might be suitable for a solid-state ESU. Table 2.2 compares these materials by listing the mass and volume needed for each of them to store 400 J between 15 K and 17 K; the equivalent copper mass needed to achieve the same energy storage is given for comparison.

Table 2.2: Sensible heat materials and their properties for 400 J of thermal energy storage between 15 K and 17 K. Density of alloys was estimated to be between 8 g/cm^3 and 12 g/cm^3 for mass calculations.

Material	Enthalpy 15 K to 17 K J/cm^3	Volume for 400 J cm^3	Mass for 400 J kg	Ref.
Copper	0.066	6077	54.4	[26]
Lead	0.849	470	5.3	[27]
$\text{ErAg}_{0.9}\text{Al}_{0.1}$	2.070	190	1.5 to 2.3	[27]
$\text{ErDy}_{0.8}\text{Ni}_2$	1.333	300	2.4 to 3.6	[27]
Erbium	0.890	450	4.0	[27]
$\text{Er}_{0.5}\text{Pr}_{0.5}$	1.252	320	2.6 to 3.8	[27]
$\text{ErCu}_{0.95}\text{Ga}_{0.05}$	1.821	220	1.8 to 2.6	[28]

A solid-state ESU made out of $\text{ErAg}_{0.9}\text{Al}_{0.1}$ that operates between 15 K and 17 K, absorbing 400 J, would have a mass between 1.55 kg and 2.32 kg and a volume of 193 cm^3 , making it the best solution amongst the selected materials at this temperature range, closely followed by $\text{ErCu}_{0.95}\text{Ga}_{0.05}$. One would need 54.5 kg of copper to absorb 400 J, whereas only 1.55 kg to 2.32 kg of $\text{ErAg}_{0.9}\text{Al}_{0.1}$ would be required to obtain the same result: this represents a 23 to 35-fold reduction in mass, which in space applications is not only desirable but sometimes also vital. This may not, however, be an indisputable solution: even though the volume is not a problem, a mass greater than 500 g at low temperature clearly surpasses what is allowed by ESA (cf. PRR 2 of Appendix A), even though there would be no additional mass at the other temperature stages. In addition to this, alloys like $\text{ErAg}_{0.9}\text{Al}_{0.1}$ often come in small spheres and as such would have to be embedded in a matrix or closed cell (such as copper) before being used (see Figure 2.10), further increasing the cryogenic mass.

2.3.2 Triple point cells

The latent heat of a first-order phase change of a cryogenic fluid can be used to absorb heat from a system: as an incremental mass dm undergoes a phase change with associated latent heat L , it absorbs thermal energy $Q = Ldm$ in the process. The phase change in question can be liquid-to-vapour, solid-to-vapour, solid-to-liquid or even solid-to-solid; the latter occurs when the substance suffers a change in its crystalline structure.

Using the solid-to-liquid phase change at the triple point of a cryogenic fluid is an

“elegant” solution in the sense that it allows for energy to be absorbed at constant temperature and pressure: according to Gibbs’ phase rule, there are three coexisting phases and therefore no available degrees of freedom: as long as the three are present, both pressure and temperature will remain constant for the duration of the phase change. In a closed triple-point cell, the working fluid is first allowed to undergo solidification, although a small percentage of vapour still coexists with the solid; when heat is applied, this mainly leads to the solid melting at a constant temperature. However, this process is accompanied by a spontaneous exothermic condensation of part of the vapour that still exists in the cell so that the pressure is kept constant throughout the whole transition; this happens because the liquid that is formed is less dense than the originating solid. As a consequence, the net energy absorbed during this transition is slightly less than that of the solid-to-liquid latent heat (Figure 2.12); nonetheless, the energy absorbed during a phase change at the triple point can be, to a good approximation, considered to be the solid-to-liquid latent heat. This solid-to-liquid latent heat is considerably smaller than the latent heat of liquid-to-vapour phase change in the temperature range near to the triple point; although this type of device allows for heat absorption at constant temperature and pressure, the price to pay for this lower latent heat is usually an increase in the size of the cold cell.

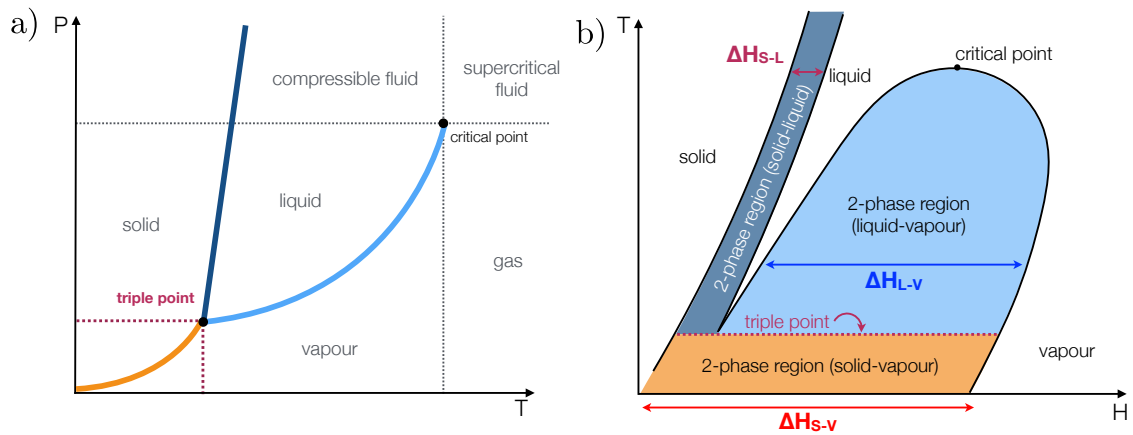


Figure 2.12: Triple point phase change: a) Pressure-temperature diagram; the phase change occurs at constant temperature and pressure. b) Temperature-Enthalpy diagram. In a triple-point ESU, only the solid-to-liquid enthalpy change is usable.

Many triple-point cells have been explored for space applications, namely Lockheed’s nitrogen triple-point thermal storage unit [29], which was able to store 18 kJ at 63.15 K. This device has a single-volume configuration, the cold volume, and no additional ones at room temperature. The triple-point cell was a 22.5 cm diameter sphere that needed to be charged with 130 bar at room temperature: this high filling pressure is often a problem when using single-volume devices, as it makes for thick-walled cells at low temperatures that may not comply with the mass budget for that interface.

As shown in Table 2.3, there is only one cryogenic fluid that has its triple-point in the temperature range of interest: hydrogen. CEA/STB has developed a triple-point cell working at the triple-point of hydrogen that was able to store 10 J at 14 K [30], shown in Figure 2.13.

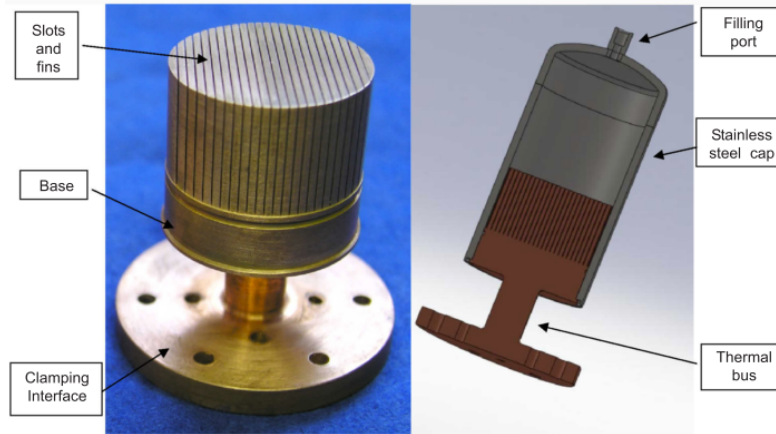


Figure 2.13: Thermal Storage Unit using the triple point of hydrogen, developed by CEA/STB [30]; the diameter of the cell is 30 mm.

To our knowledge, this is the only ESU to have been developed in the temperature range we are interested in. It used up 2.22 cm^3 of hydrogen in the solid phase and was tested in both single-volume and dual-volume configurations (see Section 2.3.3); for the single-volume configuration the cold cell needed to be filled with 80 bar at room temperature, and this set-up absorbed 10 J — we would need to absorb 40 times that amount, which in turn would lead to a cold cell capable of storing roughly 88 cm^3 of solid hydrogen. From Figure 2.13, it is evident that this increase in solid amount would lead to a very large and heavy cold cell or to prohibitive filling pressures.

Table 2.3: Triple point temperature and pressure of cryogenic fluids below 80 K. Data was calculated using REFPROP [31].

	Temperature (K)	Pressure (mbar)
hydrogen	13.957	73.6
para-hydrogen	13.803	70.3
neon	24.556	433.7
fluorine	53.481	2.4
oxygen	54.361	1.5
nitrogen	63.151	125.2

2.3.3 Liquid-to-vapour phase change

Contrary to solutions that take advantage of the specific heat of certain materials, in which heat absorption inherently leads to a temperature increase (even if a small one), a phase-change enthalpy reservoir can absorb heat without suffering a change in its temperature as long as the pressure in the system is kept constant. In Figure 2.14, these first-order transitions are displayed: for the evaporation of a substance, for example, there is a change in enthalpy ΔH_{L-V} (*i.e.* a large amount of heat can be absorbed) in a process that occurs at constant temperature.

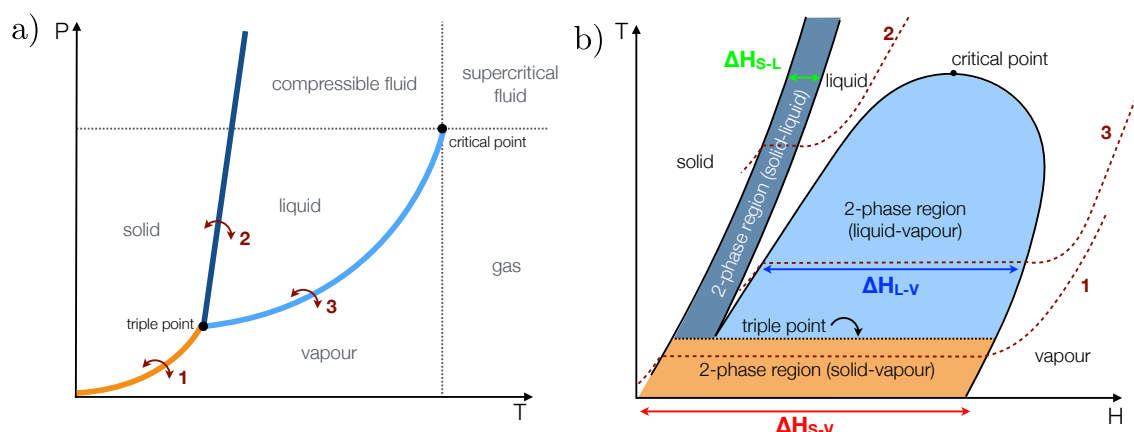


Figure 2.14: Different first-order phase changes of a pure fluid, where 1 is a solid-to-vapour transition, 2 is a solid-to-liquid transition and 3 is a liquid-to-vapour transition. These phase changes are represented in a) a Pressure-temperature diagram and b) a Temperature-Enthalpy diagram, where the relative enthalpy change for each transition can be seen.

The phase changes represented in Figure 2.14 all occur at constant pressure and hence at constant temperature; however, if this process takes place in a closed system, then the pressure can no longer be kept constant and the heat absorption will occur along the saturation curve of the substance, where the temperature increase depends on how much the pressure is allowed to increase. In the case of a liquid-to-vapour phase change ESU, there can be a considerable increase in pressure as the liquid evaporates, which is why there needs to be room to store the gas: this can be done in a single-volume or in a double-volume configuration.

A single-volume ESU consists only of a cold cell, that contains the total amount of working fluid and that is filled and sealed at room temperature; a dual-volume configuration has a cold cell and a room temperature expansion volume to house the evaporated gas (Figure 2.15). While a single-volume system can be simpler and overall more compact, it needs to be filled at high pressures at room temperature so that there is an appreciable amount of liquid at low temperature; even so it is only partially filled at low temperature. This in turn makes for thick-walled, large pressure vessels at low temperature, increasing

the overall mass of the system. Dual-volume configurations can be made lighter, smaller and with thinner walls on the cold part, with the drawback that there is a volume at room temperature that acts as a pressure buffer, housing the working fluid and hence drastically reducing the filling pressure. This way the cold volume can be designed to be completely full at low temperature, resulting in it being quite small.

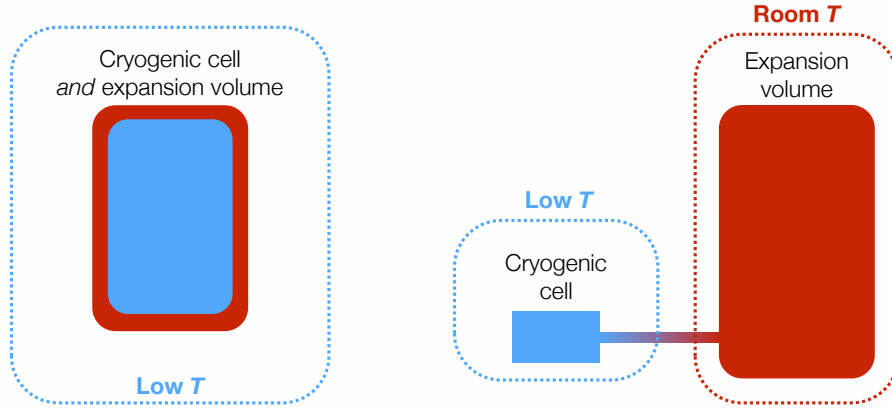


Figure 2.15: Two possible configurations for a cryogenic energy storage unit; adapted from [21].

The latent heat of vaporisation of a substance varies along the saturation curve, being the highest as it approaches the triple point and vanishing to zero when it reaches the critical point. As such, while it might not be a competitive solution to use the liquid-to-vapour transition at temperatures nearing the critical point, doing so close to the triple point can result in a device that is able to absorb a considerable amount of heat using a small quantity of liquid. Figure 2.16 depicts the cryogenic fluids whose liquid-to-vapour curves or triple points fall below 50 K; it is noticeable that for the temperature range of interest (15 K to 17 K), hydrogen is the only candidate.

Figure 2.17 shows the latent heat of normal hydrogen along its saturation curve, as well as the latent heat at the triple point. It is evident from the plot that using the liquid-to-vapour phase change can be much more advantageous than the solid-to-liquid transition at the triple point.

The amount of hydrogen needed to absorb 400 J between 15 K and 17 K is significantly lower than that needed for the same energy absorption at a triple-point transition. Considering that the latent heat L of the liquid-to-vapour phase change is kept constant at $\approx 918 \text{ J mol}^{-1}$ [31] between 15 K and 17 K, the amount of liquid hydrogen Δn_{H_2} that needs to be evaporated in order to absorb an amount of energy Q is given by:

$$\Delta n_{H_2} = \frac{Q}{L} \quad (2.1)$$

If $Q = 400 \text{ J}$, then $\Delta n_{H_2} \approx 0.44 \text{ mol}$. Since the liquid density ρ_{liq} of hydrogen in this temperature range is $\approx 37 \text{ mol/dm}^3$, it means that $\approx 12 \text{ cm}^3$ of liquid hydrogen are enough

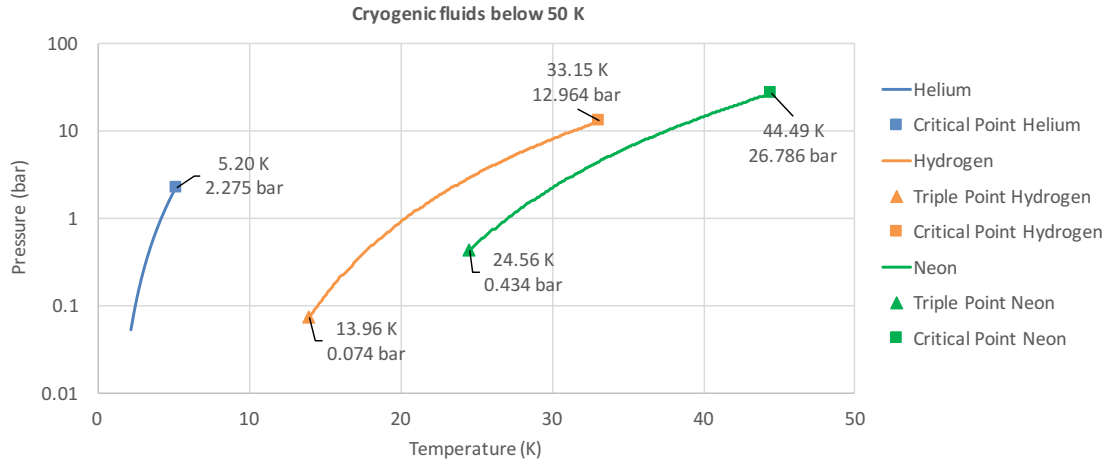


Figure 2.16: Cryogenic fluids available in the temperature range; data from [REF-PROP](#) [31].

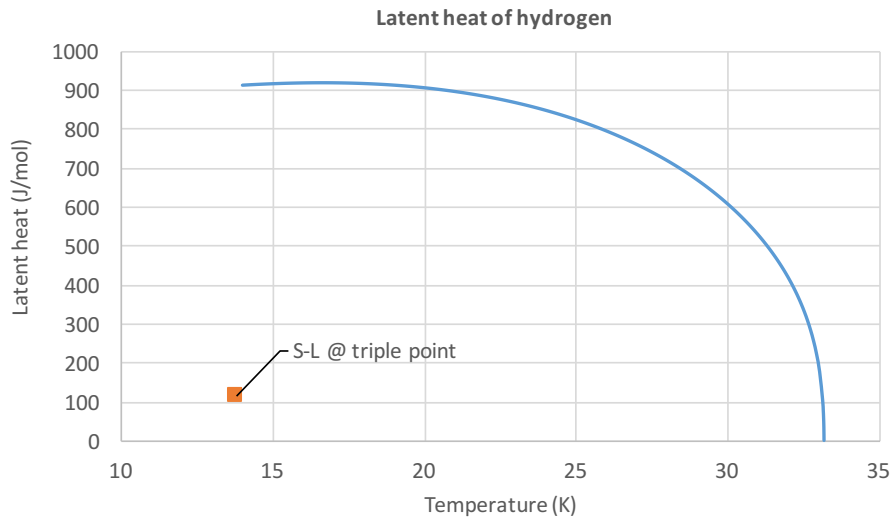


Figure 2.17: Latent heat of normal hydrogen along the liquid-to-vapour saturation curve; the square symbol indicates the solid-to-liquid latent heat at the triple point. Data from [31, 32].

to absorb the necessary thermal energy. This is a significantly smaller volume at low temperature than the one needed for the specific heat (Table 2.2) or triple-point solutions (Section 2.3.2).

However, one of the main drawbacks of using a liquid-to-vapour thermal ESU to absorb heat instead of a triple point cell is that in a closed system the pressure, and hence the temperature, are not kept constant: the temperature will increase with the pressure along the saturation curve, as the vapour formed from the evaporated liquid will exert an increasing pressure upon the system. The pressure increase will depend on the volume that is available for the gas to expand to. Actually, single-volume configurations are most often used for solid-to-solid or solid-to-liquid transitions where there is not a significant change in density, and as such the phase change does not cause a significant pressure variation. For a liquid-to-vapour ESU this option can lead to prohibitive pressures in most cases, or to volumes at low temperature that are too large to fit the budget. Table 2.4 shows some possibilities for single-volume and dual-volume solutions using the liquid-to-vapour transition of hydrogen that can absorb 400 J of thermal energy between 15 K and 17 K.

Table 2.4: Expansion volume characteristics needed at different temperature interfaces for the cold cell to be able to store 400 J between 15 K and 17 K using the liquid-to-vapour phase change of hydrogen. Computed using the model described in [33] and summarised in Section 3.4.

Configuration	Temperature (K)	Volume (ℓ)	Pressure at RT (bar)
Single volume	15-17	3.2	5.6
Dual volume	25	4.6	3.8
Dual volume	120	22	0.795
Dual volume	300	56	0.318

2.4 The proposal: a liquid hydrogen thermal buffer

Multiple options for dealing with a 400 J heat burst at 15 K have been presented and discussed throughout the previous sections, each one with its advantages and drawbacks: Table 2.5 provides a summary of the best options considered for such an ESU.

The requirements given by ESA need to be taken into account when selecting (or discarding) the best solution. In cryogenics in general, and in space applications in particular, the mass and volume at low temperature are the most costly ones, and should be avoided: this discards using $\text{ErAg}_{0.9}\text{Al}_{0.1}$ due to its ≈ 2 kg at 15 K, when it should not exceed 500 g according to PRR 2 of Appendix A. Moreover, the low temperature mass would be even higher, since the $\text{ErAg}_{0.9}\text{Al}_{0.1}$ spheres need to be embedded in a matrix that provides good thermal conductivity and homogeneity. Using the triple-point transition of hydrogen also poses its issues, since the available cooling source is at 15 K and not 14 K

Table 2.5: Summary of the different solutions proposed for an ESU operating between 15 K and 17 K. Note that the masses and volumes considered are only those of the active heat absorbing material; no housing was considered for any of the options.

	Mass at LT (g)	Volume at LT (cm ³)	Volume at RT (ℓ)	Comments
C_p of $\text{ErAg}_{0.9}\text{Al}_{0.1}$	≈ 2000	193	–	
Single-vol. S–L–V H_2	6.8	88	–	≈ 80 bar at LT
Dual-vol. S–L–V H_2	6.8	88	1.9	
Single-vol. H_2 L→V	0.9	3200	–	≈ 6 bar at RT
Dual-vol. H_2 L→V	0.9	12	56	0.3 bar at RT

which is the triple-point temperature of hydrogen, and in the case of the single-volume solution would also mean a significant mass at low temperature due to the reservoir being able to withstand 80 bar.

The solution that provides the best trade-off at the low temperature stage is a liquid-to-vapour hydrogen ESU: the useful mass for absorbing the heat load is under 1 g and has a volume of only 12 cm³, and since the working pressure is kept sub-atmospheric (≈ 300 mbar), the cold reservoir can be made small and light. Although the expansion volume at room temperature is quite large (56 ℓ) in order to restrict the temperature increase in the cold cell to 2 K, other options can be used to achieve a more compact solution. Figure 2.18 illustrates the possible integration of this device in the cooling chain.

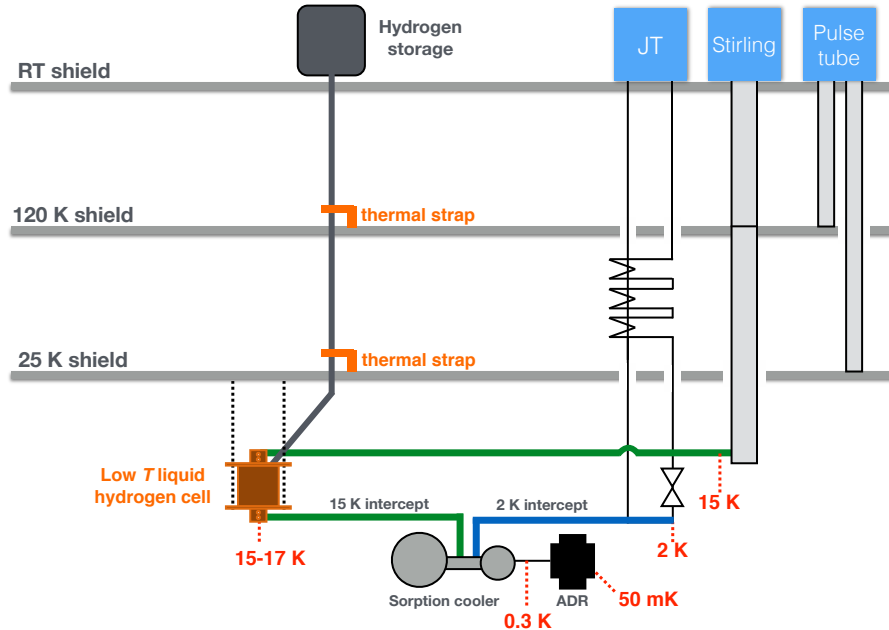


Figure 2.18: Possible cryogenic chain configuration for X-IFU on ATHENA, with the liquid hydrogen ESU integrated between the 15 K stage of the chain and the sorption/ADR cooler heat intercept.

Over the years, the Cryogenics Laboratory at [FCT/UNL](#) successfully developed and tested liquid-to-vapour Energy Storage Units for different temperature ranges using different working fluids, such as nitrogen [33, 34] or, more recently, neon [35, 36]. These previous works, having been developed in the scope of space applications, have provided the laboratory with the know-how and experience for dealing with the multiple challenges that come from working with this type of device under strict budget requirements. This previous experience, along with the fact that the liquid-to-vapour hydrogen [ESU](#) is the most suitable device to fit the low temperature constraints, led it to be chosen as the solution for dealing with the challenges at hand.

3 A liquid hydrogen thermal buffer

A liquid-to-vapour thermal Energy Storage Unit using hydrogen as the working fluid was chosen to address the 400 J heat bursts at 15 K. This chapter gives an overview of hydrogen properties and of the issues that arise when working with condensed forms of hydrogen at low temperature. Although the basics of a phase-change ESU have been briefly explained throughout the last chapter, a more detailed description of the processes that take place in this system is given, as well as the base thermal model used for the different parts of the cycle.

Hydrogen was first liquefied by James Dewar in 1898 using the Joule-Thomson effect, being the second-to-last “permanent gas” to be condensed (helium was finally liquefied in 1908 by Kamerlingh Onnes); its solid phase was obtained in 1899. Interest in the condensed forms of hydrogen was confined to the scientific community simply as a laboratory curiosity until the mid-1940’s, when aerospace and nuclear programs developed an increasing interest in hydrogen and its more compact storage: hydrogen technology was born and remains very much alive to this day, now being regarded as a promising energy carrier for the automotive industry, for example. It is the only fluid available as a liquid in the temperature range from 25 K down to 14 K: when designing a liquid-to-vapour enthalpy reservoir in this temperature range, hydrogen is the only available option. Table 3.1 summarises some key properties of parahydrogen and normal hydrogen: the difference between the two is detailed in Section 3.1.

3.1 Molecular forms of hydrogen

One of the distinguishing features of hydrogen is that it can exist in two different molecular forms (spin isomers): orthohydrogen (*o*-H₂) and parahydrogen (*p*-H₂). Orthohydrogen is the higher energy state, in which the spins of the protons ($I = 1/2$) in the two nuclei that compose the hydrogen molecule are coupled in the $J = 1$ state, which is a triplet state, while the lower energy parahydrogen state corresponds to the singlet $J = 0$ coupling; Figure 3.1 illustrates these two states and their relative energy level. The different states present differences in the specific heat and in the thermal conductivity, although these

Table 3.1: Physical constants of normal hydrogen and parahydrogen, calculated using REFPROP [31].

	Normal hydrogen	Para hydrogen
Normal boiling point	20.3 K	20.227 K
Latent heat of vaporisation at NBP	905.0 J mol ⁻¹	899.6 J mol ⁻¹
Melting point at 1 atm	13.988 K	13.831 K
Latent heat of fusion at 1 atm	914.7 J mol ⁻¹	907.3 J mol ⁻¹
Triple point temperature	13.957 K	13.803 K
Triple point pressure	73.6 mbar	70.4 mbar
Critical temperature	33.145 K	32.938 K
Critical pressure	12.96 bar	12.86 bar

differences are negligible for the temperature range of interest.

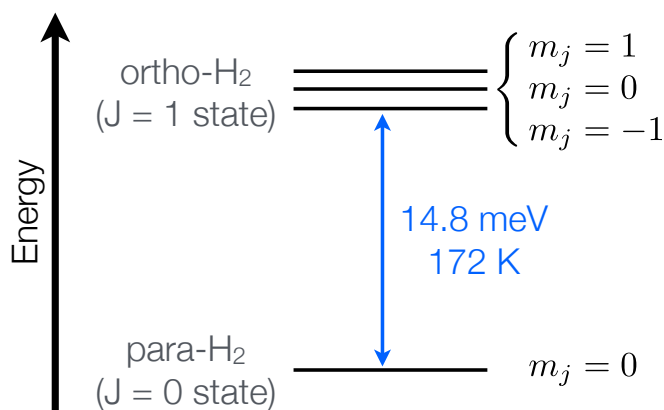


Figure 3.1: Spin isomers of the hydrogen molecule, ortho- and parahydrogen.

At room temperature, there is enough thermal energy available for equal occupation of the four quantum states, meaning that 3/4 of the hydrogen molecules will be in the ortho state and the remainder will be in the para state: equilibrium hydrogen at this temperature effectively consists of 75% ortho-hydrogen and 25% para-hydrogen (this “mixture” is called normal hydrogen). However, as temperature decreases and thermal energy ceases to be available, para-hydrogen is the dominant form (Figure 3.2). Under these conditions, ortho-hydrogen will spontaneously transition to the less energetic para-hydrogen: as this conversion from a higher to a lower energy state takes place, energy is released in the form of heat. The implications of this exothermic process are of extreme importance when dealing with liquid hydrogen, as the heat of conversion from ortho- to para-hydrogen largely surpasses the latent heat of the liquid-to-vapour transition: if hydrogen is allowed to condense without undergoing conversion, the now liquid hydrogen that still retains the 75% *o*-H₂–25% *p*-H₂ will slowly transition to the new equilibrium ratio: if we take the heat of conversion from *o*-H₂ to *p*-H₂ at 20 K, which is 1416.9 J mol⁻¹, and compare it with the latent heat of vaporisation at the same temperature (904.5 J mol⁻¹), it is easily

understood that the conversion process itself can boil-off up to 70% liquid hydrogen [32] that was condensed without reaching equilibrium. Table 3.2 gives the equilibrium composition of hydrogen at different temperatures and the heat of conversion involved in the process.

Table 3.2: Ortho-para hydrogen data (adapted from [32]): equilibrium composition of hydrogen and heat of conversion from *o*-H₂ to *p*-H₂.

Temperature (K)	H ₂ , % in para form	Heat of conversion J mol ⁻¹
10	99.9999	1416.90
20	99.821	1416.91
30	97.021	1416.90
40	88.727	1416.85
50	77.054	1416.12
60	65.569	1412.59
70	55.991	1402.48
80	48.537	1381.41
90	42.882	1345.99
100	38.620	1294.70
120	32.99	1148.40
150	25.974	866.82
200	25.264	440.16
300	25.072	74.1

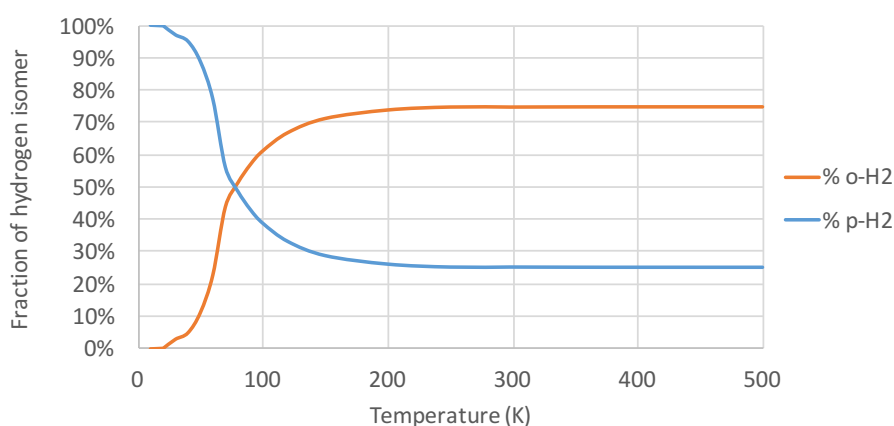


Figure 3.2: Fraction of equilibrium ortho- and para- species in hydrogen as a function of temperature.

When storing liquid hydrogen, the only reasonable solution is to convert the hydrogen to its equilibrium composition previous to condensation, while still in the liquefier. This is achieved either by using catalysts or by allowing a very slow condensation, so that there is time for the hydrogen to gradually convert from *o*-H₂ to *p*-H₂. This brings us to another peculiarity of the ortho-to-para conversion: it is a slow process when hydrogen is in the

liquid form, and it does not occur at all in the vapour phase [32, 37]. The low temperature ($< 20\text{ K}$) evolution of the percentage of $o\text{-H}_2$ over a period of time t can be given by

$$x_{ortho\text{-H}_2} = \frac{1}{a + kt} \quad (3.1)$$

where $1/a$ is the starting fraction of $o\text{-H}_2$ and k is the rate of conversion (0.0114 h^{-1} [32]). Starting at room temperature, $1/a = 0.75$ and the rate of conversion can be computed. Figure 3.3 shows the fraction of ortho-hydrogen as a function of time during a conversion process.

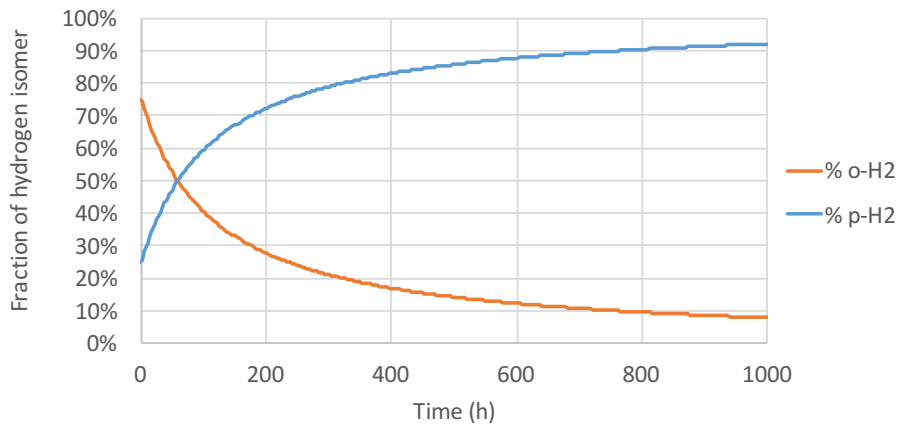


Figure 3.3: Fraction of ortho- and para-hydrogen as a function of time during a conversion process at low temperature (below 20 K).

It is evident that the conversion process is rather slow when compared to the duty cycle of the ESU, which should complete a full cycle in 24 h. Unless there are catalysts present in the system, the heat load released by conversion should be negligible, as very little $o\text{-H}_2$ should convert during one complete cycle. The consequences of this information will be discussed later, although it implies that there is no point in trying to convert hydrogen while in gas form at temperatures higher than the cold cell temperature where condensation occurs.

3.2 Basics of liquid-to-vapour phase change

For a pure substance to undergo a phase change at constant pressure, an amount of energy must be supplied to (or removed from) the system, depending on the direction of the phase change: if the transition is to a more ordered state (*i.e.* to a state with less entropy), this energy will be released in the form of heat (*e.g.* vapour-to-liquid phase change); inversely, if the transition occurs from a more ordered state to a less ordered one, the system will need to absorb energy from its surroundings in order for the phase change to occur. Figure 3.4 illustrates the changes in enthalpy for a phase change at a pressure P_1 for a generic pure substance.

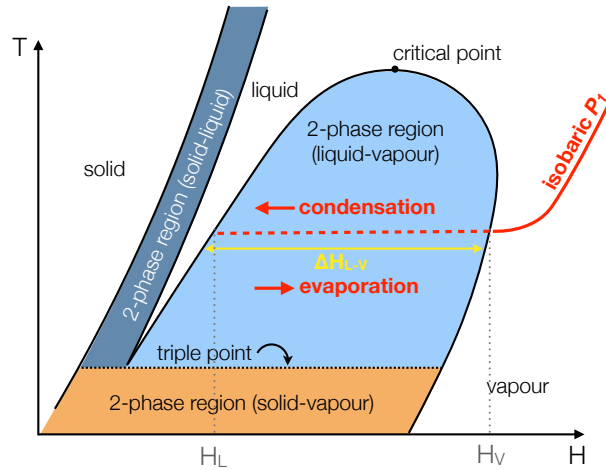


Figure 3.4: Temperature *vs.* enthalpy diagram for a generic pure substance. The red curve represents an isobaric process at pressure P_1 : if the transition occurs from left to right, it is an evaporation; if it goes from right to left, it is a condensation.

Let's take the example of an evaporative process (following the isobaric curve from left to right): as the substance transitions from the liquid state, which has an enthalpy H_L , to the vapour state (H_V), it suffers a change in enthalpy $H_V - H_L = \Delta H_{L-V}$: because the net change in enthalpy is positive, this energy needs to be supplied to the system — it can be said that this phase change *absorbs* ΔH energy from its surroundings. Inversely, if the phase change occurs from right to left (condensation process), the net change in enthalpy is negative and thus the system must *release* energy to its surroundings. The absolute value of the change in enthalpy corresponds to the latent heat L and arises from a discontinuous change in entropy at constant temperature:

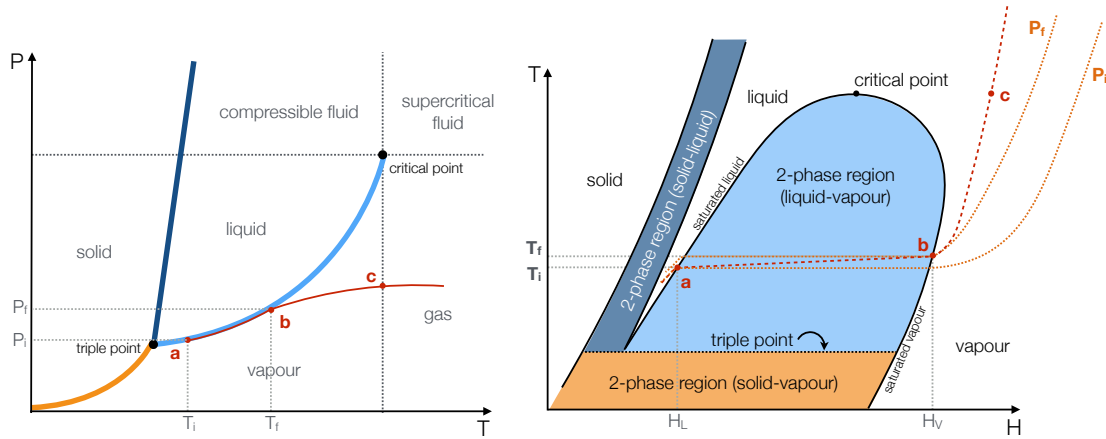
$$L = \Delta H = T \Delta S \quad (3.2)$$

where ΔS is the net change in entropy during the phase transition. Figure 3.4 also allows for some other conclusions to be taken: for example, as we approach the critical point, the energy involved in the liquid-to-vapour phase change decreases until it vanishes completely: a phase change at or above the critical point is a continuous one and therefore there is no discontinuity in entropy, and no latent heat associated to the phase change. One can also infer that a phase change from solid to liquid state involves less energy than a change from liquid to vapour: the latent heat associated with the latter is significantly larger, as seen in Figure 3.4 by the breadth of the respective shaded areas. For a constant pressure evaporation, the net absorbed energy Q is given by:

$$Q = L \Delta n \quad (3.3)$$

where Δn is the amount of liquid that underwent evaporation.

However, an evaporative process cannot occur at constant pressure (and hence neither at constant temperature) in a closed system: as the liquid evaporates the resulting gas causes the pressure inside the vessel to increase, as its density is lower than the liquid density. As a result, both the condensation and the evaporation processes are going to occur along the liquid-vapour saturation line (Figure 3.5). When the liquid undergoes evaporation, the pressure P_f and temperature T_f at which evaporation ends are different, and necessarily higher, than the initial pressure P_i and temperature T_i at which the evaporation began.



(a) Pressure-temperature diagram.

(b) Temperature-enthalpy diagram.

Figure 3.5: Schematic P - T and T - H diagrams for a generic pure substance. The red lines represent an evaporative process that occurs inside a closed system. In **a** the liquid starts to evaporate; the evaporation from **a** to **b** occurs along a pressure/temperature drift until all the liquid is evaporated at **b**. As there is no more liquid, the system is not in saturation conditions and hydrogen only exists in gas form.

In an evaporative process in a closed system, the energy involved in the evaporation process is no longer only given by Eq. 3.3: as the phase change occurs along a temperature drift, a small amount of energy will be absorbed by the liquid hydrogen in the form of sensible heat due to the temperature increase of the system, and also by the work done by pressure forces at the free surface.

3.3 Thermodynamics of a dual-volume ESU

As an evaporative process occurs in a closed system, the heat entering the system causes the liquid hydrogen inside the cell to evaporate. The pressure will increase due to the newly generated vapour, which in turn will cause the temperature to increase as the phase change occurs along the liquid-vapour saturation curve. Since the amount of energy that the ESU is capable of absorbing is no longer given simply by the latent heat, a thermal model needs to be devised to calculate this energy — a step that is essential when dimensioning the whole system. After the evaporation phase, hydrogen needs to

be re-condensed in the cell so that a new cycle can begin: Figure 3.6 illustrates the cyclic operation of an ESU. As a dual-volume configuration was chosen (cf. Figure 2.15), part of the gas is stored at room temperature and thus the amount of energy needed for cooling the gas and condensing it is higher than the energy absorbed during evaporation, a fact that needs to be taken into account in a system with limited cooling power. This section describes the thermal models used when dealing with the evaporation and condensation phases, as well as the influence of the expansion volume size and temperature in a dual-volume configuration.

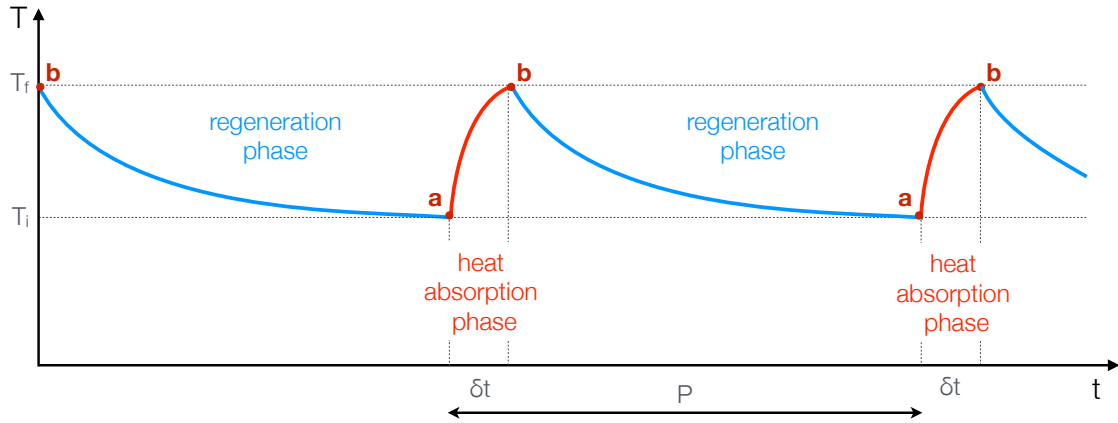


Figure 3.6: Time evolution of a liquid ESU as a function of the cold part temperature. States **a** and **b** are in saturation conditions and represent the minimum and maximum temperatures achieved during ESU operation.

3.3.1 Heat absorption phase

Consider a dual-volume liquid-to-vapour ESU: it is composed by the low temperature cell, where heat is applied and where evaporation occurs, and by the expansion volume at room temperature that houses the fluid in gas form. As evaporation occurs, the resulting vapour will migrate from the cold cell to occupy the expansion volume, as pressure remains homogeneous throughout the whole system. Although the dual-volume ESU is a closed system, the cold cell needs to be considered as an open system, since it exchanges matter (vapour) with its surroundings (expansion volume).

By using a standard “control volume” approach in the low temperature reservoir [33], one can consider that the reservoir volume “increases” by ΔV in order to accommodate the newly generated vapour: the amount of matter in the control volume $V_{C,t}$ is the same as in $V_{C,t+\Delta t}$. It should be noted that the following considerations are only valid for an infinitesimal change in temperature and pressure: the indices 1 and 2 refer to the two states of the system represented in Figure 3.7.

In Figure 3.7, heat Q is applied between t and $t + \Delta t$, causing evaporation. Part of this heat will be converted into work W due to the displacement of the imaginary piston (that

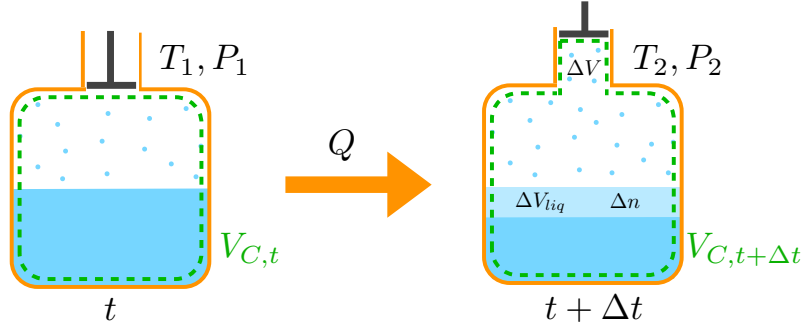


Figure 3.7: Evolution of a control volume in an evaporative process in an enthalpy reservoir, considering the whole system as a closed one; adapted from [36].

separates the control volume of its surroundings) that allowed for the increase in volume and the rest will be translated into a change in the internal energy ΔU of the system:

$$Q = \Delta U - W = \Delta U + P_2 \Delta V \quad (3.4)$$

where P_2 is the pressure inside the cell at $t + \Delta t$. The change in internal energy can be written as:

$$\Delta U = U_{V_{C,t+\Delta t}} - U_{V_{C,t}} = U_{V_{C,t}}(T_2, P_2) + U_{\Delta V}(T_2, P_2) - U_{V_{C,t}}(T_1, P_1) \quad (3.5)$$

If we take this result, combine it with Eq. 3.4 and rearrange the terms, it becomes:

$$Q = U_{V_{C,t}}(T_2, P_2) - U_{V_{C,t}}(T_1, P_1) + U_{\Delta V}(T_2, P_2) + P_2 \Delta V \quad (3.6)$$

where $U_{\Delta V}(T_2, P_2) + P_2 \Delta V$ defines the enthalpy $H_{\Delta V}$ of the gas that exists in the volume ΔV . The amount of energy that can be absorbed in the cold cell by the fluid is then given by

$$Q = \Delta U_V + H_{\Delta V} \quad (3.7)$$

The enthalpy $H_{\Delta V}$ can be rewritten as $h_{vapour}(T_2, P_2)\Delta n$, where Δn is effectively the number of moles that exited the cold cell to the expansion volume and h_{vapour} is the molar enthalpy of the vapour. Since V is the volume of the cold reservoir, ΔU_V can be renamed ΔU_{cell} .

For the amount of stored energy to be correctly calculated, the sensible heat of the reservoir (*i.e.* the vessel that contains the liquid hydrogen) needs to be taken into account. An object with heat capacity C will absorb $C\Delta T$ energy along a temperature drift $\Delta T = T_2 - T_1$, and will contribute to the total amount of energy absorbed at low temperature:

$$Q_{heat} = \Delta U_{cell} + h_{vapour}(T_2, P_2)\Delta n + C\Delta T \quad (3.8)$$

By numerical integration and knowing the parameters of the system such as its initial filling pressure, total amount of moles in the system and the initial temperature, this

balance allows us to size the needed volume of the cell, as well as the temperature drift it will undergo as it absorbs energy during the evaporation phase. This is the thermal model behind the predictions during the heat absorption phase for an ESU with an expansion volume. Its implementation was achieved by numerical integration in a spreadsheet, in which hydrogen properties at a given temperature are calculated using REFPROP [31] and the solid vessel heat capacity. Other parameters such as the input power, expansion volume and cold cell size, filling pressure and starting temperature are used, and the amount of energy stored Q_{heat} per temperature increment can be calculated; knowing the input power, this in turn allows for the calculation of the time interval needed for this temperature increase to happen.

3.3.2 Regeneration phase

After the heat absorption phase is over and the liquid has been completely or partially evaporated, the system needs to be regenerated, *i.e.* the hydrogen gas that resulted from evaporation needs to be condensed again. This means going from point c to point a in Figure 3.5: not only do we need to remove the energy due to condensation and change of cold cell temperature (which is given by Eq. 3.8), but because the expansion volume where the gas is stored is not at the same temperature as the cold reservoir, we also need to remove the enthalpy of the gas coming from the expansion volume to the cell prior to condensation. This enthalpy depends of the temperature at which the gas is stored: storing the gas at higher temperatures means that more energy needs to be removed from the gas for it to achieve the temperature of the cold cell. The total amount of energy needed to condense Δn moles along a temperature drift $\Delta T = T_2 - T_1$ is given by

$$Q_{condensation} = \Delta U_{cell} + h_{vapour}(T_2, P_2)\Delta n + C\Delta T + h_{cool}\Delta n \quad (3.9)$$

where $h_{cool} = h(T_E) - h(T)$ is the molar enthalpy difference of the gas between the temperature T_E of the expansion volume and the cell temperature T at the onset of condensation. At these low pressures the hydrogen gas can be considered to behave as an ideal gas, and as such the enthalpy can be considered to be pressure-independent and therefore only depends on the temperature of the gas. This energy that needs to be removed from the gas prior to condensation, or *pre-cooling* energy, is not at all negligible and can be higher than the energy needed to condense the same number of moles into liquid, depending of what temperature the expansion volume is at. This is a critical item on designing a liquid-to-vapour ESU: as the pre-cooling energy is often significant, there might be the need to intercept the heat at interfaces that are at higher temperatures than the cold reservoir, pre-cooling the gas gradually instead of dumping the whole heat load on the coldest temperature interface. Whether or not to pre-cool the gas at various interfaces should be assessed carefully as it adds complexity to the system: ultimately it requires fitting the solution to comply with the given restrictions as best as possible. Table 3.3 breaks down

the energy that needs to be removed from 0.44 mol (400 J) of hydrogen gas at the several interfaces in order to pre-cool it from 300 K down to 15 K and condense it.

Table 3.3: Energy that needs to be removed from 0.44 mol of hydrogen gas to pre-cool it from 300 K down to 15 K and condense it in the cold cell, and evaluation of the cooling power needed if spread out during a 24h condensation period; comparison with the requirements given in IR 1 of Appendix A. Data calculated using REFPROP [31].

	Process	Q (J)	$\dot{Q}/24\text{h}$ (mW)	Req. (mW)
I/F 1	Gas pre-cooling from 300 K to 120 K	2149	24.9	40
I/F 2	Gas pre-cooling from 120 K to 25 K	908	10.5	15
Cold I/F	Gas pre-cooling from 25 K to 15 K	91	5.7	15
	Condensation at 15 K	404		

We can conclude that full regeneration of the ESU is possible in under 24h without exceeding the available heat load at each interface, if perfect heat exchange between the interfaces and the gas is achieved. However, other phenomena such as ortho-to-para-hydrogen conversion can occur at the lower temperature stages, causing the heat loads calculated in Table 3.3 to change; this will be further discussed in Section 4.6. It can also be observed that all three interfaces made available by ESA need to be used for pre-cooling, as the Cold I/F would not be able to support the heat load of a gas coming at 300 K without exceeding the budget.

3.4 Dimensioning the expansion volume

The importance of an expansion volume in a liquid-to-vapour ESU has been previously highlighted: this volume is responsible for storing the evaporated gas. But the expansion volume is also deeply related to the temperature drift experienced during the evaporation process: the larger the volume, the smaller the final pressure increase, which in turn leads to a smaller temperature drift in the cold cell. This means that for a hydrogen evaporative process that starts at 15 K, the pressure should be kept as close as possible to 128 mbar, which is the saturation pressure of hydrogen at 15 K.

Considering a small temperature difference dT during evaporation, the pressure increase is negligible and so the latent heat can be considered constant. In this case, the energy stored during the temperature increase dT in an evaporative process is given by

$$dE = Ldn \quad (3.10)$$

where L is the latent heat and dn is the amount of evaporated fluid. Using the ideal gas law and considering the expansion volume V and respective temperature T_E , dn can be written as $dn = VdP/(RT_E)$ and Eq. 3.10 becomes

$$dE = L \frac{V}{RT_E} dP \quad (3.11)$$

Since the evaporation process occurs along the saturation curve, the relationship between pressure and temperature can be used to write dP as a function of the temperature:

$$dP = \left(\frac{\partial P}{\partial T} \right)_{sat} dT \quad (3.12)$$

The equation that describes the variation of energy for a small temperature difference then becomes

$$dE = L \left(\frac{\partial P}{\partial T} \right)_{sat} \frac{V}{RT_E} dT \quad (3.13)$$

$$\frac{dE}{dT} = L \left(\frac{\partial P}{\partial T} \right)_{sat} \frac{V}{RT_E} \quad (3.14)$$

The latter equation [33] describes the amount of energy stored between T and $T + dT$ for a given expansion volume V at a temperature T_E , valid only for a small temperature drift; this restriction is due to the slope $(\partial P/\partial T)_{sat}$ and the latent heat not being constant throughout the whole saturation curve. For the problem at hand, the temperature range (15 K to 17 K) and hence $(\partial P/\partial T)_{sat}$ and L , which depend on temperature, are fixed. That leaves only one variable to work with in order to store a certain amount of energy: the temperature drift dT , that will in turn determine the expansion volume needed to maintain that temperature drift. The larger the expansion volume, the smaller the temperature increase: this trade-off is presented in Table 3.4.

Table 3.4: Expansion volume requirements for different temperature drifts in the hydrogen cold cell. Data for expansion volumes at room temperature, and for an energy storage in the cold cell of 400 J, computed using the model described in [33].

RT volume	Filling pressure	T rise in the cold cell
100 ℓ	0.240 bar	From 15 K to 16.3 K
50 ℓ	0.345 bar	From 15 K to 17.2 K
10 ℓ	1.170 bar	From 15 K to 20.8 K
6 ℓ	1.800 bar	From 15 K to 22.3 K

For the temperature drift at the low temperature stage to be kept between 15 K and 17 K, a 56 ℓ volume is needed at room temperature, and if the temperature increase is limited even further, *e.g.* from 15 K to 16 K, it adds up to a 100 ℓ volume. Volumes as large as the ones presented are rendered unusable for a space application: there is simply not enough room to accommodate an expansion volume of this size, even at room temperature (maximum 5 ℓ allowed, see PRR 4 of Appendix A). New methods of storing hydrogen at a pressure close to its saturation pressure at 15 K need to be investigated if this solution is to be made space-ready.

3.5 Finding a compact storage solution

As previously mentioned, the requirements for maximum temperature increase in the cold cell during the heat absorption phase are rather strict: maximum temperature increase from 15 K to 17 K, with no more than 10 min above 16 K. In order to achieve this with a traditional room temperature expansion volume a staggering 100 ℓ would be needed. Other temperature interfaces are available: one at 25 K and another one at 120 K, but the volume budget is even more restricted (0.1 ℓ and 0.2 ℓ , respectively). A more compact solution for storing hydrogen gas at low pressure is needed, and two options have been considered:

- Adsorption materials such as activated carbon;
- Chemical absorption of hydrogen.

Although each of these solutions presents its challenges, both are assessed and discussed over the next sections.

3.5.1 Physical adsorption at low temperatures

Essentially, physical adsorption is the accumulation of molecules on the surface of a material with a large surface area, such as micro-porous fibres or activated carbons: the weak interaction forces between gas molecules and the adsorbent material are responsible for “trapping” the gas, storing it. The capacity of adsorbing a gas depends strongly on the temperature and pressure at which it is stored, and on the material itself. Adsorption phenomena for hydrogen have been studied for micro-cryopumps used in gas-gap heat switches [38] although not for “large-scale” gas storage.

The use of adsorption for large-scale storage of hydrogen gas would be challenging: hydrogen is a notoriously difficult gas to adsorb, and a high adsorption capacity (4 wt% to 6 wt%) can only be obtained at low temperatures or at very high pressures [39]. For this project, the operating pressure needs to be kept close to that of saturation at 15 K (≈ 0.1 bar), which eliminates the option of producing high pressures for adsorption. Cryogenic temperature stages are available at 15 K, 25 K and 120 K, but the mass and volume budget is low at those interfaces, and so is the available cooling power.

Because adsorbing hydrogen at temperatures higher than 77 K is practically unachievable, we considered the hypothesis of having hydrogen adsorbed at or below that temperature: this enables adsorption, but the heat generated during the process (typical heat of absorption in activated carbon of 2 kJ mol^{-1} to 5 kJ mol^{-1}) is still too large to deal with at the low temperature stages and would lead to a large increase in the activated carbon temperature. There are three options for an enthalpy reservoir (another [ESU](#)) that could be used to manage the heat of adsorption:

- using the sensible heat of ice water due to its relatively high specific heat at low temperature ([Appendix B](#));

- using the sensible heat of a copper block as a benchmark;
- using the high latent heat from the evaporation of liquid nitrogen.

Even with ice water, the amount of carbon needed to adsorb the hydrogen gas at a pressure between 100 mbar and 300 mbar is quite large, making these options rather cumbersome and impractical. Figure 3.8 shows the amount of carbon for adsorbing 0.5 mol of hydrogen gas in activated carbon (Prolabo[®] pellets, data collected in our laboratory [38]) at a pressure of 100 mbar, where the activated carbon is either at 25 K or at 120 K. A hydrogen amount of 0.5 mol is used for ease of calculation, while the amount needed to absorb 400 J has been calculated before (Section 2.3.3) to be 0.44 mol. The right-hand side of the plots in Figure 3.8 shows the amount (in kg) of copper and ice water needed to manage the heat of adsorption released by the carbon, as a function of the allowed temperature increase.

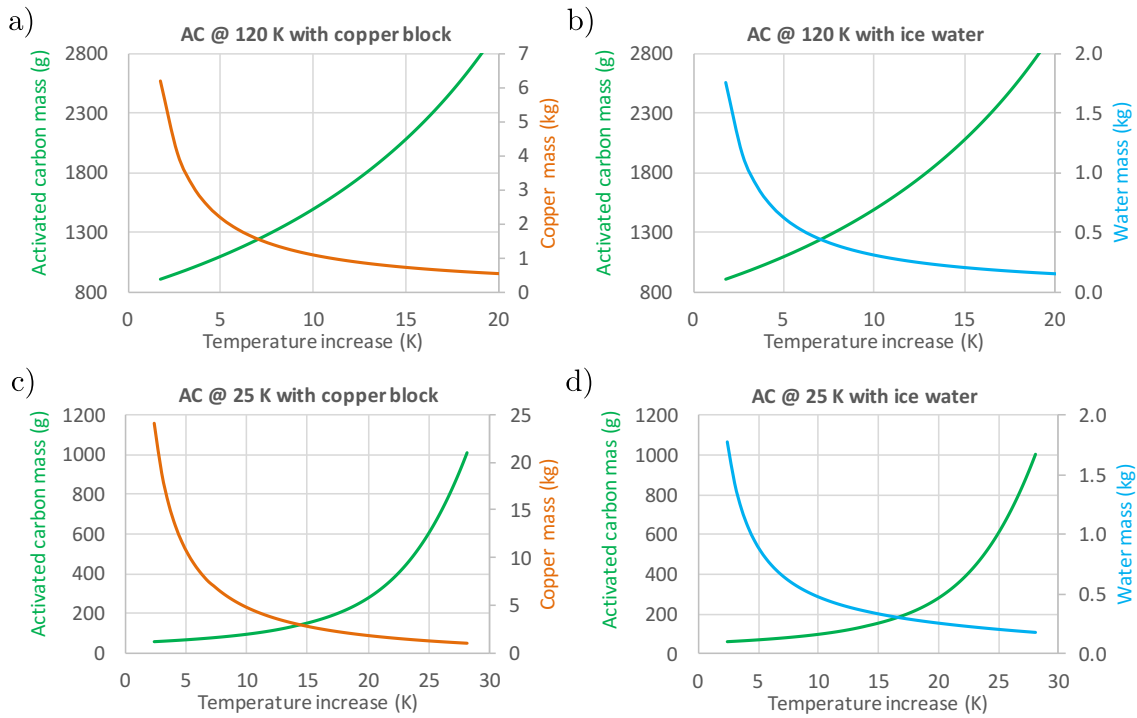


Figure 3.8: Amount of activated carbon needed to adsorb hydrogen at 100 mbar as a function of the increase in the carbon temperature (green curve). a) and b) represent data for hydrogen adsorption at 25 K and c) and d) for adsorption at 120 K. The right-hand side of the plots depicts the amount of copper (a) and c)) and ice water (b) and d)) needed to absorb the released heat of adsorption at that temperature (orange and blue curves).

The third solution is a second enthalpy reservoir using liquid nitrogen to manage the heat load by using a hypothetical stage at 77 K [40]. The evaporated nitrogen is in turn adsorbed by activated carbon at room temperature: Figure 3.9 shows this cascade of

elements in their thermal environment, and Table 3.5 gives a summary of the necessary conditions that would need to be met for this solution to operate.

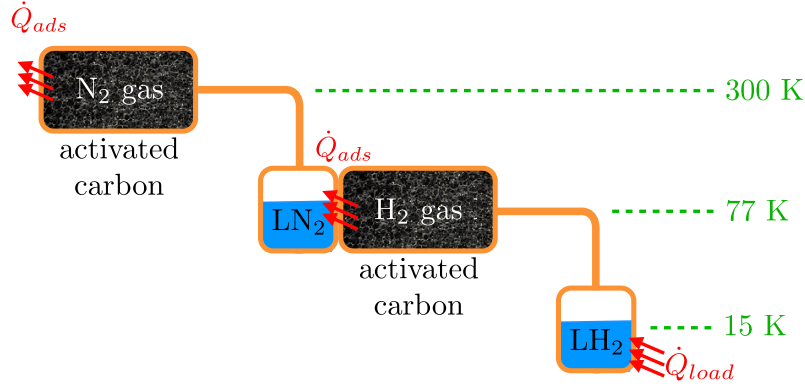


Figure 3.9: Schematic of cascading LN₂ and LH₂ vessels with activated carbon for adsorption of the gas at various temperature stages. As hydrogen evaporates, the generated gas is adsorbed by the activated carbon at 77 K, and the released heat of adsorption causes the liquid nitrogen to evaporate; the nitrogen gas is in turn adsorbed by the activated carbon at room temperature, releasing heat at that temperature.

Table 3.5: Parameters for operation of a cascading LN₂ and LH₂ system with activated carbon for adsorption of hydrogen gas at 77 K and adsorption of the nitrogen gas at room temperature (273 K).

	Hydrogen stage	Nitrogen stage
Operating pressure	100 mbar	2.8 bar
Operating temperature of AC	77 K	273 K
Maximum temperature increase	10 K	10 K
Amount of gas to adsorb	0.5 mol	0.4 mol
Amount of AC needed	600 g	530 g

It can be inferred that neither of the three proposed solutions is feasible given that the mass of activated carbon alone largely surpasses the mass budget for the cryogenic part of the system (500 g, PRR 2 of Appendix A), and it becomes impossible to manage once the mass of either copper, ice water or nitrogen is added on top of that. Furthermore, the heat released by the activated carbon during adsorption is not compatible with the available cooling power at the intermediate temperature stages. In summary, for the available mass and volume constraints, physical adsorption is not a viable solution for storing hydrogen gas.

3.5.2 Chemical absorption

Chemical absorption of hydrogen can exist, in which it reacts to form metal hydrides (MH) with some metals and alloys, leading to solid-state storage under a wide range of

temperature and pressure; these parameters depend upon the type of compound. Unlike adsorbent materials, which are only competitive when used for storing hydrogen at high pressure or at low temperatures, metal hydrides can outperform adsorption materials in the high (non-cryogenic) temperature range; moreover, the hydrogen density can be quite high: some compounds enable hydrogen to be stored at higher densities than that of liquid hydrogen.

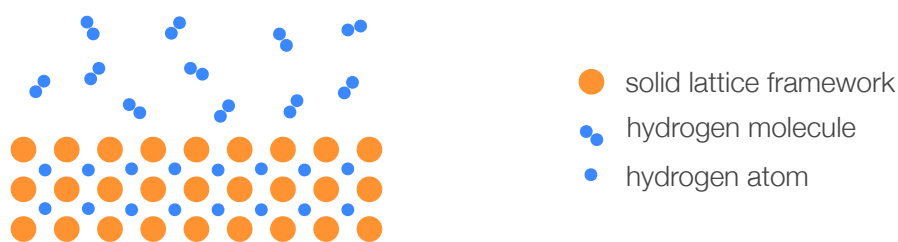


Figure 3.10: Inter-metallic hydrides. Upon contact, the hydrogen molecule dissociates into two hydrogen atoms that chemically bond with the metallic compound.

Metal hydrides are composed of metal atoms that constitute a host lattice and of hydrogen atoms (Figure 3.10); they essentially form two kinds of hydrides: an α -phase at which only some of the hydrogen is absorbed and a β -phase at which the hydride is fully formed [41]. In these materials hydrogen is *chemically* absorbed forming a chemical bond and sharing electrons with the metallic lattice, instead of being adsorbed at the surface by van der Waals forces as is the case of physisorption; the chemisorption process can be divided into four steps:

1. Molecular hydrogen is first adsorbed at the surface (physical process) due to weak van der Waals (intermolecular) forces;
2. Molecular hydrogen is then dissociated into H atoms;
3. Hydrogen atoms are absorbed (chemical bonding process), and there is formation of a mono-layer of hydride (α -phase);
4. The newly hydrided layer is diffused toward the bulk of the material (β -phase). This part of the process is temperature and pressure dependent, as it will determine the extent to which the hydride H^- species will penetrate into the bulk, and is reversible [42].

These two phases can be seen in a Pressure-Temperature-Composition (PCT) diagram as shown in Figure 3.11. A PCT diagram is essentially a “special” phase diagram (similar to the pressure-density diagram of a fluid) that consists of a number of isotherms that relate the equilibrium pressure of hydrogen with its concentration within the solid (metal or alloy). Initially, at low hydrogen concentrations, the isotherm rises steeply: this is the α -phase where hydrogen dissolves in the metal to form a solid solution. Point A marks

the end of hydrogen solubility in the α -phase, and the start of a new phase: the β or hydride phase. With the existence of both phases the hydrogen pressure remains constant (forming a “plateau”) as more hydrogen is added to the system; this is a consequence of Gibbs’ phase rule and as such the equilibrium pressure will remain constant for as long as the two solid phases coexist. At point B the α -phase ceases to exist and the pressure will rise sharply with the increase of hydrogen concentration.

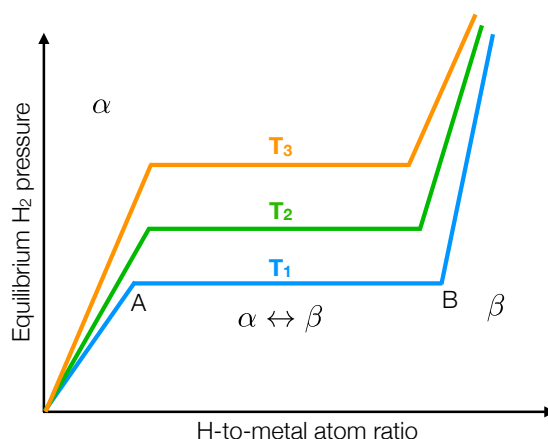


Figure 3.11: Ideal Pressure-Temperature-Composition diagram, with the hydride phases α and β displayed; the length of the pressure plateau AB represents the effective hydrogen storage capacity. Adapted from [43].

In most metal hydride systems there is a significant hysteresis effect during the AB phase, and the absorption process or hydride formation will have a plateau pressure at a higher temperature than the dissociation process. With a practical application in mind such as ours, an ideal metal hydride (or any other hydrogen storage material) should have the following characteristics:

- high hydrogen storage capacity per unit mass and unit volume;
- low dissociation (desorption) temperature;
- low to medium dissociation pressure;
- low heat of formation during exothermic metal hydride formation (low heat of absorption);
- both the absorption and desorption processes should be reversible;
- fast kinetics of hydride formation/dissociation;
- high stability against contamination (mainly O_2 and moisture);
- reproducibility throughout a large number of cycles.

For this project, hydrogen storage using metal hydrides would only be feasible at the room temperature stage for a number of reasons: its high heat of absorption ($\approx 30 \text{ kJ mol}^{-1}$) can only be manageable at this temperature, and the mass and volume budget at the lower stages is so strict that the best option for implementation is still at the higher stages; moreover, the absorption dynamics of metal hydrides decrease drastically at low temperatures. Regarding the desired properties, in addition to those listed above, the low dissociation temperature would have to mean near room-temperature and the pressure should be kept close to the saturation pressure at 15 K (100 mbar). The AB_5 family of metal hydrides (where A is a rare earth metal while B is usually either nickel or cobalt) has been the most thoroughly investigated one among the vast quantity that is available nowadays, and seems to be the most suitable for the needs of this project. The nominal reaction for this type of compound is written as



where Q is the exothermic heat of absorption, *i.e.* the heat of reaction during the formation of the hydride phase AB_nH_X . The reaction rates are extremely high and exothermic, and measures need to be taken when designing a metal hydride sorbent vessel if one needs to maintain isothermal conditions. The archetype and most studied of these alloys is LaNi_5 , and it has several advantages: it reacts rapidly with hydrogen at room temperature and has a relatively small hysteresis effect. On the downside, the equilibrium pressures for LaNi_5 are higher than those needed for the project. But AB_5 hydrides are highly “customisable”: the properties of the alloy can be tailored to the needed specifications by substituting (in whole or in part) the original lanthanum or nickel by other metal.

Substituting a portion of nickel with either cobalt, aluminium, manganese or tin can increase the stability of the alloys and decrease the equilibrium hydrogen pressure at the plateaus [44]: this is a key factor, as it can allow for metal hydrides to be used in the pressure range of 100 mbar to 300 mbar.

The “right” alloy, one that could meet the storage capacity, temperature and pressure specifications of this project was singled out by R. C. Bowman Jr., one of the leading researchers on the development of the metal hydride sorption coolers for the Planck mission: his help was invaluable when selecting and understanding metal hydride systems. $\text{LaNi}_{4.8}\text{Sn}_{0.2}$ was the alloy used for the Planck compressors [45, 46] (although for a much larger temperature and pressure range) and was selected due to its special attributes. This particular alloy enables the material to absorb hydrogen at low pressures (100 mbar to 300 mbar range) at near room-temperature, and tin also has the (unusual) role of dramatically decreasing degradation and improving the stability of the hydride [47]; this capability to withstand long cycling without losing storage capacity is highly desirable for space applications. The use of tin also reduces hysteresis, but slightly decreases the storage capacity; it has been recognised as one of the more resistant hydrides, losing only 15% of its initial storage capacity after 10,000 cycles [48]. Its PCT diagram is shown in

Figure 3.12.

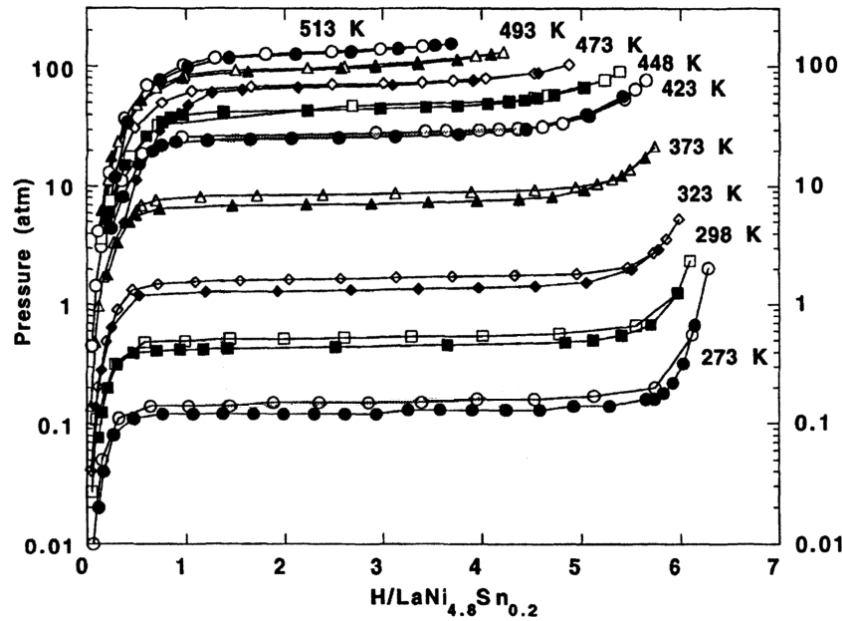


Figure 3.12: $\text{LaNi}_{4.8}\text{Sn}_{0.2}$ isotherms at various temperatures, as used in the Planck sorption cooler; adapted from [49]. Full symbols represent the desorption process and empty symbols the absorption process.

It can be observed that the equilibrium pressure is 100 mbar at 273 K which is ideal for our application, since this is the saturation pressure of hydrogen at 15 K. Hence, if the metal hydride is kept at 273 K hydrogen will be condensed in the cold part of the system at a near-constant temperature of 15 K; if we are able to manage the heat of absorption during the evaporation phase, the heat load at the cold end can be absorbed with very little temperature increase since the plateaus for this material are virtually flat.

The main properties of this compound are listed in Table 3.6. The high heat of absorption (when compared to physisorption phenomena) is one of the main drawbacks of using this type of materials; the high heat load upon absorption during a short period of time, plus the poor thermal conductivity of these materials calls for special care on designing the sorbent bed; this issue will be addressed later on.

Table 3.6: Main properties of the $\text{LaNi}_{4.8}\text{Sn}_{0.2}$ metal hydride [50].

$\text{LaNi}_{4.8}\text{Sn}_{0.2}$		
Density	8.4	g/cm^3
Molar mass	444.4	g mol^{-1}
Heat of absorption ΔH	32.8	kJ mol^{-1}
Equilibrium pressure @ 25 °C	0.5	bar
Temperature for 1 atm	39	°C
Maximum hydrogen storage capacity	1.4	wt%

4 The approach: designing according to specs

As the proposed liquid hydrogen [ESU](#) is intended to integrate the cryogenic chain of [ATHENA](#), some considerations must be made such as adapting its design to fit the mass/volume budget, rendering it capable of working in a micro-gravity environment or surviving launch. This chapter describes the steps taken to design a tailored solution that is able to operate as desired from an operational standpoint, and can also meet the specifications given by [ESA](#): these range from structural requirements needed to ensure easy assembly, to thermal constraints during operation.

4.1 System requirements

Under a Core Technology Programme (CTP) funded by [ESA](#), the objective of this work is to develop an Energy Storage Unit as a solution for absorbing 400 J at 15 K, under strict requirements regarding performance, mass and available cooling power. This [ESU](#) shall be able to absorb this heat load (of up to 1 W) during 30 min according to a specific heat load profile, between 15 K and 17 K, over a baseline cooling power of 15 mW at 15 K. When designing equipment for space applications there is an increased number of requirements that must be met. These constraints can be due to the total size and mass of the payload, or to the fact that there is no repairing a system in space if any part of it should fail: this means being extra cautious and careful when designing a system for a satellite, as it needs to have the least possible sources of failure.

For this project, a complete list of requirements was compiled: its full version can be consulted in [Appendix A](#). Requirements range from maximum available cooling power at the several temperature stages to maximum dimensions of the whole system, and are divided according to their type:

- **Functional & Performance Requirements:** Specifications on how the system is expected to perform.

- **Interface Requirements:** Describes the available interfaces at different temperatures and the available cooling power on each one.
- **Environmental Requirements:** Describes what conditions the system must be designed to withstand, including vibrational tests and radiative environment.
- **Physical & Resource Requirements:** Refers to the maximum allowed dimensions and mass of the different components at each interface.
- **Operational Requirements:** Describes minimum and goal lifetime of the system, and conditions of operation.
- **Product Assurance Requirements:** Defines Quality Assurance, Reliability, Safety and Maintainability requirements.
- **Configuration & Implementation Requirements:** Defines design requirements for implementation and Verification & Testing requirements.

All of these requirements need to be taken into account when selecting the appropriate solution: some of the constraints imposed by the requirements might render an otherwise viable solution unusable. Some of the major constraints that were taken into account are summarised in Table 4.1.

Table 4.1: Main requirements for the design and performance of the ESU. Adapted from [51].

Requirement	Description
FPR 1	The ESU shall be able to absorb a heat peak of 400 J at 15 K during 30 min according to a specific heat load profile.
FPR 2	The ESU shall be able to regenerate within 24 h.
FPR 4	As a goal, the ESU shall be able to provide a temperature below 15 K during absorption of the peak.
FPR 5	A temperature increase above 16 K is acceptable for a duration shorter than 10 min.
IR 1	Four thermal interfaces are available, with limited cooling power at each one.
ER 2	The ESU shall be capable of surviving the specified mechanical environment, compatible with a launch.
PRR 1	The overall mass of the ESU shall be less than 5 kg.
PRR 2	The cryogenic mass of the ESU shall be less than 500 g.
PRR 3	The cold volume of the ESU shall be less than 0.2 ℓ at I/F 1, 0.1 ℓ at I/F 2 and 0.1 ℓ at the Cold I/F.
PRR 4	The ambient volume of the ESU shall be less than 5 ℓ.
OR 2	The ESU shall be capable to operate on ground under any orientation and in a micro-g environment.
DR 6	All materials used in the ESU shall be flight approved.

4.2 System outline

Since the chosen design for the liquid hydrogen ESU is a dual-volume configuration, the system will be composed of a room temperature storage volume, where hydrogen will be stored after it has been evaporated, a cold part where hydrogen is condensed and where the heat load is absorbed, and an intermediate stage that consists of a filling capillary that connects both parts. This intermediate interface is not only a tube running from room temperature to the lowest temperature part, as it will be connected to two intermediate stages. Figure 4.1 gives a simplified overview of the system.

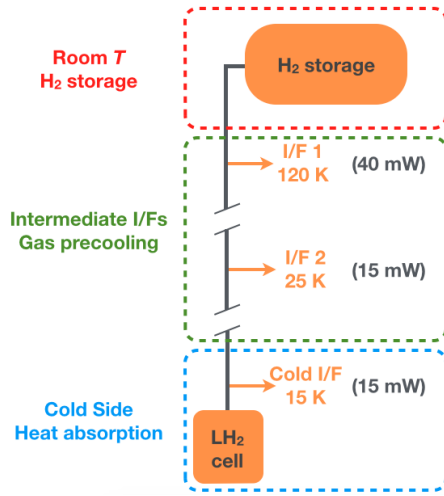


Figure 4.1: Overall schematic of the ESU and its three main components: the room temperature gas storage, the intermediate interfaces for gas pre-cooling, and the cold cell where the heat load is absorbed. The available cooling power (cf. ESA requirements) is indicated for each of the interfaces.

4.3 Sizing the cold cell

The ESU needs to be capable of absorbing 400 J of thermal energy at the cold end, and if the temperature is kept constant, virtually all of this energy is going to be absorbed using the latent heat of evaporation of hydrogen; the sensible heat capacity of both the cell and the liquid itself is, in a first approximation, negligible, as will be demonstrated further on. Also, according to DR 1 of Appendix A, the ESU shall be designed with 10% extra in energy storage capabilities to provide a safety margin. With this in mind, the cell needs to accommodate an amount of liquid hydrogen whose evaporation is capable of absorbing 440 J. Taking Eq. 3.3 and considering an average value for the latent heat L in the range 15 K to 17 K, the amount of liquid hydrogen needed can be computed:

$$Q = \Delta n_{H_2} L \Leftrightarrow \Delta n_{H_2} = \frac{Q}{L} \Leftrightarrow \Delta n_{H_2} = \frac{440 \text{ J}}{918 \text{ J mol}^{-1}} = 0.479 \text{ mol} \quad (4.1)$$

Since the liquid density in this temperature range is $\approx 37 \text{ mol/dm}^3$, the 0.479 mol corresponds to 12.9 cm^3 of liquid hydrogen: this is hence the minimum free volume for the cold cell. This cell will be filled with a porous material whose purpose is to confine the liquid hydrogen against gravity; this will be described in Section 4.4. When calculating the total size of the cell, the volume occupied by the porous material also needs to be

taken into account: for the selected materials the minimum porosity is 90%, so 10% is the maximum extra volume that needs to be available to accommodate the foam.

Results from other Energy Storage Units developed at the Cryogenics Laboratory [33, 35, 36, 52] have shown that, when the amount of liquid inside the cold cell drops below a certain level (usually less than 10-20% of the cell volume), the remaining liquid droplets get trapped inside the small pores of the material that fills the cell. Below this “critical level” the liquid droplets become thermally decoupled from the cell walls (since the porous materials used have a rather low thermal conductivity), and it becomes very difficult for the heat load to be transferred onto the liquid and evaporate it; this renders that remaining liquid unusable for heat absorption, and without evaporation the cell itself rises very abruptly in temperature, as if there was no liquid left. Preliminary studies with both porous materials (see Section 4.4) show that this phenomenon does occur, although for a lower percentage of liquid left: both for alumina and vitreous carbon, it consistently occurred when there was less than 10% liquid left. In order to avoid this abrupt temperature rise the decision was made to have an additional 8% of the total amount of liquid hydrogen needed inside the cell: this compensates for possible issues with the last droplets of liquid, as it is never intended to be used during a normal heat absorption phase, even considering the safety margins.

Another lesson learnt from previous works is that if the cold cell is completely filled with liquid (*i.e.* a filling ratio of 100%), some of this liquid can spill from the cell at the beginning when a heat load is applied. This was extensively studied for the neon ESU [35] and some hypotheses were formulated as to why this happens: in short, depending on where the heater is placed, the generated vapour forms far from the exhaust and pushes the existing liquid while travelling along the cell towards the exit. Two other factors can further worsen this issue, namely how close the porous material gets to the capillary exhaust and how much of the capillary tube is inserted inside the cell. Both factors help create percolation paths that make it easier for the liquid to drain from the porous material through the capillary exit. For this project, this was avoided by allowing the cell to be filled only to 90% of its capacity. This way there is free room for the vapour to circulate without pushing the liquid out of the cell, even for heat loads of 1 W.

13.0	cm ³ of liquid volume for 440 J
1.0	cm ³ (8% additional liquid to avoid trapped liquid)
1.6	cm ³ (volume occupied by a material with 90% porosity)
1.6	cm ³ (extra 10% of total capacity for vapour circulation)
<hr/>	
17.2	cm ³ total volume of the cold cell

The total capacity of the cell is then the sum of all the volumes that originate from the above considerations, and adds up to 17.2 cm³; Figure 4.2 illustrates the distribution of the volumes inside the cold cell. Even though 17.2 cm³ is the value for the inner capacity of the cold cell, it is well below the 0.1 ℓ limit imposed by PRR 3; this small volume at low temperature is one of the main advantages of a dual-volume ESU.

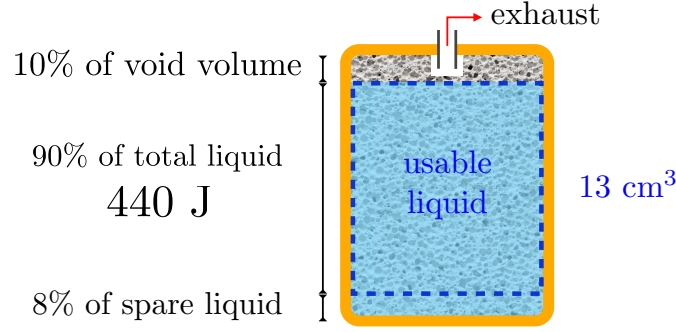


Figure 4.2: Schematic of the distribution of volumes inside the cell. The total capacity of the cell is 17.2 cm^3 and the void volume is 90% of that (15.5 cm^3).

4.3.1 Mechanical design

The cold cell was designed to be a cylinder with its diameter equal to its height: this way the necessary capillary height (see Eq. 4.5) needed to confine the liquid is the same regardless of the orientation of the cell. For an inner volume of 17.2 cm^3 and considering $h = d$, the dimensions of the cell can be computed as follows:

$$V = \frac{\pi h d^2}{4} = \frac{\pi d^3}{4} \leftrightarrow d = \sqrt[3]{\frac{4V}{\pi}} \quad (4.2)$$

which gives $d = 28 \text{ mm}$ for both the inner height and diameter.

Since the system will be operating in the sub-atmospheric pressure range (100 mbar to 300 mbar), no rigorous study needs to be performed when deciding the wall thickness for the cell from an operational standpoint; however it should be sized to account for higher pressures should the system suffer a failure and pressure builds up inside it. Considering the cell as a thin-walled cylinder with height h and diameter d subject to a maximum internal pressure P_{max} (as shown in Figure 4.3), the following force balance can be written:

$$F_{max} = P_{max} \times h \times d = 2 \times t \times h \times \sigma_y \quad (4.3)$$

where t is the minimum wall thickness, F_{max} is the circumferential stress acting upon the cell and σ_y is the yield strength of the material that the cell is made of. The minimum wall thickness needed for the cell to withstand an internal pressure P_{max} is then given by:

$$t_{min} = \frac{P_{max} \times d/2}{\sigma_y} \times f_{safety} \quad (4.4)$$

where f_{safety} is the safety factor used when sizing the cell. Assuming copper as the material for the cell, since it has good thermal properties, there are two values for the yield strength: while the standard yield strength for oxygen-free high conductivity (OFHC) copper is 69.0 MPa [53], the cell is going to be exposed to high temperatures during the brazing process, and as such the (lower) yield strength of annealed copper (33.3 MPa [54]) was considered. Hence, for $f_{safety} = 2$, $\sigma_y = 33.3 \text{ MPa}$ and $P_{max} = 12 \text{ bar}$ (twice the value of

the proof pressure specified for the mechanical testing in [Appendix A](#)), the minimum wall thickness is $t_{min} = 1.0\text{ mm}$ when considering circumferential stresses. For the longitudinal stress, the obtained expression is similar to [Eq. 4.4](#) but divided by a factor 2; this leads to thinner walls, and as such the safer value of 1.0 mm was considered.

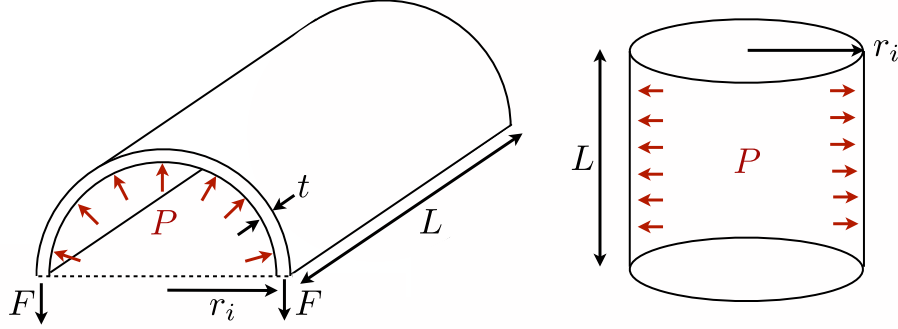


Figure 4.3: Circumferential stresses on a thin-walled cylinder under internal pressure.

Since the results obtained for copper do not produce overly thick walls, which would in turn lead to a high mass at low temperature, the decision was made to build the cell out of copper, since it is the material which presents the best thermal conductivity in the temperature of interest.

4.4 Liquid confinement in micro-g

According to [OR 2](#) ([Section 4.1](#) and [Appendix A](#)), and considering that the [ESU](#) is potentially going to be integrated in [ATHENA](#)'s cryogenic chain, it needs to be able to operate in a micro-gravity environment: this means that the liquid needs to be confined in the cell by means other than gravity, otherwise it will most likely exit the cold cell and be evaporated elsewhere, thus significantly decreasing the amount of energy that can be absorbed at the cold end. As testing under micro-g conditions is not feasible under laboratory conditions, the system should also be designed to work under any orientation in a ground set-up: this means, in the worst case scenario, that it will be operating in "anti-gravity" conditions, *i.e.* where the liquid needs to remain inside the cell even if the exhaust is located at the lowest part of the cell (as shown in [Figure 4.4](#)).

Liquid confinement is a recurring concern when developing devices for space applications that include cryogenic liquids, a breakthrough example being the Surface Tension Confined Liquid Cryogen Cooler [55] developed by [NASA](#) in 1988. This remains a very real problem to this day, as the more recent developments in some cryogenic systems (such as the sorption cooler used in [Herschel](#) [17] or the closed-cycle dilution refrigerator [16]) depend on the capability of efficiently retaining liquids inside their vessels. In all of the cases mentioned above, liquid confinement has been achieved by taking advantage of surface tension or capillary action: a porous material is used to "absorb" the liquid as a sponge, preventing the presence of liquid in undesired parts of the system. It also

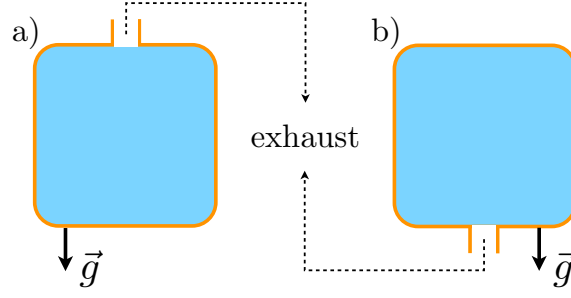


Figure 4.4: Ground configurations for testing liquid confinement: a) Baseline or normal configuration, where the exhaust is located at the top of the cell, preventing liquid exit; b) Anti-gravity configuration. In this configuration the exhaust is at the bottom of the cell, and liquid needs to be confined or it will be spilled due to the effect of gravity.

has the advantage of virtually eliminating sloshing effects that could induce vibrations and disturb sensitive measurements. The use of a porous media has been widely tested in previous Energy Storage Units developed at the Cryogenics Laboratory [33, 35] using different materials and cryogenic fluids. In a first approximation, the porous material is modelled as a series of capillary tubes, with each tube having a diameter equal to the mean pore size of the material (Figure 4.5); the maximum height h that a certain cryogenic fluid with liquid density ρ_L and vapour density ρ_V can rise in a tube with diameter \varnothing is given by Jurin's law:

$$h = \frac{4\gamma \cos \theta}{\varnothing (\rho_L - \rho_V) g} \quad (4.5)$$

where γ is the surface tension of the cryogenic liquid, g is the acceleration of gravity and θ is the contact angle between the liquid and the tube walls. The parameters ρ_L , ρ_V and γ can be computed using REFPROP [31] at saturation conditions (see Appendix B), and for cryogenic liquids the contact angle approaches zero [56, 57]. Since the temperature range of interest is close to hydrogen's triple point, surface tension will be at its highest, thus having a positive effect in the obtainable capillary height; a contact angle of 0° ensures perfect wettability and further increases the achievable height.

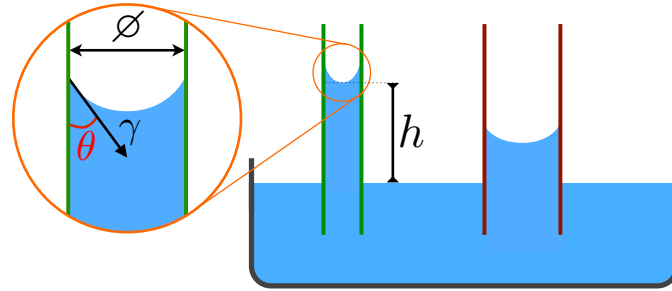


Figure 4.5: Capillary action inside tubes with different diameters.

The capillary height h should be enough to ensure that the liquid is retained inside

the cell no matter what distance to the walls is being considered. Since the cold cell was designed to be a cylinder with equal diameter and height, h should remain larger than the cold cell's height of 28 mm. Figure 4.6 shows the capillary height for hydrogen inside different pore sizes along the temperature range 14 K to 32 K, compared to the cell height, 28 mm.

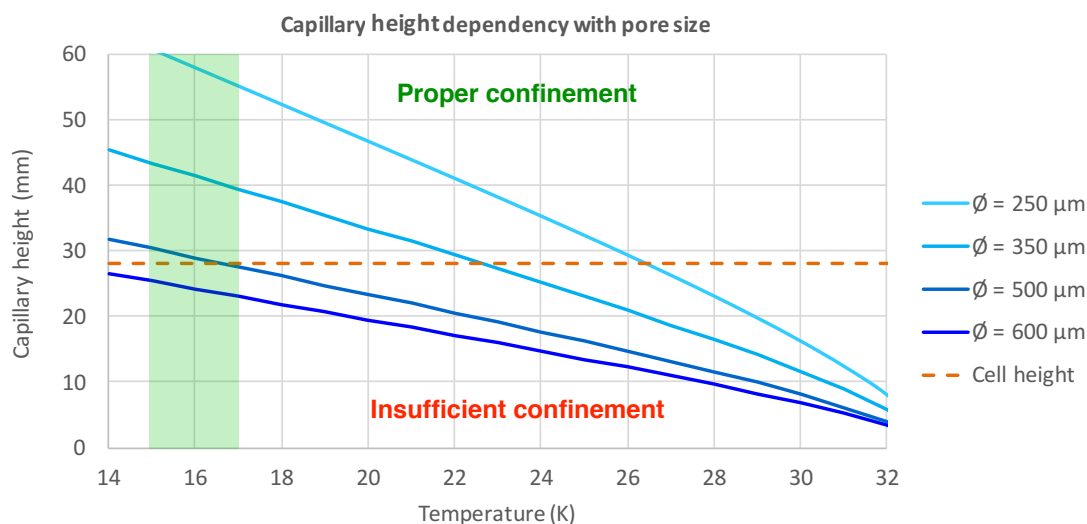


Figure 4.6: Wicking or capillary height for hydrogen along the temperature range 14 K to 32 K for different pore sizes. The red dashed line indicates the cell height.

Any pore size whose curve falls below the red line for the operating temperature range (15 K to 17 K) should not be considered as it won't be able to adequately confine the liquid inside the whole volume of the cell. This means that only porous materials with a mean pore size lower than $350 \mu\text{m}$ are suitable for this application; taking safety factors into consideration, only pores equal or smaller than $250 \mu\text{m}$ should be used. It should be noted that these calculations give the needed pore size to confine the liquid in an *anti-gravity* configuration, which is the worst case scenario; in micro-g conditions, the forces acting against capillary action will be considerably smaller. This ensures that no problems will arise when confining the liquid in a space environment.

Two porous materials were selected for testing: an alumina ceramic foam KVR 164-242 (Figure 4.7) manufactured by RATH® and a vitreous carbon foam (Figure 4.8) supplied by Goodfellow®. The main characteristics of these two materials can be found in Table 4.2.

The main functional difference between the two materials is the estimated mean pore size: the alumina foam has an estimated pore size of $\approx 100 \mu\text{m}$ while the pores in the vitreous carbon one have a mean diameter of $250 \mu\text{m}$. While both foams seem perfectly able to confine liquid hydrogen adequately even accounting for safety margins, there are other aspects to take into consideration when choosing a pore size and a porous material.

Table 4.2: Properties of the selected porous materials used for liquid confinement testing.

	Alumina foam	Vitreous carbon foam
Reference	KVR 164-242	VC003830
Supplier	RATH [®]	Goodfellow [®]
Composition	98% Al ₂ O ₃ , 2% SiO ₂	Pure carbon
Density (g/cm ³)	0.240	0.050
Thermal cond. (W m ⁻¹ K ⁻¹)	0.131	0.033 to 0.050
Porosity	≈ 90%	96.5%
Mean pore size (μm)	≈ 100	≈ 250

Having a material with a narrow pore size such as the alumina foam may further ensure liquid confinement, but it can also “trap” the liquid inside the small pores making it of difficult access when evaporation occurs (see [Section 4.3](#)); a compromise between pores that allow for adequate capillary action and ones that are too narrow must be reached.

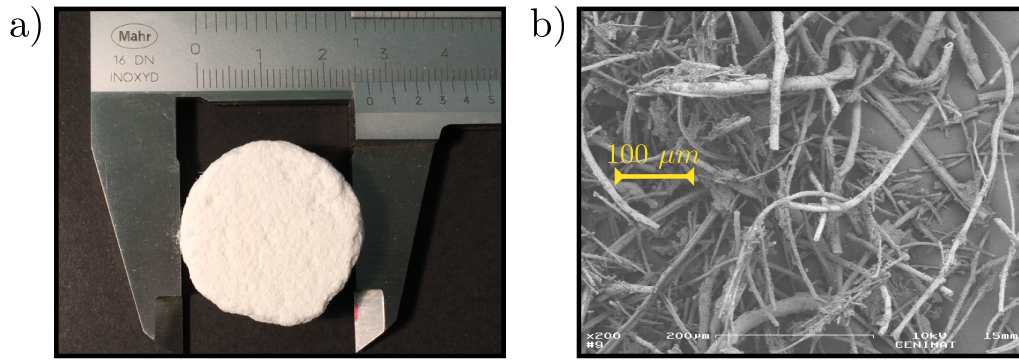


Figure 4.7: Alumina foam KVR 164-242: a) macroscopic appearance of a sample of foam; b) SEM image of its microscopic structure (scale: 200 μm). The equivalent estimated pore size is indicated (≈ 100 μm).

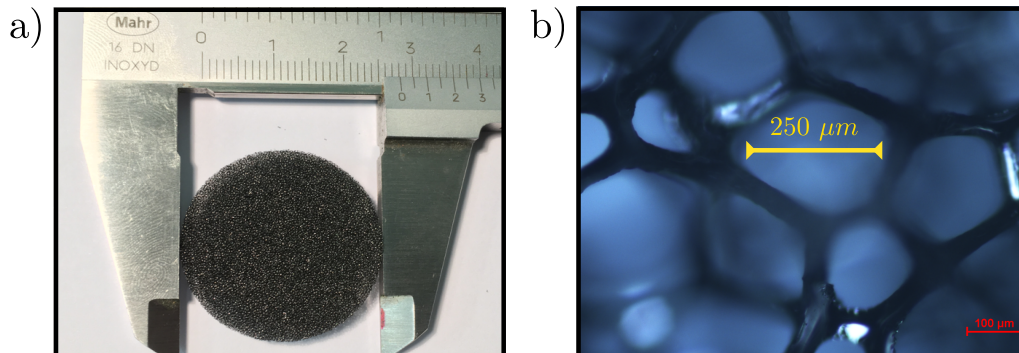


Figure 4.8: Vitreous carbon foam: a) macroscopic appearance of a sample of foam; b) Optical microscope image the foam structure (scale: 100 μm). The estimated pore size is ≈ 250 μm.

Another consideration must be the porosity of the material, *i.e* the volume fraction of

the material that is void space: the higher the porosity, the more void volume for hydrogen to condense and circulate. In principle, a material with higher porosity will produce a smaller pressure drop across it, which is desirable inside the cold cell. In addition to these properties, having a porous material with a thermal conductivity comparable to that of copper would highly increase thermal homogeneity inside the cell and within the liquid; however, both of the selected materials have thermal conductivities that are several orders of magnitude below the desired one. Sintered metal foams with the desired thermal conductivity and pore size were considered for this project, but their low porosity and high density render them less suitable for practical use as the cold cell would be much heavier and bulkier.

4.5 Intermediate temperature stages

As mentioned in [Section 4.2](#), there are two additional interfaces between the cold stage (Cold I/F, 15 K) and the room temperature stage (RT I/F, 300 K): these are I/F 1 and I/F 2, at 120 K and 25 K, respectively. The filling capillary that connects the room temperature storage to the cold cell is going to be thermally coupled to each one of these intermediate interfaces, so we can take advantage of the cooling power available for pre-cooling the gas during the regeneration phase. Because this capillary is subject to a temperature gradient, it is subject to an inherent heat load coming from the warmer stages by solid conduction through the capillary tube walls: this parasitic heat load needs to be accounted for and minimised, as it can hinder the available cooling power at the lower temperature stages.

Sizing the capillary length between each stage must be a compromise between reducing both the parasitic heat load and the pressure drop during the evaporation phase, where hydrogen flow rate is at its highest: having thin-walled, long capillaries with a small diameter can minimize heat loads through solid conduction from the warmer stages to the colder ones, but it may negatively impact the system by causing a non-negligible pressure drop in the gas flow inside those capillaries. A middle ground must be found: the following sections aim to study both issues and reach a compromise that can comply with the requirements.

4.5.1 Heat load through solid conduction

Since the cooling power is limited at the intermediate temperature stages (25 K and 120 K), and at the 15 K stage as well, any parasitic heat loads must be minimised. The cryogenic part of the system should be able to demonstrate its performance in a 50 K radiative environment according to [ER 1 of Appendix A](#); that leaves heat loads through conduction to be assessed. [Figure 4.9](#) illustrates the different stages and the heat load along the capillary tube.

An acceptable upper limit was defined for the heat load across each section of the capillary tube, shown in [Table 4.3](#). The table also shows the available cooling power at

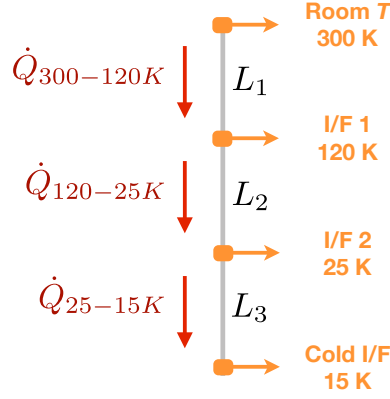


Figure 4.9: Schematic drawing of the different interfaces which the capillary tube must cross; L_1 , L_2 and L_3 represent the length of capillary tube between each interface.

the coldest part of each segment of capillary tube for comparison.

Table 4.3: Maximum allowed parasitic heat load through conduction between each stage of the system.

Capillary section	Cooling power @ I/F	Heat load
300 K to 120 K	40 mW @ 120 K	< 5 mW
120 K to 25 K	15 mW @ 25 K	< 2 mW
25 K to 15 K	15 mW @ 15 K	< 1 mW

In order to respect the given limits for the heat loads through conduction, each section L_1 , L_2 and L_3 of capillary tube needs to be sized accordingly. The heat flow by solid conduction along a tube of length L subject to a temperature gradient $\Delta T = T_1 - T_2$ is given by:

$$\dot{Q} = \frac{S}{L} \int_{T_2}^{T_1} k(T) dT = \frac{\pi(\varnothing_{out}^2 - \varnothing_{in}^2)}{4L} \int_{T_{cold}}^{T_{hot}} k(T) dT \quad (4.6)$$

The integral of thermal conductivity can be calculated from the thermal conductivity data for cryogenic materials [58] or from tables that give the integral itself [59].

Stainless steel 304 was chosen for the capillary tube due to its low thermal conductivity when compared to other metals, coupled to excellent mechanical properties in the low temperature range. As for the dimensions of the tube, two inner/outer diameter combinations were considered:

- a SS 304 capillary tube with inner diameter $\varnothing_{in} = 1.5$ mm and outer diameter $\varnothing_{out} = 2$ mm, for which the cross-section S is 1.4 mm^2 ;
- a SS 304 capillary tube with inner diameter $\varnothing_{in} = 2$ mm and outer diameter $\varnothing_{out} = 2.5$ mm, for which the cross-section S is 1.8 mm^2 .

The integral of $k_{SS}(T)$ can be obtained for the different sections of capillary tube and the minimum length of each segment can be calculated so that the heat load remains below the accepted level: results are presented in Table 4.4.

Table 4.4: Required length for the different segments L_1 , L_2 and L_3 of capillary tube using stainless steel 304.

	L₁ 300 K to 120 K	L₂ 120 K to 25 K	L₃ 25 K to 15 K
\dot{Q}_{cond}	< 5 mW	< 2 mW	< 1 mW
T_{hot}	300 K	120 K	25 K
T_{cold}	120 K	25 K	15 K
Integral of $k_{SS}(T)$	2316 W m ⁻¹	685 W m ⁻¹	22 W m ⁻¹
S/L	< 2 μm	< 3 μm	< 46 μm
Min. L if 2 × 2.5 mm tube	819 mm	605 mm	38 mm
Min. L if 1.5 × 2 mm tube	637 mm	471 mm	30 mm

The results obtained for both capillary sizes must be checked to assess whether or not they lead to a significant pressure drop, which can hinder the performance of the ESU; this issue is studied over the next section for both inner/outer diameter combinations of capillary tube as to assess whether the sizing of the tube length from a thermal point of view does not clash with flow constraints.

4.5.2 Pressure drop

As described in Section 4.5.1, the longer the capillary tube between each temperature stage, the smaller the parasitic heat loads between stages. However, it must be noted that the filling capillary length must always be a compromise between avoiding excessive parasitic heat load and avoiding significant pressure drops in the tube. During the heat absorption phase this issue is in no way negligible, mainly due to low working pressures (between 100 mbar and 300 mbar) coupled to a small diameter tube and a heat load on the cell that can reach up to 1 W, leading to a rather high hydrogen mass flow. The pressure drop (ΔP) along a tube of inner diameter ϕ_{in} and length L can be given by:

$$\Delta P = \frac{\rho v_m^2}{2} \frac{L}{\phi_{in}} f \quad (4.7)$$

where ρ is the fluid's density and v_m its mean velocity. f is the friction coefficient, and its calculation depends upon the type of flow that has developed inside the tube; this is in turn defined by the Reynolds number, Re :

$$Re = \frac{\text{inertial forces}}{\text{viscous forces}} = \frac{\rho v_m \phi_{in}}{\mu} \quad (4.8)$$

where μ is the dynamic viscosity of the fluid. The Reynolds number allows for the determination of the type of flow that has developed inside the tube, and the friction coefficient for smooth pipes can be calculated accordingly:

$$f = \begin{cases} 64/Re & \text{for a fully developed laminar flow (Re} \leq 2000) \\ 0.316Re^{-0.25} & \text{for a fully developed turbulent flow (Re} > 3000) \end{cases} \quad (4.9)$$

The filling capillary is subject to a temperature gradient between 300 K and 15 K, and because both the viscosity and density of a fluid vary with temperature, the pressure drop should be calculated for these two extremes in order to get the best- and worst-case scenarios for the pressure drop along the capillary. Pressure drop depends on the flow rate, *i.e.* on the rate of evaporation of liquid hydrogen from the cell, and this flow rate is in turn a function of the heat load applied on the cold cell. The flow is found to be laminar, and the results presented in Figure 4.10 give the pressure drop per meter of tube as a function of the applied heat load, as this was considered more useful for design purposes than the flow rate itself. The results are displayed for the two sizes of capillary tube studied in the previous section regarding parasitic heat loads.

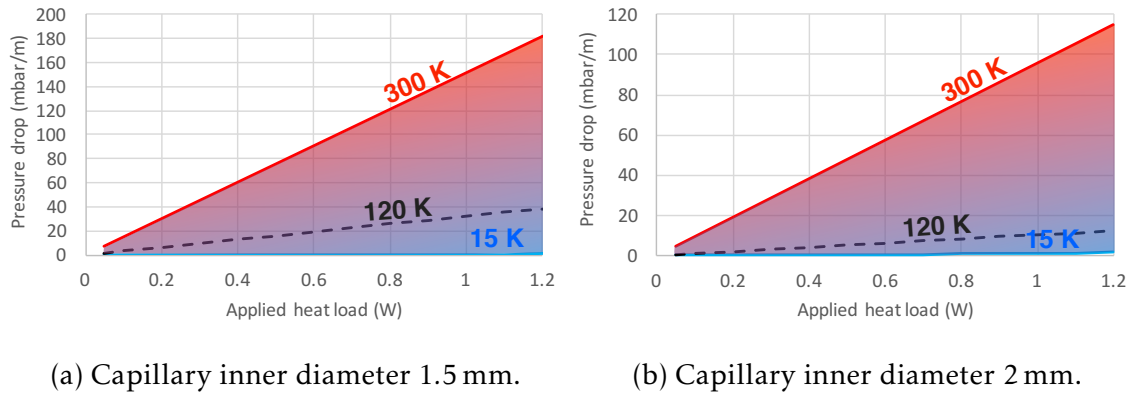


Figure 4.10: Pressure drop per meter of tube length for the temperature range 15 K to 300 K, given as a function of the heat load applied to the cold cell.

Considering the worst case for the ESU, *i.e.* the capillary being at room temperature during the maximum expected heat load of 1 W, the pressure drop amounts to $\approx 150 \text{ mbar m}^{-1}$ for $\varnothing_{in} = 1.5 \text{ mm}$ and to $\approx 95 \text{ mbar m}^{-1}$ for $\varnothing_{in} = 2 \text{ mm}$; this is very significant since the working pressure for ESU operation is between 100 mbar and 300 mbar. However, there is only a small portion of the tube that is effectively at high temperature: at least half of it will be between 120 K and 15 K (cf. Table 4.4). The pressure drop for this temperature range is significantly smaller, and as such should pose no problem, even for high heat loads. Results will show through various types of measurements that the pressure drop is negligible (if the capillary tube is unobstructed!). It should be noted that for high heat loads on the cold cell, there is a high hydrogen flow rate: this means that the evaporated hydrogen does not have enough time to be heated up to the temperature of the intermediate interfaces; this further helps minimize pressure drop as the gas coming from the cell is still cold.

Since we are working in saturation conditions, pressure measurements can be used to deduce the temperature of the liquid-vapour interface inside the cold cell. Because these pressure measurements are taken at room temperature, its values are influenced by the potential pressure drop along the tube. Results for this error in calculated temperature relative to the real cold cell temperature are shown in Figure 4.11 using the values of pressure drop calculated and shown in Figure 4.10.

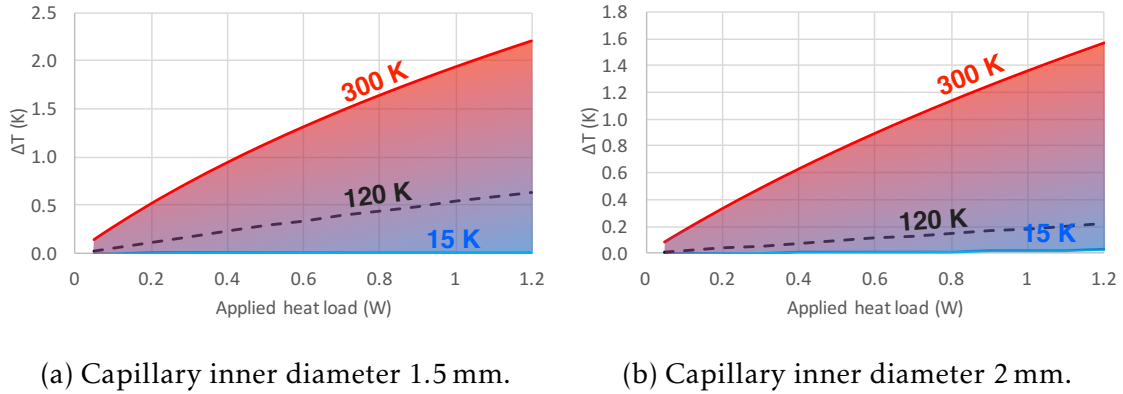


Figure 4.11: Error in cold cell temperature as computed from pressure measurements in saturation conditions for the temperature range 15 K to 300 K, given as a function of the heat load applied to the cold cell.

4.6 Heat exchange at the intermediate interfaces

Since the cooling power at the 15 K stage is limited and there are two intermediate stages available, these can be used to pre-cool the gas before it reaches the cell to be condensed by removing the enthalpy of the gas at the heat intercepts. During the regeneration period, when the hydrogen is being condensed, the gas will flow across the capillary tube, which will be thermally coupled to the 120 K and 25 K stages. Since the regeneration phase should take no longer than 24 h (FPR 2 of [Appendix A](#)) and there are limits as to how much heat load each interface can take, a study was carried out in order to assess whether the gas can be pre-cooled down to the desired temperature for a certain condensation time, while staying within the cooling power budget.

The heat exchanger for these interfaces will be a tube that is thermally coupled to the interfaces; the intermediate interfaces can be considered as heat sinks that will provide the tube with a constant and uniform local wall temperature along the thermally coupled length: Figure 4.12 illustrates this process.

For a cooling process ($T_0 < T$), the heat load across the tube walls along a length dx is given by

$$d\dot{Q} = -U\pi d(T - T_0)dx \quad (4.10)$$

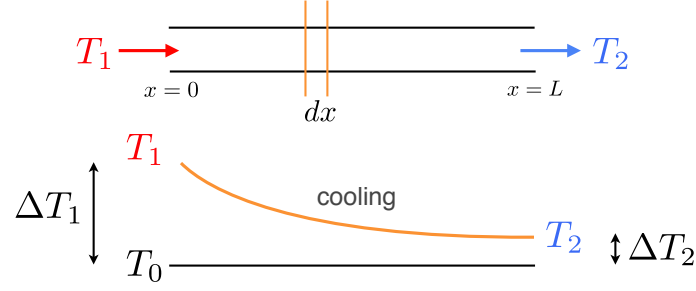


Figure 4.12: Fluid temperature distribution along a tube with uniform wall temperature; adapted from [60].

where d is the tube diameter and U is the heat transfer coefficient. On the other hand, the heat removed from the gas is given by

$$d\dot{Q} = \dot{m}c_p dT \quad (4.11)$$

where c_p is the specific heat of the gas and \dot{m} is the gas mass flow across the tube. The two expressions can be set equal, giving:

$$\dot{m}c_p dT = -U\pi d(T - T_0)dx \quad (4.12)$$

This expression can be integrated and allows for the determination of the fluid temperature T at the tube position x :

$$\frac{T_0 - T}{T_0 - T_1} = e^{-\frac{\pi U dx}{\dot{m}c_p}} \quad (4.13)$$

If one only wishes to know the temperature at the tube exit L (*i.e.* the outlet temperature T_2), T can be replaced by T_2 and x by L . Rearranging the expression gives:

$$T_2 = T_0 - (T_1 - T_0)e^{-\frac{\pi U d L}{\dot{m}c_p}} \quad (4.14)$$

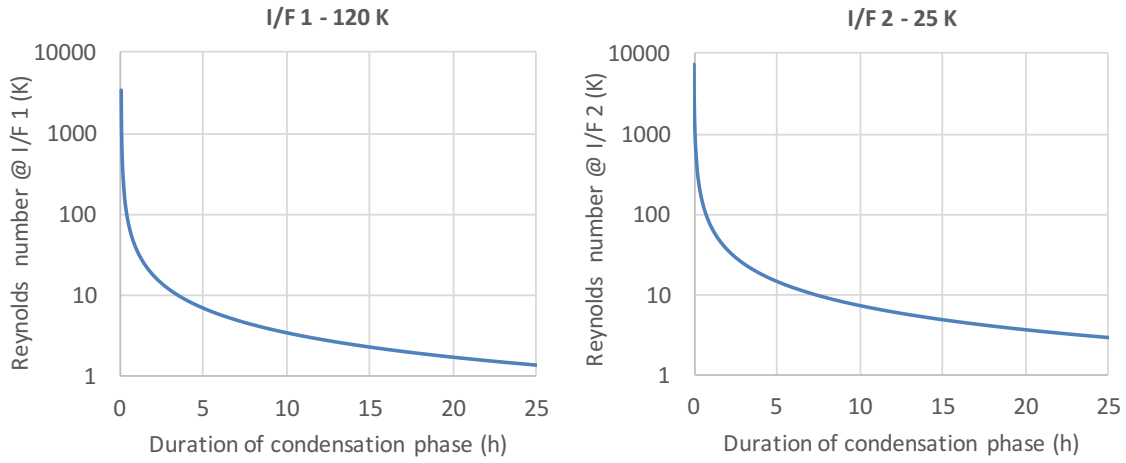
The only parameter that is unknown is the heat transfer coefficient U , which can be given by the Nusselt number:

$$\text{Nu} = \frac{\text{Convective heat transfer}}{\text{Conductive heat transfer}} = \frac{UD_h}{k_f} \quad (4.15)$$

where k_f is the thermal conductivity of the fluid. The Nusselt number is a function of the Prandtl number (Pr) and the Reynolds number (Re): as a consequence, the type of flow inside the tube must be known. The Reynolds number, as given by Eq. 4.8, can be calculated for various flow rates, *i.e.* for different condensation times. Table 4.5 summarises the parameters used for the calculation of both the Reynolds number and the exit temperature of the gas; Figure 4.13 shows the Reynolds number for both interfaces, given as a function of the condensation time.

Table 4.5: Parameters used for determination of the Reynolds number and outlet temperature of the gas at I/F 1 and I/F 2.

	I/F 1	I/F 2
Inlet temp. T_1	300 K	120 K
Heat sink temp. T_0	120 K	25 K
Properties calculated at $T_m = (T_1 + T_0)/2$	210 K	72.5 K
Properties calculated at P	0.3 bar	0.3 bar
Length of tube at T_0	10 mm	10 mm
Inner tube diameter D	1.5 mm	1.5 mm
ΔH of gas from T_1 to T_0	4883 J mol ⁻¹	2064 J mol ⁻¹
Amount of hydrogen to be condensed	0.5 mol	0.5 mol



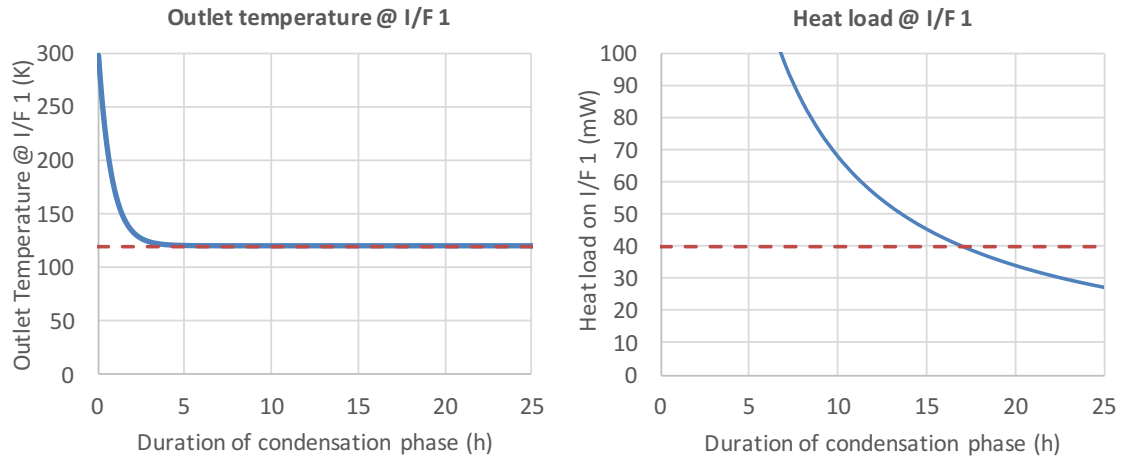
(a) Reynolds number at I/F 1.

(b) Reynolds number at I/F 2.

Figure 4.13: Reynolds number as a function of the condensation time for interfaces I/F 1 and I/F 2.

It can be concluded that for both interfaces Re remains below 1000, indicating that regardless of the rate of condensation, the flow inside the capillary tube is a fully developed laminar flow. Since the flow is laminar, the Nusselt number for convection with uniform surface temperature in a circular tube is constant: $Nu = 3.66$ [61]. From here the outlet temperature of the gas at each interface can be computed (using Eq. 4.14), as well as the resulting heat load as a function of the condensation time (using Eq. 4.11): results for I/F 1 are given in Figure 4.14 and for I/F 2 in Figure 4.15.

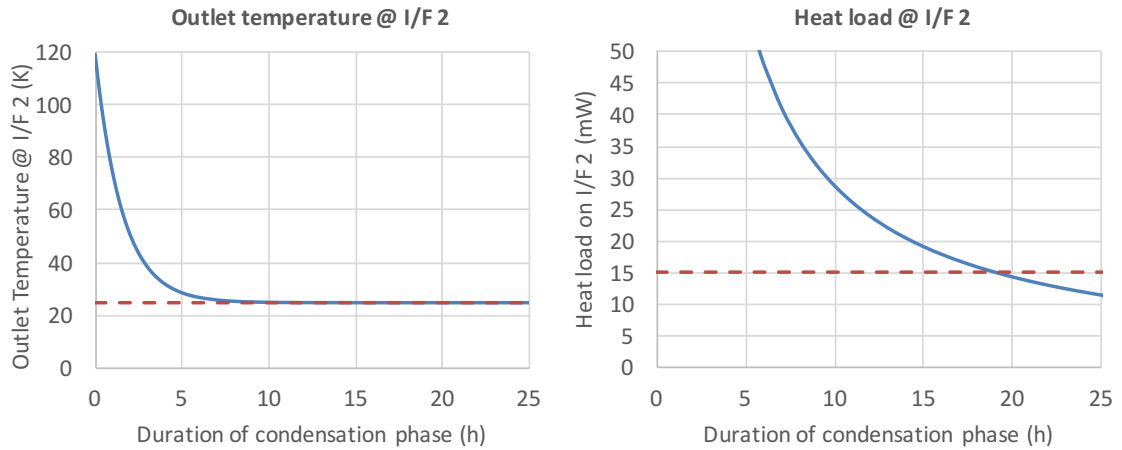
In both cases, the gas reaches the temperature of the interface or heat sink relatively fast: less than 5 h for I/F 1 and 10 h for I/F 2: we can conclude that the gas can indeed be satisfactorily pre-cooled at each interface. However, we must also take into account the heat load released as a function of the condensation time, as it exceeds the allowed cooling power budget if the condensation happens during less than 17 h for I/F 1 and 20 h for I/F 2.



(a) Temperature of gas exiting I/F 1.

(b) Heat load released by gas at I/F 1.

Figure 4.14: Heat exchange at intermediate interface I/F 1 (120 K) for condensation of 0.5 mol of hydrogen: a) Temperature of gas as it exits I/F 1 as a function of the condensation time. The orange dashed line represents 120 K; b) Heat load on that interface as a function of the condensation time. The dashed line represents the maximum available heat load, 40 mW.



(a) Temperature of gas exiting I/F 2.

(b) Heat load released by gas at I/F 2.

Figure 4.15: Heat exchange at intermediate interface I/F 2 (25 K) for condensation of 0.5 mol of hydrogen: a) Temperature of gas as it exits I/F 2 as a function of the condensation time. The orange dashed line represents 25 K; b) Heat load on that interface as a function of the condensation time. The dashed line represents the maximum available heat load, 15 mW.

Finally, the heat load at the Cold I/F must be determined. Here, the enthalpy of the gas between 25 K and 15 K needs to be removed, but also the latent heat of condensation. Table 4.6 breaks down the energy that needs to be removed according to its origin, and Figure 4.16 shows the resulting heat load as a function of the duration of the condensation period.

Table 4.6: Data for calculation of the heat load at the Cold I/F.

	Cold I/F
Inlet temp. T_1	25 K
Heat sink temp. T_0	15 K
Properties calculated at P	0.3 bar
ΔH of gas from T_1 to T_0	205 J mol^{-1}
ΔH from latent heat	920 J mol^{-1}
Amount of hydrogen to be condensed	0.5 mol

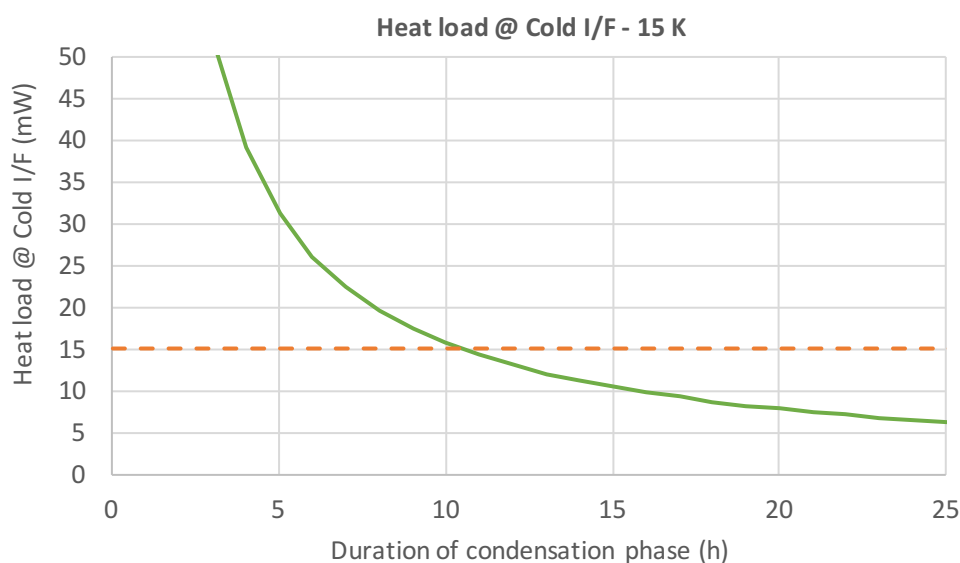


Figure 4.16: Heat exchange at the cold interface (15 K) for condensation of 0.5 mol of hydrogen, given as a function of the condensation time; the dashed line represents the maximum available heat load, 15 mW.

Analysing the heat load plots for the three interfaces, it can be concluded that the heat load at I/F 2 is the limiting factor during condensation: if the heat load at both stages is to be kept under the allowed limit, the condensation phase should take between 20 h and 24 h. The obtained results are of vital importance for the overall operation of the ESU. This study validated the need for using the heat intercepts at 120 K and 25 K and enables determination of the heat load associated to a determined condensation time; it also defined the maximum operating conditions for the system during the regeneration phase for compliance with the requirements.

4.7 Influence of ortho-to-para conversion

The phenomenon of ortho-to-para conversion of hydrogen at low temperatures has been detailed in the previous chapter, and it was mentioned that this conversion process will only occur (at least one that is not negligible) in the condensed, *i.e.* solid and/or liquid phases. The matter of the energy released upon conversion should not be overlooked: during the condensation process, the heat generated from converting *o*-H₂ to *p*-H₂ needs to be removed in addition to the enthalpy of the gas and the latent heat of condensation. Since the available cooling power is limited at the Cold I/F where condensation occurs, the heat load from conversion needs to be quantified, as it might cause us to exceed the budget at that interface.

Because conversion is only significant when hydrogen is in the condensed state, it was considered that the heat load generated from conversion will only affect the last stage, *i.e.* the Cold I/F. As such, the heat load at this interface was recomputed with the addition of the heat load from conversion: the values considered for this calculation are given in Table 4.7.

Table 4.7: Data for calculation of the heat load at the Cold I/F considering ortho-to-para conversion.

	Cold I/F
Inlet temp. T_1	25 K
Heat sink temp. T_0	15 K
Properties calculated at P	0.3 bar
ΔH of gas from T_1 to T_0	205 J mol ⁻¹
ΔH from latent heat	920 J mol ⁻¹
Energy released by conversion	1417 J mol ⁻¹
% of <i>o</i> -H ₂ to convert	75%
Amount of hydrogen to be condensed	0.5 mol

Figure 4.17 shows the results for this calculation. It assumes condensation of 0.5 mol of hydrogen, and conversion of the entire amount of *o*-H₂ (75% of 0.5 mol). It also assumes that the conversion process takes place as soon as the gas is liquefied, *i.e.* that all of the hydrogen is converted each time: this is highly unlikely as hydrogen conversion is a considerably slow process [32, 37], and is considered the worst-case scenario. However, the conversion process can be sped up (when compared to the nominal time constant, see Section 3.1) due to the large surface area produced by the porous foam inside the cold cell, that could have a catalyst effect on this transformation.

As expected, the heat load generated due to ortho-to-para conversion is not negligible at all: it is responsible for a two-fold increase in the total heat load in the cold cell. The conversion can be handled within the heat load budget for condensation times longer than 21 h, which is compatible with the requirements imposed by the other interfaces and with the 24 h threshold.

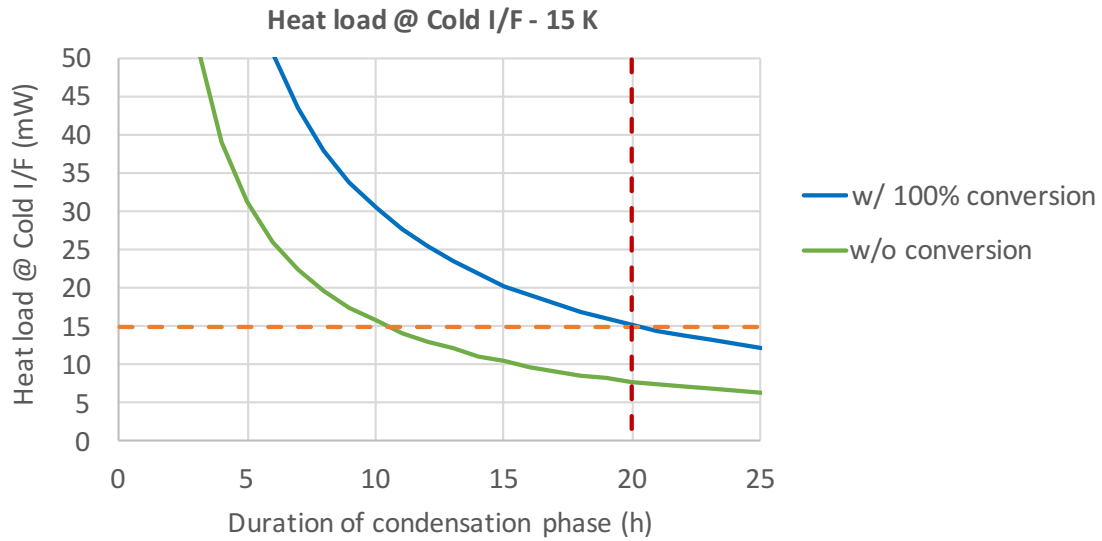


Figure 4.17: Heat exchange at the cold interface (15 K) as a function of the condensation time, considering that all of the hydrogen is converted into $p\text{-H}_2$; the dashed line represents the maximum available heat load, 15 mW.

4.8 Room temperature storage

The options for storing hydrogen gas generated during the heat absorption phase at room temperature have been discussed in [Chapter 3](#), and they included using an ordinary expansion volume, using adsorbent materials at low temperature and using metal hydrides for chemically absorbing hydrogen. The pros and cons of each were assessed, and it was concluded that the most efficient way to store hydrogen at room temperature from a mass and volume budget point of view would be the metal hydride solution. However, although not viable for space, the expansion volume solution is useful for preliminary ground testing and thus should be adequately sized and studied.

4.8.1 Sizing the expansion volume

As mentioned, an expansion volume can be used for ground operation of the [ESU](#) as it allows for testing of the cold part of the system in an independent way. This makes the verification of some phenomena significantly easier when using an ordinary expansion volume as opposed to sorption materials to store hydrogen, such as verification of the amount of liquid inside the cell; this will be further discussed in [Section 4.10.1](#). [Figure 4.18](#) shows the size of the expansion volume at room temperature for a given temperature drift in the cold cell, starting at 15 K and for a total of 400 J of thermal energy stored; these results were obtained by numerical integration of [Eq. 3.14](#), according to the model briefly described in [Section 3.4](#). As the expansion volume is increased, the increase in pressure due to evaporation is reduced, which in turn leads to a smaller temperature

increase inside the cold cell. The choice of expansion volume is a compromise between the available space and the total increase in the cold cell temperature one is willing to allow.

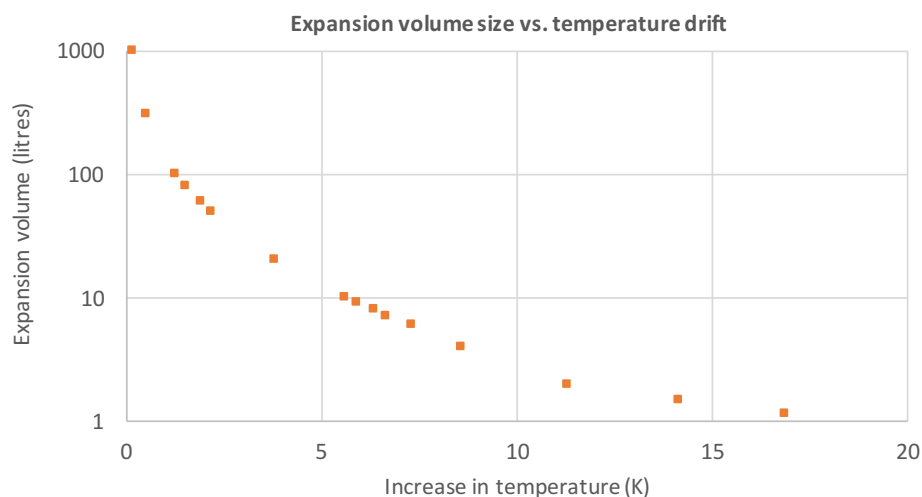


Figure 4.18: Expansion volume needed as a function of the temperature increase in the cell. Data given for a total energy absorption of 400 J and for a starting temperature of 15 K.

For this project, the temperature inside the cell must be maintained between 15 K and 17 K at all times, which would require a 56 ℓ volume; if we take requirement FPR 5 of [Appendix A](#) into consideration, a temperature drift of only 1 K (from 15 K and 16 K) would mean a 135 ℓ volume at room temperature. For practical purposes, a volume of 56 ℓ was considered adequate for the foreseen preliminary experiments; it allows for observation of the system's behaviour without a large temperature increase, while comprising the maximum allowed temperature range.

4.8.2 Metal hydride storage

It was established that using the metal hydride $\text{LaNi}_{4.8}\text{Sn}_{0.2}$ to store hydrogen gas at room temperature is the best solution in light of the constraints imposed by [ESA](#), since its absorption/desorption isotherms are compatible with the required working pressure and are accessible for a metal hydride temperature range that is available at the room temperature interface. The amount of $\text{LaNi}_{4.8}\text{Sn}_{0.2}$ required to absorb 0.5 mol of hydrogen gas (1 mol H) can be calculated, so that the rest of the room temperature storage vessel can be designed. Materials of the AB_5 -type like $\text{LaNi}_{4.8}\text{Sn}_{0.2}$ are able to absorb up to 6 atoms (1.37 wt%) of hydrogen per AB_5 unit of metallic alloy; however the calculations below consider only 5 atoms per molecule, as the absorption of the 6th H atom can occur with a non-negligible pressure increase (see [Figure 3.12](#)). [Table 4.8](#) shows the needed mass to absorb the desired amount of hydrogen.

Table 4.8: Amount of $\text{LaNi}_{4.8}\text{Sn}_{0.2}$ needed to absorb 0.5 mol of hydrogen.

Amount of $\text{LaNi}_{4.8}\text{Sn}_{0.2}$ needed	
Molar mass H_2	$2.01588 \text{ g mol}^{-1}$
Amount of H_2 to be absorbed	$0.5 \text{ mol} = 1 \text{ g}$
$\text{LaNi}_{4.8}\text{Sn}_{0.2}$ density	8.4 g cm^{-3}
Molar mass $\text{LaNi}_{4.8}\text{Sn}_{0.2}$	444.4 g mol^{-1}
H atoms per $\text{LaNi}_{4.8}\text{Sn}_{0.2}$ molecule	5 atoms
$\text{LaNi}_{4.8}\text{Sn}_{0.2}$ mass needed	88.9 g
Bulk $\text{LaNi}_{4.8}\text{Sn}_{0.2}$ volume needed	10.6 cm^3

Calculations give 88.9 g of $\text{LaNi}_{4.8}\text{Sn}_{0.2}$ with a *bulk* volume of 10.6 cm^3 ; however, metal hydrides suffer pulverisation upon activation and contact with hydrogen, turning into a very fine powder with particle diameter in the $10 \mu\text{m}$ range. Hence, the packing density of these particles needs to be taken into account when sizing the volume needed to contain the 88.9 g of material; the maximum packing density for identical spheres in three dimensions is $\eta_{\text{max}} = 77.96\%$ [62] assuming a close and organised packing of the particles, whereas $\eta_{\text{max}} = 63\%$ is obtained for an irregular packing. Since the powder may not have an equal size distribution and have a more coarse shape, and also is not going to be compacted, the packing density assumed for activated $\text{LaNi}_{4.8}\text{Sn}_{0.2}$ is $\eta = 43\%$; this value was reached after initial discussions with R. C. Bowman Jr., and the CNRS team who synthesised the material used in this project. Considering this packing factor the volume needed to house 88.9 g of metal hydride powder rises to 24.7 cm^3 . Even though $\text{LaNi}_{4.8}\text{Sn}_{0.2}$ has shown remarkable resistance to degradation and ageing [47], because the system needs to be designed for 10 years of uninterrupted operation in a space environment, a safety factor of 4¹ was added to the mass of material. As such, the total mass (and volume) of $\text{LaNi}_{4.8}\text{Sn}_{0.2}$ that needs to be housed in the room temperature vessel is summarised in Table 4.9.

Table 4.9: Total mass and volume of $\text{LaNi}_{4.8}\text{Sn}_{0.2}$ needed considering safety factors.

Amount of $\text{LaNi}_{4.8}\text{Sn}_{0.2}$ considering safety factors	
Packing density of powdered material	43%
Safety factor in hydride mass	4
$\text{LaNi}_{4.8}\text{Sn}_{0.2}$ mass needed	356 g
$\text{LaNi}_{4.8}\text{Sn}_{0.2}$ volume needed	98.8 cm^3

Knowing the volume needed to house the $\text{LaNi}_{4.8}\text{Sn}_{0.2}$ powder is the first step for sizing the room temperature vessel (or *canister*): its minimum inner volume is now known. However, the canister is far from being a simple container with no other purpose than to contain the hydride: it will serve a functional purpose and will need certain features to enhance heat transfer and thermal homogeneity; the mechanical and thermal design will

¹Based on the data obtained from Planck, M. Linder, private communication.

be described in the next section.

4.9 Sizing the metal hydride canister

As mentioned, the chemisorption of hydrogen by $\text{LaNi}_{4.8}\text{Sn}_{0.2}$ is an exothermic process which releases 32.8 kJ per mole of H_2 absorbed. This means that the canister needs to be sized not only for the amount of hydride that it needs to contain, but also for the thermal load that needs to be managed upon hydrogen absorption. According to IR 1 (Appendix A), the cooling power available at the room temperature interface is 10 W at 273 K. The first step is to assess whether 10 W is enough to manage the heat load released by the metal hydride when it absorbs hydrogen during the HLP without a significant temperature increase: if the metal hydride temperature increases, so does the absorption pressure (Figure 3.12) and hence the cold cell temperature, assuming there is liquid hydrogen in saturation conditions. The thermal load released by the metal hydride upon absorption of 0.5 mol can be calculated as follows:

$$Q_{MH} = 32.8 \text{ kJ mol}^{-1} \times 0.5 \text{ mol} = 16.4 \text{ kJ} \quad (4.16)$$

In a first approximation, the average heat load in the canister can be calculated for the duration of the heat load profile in the cold cell:

$$\dot{Q}_{MH,avg} = \frac{16.4 \text{ kJ}}{30 \text{ min}} = 9.1 \text{ W} \quad (4.17)$$

The average heat load released at room temperature is 9.1 W during the 30 min that the HLP lasts for: this seems to be below the 10 W budget, meaning that no further cooling would be needed. However, the heat load in the HLP is not evenly distributed: there is a critical 2 min-period where the heat load in the cell is constant at 1 W, which results in roughly 0.13 mol of hydrogen being evaporated from the cell (and hence absorbed by the metal hydride) in 2 min. The heat load in the canister can be calculated for that period of time:

$$\dot{Q}_{MH,1W} = \frac{32.8 \text{ kJ} \times 0.13 \text{ mol}}{2 \text{ min}} = 35.5 \text{ W} \quad (4.18)$$

Figure 4.19 shows the heat load generated by the hydride when the Heat Load Profile (HLP) is applied to the cold cell. It is now evident that the 10 W cooling power at room temperature is not enough to deal with the heat load generated upon absorption, and that extra measures need to be considered; otherwise the temperature increase in the canister during that period of time will be significant, which would in turn lead to the increase of the cold cell temperature.

We can use the hydride container itself to act as an enthalpy reservoir by taking advantage of its sensible heat along a small temperature increase. Two materials were considered for the canister: copper and stainless steel. In the temperature range of interest (270 K to 300 K), stainless steel has a better heat capacity per unit mass than copper,

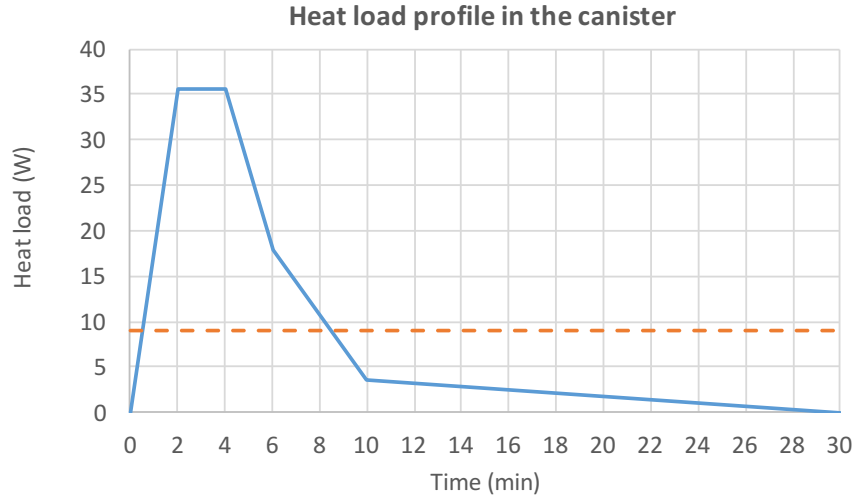


Figure 4.19: Heat load on the room temperature canister as a result of hydrogen absorption during the HLP applied to the cold cell. The dashed line represents the average heat load.

making it more suitable for an enthalpy reservoir that is wanted as light as possible. This is not the only point in favour of using stainless steel: upon contact, hydrogen can reduce the oxide and hydroxide layers present on the copper surface and form free oxygen and water molecules, which in turn can react with metal hydride particles and start a chain reaction that would severely contaminate the metal hydride and hinder its performance. On the other hand, stainless steel has a poor thermal diffusivity ($\approx 3 \text{ mm}^2 \text{ s}^{-1}$), which can cause thermal homogeneity issues.

The temperature profile $T(t)$ of the canister can be calculated using the enthalpy of stainless steel and the energy released by the metal hydride at each instant:

$$\Delta T(t) = \frac{\Delta E_{abs.}(t)}{C_{p,SS} \times m_{SS}} \quad (4.19)$$

where $E_{abs.}(t)$ is the energy released by the canister each instant due to the absorption of Δn moles of hydrogen and m_{SS} is the mass of stainless steel. The variable parameter here is the mass: Figure 4.20 plots the temperature profile of the canister upon absorption of hydrogen during the heat load profile for different values of SS 316 mass, with no cooling source — heat is absorbed only using the sensible heat of stainless steel, assuming a homogeneous temperature along the material.

The 281 K threshold indicated in Figure 4.20 is a consequence of the metal hydride isotherms: in order to maintain the pressure below 0.2 bar, *i.e.* the cell temperature below 16 K, the metal hydride must be kept below 281 K, 8 K above the starting temperature of 273 K. As was expected, increasing the mass of the canister attenuates the temperature increase in the metal hydride. But to limit the total temperature increase to less than 8 K using only the sensible heat of the stainless steel container, a mass higher than 3.5 kg

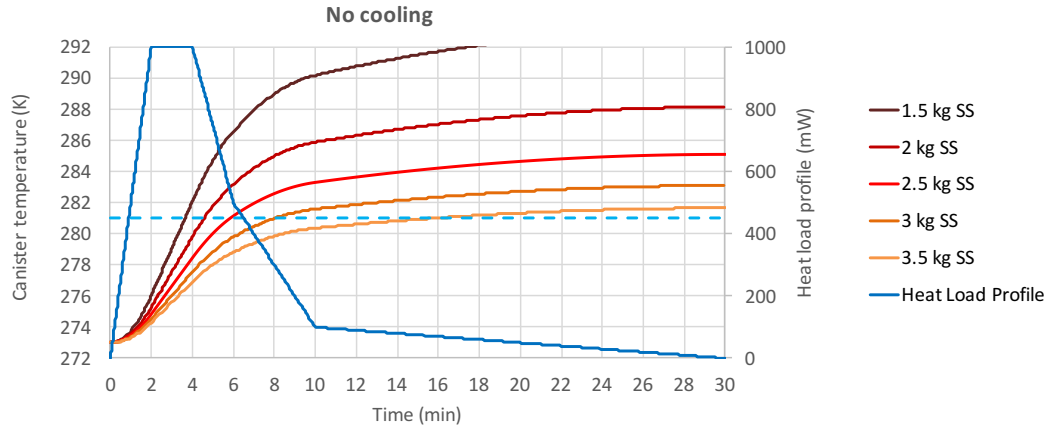


Figure 4.20: Temperature increase in the metal hydride canister when the heat load is applied to the cold cell for different canister masses using SS 316, with no added cooling power. The dashed line represents the 8 K limit on temperature increase.

would be required. Even though this mass does not exceed the mass budget by itself, it makes for little manoeuvring on sizing the other parts of the system, as we need to consider not only the mass of the metal hydride powder, but also instrumentation and the cryogenic mass of the ESU. As mentioned a few paragraphs earlier, 10 W of cooling power are available at this interface: the mass of the canister is only supposed to help manage the heat load during the period of time when it exceeds the available 10 W. Figure 4.21 shows the results for the temperature profile as calculated for Figure 4.20, but considering a constant cooling power of 10 W during the whole duration of the heat load profile.

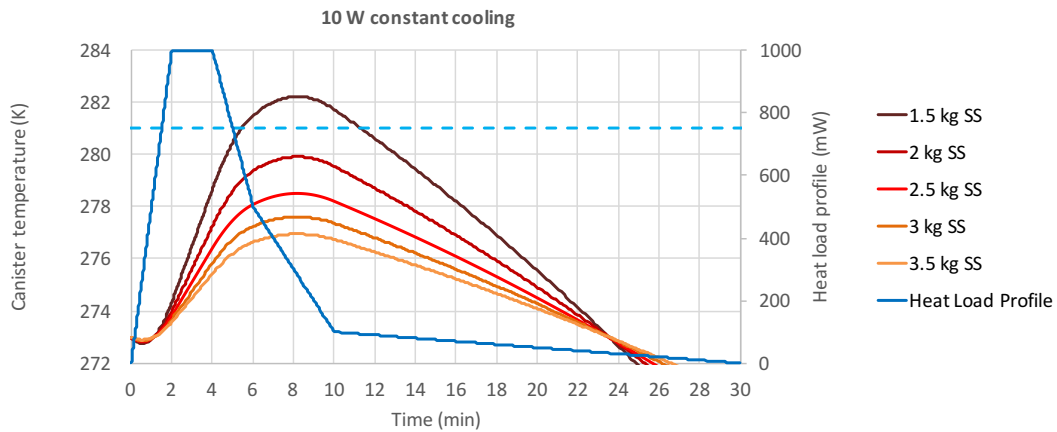


Figure 4.21: Temperature increase in the metal hydride canister when the heat load is applied to the cold cell for different canister masses using SS 316, with 10 W constant cooling power. The dashed line represents the 8 K limit on temperature increase.

Now that the cooling power at 273 K is considered, the only case where the temperature increase is exceeded is for a canister mass of 1.5 kg; a larger mass achieves the objective of effectively managing the heat load and hence the canister temperature during the heat load profile. Figure 4.21 also shows another effect of this configuration: once the heat load generated in the canister becomes lower than the available cooling power, the canister (and hence the metal hydride) is cooled down, allowing for the equilibrium pressure of the hydride to decrease, which in turn allows the temperature of the cold cell to decrease, even if it is still absorbing the heat load. This is an important result since, even if the 16 K limit on the cell is exceeded, the heat load can still be absorbed within specification as long as it only stays above 16 K for less than 10 min — which is possible since the canister is able to cool back down to its base temperature.

Although it would be possible to maintain the canister below 281 K using a stainless steel mass of 2 kg, the decision was made to use 2.5 kg: this value is still well within the mass budget and, from a thermal point of view, the more mass, the less the temperature increase, which is beneficial for the overall performance of the system as it allows the heat load in the cell to be absorbed at a near-constant temperature. It can also compensate for other issues such as the thermal diffusivity within the stainless steel canister or poor thermal coupling between the metal hydride, the canister body and its cooling source.

4.10 Thermal model for metal hydrides

The thermal model for a liquid-to-vapour ESU has already been presented in Section 3.3, where it presented the baseline equations for predicting the amount of energy absorbed in the cell for a given temperature drift as well as the amount of energy that needed to be removed from the system during the regeneration phase. However, the aforementioned thermal model is only valid when using an expansion volume: it cannot be used when using metal hydrides to store hydrogen, as ideal gas laws no longer apply in this situation. One of the assumptions for the model used to calculate the liquid filling ratio inside the cell was that the number of moles $n_{Exp.Vol.}$ in the room temperature volume was known at all times, and because the total number of moles n_{total} in the system was constant, the number of moles in the cold cell n_{cell} was easily obtained:

$$n_{cell}(t) = n_{total} - n_{Exp.Vol.} = n_{total} - \frac{P(t)V_{Vol.Exp.}}{RT_{Vol.Exp.}} \quad (4.20)$$

where $P(t)$ is the global pressure of the system at any given time. With the expansion volume, this allowed for the determination of the amount of liquid in the cell at all times; with the metal hydride canister, a different method for determining the liquid ratio must be found, since an accurate filling ratio cannot be computed from pressure measurements.

4.10.1 Regeneration phase

When using metal hydrides to store hydrogen, three sources of error appear when trying to calculate the liquid filling ratio of hydrogen in the cold cell or the molar flow rate at which a condensation is taking place: these are described in Figure 4.22.

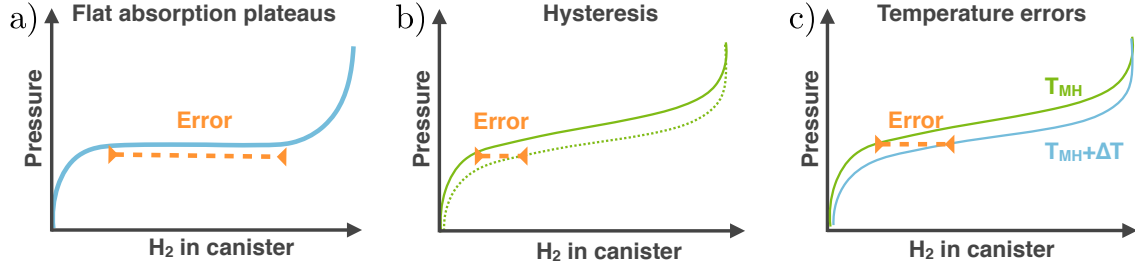


Figure 4.22: Sources of error in hydrogen quantity when computed from pressure measurements: a) flat absorption plateaus along the same isotherm; b) hysteresis in the absorption/desorption pair for the same temperature; c) temperature measured outside ($T_M H + \Delta T$) is different from the true temperature of the hydride ($T_M H$).

The first problem is that, since the plateaus are fairly flat, the same pressure can be measured regardless of the amount of hydrogen in the canister, which in turn would give the amount of hydrogen inside the cell; nor can dP/dt be computed to give the flow rate of condensation, since it remains roughly the same throughout the process. Adding to this is the fact that hysteresis is invariably observed during absorption and desorption of hydrogen for the same temperature and that the temperature that is measured at the outer surface of the canister may not be the exact temperature of the hydride: this would lead to one reading the hydrogen amount at an isotherm that is not the real one. If the temperature of the hydride is not kept constant during the whole process, the task of calculating both the liquid ratio and flow rate becomes next to impossible.

An independent way to obtain the filling rate and ratio was devised that does not rely on pressure measurements, but on the intermediate interfaces of the so-called Qmeters instead (Figure 4.23): when correctly measured, the heat load at each interface can provide the molar flow rate of hydrogen (*e.g.* the flow rate during condensation). Consider the example of the cold cell: the heat load \dot{Q}_{QM3} that is evacuated at Qmeter 3 must be the same as the heat load due to the changes in the enthalpy of hydrogen (if T_{cell} is kept constant), which in turn originate from the gas pre-cooling and condensation. The molar flow rate \dot{n} can hence be computed:

$$\dot{Q}_{QM3} = K(T_{cell} - T_{CF}) = \dot{n} [H(T_{QM2}) - H(T_{cell}) + L_{L-V}] \quad (4.21)$$

$$\dot{n} = \frac{K(T_{cell} - T_{CF})}{[H(T_{QM2}) - H(T_{cell}) + L_{L-V}]} \quad (4.22)$$

where the Qmeter conductance K is known, and so are the temperatures T_{cell} , T_{CF} and T_{QM2} . The changes in enthalpy and the latent heat can be obtained for each temperature using REFPROP [31].

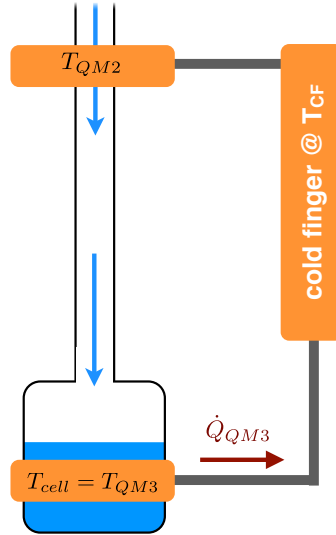


Figure 4.23: Calculation of the condensation rate when using pressure measurements is not viable: as long as the Qmeters such as Qmeter 3 are calibrated, the heat load at every instant can be related to the changes in enthalpy, which in turn allows for the determination of the flow rate.

This type of measurement can be performed between each interface, although one must carefully calibrate the Qmeters for the measurements to be reliable.

4.10.2 Heat absorption phase

During the heat absorption phase in the cold cell, the hydrogen gas generated by evaporation is going to be absorbed by the metallic alloy $\text{LaNi}_{4.8}\text{Sn}_{0.2}$, forming a metal hydride and releasing heat in the process: this heat of absorption is released directly by the metal hydride and needs to be efficiently evacuated from the material to its container and to the cooling source at room temperature. Some measures were taken in order to improve the heat transfer inside the metal hydride canister (to be described in [Section 5.1.4](#)): however, as shown over the last section, the heat load is significant enough to generate a thermal gradient between the material that is inside the canister and its outer walls. This means that the temperature that is measured in the canister (where thermometers are placed in the outside walls) does not necessarily correspond to the real temperature of the metal hydride, and this situation worsens as the heat load increases. It was thus found necessary to model this thermal decoupling between the $\text{LaNi}_{4.8}\text{Sn}_{0.2}$ powder and the canister outside walls, since knowing the temperature of the metal hydride allows for an accurate prediction of the system's overall pressure and, hence, of the saturation temperature in the cold cell during evaporation.

For every instant during the heat absorption phase, there is a certain heat load $\dot{Q}_{cell} = \Delta E_{cell}(t)/\Delta t$ applied on the cold cell, that generates $\Delta n_{evap}(t) = \Delta E_{cell}(t)/L$ evaporated moles of hydrogen gas, where L is the latent heat of evaporation. This amount $\Delta n_{evap}(t)$ is in turn going to be absorbed by the metal hydride, generating heat:

$$\Delta E_{abs}(t) = \Delta n_{evap}(t) \times Q_{MH} \quad (4.23)$$

where Q_{MH} is the heat of absorption (32.8 kJ mol^{-1}). It is assumed that the thermal contact between the metal hydride powder and the canister walls is not perfect, and that there is a small hydrogen gas gap between the two that limits conduction as shown in [Figure 4.24](#). In this case, the temperature T_{MH} of the metal hydride is not the same as the temperature T_{SS} of the canister inner walls: considering this thermal decoupling, the simplification can be made to consider the stainless steel vessel isothermal, so T_{SS} is the temperature of both the canister inner and outer walls.

The heat load through the gap can be calculated as a function of the uniform thickness of the gas gap Δx and using the temperatures of the previous instant, which are known:

$$\dot{Q}_{gas}(t) = K_{gas}(\Delta x) (T_{MH}(t - \Delta t) - T_{SS}(t - \Delta t)) \quad (4.24)$$

where $K_{gas}(\Delta x)$ is the thermal conductance of the gas gap. The heat that is not transferred across the stainless steel will lead to an increase in the metal hydride's temperature:

$$E_{MH}(t) = \Delta E_{abs}(t) - \dot{Q}_{gas}(t)\Delta t \quad (4.25)$$

$$\Delta T_{MH}(t) = \frac{E_{MH}(t)}{C_{p,MH}} \quad (4.26)$$

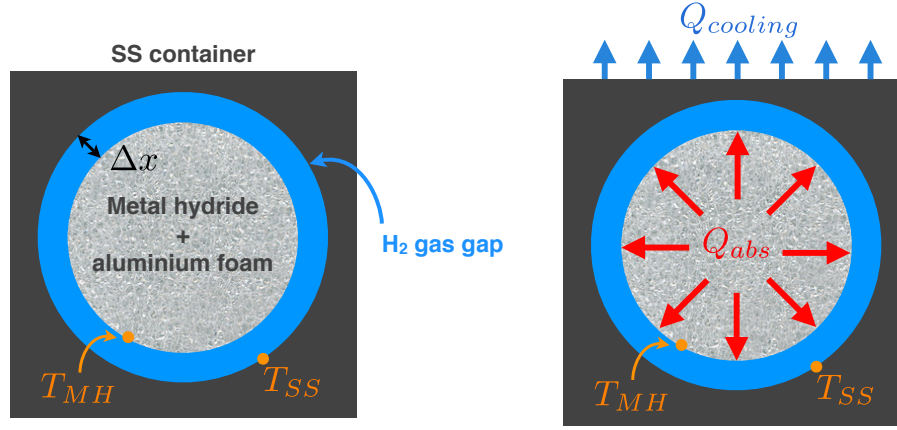


Figure 4.24: Gas gap thermodynamic model for the heat absorption phase in the canister. Δx is the thickness of the hydrogen gas gap.

where $C_{p,MH}$ is the heat capacity of the metal hydride. The temperature of the metal hydride can then be calculated for that instant:

$$T_{MH}(t) = \Delta T_{MH}(t) + T_{MH}(t - \Delta t) \quad (4.27)$$

The temperature of the stainless steel walls can be calculated now that $\dot{Q}_{gas}(t)$ is known:

$$\Delta T_{SS}(t) = \frac{\dot{Q}_{gas}(t)\Delta t - E_{cooling}(t)}{C_{p,canister}} \quad (4.28)$$

where $E_{cooling}$ is the energy removed by the cooling source at every instant, which in turn depends on the available cooling power at room temperature. Figure 4.25 shows the temperature evolution of the metal hydride inside the canister compared to the canister outer walls; this result considers the predicted masses for the canister and heat exchanger, the approximate available cooling power at room temperature, and a hydrogen gas gap of $500\mu\text{m}$ between the $\text{LaNi}_{4.8}\text{Sn}_{0.2}$ powder and the canister inner walls.

It can be seen that the behaviour of the metal hydride temperature is quite different than what can be observed by measuring the temperature on the outside of the canister. Experimental results will show that this is indeed a good model for what happens inside the canister, and it will allow for the determination of the metal hydride temperature from outer canister temperature measurements alone; this is an important result since knowing the actual metal hydride temperature allows for an accurate determination of the equilibrium pressure inside the system, which in turn allows for the determination of the temperature of the cold cell at saturation conditions. This model will be further discussed and validated against experimental results.

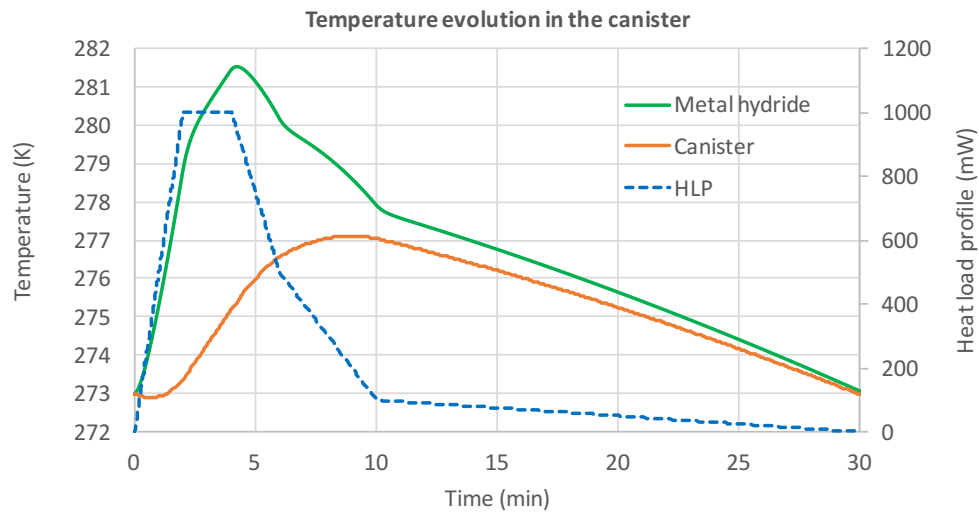


Figure 4.25: Evolution of the temperature inside the metal hydride and at the outer walls of the canister when considering a gas gap between the canister and the contents of the canister, during hydrogen absorption due to a heat load.

5 System Implementation

This chapter describes the actual implementation of the liquid-to-vapour hydrogen [ESU](#), namely its construction according to the dimensioning and specifications and assembly into the cryocooler for operation. It is divided into two main parts: the implementation of the Development Model ([DM](#)), which is a breadboard device for preliminary testing and the Engineering Model ([EM](#)), the final model that is to be delivered to [ESA](#) and that complies with more strict requirements, especially on the mechanical aspect.

5.1 Development Model

The Development Model of the [ESU](#) is intended to be a breadboard device for preliminary testing, so that the main aspects of operation can be validated and, if need be, adjusted. It was designed to be easily dismountable, so that some items could be tested separately and some configurations could be changed if it was deemed necessary. This device was tested with both an expansion volume and using a metal hydride canister. The overall outline of the development model is pictured in Figure 5.1.

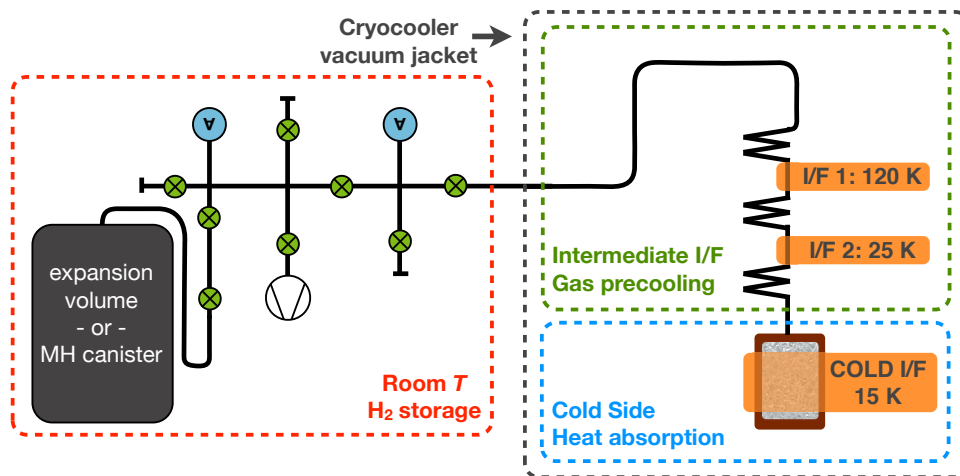


Figure 5.1: Overall schematic of the Development Model assembly.

At room temperature, either the expansion volume or the metal hydride is mounted; the canister requires its own heat exchanger and cooler so its temperature can be lowered to $\approx 273\text{ K}$, which will be described in detail over the next sections. The intermediate part of the system includes the two interfaces for gas pre-cooling at 25 K and 120 K that are thermally coupled to the capillary tube that runs from room temperature down to the cold cell. This last stage is composed of the cell that is mounted on the 15 K stage. Over the next sections the steps taken to adapt the instrumentation that was available at the laboratory to the needs of this project will be described, as well as the manufacturing of the parts that compose the ESU. The different stages of a 4 K cryocooler were used as heat sinks for the three cryogenic interfaces of the system.

5.1.1 Cold cell

The cold cell was sized in the last chapter (Section 4.3) regarding its internal volume and wall thickness, and it was determined it was going to be made out of copper as it ensures good thermal homogeneity. It needs, however, to have mechanical interfaces than can connect both to the cooling source and to thermal straps that would lead to the sorption cooler, which for laboratory testing will be replaced by a resistive heater; it also needs interfaces for instrumentation such as thermometers and additional heaters. Table 5.1 summarises the requirements for the cold cell.

Table 5.1: Specifications to be considered for the design of cold cell of the Development Model.

Specification	Comment
Inner free volume of 17.2 cm^3	See Section 4.3; volume considering amount of LH_2 with margins and volume occupied by porous material.
Shape of a cylinder with equal diameter and height	See Section 4.3.1: both diameter and height were computed to be 28 mm for the needed volume.
Wall thickness of 1 mm	Provides good thermal homogeneity and structural resistance to pressure in the operational and proofing range.
Material should be copper	Provides good thermal homogeneity at low temperature and both parts can be easily soldered, making the cell dismountable.
Flat mounts for thermal straps	Two flat mounts, one at each end, were considered for instrumentation placement and connection to the other parts of the system.
RT pressure measurements	Need to test pressure drop along the filling capillary.

The cell consists of a main part, the body, and a lid; both are soldered together using

soft solder so that it can be easily disassembled, making it a multi-purpose cell where the porous material can be changed if needed. The final design for the cold cell is depicted in Figure 5.2: the filling capillary was brazed to the cell lid, as this symmetrical design allows for the cell to be tested in both configurations simply by inverting the mounting of the cell into the cryocooler to study liquid confinement.

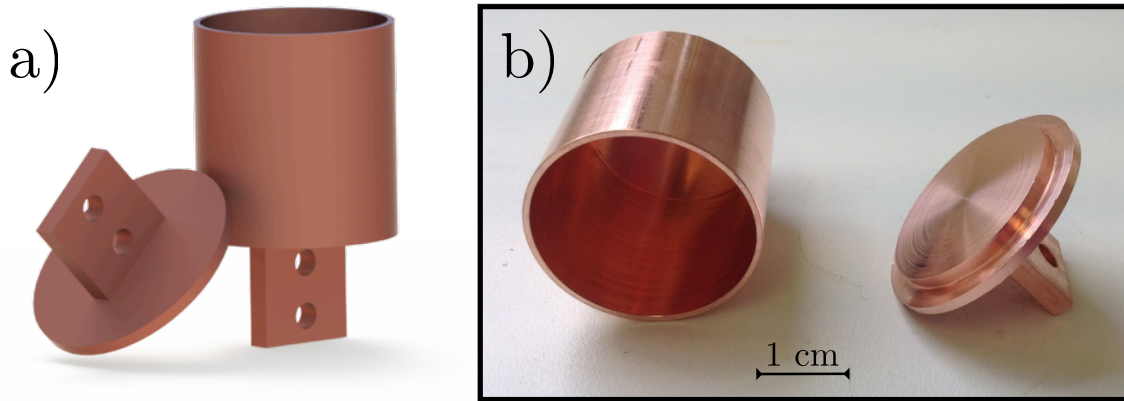


Figure 5.2: Cold cell as designed for the Development Model: a) Solidworks® rendered image; b) Cell after machining and prior to filling and soldering.

For liquid confinement, two porous materials have been selected for their properties: an alumina foam and a vitreous carbon foam. However, during preliminary testing, the vitreous carbon was shown not to confine the liquid properly, which led to the conclusion that the capillary height was shorter than estimated; it was also observed that this material seemed to speed up ortho-to-para conversion. As such the carbon foam, despite being a more robust solution, was discarded for the Development Model; only the alumina foam was used as it performed as expected during exploratory (pre-Development Model) tests. These conclusions will be addressed in more detail in the next chapter.

Calculations (Section 4.5.2) showed that the pressure drop in the filling capillary might not be negligible and as such needs to be investigated; for this reason, a second capillary was connected with the cell at one end and a second pressure sensor at the other, running parallel to the one used to transport the evaporated gas to the room temperature volume: since there is no hydrogen gas circulation in this capillary, the pressure measurements can be taken as the actual cell pressure. This allows for both the pressure inside the cell and the pressure of the expansion volume to be measured and compared, to verify the extent of pressure drop along the filling capillary that connects to the expansion volume. This configuration is shown in Figure 5.3.

5.1.2 Filling capillary

In order to minimize the effects of pressure drop at the room-temperature part of the filling capillary (from the results presented in Section 4.5.2 and taking into account the

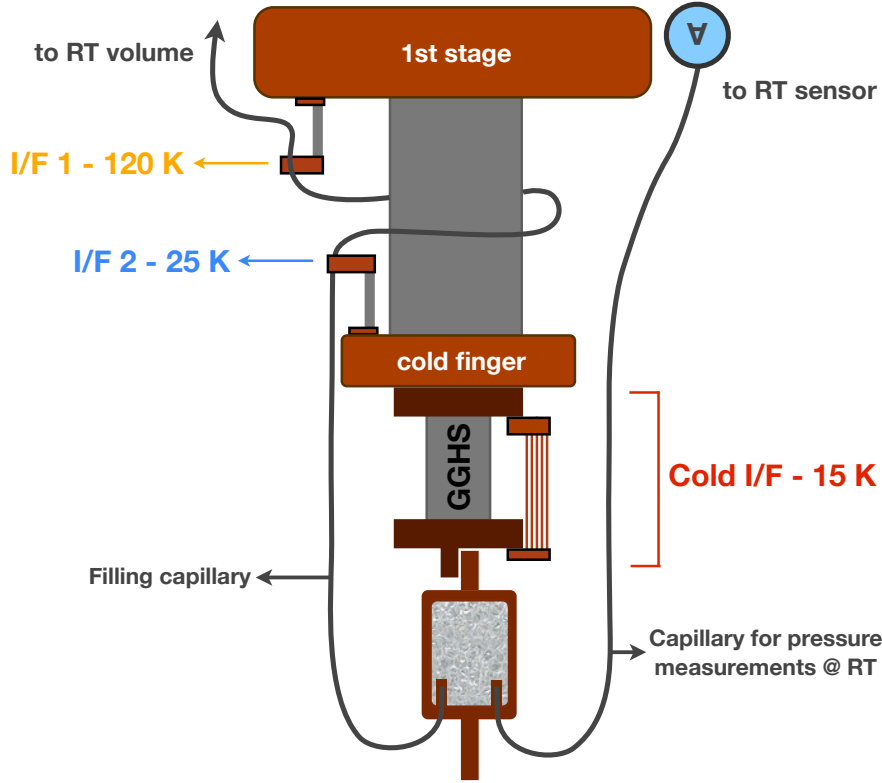


Figure 5.3: Schema of the cold part of the ESU (shown in the anti-gravity configuration): it features two separate capillary tubes, one for pressure measurements and one that connects to the expansion volume; the three intermediate interfaces with the Qmeters can be seen mounted on the 1st stage and cold finger.

solid heat conduction in Section 4.5.1), different sizes of stainless steel capillary tube were chosen:

- For the 300 K to 120 K part (L_1): 2×2.5 mm capillary with $L = 700$ mm;
- For the 120 K to 25 K part (L_2): 1.5×2 mm capillary with $L = 1100$ mm;
- For the 25 K to 15 K part (L_3): 1.5×2 mm capillary with $L = 250$ mm.

This solution allows us to reduce the pressure drop where it is most critical (*i.e.* at near room-temperature) by using a capillary tube with a larger inner diameter; the parts of the tube that suffer negligible pressure drop can be made with the 1.5×2 mm capillary as it is a better choice from a thermal standpoint (smaller heat load per unit length of capillary).

5.1.3 Intermediate interface heat exchangers

The development model was assembled for testing in a two-stage 1 W at 4 K Gifford-McMahon cryocooler manufactured by Sumitomo Heavy Industries; its first stage sits at around 30 K when the cold finger is controlled at 15 K. Since there are no 25 K or 120 K

interfaces available to mimic ESA requirements for their I/Fs, they need to be artificially created from the first and second stages of the cryocooler: a “heat leak” must be created for each interface. These heat leaks must be designed so that the temperature at which the filling capillary is thermally coupled is the temperature of the interfaces specified by ESA, and that the heat load allowed through the heat leaks does not exceed the given limit for that temperature. Figure 5.4 illustrates these heat leaks or “Qmeters” (QM), and Table 5.2 summarises the requirements for each interface.

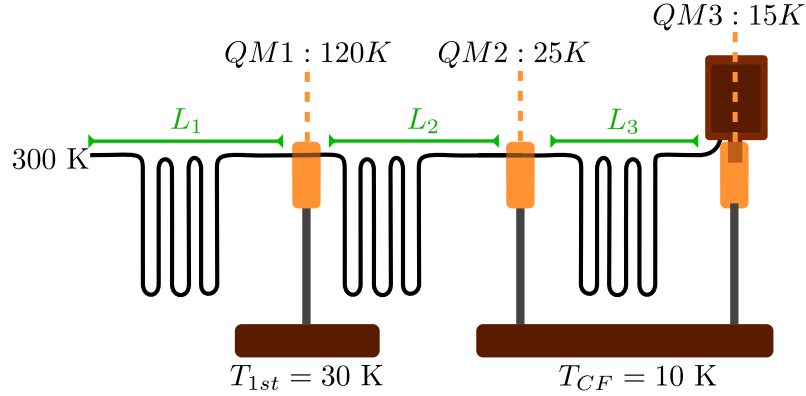


Figure 5.4: Overall schematic of the Development Model assembly.

Table 5.2: Parameters for calculation of the heat leaks at the three interfaces.

	I/F 1	I/F 2	Cold I/F
Requirement @ T_h	40 mW	15 mW	15 mW
Base temperature T_c	30 K	10 K	10 K
Qmeter temperature T_h	120 K	25 K	15 K
Conductance @ T_h	0.44 mW K^{-1}	1 mW K^{-1}	3 mW K^{-1}

For each Qmeter a different solution was adopted that could not only meet the requirements but that would also provide some structural support to the filling capillary. Among these solutions a gas-gap heat switch [63] was used, providing a rigid mechanical interface between the cryocooler cold finger and the cold cell. During the early stages of testing, its high thermal conductance state (ON state) allowed for a fast condensation period between experiments; later it was used only in its low thermal conductance state (OFF state) at all times, where heat transfer was mainly carried out by Qmeter 3. When sizing Qmeter 3, that runs from the cold finger to the cell, the heat switch was considered part of it and as such its (OFF state) conductance was considered. Table 5.3 describes the solutions adopted for each Qmeter/interface pair in order to respect the requirements stated in Table 5.2.

The Qmeters were built with the characteristics displayed in Table 5.3: this constitutes the heat leak itself. A copper mounting surface was soldered to each end of the heat leak so that one end could be mounted onto the cryocooler flange and the other could be

Table 5.3: Solutions adopted for the heat leaks or Qmeters at each interface.

	Material	i.d. (mm)	o.d. (mm)	L (mm)	Calculated \dot{Q} (mW)
Qmeter 1	SS 316 tube	2	3	65.8	39.9
Qmeter 2	SS 316 tube	1	1.5	30	14.9
	Cu RRR 100 wire	0	0.2	41	
Qmeter 3	5 × Cu RRR 100 wire	0	0.2	53	15.0
	SS 316 shell (GGHS)	13.8	14	38	

soldered to the filling capillary. This copper-capillary soldered contact needs to be done along a length of 10 mm in order for it to be in accordance with the calculations made in Section 4.6 for heat transfer while pre-cooling the gas. Figure 5.5 shows the actual Qmeters after being made and before integration in the cryocooler.

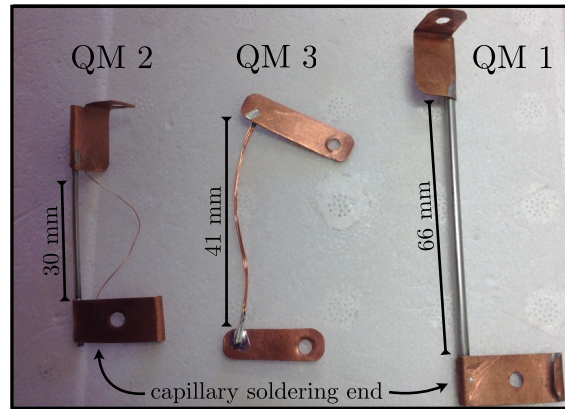


Figure 5.5: Qmeters as built for the Development Model.

The Qmeters were mounted into the appropriate stages of the cryocooler, and thermally coupled to the filling capillary (Qmeters 1 and 2) and to the cold cell (Qmeter 3). Measurements were carried out in order to calibrate the Qmeters, so that they could be used for precise heat load measurements. Figure 5.6 shows the result of the calibration for each interface.

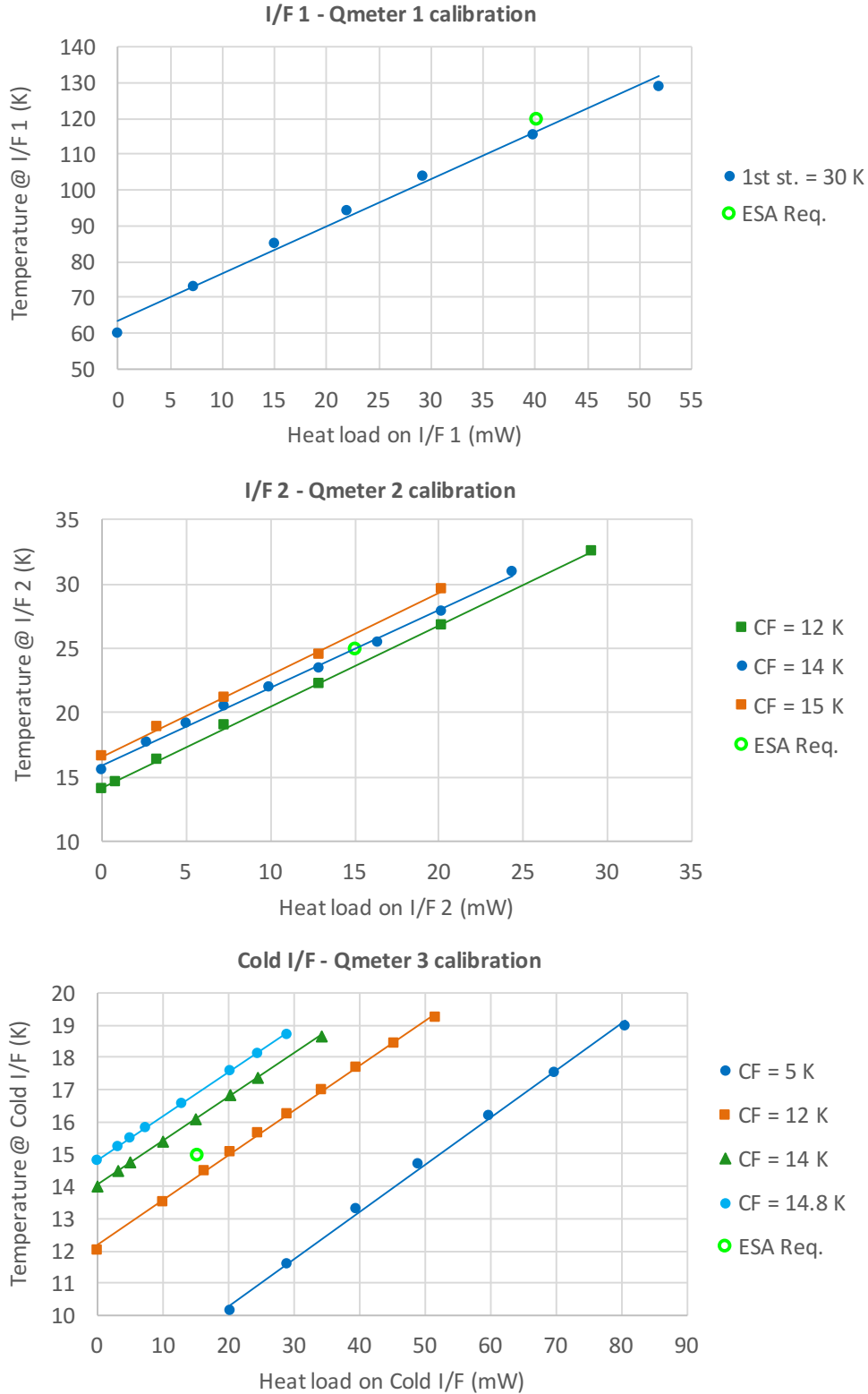


Figure 5.6: Temperature measured at the interface as a function of the applied heat load for I/F 1, I/F 2 and Cold I/F. In the case of I/F 2 and Cold I/F, different cold finger temperatures were tested.

5.1.4 Metal hydride canister design

From the dimensioning phase described in the last chapter, it was determined that the vessel (or canister) that houses the metal hydrides needs to have a capacity for $\approx 99 \text{ cm}^3$ of $\text{LaNi}_{4.8}\text{Sn}_{0.2}$ powder, and needs to have a SS mass of at least 2.5 kg; it was also determined that, due to the heat released by the hydride during absorption, heat transfer inside the canister should be improved, since the powder itself has a poor thermal conductivity: this can be achieved by using a metallic open-pore foam matrix that can house the powder and increase heat transfer from the powder to the canister walls. Since the powdered $\text{LaNi}_{4.8}\text{Sn}_{0.2}$ is fine and should not migrate from the canister to the other parts of the system (like the filling capillary), the design should also incorporate a filter at the exit of the canister to prevent this from happening. A list of specifications for the canister design is shown in Table 5.4.

Table 5.4: Specifications to be considered for the design of the room temperature metal hydride canister.

Specification	Comment
Mass equal or higher than 2.5 kg	See Section 4.9; this mass allows for heat absorption using the heat capacity of the canister material.
Material should be stainless steel 316	See Section 4.9: considerable heat capacity in the room temperature range and is non-reactive with the metal hydride since it does not form oxidized layers.
Internal volume $> 99 \text{ cm}^3$	See Section 4.8.2: minimum inner volume for housing the $\text{LaNi}_{4.8}\text{Sn}_{0.2}$ powder considering a packing factor of 43%.
Must have a flat surface	Needs a flat mount so it can be attached to a radiator, which is the predicted cooling source if adapted for satellite conditions.
Micro-porous filter at exit	Needed to prevent migration of the $\text{LaNi}_{4.8}\text{Sn}_{0.2}$ powder to other parts of the system.
Improve heat transfer across $\text{LaNi}_{4.8}\text{Sn}_{0.2}$	Thermal conductivity of metal hydride is poor and large amounts of heat are released upon absorption; measures should be taken to increase heat transfer e.g insert the powder into a metallic high conductivity matrix.

The solution chosen to address the heat transfer issue inside the canister was largely inspired by the work of R. C. Bowman Jr. in the hydrogen compressors for the Planck satellite [64]: an aluminium foam matrix was used to improve the heat transfer in the

$\text{LaNi}_{4.8}\text{Sn}_{0.2}$ powder. The metal hydride powder fills the pores in the foam matrix, which is in turn in contact with the canister walls: this should improve overall heat transfer. This aluminium foam was supplied by Goodfellow® and its properties are summarised in Table 5.5.

Table 5.5: Properties of the 8% nominal density Duocel® aluminium foam matrix used inside the metal hydride canister.

Aluminium foam	
Reference	AL003860710
Grade	Aluminium 6101
Bulk Density	0.2 g cm^{-3}
Porosity	93%
Pores/cm	16
Purity	98.5%
Thermal conductivity	$5.8 \text{ W m}^{-1} \text{ K}^{-1}$

The foam was cut into the desired shape by Electrical Discharge Machining (EDM). It was machined in such a way that it has an extremely tight fit against the canister walls to increase thermal contact between the two; five cylinders or “wafers” were produced in total. Figure 5.7 shows the resulting aluminium wafers.

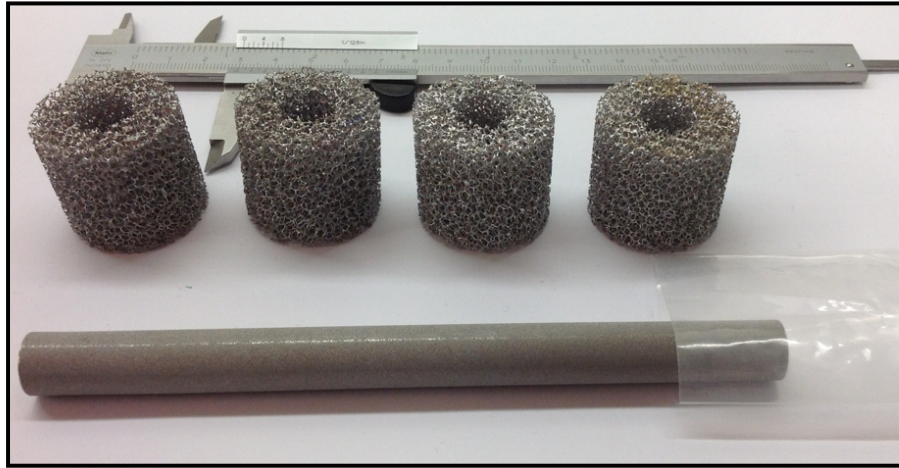


Figure 5.7: Aluminium foam wafers produced by electro-discharge machining and porous filter.

As already mentioned, in order to prevent $\text{LaNi}_{4.8}\text{Sn}_{0.2}$ particles from migrating to the filling capillary, a filter needs to be placed between the inside of the canister and its exit that allows hydrogen gas to flow freely but that prevents the passage of particles larger than $\approx 10 \mu\text{m}$. A Media Grade 5 porous filter manufactured by Mott Corporation® was selected; according to the manufacturer, a Media Grade 5 filter retains 99.9% of particles with a diameter larger than $5 \mu\text{m}$, which seems enough to prevent the $\text{LaNi}_{4.8}\text{Sn}_{0.2}$ powder from migrating; it is made out of sintered SS 316 particles so it is not reactive with either

hydrogen or the metal hydride. Since the pores are extremely small, this might induce an undesirable pressure drop between the metal hydride bed and the rest of the system: this pressure drop was computed using data from Mott Corporation® for a filter tube with length $L = 15.2$ cm, inner diameter $\varnothing = 95$ mm and wall thickness 1.6 mm:

$$\Delta P_{gas} = K_{gas} \times Flux \times Viscosity \times thickness \quad (5.1)$$

where $K_{gas} = 11$ for Media Grade 5; this gives a 3.6 mbar pressure drop along the filter tube walls when the hydrogen flow is maximum, which is reasonable on a 2 min time-scale for practical purposes and was accepted. Because the filter is a tube (with a cap at one end), the hydrogen will enter the canister from this tube placed in the centre of the canister, allowing for a more even distribution of the flow through the metal hydride bed.

The overall shape of the canister that resulted from these requirements is given in Figure 5.8. It features a flat mount for the radiator or other heat exchanger, flat surfaces for mounting heaters and inserts for Pt100-type thermometers. Its inside is cylindrical in shape, and has a total free volume of 128 cm^3 , enough to house the metal hydride powder, the aluminium foam matrix and the porous filter. A cut view of the canister is presented in Figure 5.9, where the filter and the aluminium foam wafers can be seen. Both lids are threaded to provide a temporary seal so the canister can be moved from the filling chamber to the welding chamber without being directly exposed to air, avoiding contamination of the metal hydride.

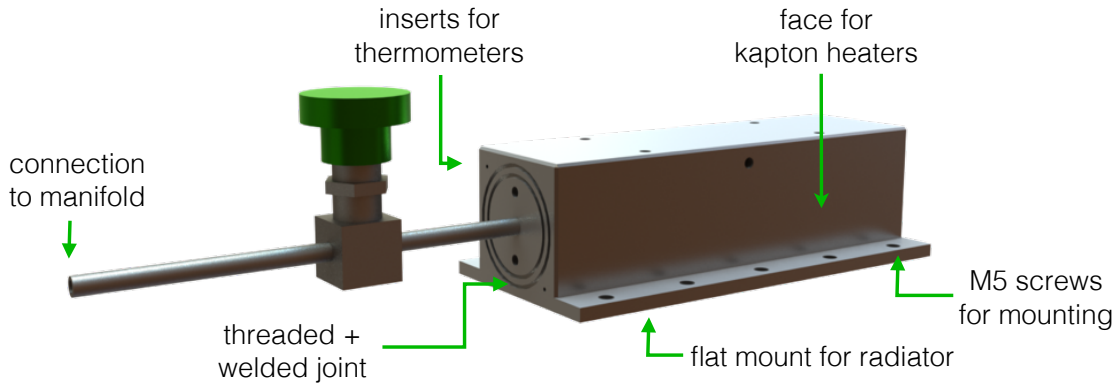


Figure 5.8: Development Model metal hydride canister as designed. Some of the external features can be seen such as the flat mounts for the radiator and heater placement, as well as inserts for the thermometers.

To prevent the metal hydride powder from shifting to either side of the canister during transport or vibrational testing, two stainless steel mesh discs ($\approx 70 \mu\text{m}$ opening) were inserted between each wafer.

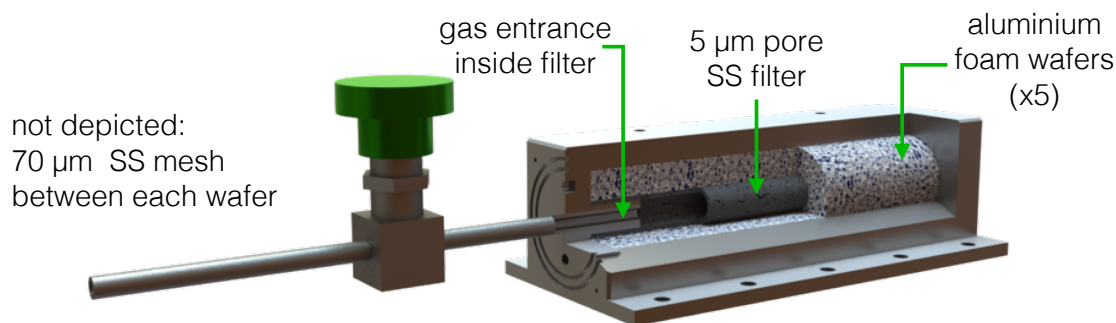


Figure 5.9: Section cut of the canister. The porous filter is mounted at the entrance of the canister and allows for hydrogen to evenly reach the metal hydrides that are embedded in the aluminium foam matrix.

5.1.5 Metal hydride production

The $\text{LaNi}_{4.8}\text{Sn}_{0.2}$ ingots were synthesised by P. de Rango and her collaborators at [CNRS](#) in Grenoble, France. They are produced by arc-melting of high-purity lanthanum, nickel and tin together for 24 h, which forms an ingot of the metallic alloy. The ingots are then annealed for a further 24 h at 950 °C for homogenisation of the alloy. Figure 5.10 shows one of the ingots after the annealing process.

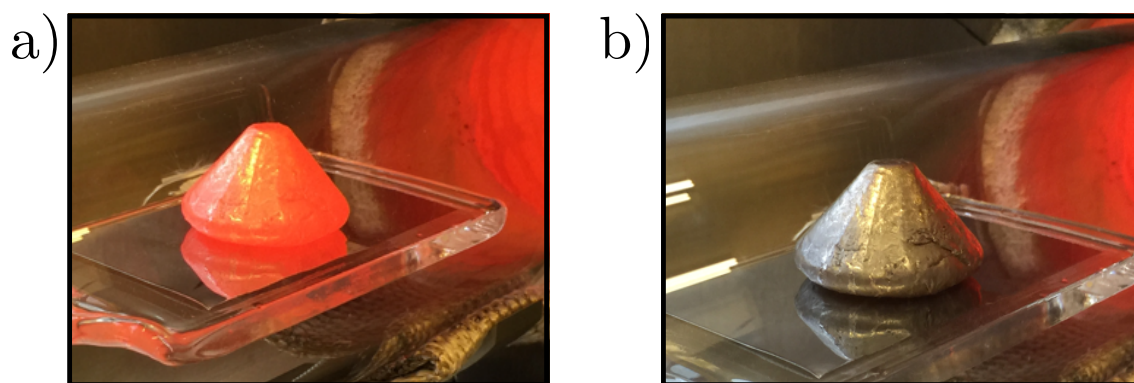


Figure 5.10: $\text{LaNi}_{4.8}\text{Sn}_{0.2}$ ingot after annealing: a) ingot right after exiting the oven, still incandescent; b) ingot after natural cooling down to room temperature.

At this point the ingots have not been activated and as such are not reactive and can be handled while exposed to air. A total of 5 ingots were produced in the same way, and 4 were selected for use in the Development Model. The selected ingots were then crushed by hand into coarse 10 mm chunks, and loaded into a high-pressure stainless steel vessel for activation onwards.

The activation (hydriding) process consists of allowing the $\text{LaNi}_{4.8}\text{Sn}_{0.2}$ chunks to come into contact with pure hydrogen gas at room temperature at a pressure several atmospheres higher than the equilibrium plateau pressure: this forces hydrogen into the

alloy and causes it to start the absorption process. After a first activation the alloy is subjected to repetitive absorption/desorption (hydriding/dehydriding) cycles, producing a very fine powder ($\approx 10\mu\text{m}$) that is highly reactive. This powder has a typical surface area ranging from $0.2\text{ m}^2/\text{g}$ to $0.5\text{ m}^2/\text{g}$ [43] and is highly pyrophoric: it can ignite spontaneously in air at or below 55°C ; this, combined with the fact that moisture and oxygen can deactivate the material by contamination, means that the metal hydride can no longer be exposed to air and should be handled exclusively in an inert (argon) atmosphere from the point of activation.

Activation was performed at room temperature and the pressure vessel that contained the alloy was filled with a pressure of 25 bar of high-purity hydrogen. As soon as the $\text{LaNi}_{4.8}\text{Sn}_{0.2}$ came into contact with hydrogen it began to heat up significantly, which was noticeable by touching the exterior of the pressure vessel; this is a sign that the absorption process started to take place and that the heat of absorption was being released. This process was allowed to continue overnight, so that the alloy could cool down and be fully activated. Then the material was cycled a few times at lower pressures (0.1 bar to 0.3 bar) in order to become fully reactive. The pressure vessel was then transported into a glove-box with a controlled atmosphere (overpressure of argon gas, $< 0.5\text{ ppm H}_2\text{O}$ and O_2) where it was opened. Figure 5.11 shows the $\text{LaNi}_{4.8}\text{Sn}_{0.2}$ before and after the activation process.

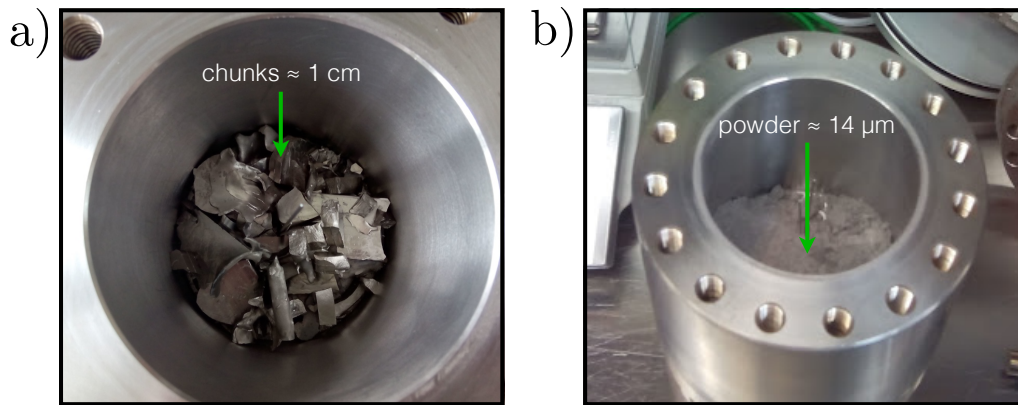


Figure 5.11: $\text{LaNi}_{4.8}\text{Sn}_{0.2}$ activation process: a) before activation, where the ingot was broken into 10 mm chunks and is still exposed to air; b) after activation, where the resulting powder can be seen; at this stage the pressure vessel was opened and kept in a controlled atmosphere glove-box.

5.1.6 Filling the canister

After the canister was built (final drawing for the Development Model in [Appendix C](#)), it was taken to [CNRS](#) in Grenoble (France) for filling and welding. The first parts (valve and first lid) were welded together using a [TIG](#) welding technique at Institut Néel.

The metal hydride had already been synthesised and activated at this point, and

the whole filling process was performed inside a glove-box with a controlled argon atmosphere; Figure 5.12 shows the canister inside the glove-box ready for filling. After inserting the porous filter, the aluminium wafers were added and filled with $\text{LaNi}_{4.8}\text{Sn}_{0.2}$ one at a time, with two discs of SS mesh in between each wafer after filling.

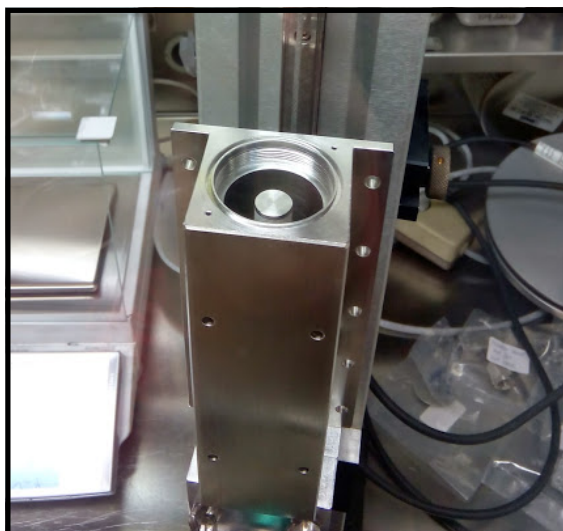


Figure 5.12: Canister inside the glove-box ready for the filling process. The filter is visible in the centre of the inner cylinder.

This was a very time-consuming process, as the metal hydride powder is not smooth: its consistency resembles flour, which made it extremely difficult to insert the powder into the aluminium foam. In the end, the resulting powder was less dense than expected (3.094 g cm^{-3} against 3.526 g cm^{-3}), allowing for a packing factor of only 37.8% (compared to the expected 43%); this led to a smaller amount of $\text{LaNi}_{4.8}\text{Sn}_{0.2}$ being inserted into the canister. Density measurements were performed with a sample of the powder; the effective amount of $\text{LaNi}_{4.8}\text{Sn}_{0.2}$ inside the Development Model canister is given in Table 5.6.

Table 5.6: Effective amount of $\text{LaNi}_{4.8}\text{Sn}_{0.2}$ inside the DM canister.

Development Model canister	
Density of $\text{LaNi}_{4.8}\text{Sn}_{0.2}$ powder	3.094 g cm^{-3}
Total mass of $\text{LaNi}_{4.8}\text{Sn}_{0.2}$	320 g
Packing factor	37.8%
Maximum H_2 storage capacity	1.3 wt%
Equivalent normal litres of H_2	46.6 ℓ
Safety factor in H_2 storage	3.6

After the filling process was complete, the final lid was screwed in tight, providing a temporary seal. The canister was put into a sealed bag with argon and readily transported to the welding facilities, where the chamber was filled with pure argon; after the final welding a leak test was performed. After the canister was complete, it was filled with

hydrogen for transport and to confirm its storage capabilities had not been hindered by contamination: it was able to absorb the expected 47 ℓ . It was then shipped back to Portugal, where instrumentation was added: two Pt100 thermometers were inserted into the outside holes of the canister and resistive kapton heaters were glued to each side: the final assembly is depicted in Figure 5.13.

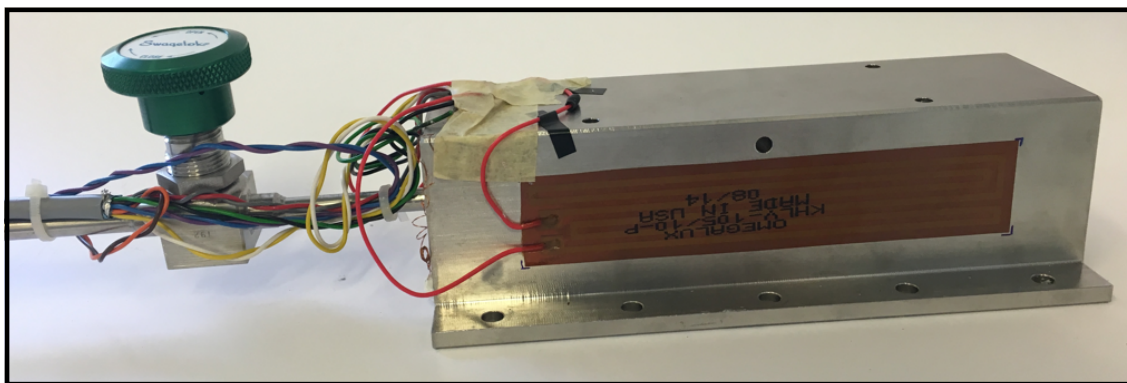


Figure 5.13: Development Model canister ready for use; resistive kapton heaters can be seen on the side walls, as well as the wiring for the Pt100 thermometers.

The experimental set-up used for PCT measurements in Grenoble only allows for small batches of metal hydride to be tested at different temperatures, and for that reason samples of the $\text{LaNi}_{4.8}\text{Sn}_{0.2}$ powder that was used to fill the canister were taken for measurement at temperatures different that ambient temperature, rather than the whole canister. The PCT measurements are presented in Figure 5.14 for three different metal hydride temperatures.

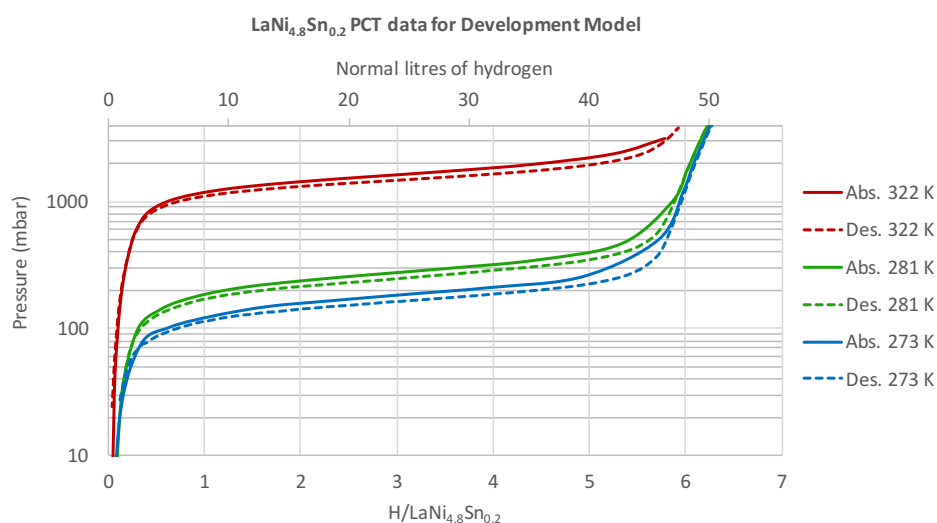


Figure 5.14: Pressure-Composition-Temperature measurements for a sample of $\text{LaNi}_{4.8}\text{Sn}_{0.2}$ powder. The solid curves denote an absorption process whereas the dashed lines represent a desorption process.

The lower x-axis represents the mean number of hydrogen atoms absorbed into one unit of $\text{LaNi}_{4.8}\text{Sn}_{0.2}$, and the fairly flat plateaus of the curves denote the progressive absorption of hydrogen into the β -phase of $\text{LaNi}_{4.8}\text{Sn}_{0.2}\text{H}_6$. The upper x-axis shows the equivalent normal litres of hydrogen that can be stored inside the canister taking into account the mass of $\text{LaNi}_{4.8}\text{Sn}_{0.2}$ that the canister was filled with.

5.1.7 Thermal environment for the metal hydride canister

According to IR 1 ([Appendix A](#)), the room temperature thermal interface has a cooling power of 10 W at 270 K: this interface is intended to be a 20×20 cm radiator looking into outer space in the satellite, and we need to make use of this cooling power to help manage the temperature of the metal hydride canister during the Heat Load Profile. To simulate the radiator thermal conditions in a laboratory environment for ground testing another cooling source was devised: it consists of a constant temperature bath, to which the room temperature canister can be coupled through a heat exchanger. The bath itself consists of a 50%/50% water/ethylene glycol solution, cooled by a Haake® EK12 immersion cooling unit that is able to keep the bath at a fairly constant temperature of $\approx -30^\circ\text{C}$ ¹. The heat exchanger consists of a copper plate to which the canister is coupled to, and of two “legs” that are immersed in the cooling bath. Figure 5.15 shows the canister coupled to the heat exchanger, which is partially immersed in the cooling bath.

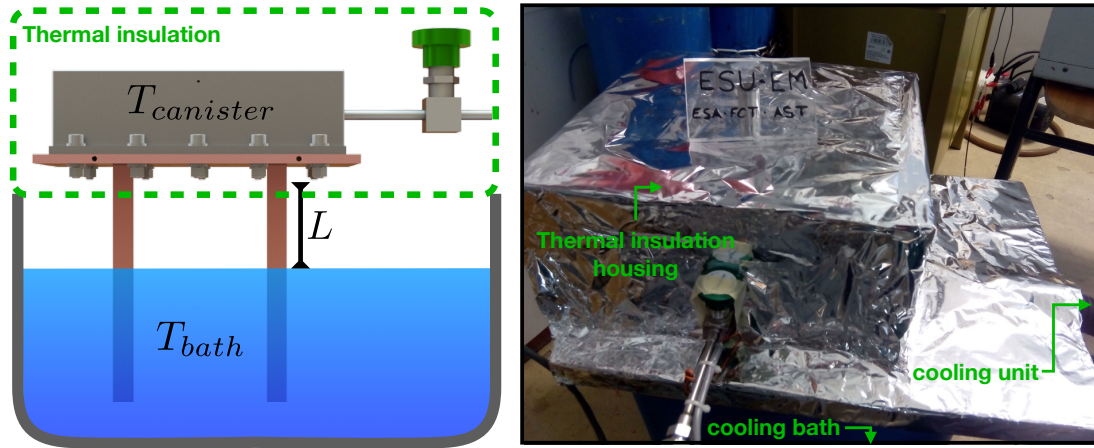


Figure 5.15: Heat exchanger at room temperature for the metal hydride canister immersed in a cooling bath. By controlling the length L the cooling power can be tuned. On the right-hand side, image of the actual system showing the insulation housing and parts of the cooling unit and bath.

The cooling power available for the canister with this set-up can be tuned: by varying the amount of liquid in the cooling bath, one can vary the effective thermal length L of the copper “legs”, and hence the thermal conductance of the heat exchanger. The overall

¹We thank S. Barreiros at the Chemistry Department of [FCT/UNL](#) for lending us this cooling unit.

dimensions of the heat exchanger are presented in Table 5.7 for its normal operating conditions of 10 W at 270 K.

Table 5.7: Dimensions of the room temperature canister heat exchanger.

Canister heat exchanger	
Requirement	10 W @ $T_{\text{canister}} = 270$ K
Material	Copper RRR 50
T_{bath}	$-30^\circ\text{C} = 243$ K
Cross section of each leg	128 mm^2
Number of legs	2
L for 10 W @ 270 K	135 mm

The whole canister + heat exchanger assembly was housed inside a Styrofoam case filled with insulating foam in order to minimize heat exchange with the environment through convection, which would lead to losses in the cooling power effectively delivered to the canister. This set-up was calibrated by applying different heat loads to the canister for a determined cooling bath temperature and registering the resulting temperature on both the canister and the copper heat exchanger: Figure 5.16 shows the results of the calibration process.

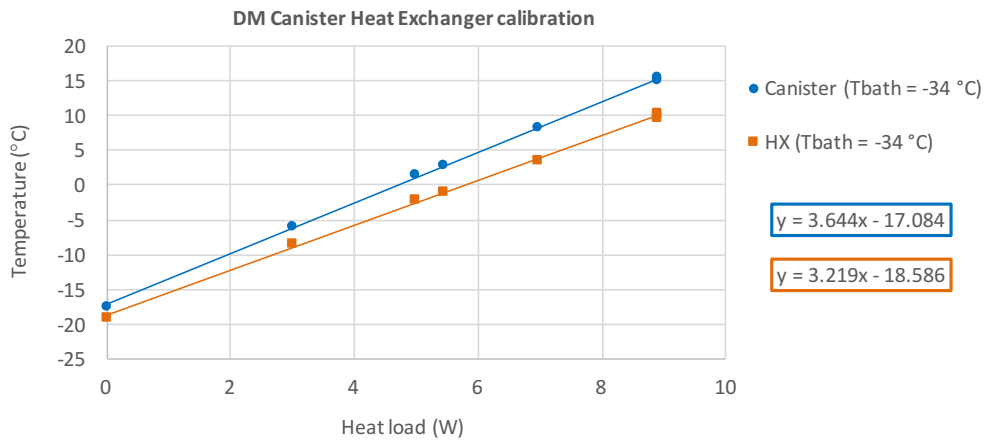


Figure 5.16: Temperatures of the canister and heat exchanger as a function of the applied heat load, for a cooling bath temperature of -34°C .

5.1.8 Cryocooler assembly

The cold part of the [ESU](#) was mounted into a 1 W at 4 K Sumitomo Heavy Industries Gifford-McMahon cryocooler. When the cold finger is kept in the 10 K to 20 K temperature range, the first stage is at ≈ 30 K. As previously described, Qmeter 1, which mimics [I/F 1](#) at 120 K, is coupled to the first stage, whereas [I/F 2](#) (25 K) and Cold [I/F](#) (15 K) are coupled to the cold finger. Figure 5.17 shows the cold part of the Development Model.

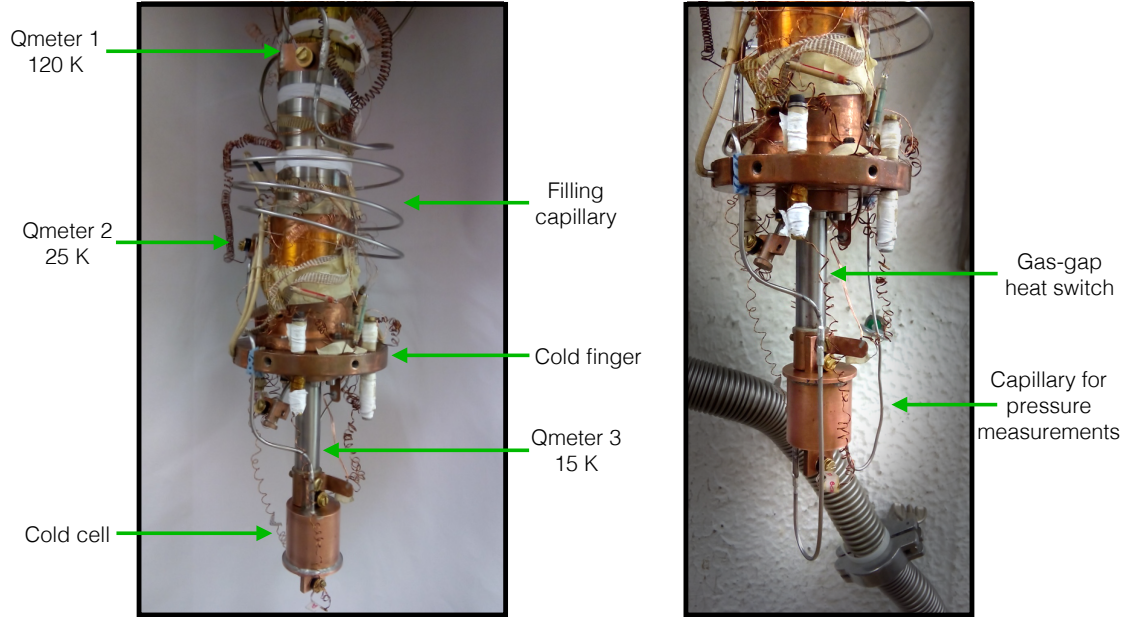


Figure 5.17: Cold part of the Development Model of the [ESU](#). All three interfaces can be seen, as well as the cold cell and both capillary tubes: one that connects to the room-temperature volume and one for pressure measurements inside the cell free of pressure drop.

5.2 Engineering Model

This section describes the steps taken to implement the Engineering Model of the [ESU](#). This is an advanced model, which must not only be able to perform as requested but also be capable of withstanding the qualification tests. These tests are mainly mechanical, including vibrational, thermal shock and thermal cycling tests. This need to withstand severe conditions dictated the design aspects of the Engineering Model, although its core features are heavily based upon the Development Model. The design and construction of the [EM](#) was carried out by Active Space Technologies ([AST](#)), that managed to use design input from the [DM](#) and adapt it to render the [EM](#) mechanically sound. Figure 5.18 illustrates the complete Engineering Model as designed by [AST](#).

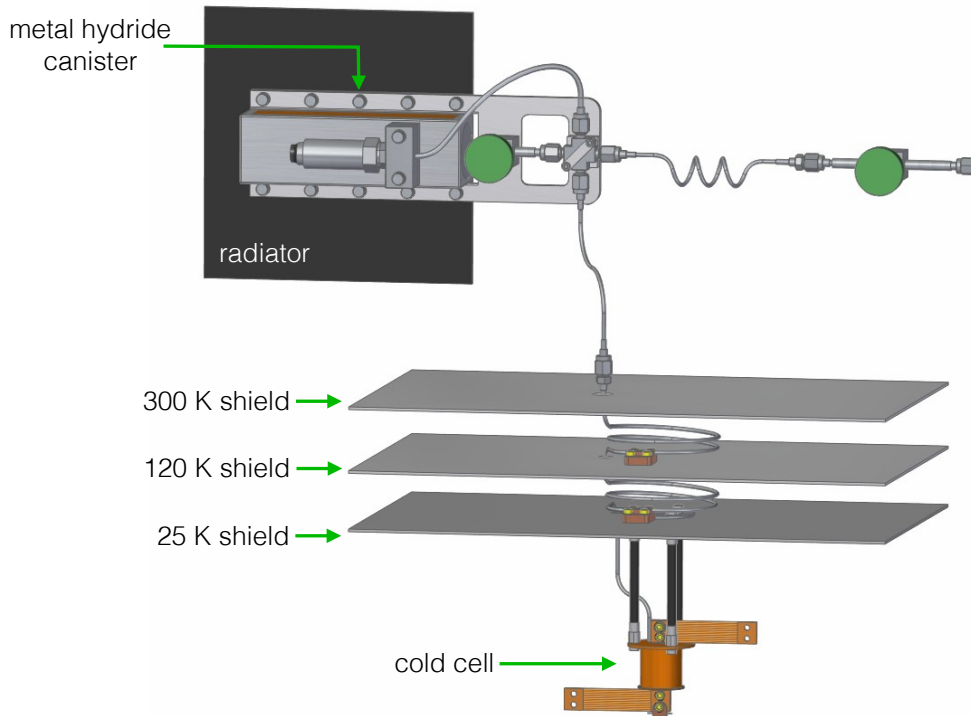


Figure 5.18: Overview of the Engineering Model of the [ESU](#), complete with its mechanical and thermal interfaces. Image courtesy of [AST](#).

It is comprised of the metal hydride canister, intermediate interfaces and cold cell as was the case for the Development Model; the main changes and improvements will be described throughout the next sections.

5.2.1 Cold cell

For the [EM](#), the cold cell maintains its overall shape and inner volume, as well as the mechanical interfaces for thermometry and connection to the thermal interfaces, *i.e.* cooling source and resistive heater. It was made out of [OFHC](#) copper and its cover was brazed to the main body instead of using soft solder. Since the 15 K stage should be considered

merely as a thermal interface, as it cannot support the cold cell mechanically, the main departure from the [DM](#) design is that it now needs to include mechanical interfaces to support it from the 25 K stage: Figure 5.19 shows the final design adopted for the cold cell.

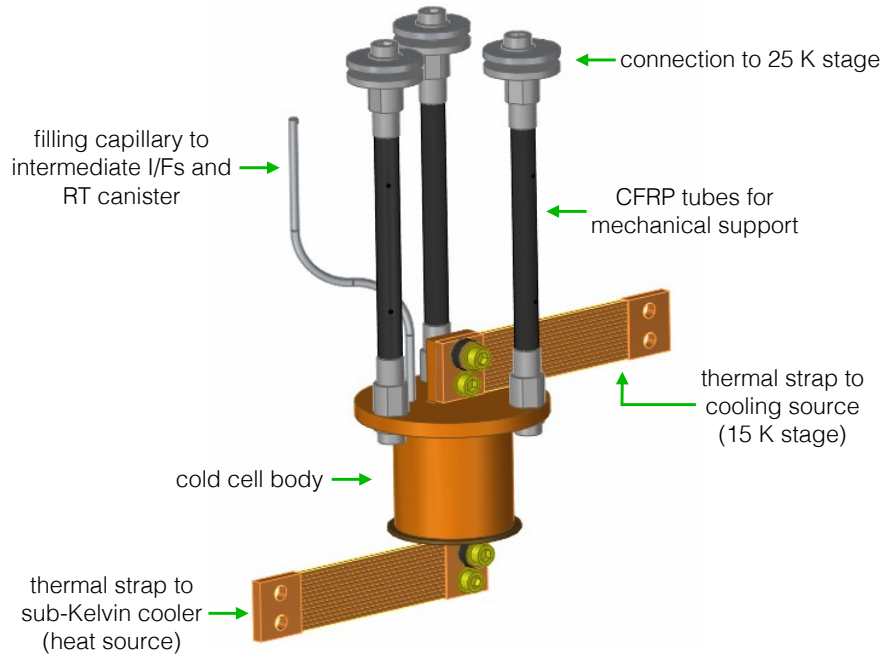


Figure 5.19: Cold cell of Engineering Model. The copper straps connect to the thermal interfaces and the carbon tubes provide mechanical support from the 25 K stage. Image courtesy of [AST](#).

This connection should ideally have the lowest possible effect on the thermal balance of the cell while being sturdy enough to support the cell during vibration tests that mimic launch conditions. The [EM](#) cold cell features three carbon fibre reinforced plastic ([CFRP](#)) tubes that provide mechanical support to the cell, while limiting heat transfer from the 25 K stage. Assuming the thermal conductivity of the [CFRP](#) tubes to be that of M40A II ([Appendix B](#)), the heat load along the tubes that reaches the 15 K stage can be calculated and is presented in Table 5.8.

The total expected heat load that flows to the cold cell from the [CFRP](#) tubes is less than 1 mW, which is reasonable taking into account the 15 mW cooling power available at the 15 K interface. The [CFRP](#) tubes are bonded with epoxy to titanium fittings that connect both to the cold cell and the 25 K stage.

Figure 5.19 also depicts two thermal straps that would connect to the cooling source and to the sub-Kelvin cooler. For ground testing these thermal straps are not a part of the [ESU](#) and, and for the [EM](#), a resistive heater is directly coupled to the cold cell and the connection to the cooling source is going to be described over the next sections.

Table 5.8: Heat load along the CFRP tubes from 25 K to 15 K.

CFRP tubes between 15 K and 25 K	
Material	M40A II
Length of each tube	74 mm
Inner diameter of tube	5 mm
Outer diameter of tube	6.3 mm
Thermal conductivity at 20 K	$0.2 \text{ W m}^{-1} \text{ K}^{-1}$
Heat load for each tube	0.3 mW
Total heat load along tubes	0.9 mW

5.2.2 Filling capillary and Heat exchangers

Contrary to what was decided for the DM, the filling capillary of the Engineering Model consists entirely of $2 \times 2.5 \text{ mm}$ SS 316 tubing: this avoids additional welded joints that would be needed if the capillary was not the same throughout the whole length. The pressure drop can be considered negligible with this capillary size and the heat load through solid conduction is still manageable. Figure 5.20 shows the capillary tube, from the 300 K fitting down to the cold cell, and the copper heat exchangers for I/Fs 1 and 2.

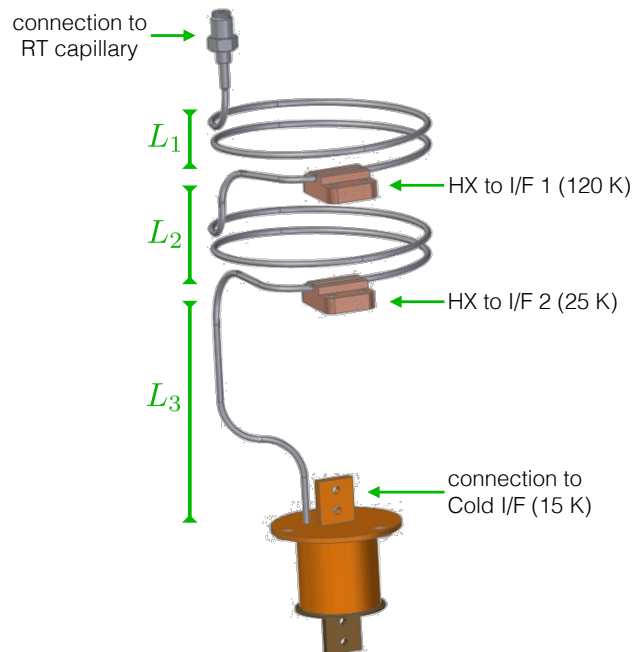


Figure 5.20: Cold cell, filling capillary and intermediate interfaces coupled to the capillary tube. The length of each section of tube is identified. Image courtesy of AST.

The length of each section of capillary tube and the corresponding heat load through solid conduction is summarised in Table 5.9. Although the heat load is exceeded for the section that runs from 300 K to 120 K (5.8 mW against 5 mW, see Section 4.5.1) from what is shown in the table, these calculations don't take into account the additional 100 mm of

tube that are part of the cryocooler assembly, and that ensure that the load from 300 K to 120 K stays below the 5 mW limit.

Table 5.9: Heat load across the filling capillary.

Capillary section	Length (mm)	$\dot{Q}_{\text{conduction}}$ (mW)
L_1	700 mm	5.8 mW between 300 K and 120 K
L_2	600 mm	2.0 mW between 120 K and 25 K
L_3	150 mm	0.3 mW between 25 K and 15 K

As for the Qmeters, special heat exchangers (also shown in Figure 5.20) were designed for intermediate interfaces I/F 1 and I/F 2: they consist of a copper block that has been brazed to the capillary tube and that could be coupled to the radiation shields that make up the 25 K and 120 K stages in the actual cryogenic chain set-up. Each of these copper blocks has been brazed along a minimum length of 10 mm to ensure that the gas is properly pre-cooled as calculated in the previous chapter.

As described in Section 5.1.3, there was the need to create Qmeters to mimic the 25 K and 120 K interfaces. The thermal environment in the cryocooler where the EM is to be assembled is somewhat different than what was the case for the DM: a 2 W at 20 K CTI Cryogenics Model 22 cryocooler was used. The first stage sits at ≈ 50 K when the cold finger is between 10 K and 20 K, so the Qmeters were sized accordingly: Table 5.10 shows the characteristics of the Qmeters for the EM. The conductance of the Cold I/F was designed to be 6 mW K^{-1} in order to limit the condensation rate (and thus the gas flow) so that the 15 mW heat load at I/F 2 would not be exceeded.

Table 5.10: Parameters for calculation of the heat leaks at the three interfaces.

	I/F 1	I/F 2	Cold I/F
Requirement @ T_h	40 mW	15 mW	6 mW
Base temperature T_c	50 K	14 K	14 K
Qmeter temperature T_h	120 K	25 K	15 K
Conductance @ T_h	0.57 mW K^{-1}	1.36 mW K^{-1}	6 mW K^{-1}

Based on the information given in Table 5.10, the dimensions of each Qmeter were calculated and built: the solution adopted for each thermal link is described in Table 5.11 and shown in Figure 5.21.

Table 5.11: Dimensions of the Qmeter links in the Engineering Model: in every case, the material used was Cu RRR 100.

	# of wires	\varnothing (μm)	L (mm)	Total \dot{Q} (mW)
Qmeter 1	2	200	62	40.0
Qmeter 2	1	200	54	15.0
Qmeter 3	10	200	100	5.9

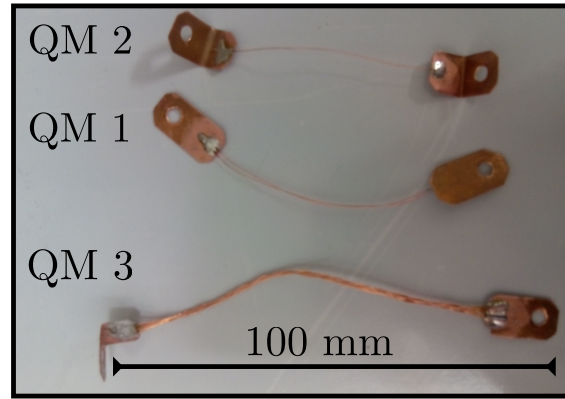


Figure 5.21: Qmeters as built for the Engineering Model.

The Qmeters were assembled in the cryocooler with the Engineering Model, and calibrated prior to operation for different temperatures. The result of this process is shown in Figure 5.22 for each interface. In the case of Qmeter 2 and Qmeter 3, the results of the calibration were fitted into a single linear equation $f(T_{CF}, T_{I/F})$ that allowed for the determination of the heat load at the interface as a function of both the cold finger temperature and the temperature of the corresponding interface.

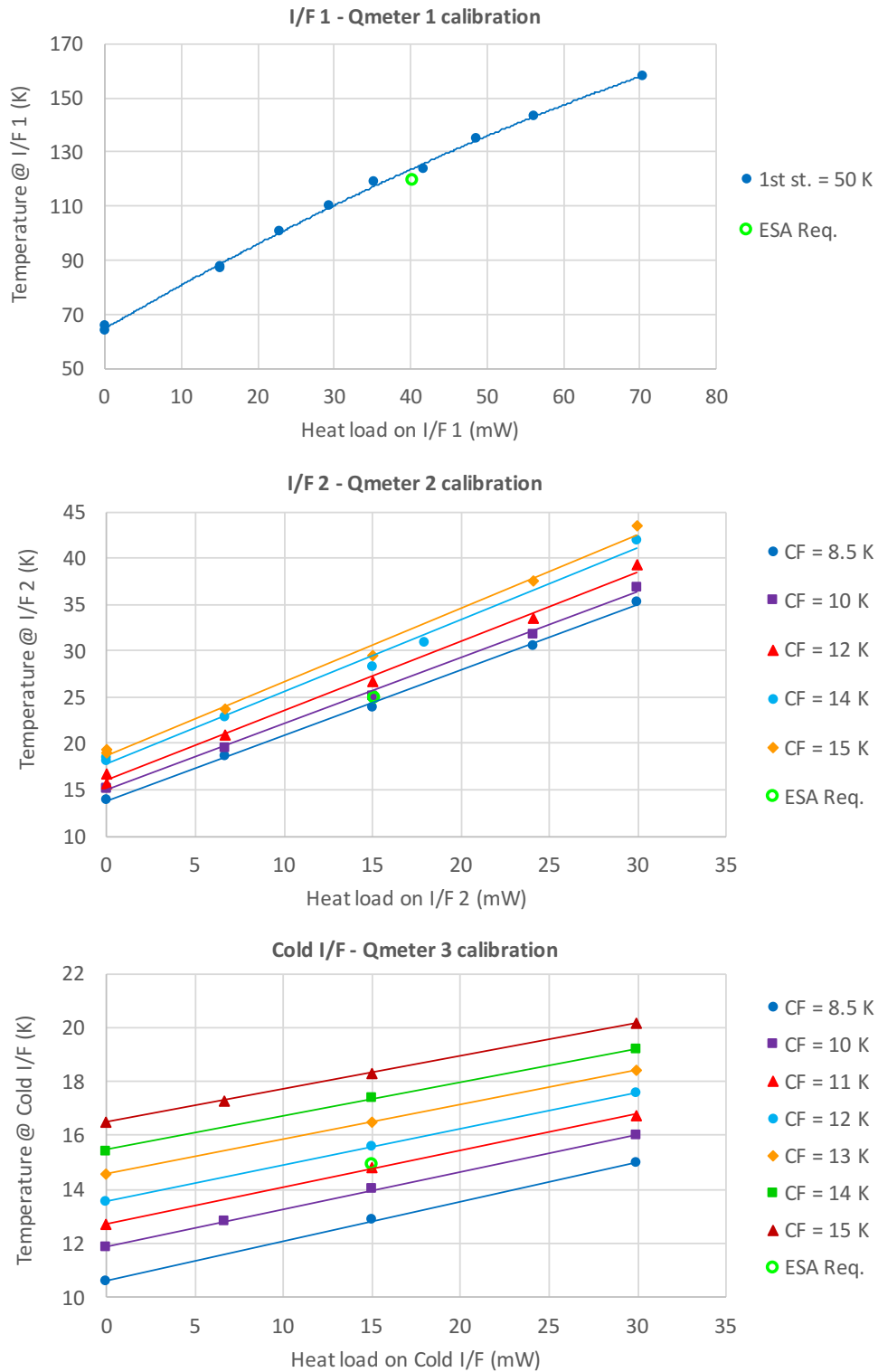


Figure 5.22: Temperature measured at each interface as a function of the applied heat load for I/F 1, I/F 2 and Cold I/F.

5.2.3 Metal hydride canister

The metal hydride canister for the Engineering Model is also largely based on the design of the one used in the Development Model; the design changes were mostly to improve its ability to withstand the mechanical tests for qualification in vibration tests. The inside of the canister is built in the same way as the DM, as can be seen in Figure 5.23.

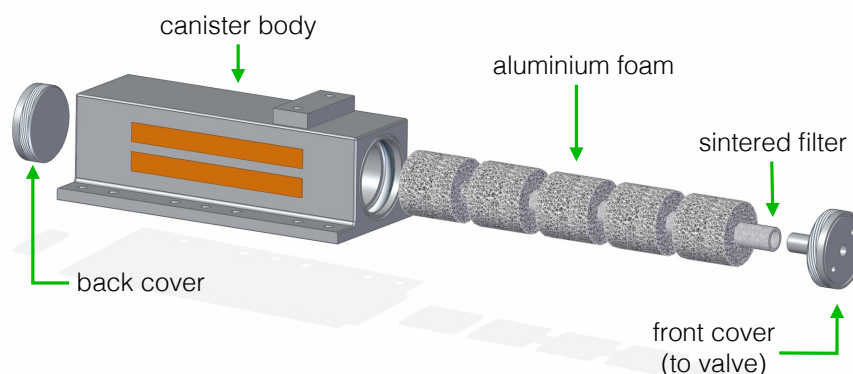


Figure 5.23: Exploded view of the metal hydride canister for the Engineering Model. Image courtesy of AST.

The same type of aluminium foam was used, as well as a $5\text{ }\mu\text{m}$ stainless steel porous filter; both covers are threaded to ensure leak tightness between the canister filling process and the final welding of the covers. The outside part of the canister (Figure 5.24) is where the most changes can be observed: it now features an anodised aluminium “flap” that provides structural support to the exhaust tube and valve that connects the canister to the manifold, which is essential if the canister is expected to survive the vibrational tests. This dedicated manifold features a pressure sensor that can function without the need to connect the canister to additional wall-mounted manifolds, and has a short copper section for filling the system with hydrogen gas that can be pinched-off prior to launch.

The $\text{LaNi}_{4.8}\text{Sn}_{0.2}$ ingots for the EM were again synthesised at CNRS following a slightly modified procedure than the one described in Section 5.1.5 in order to improve the homogeneity of the produced material. The canister was filled under the same controlled conditions, although the packing factor of the produced powder was slightly different: the EM canister has slightly less $\text{LaNi}_{4.8}\text{Sn}_{0.2}$ powder than what was predicted (cf. Table 5.12) due to the difficulties in filling the canister with this less compact powder. Nevertheless, the amount of $\text{LaNi}_{4.8}\text{Sn}_{0.2}$ inside the EM canister still provides a 3.6 safety factor in hydrogen storage capabilities.

The PCT analysis was performed in Grenoble in the same way as was carried out for the Development Model, and the results are presented in Figure 5.25.

One of the main improvements from the metal hydride synthesised for the Development Model is that the absorption plateaus are flatter, meaning that the pressure remains

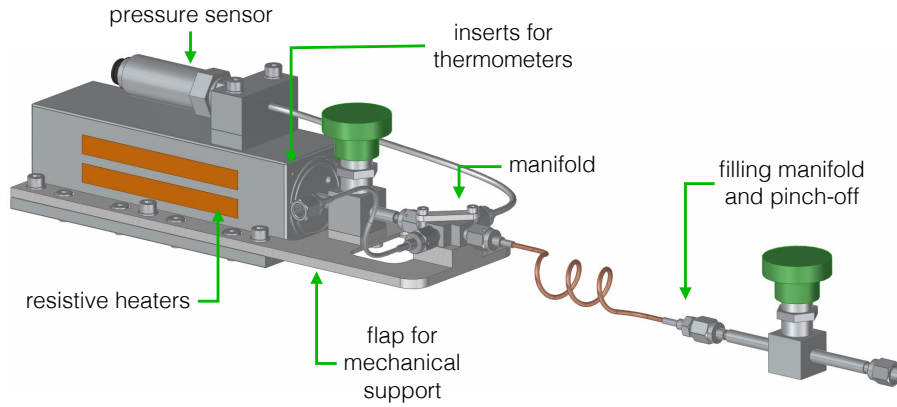


Figure 5.24: View of the exterior of the EM canister; the flap for structural support and a manifold that includes a pressure sensor are the main additions when compared to the DM. Image courtesy of AST.

Table 5.12: Effective amount of $\text{LaNi}_{4.8}\text{Sn}_{0.2}$ inside the EM canister.

Engineering Model canister	
Density of $\text{LaNi}_{4.8}\text{Sn}_{0.2}$ powder	3.094 g cm^{-3}
Total mass of $\text{LaNi}_{4.8}\text{Sn}_{0.2}$	316 g
Packing factor	37%
Maximum H_2 storage capacity	1.3 wt%
Equivalent normal litres of H_2	46 ℓ
Safety factor in H_2 storage	3.56

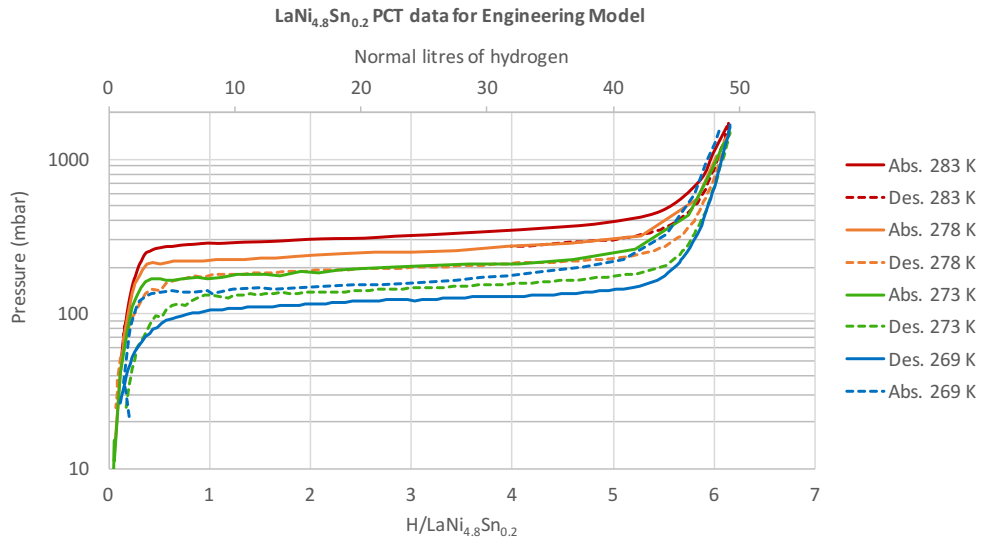


Figure 5.25: Pressure-Composition-Temperature measurements for a sample of $\text{LaNi}_{4.8}\text{Sn}_{0.2}$ powder as synthesised for the EM. The solid curves denote an absorption process whereas the dashed lines represent a desorption process.

more stable throughout the plateau. A stable pressure provides a more stable temperature in the cold cell, which is advantageous during the heat absorption phase.

The finished canister is shown in Figure 5.26: the parts were manufactured by AST, with the exception of welding processes that were carried out at Institut Néel. The pressure sensor is directly mounted on top of the canister as well as the manifold with the supporting flap and the kapton heaters. The white wires coming from the canister are from thermometers nested on the top and bottom faces of the canister.

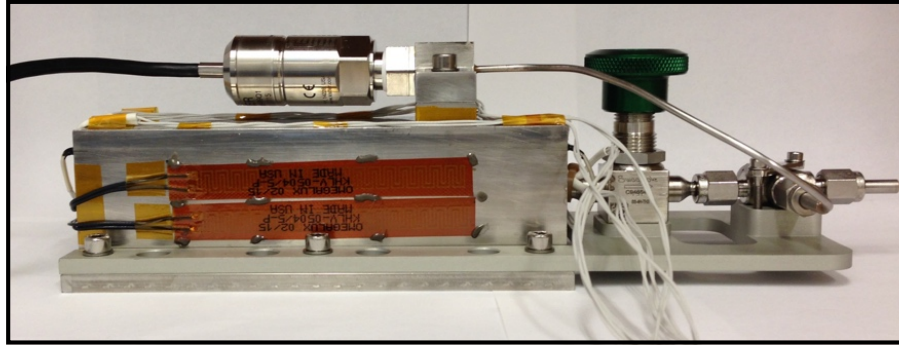


Figure 5.26: Engineering Model canister ready for use, where kapton heaters are placed on the side walls and a pressure sensor can be seen mounted on top of the canister. The aluminium flap provides support for the manifold.

The thermal environment used for the canister to simulate the radiator is the same ethylene glycol bath + copper heat exchanger as the one described in Section 5.1.7 and that was used for the Development Model. It was, however, calibrated again, as ambient conditions changed from the testing of the Development Model and the Engineering Model, and the temperatures reached in the cooling bath did not remain the same. Some adjustments were made and the results of the calibration process are shown in Figure 5.27.

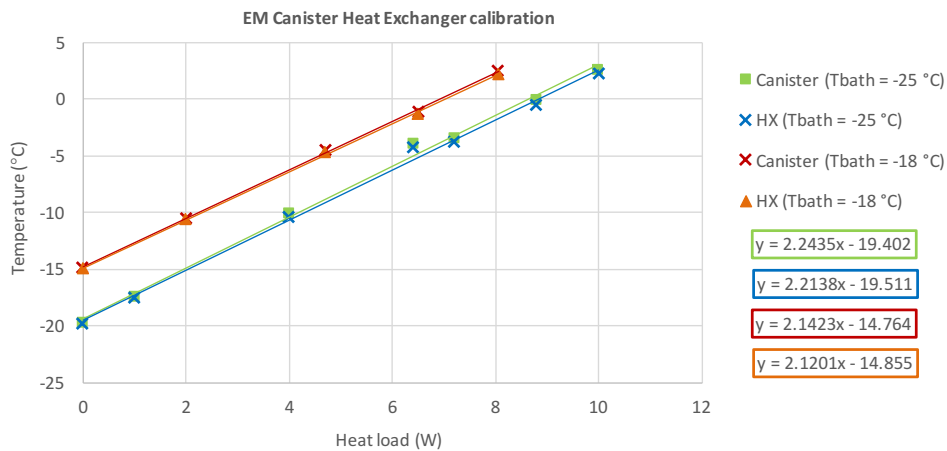


Figure 5.27: Temperatures of the canister and heat exchanger as a function of the applied heat load, for cooling bath temperatures of -18°C and -25°C .

5.2.4 Cryocooler assembly

The Engineering Model was assembled in a GM cryocooler by CTI Cryogenics, Model 22 (2 W at 20 K). Though this was an existing working cryocooler, it was completely re-vamped: the instrumentation skirt, vacuum jacket and radiation shielding were designed in order to expand the cryocooler's experimental room. Figure 5.28 shows the cryocooler as redesigned for the EM.

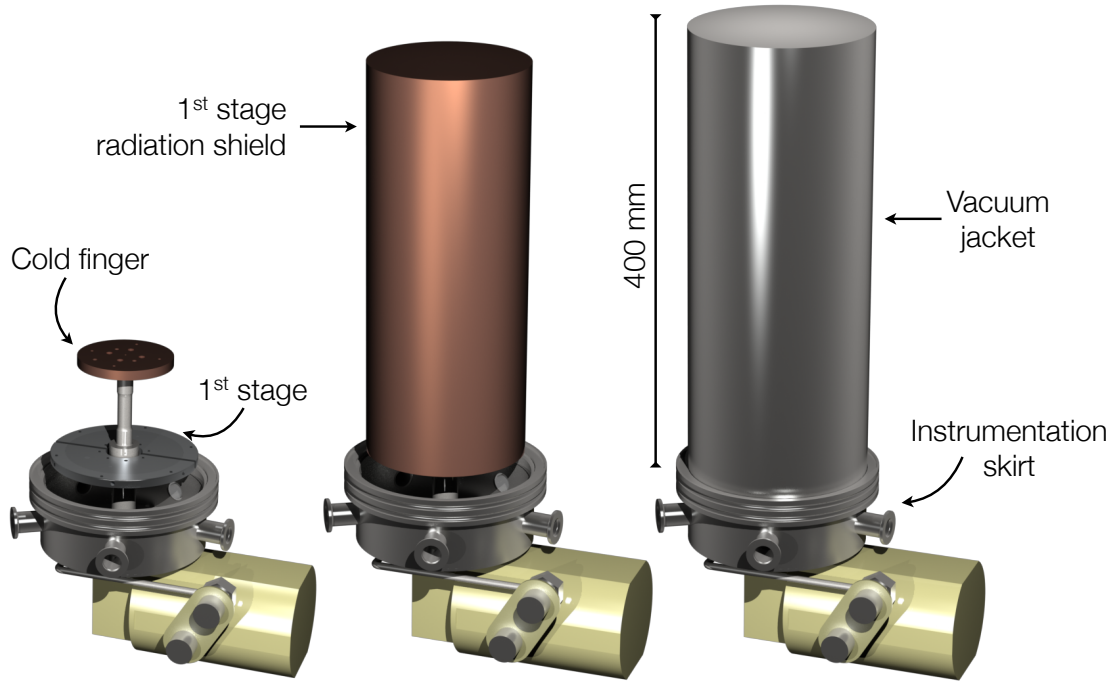


Figure 5.28: Drawing of the GM cryocooler assembly, as designed for testing of the Engineering Model.

The vacuum jacket has a fairly large diameter and is subject to 1 bar of external pressure, since it has a high vacuum in its interior and atmospheric pressure on the exterior: as such, its minimal thickness must be carefully evaluated to avoid collapse under vacuum conditions. When calculating the collapsing pressure for a given vessel, it is assumed that the shell is perfectly round of uniform thickness, that the material obeys Hooke's law and that the radial stress is negligible, while the normal stress distribution is linear. Assuming a vessel shaped like a cylinder of length L , outer diameter D_o and constant wall thickness t , the buckling or collapsing pressure can be determined by [32]:

$$p_c = KE \left(\frac{t}{D_o} \right)^3 \quad (5.2)$$

where E is the Young's modulus for the material and K a numerical factor that depends upon L/D and D/t , on the kind of end support and whether pressure is applied radially

only or at the ends as well; the values for K can be retrieved from the American Society of Mechanical Engineers (ASME) Code. In this analysis, a cylinder is considered short if

$$\frac{L}{D_o} < 1.14(1 - \mu^2)^{1/4} \sqrt{\frac{D_o}{t}} \quad (5.3)$$

where μ is Poisson's ratio. The vacuum jacket was sized to have $L = 400$ mm and $D_o = 159$ mm, which leads to $L/D_o = 2.52$. Considering SS 304 and aluminium 6061 as candidates for the vacuum jacket, the right side of the equation becomes ≈ 14 for both cases: it can be considered to be a short cylinder. The collapsing pressure can then be estimated from

$$p_c = \frac{2.42E(t/D)^{5/2}}{(1 - \mu^2)^{3/4} [L/D - 0.45(t/D)^{1/2}]} \quad (5.4)$$

Table 5.13 shows the material properties and collapsing pressure for a wall thickness of 1 mm for both stainless steel and aluminium.

Table 5.13: Estimation of the collapsing pressure for a vacuum vessel of $L = 400$ mm, $t = 1$ mm and $D_o = 159$ mm.

Material	Poisson's ratio	Young's Modulus (GPa)	Collapsing P (bar)
Al 6061 [65]	0.33	68.9	2.3
SS 304 [66]	0.29	193.0	6.3

Both materials provide a collapsing pressure with a safety factor of over 2 for atmospheric pressure. While using aluminium would have made the assembly considerably lighter, it posed some difficulties in welding the parts together. In the end, stainless steel was deemed not only safer but also easier to work with, and as such was chosen for the vacuum jacket, with a thickness of 1.5 mm for convenience; the end cap for the vacuum jacket was designed to be twice as thick as the cylinder walls.

The rest of the components were designed mostly taking the size of the EM into account, as there were no other mechanical requirements. Table 5.14 shows the dimensions and approximate mass of the new components built for the cryocooler.

Table 5.14: Properties of the components designed and built for the cryocooler assembly.

Component	Material	Mass	Dimensions (mm)	
Vacuum jacket	SS 304	3.2 kg	$L = 400$	$\varnothing = 160$
Instrumentation skirt	SS 304	1.7 kg	$L = 60$	$\varnothing = 160$
50 K radiation shield	Copper	N/A	$L = 350$	$\varnothing = 140$
50 K flange	Aluminium	300 g	$L = 8$	$\varnothing = 140$
15 K flange	Copper	490 g	$L = 10$	$\varnothing = 90$

The cold cell of the EM was then mounted onto this “new” cryocooler. As previously described, Qmeter 1, which mimics I/F 1 at 120 K, is coupled to the first stage, whereas

I/F 2 (25 K) and Cold I/F (15 K) are coupled to the cold finger. Figure 5.29 shows the cold part of the Engineering Model.

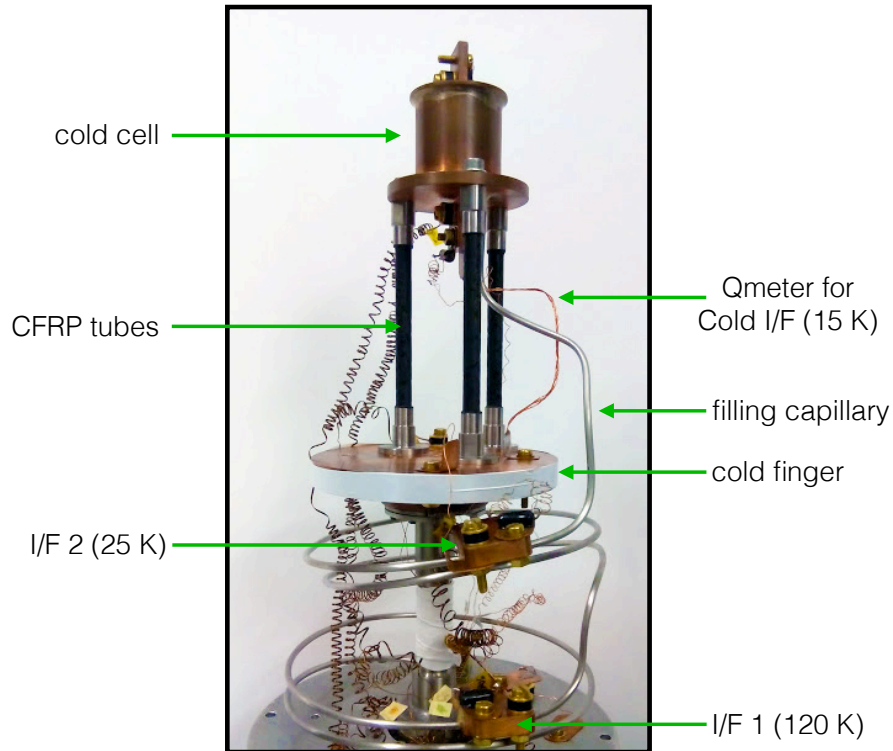


Figure 5.29: Cold cell of the Engineering Model as assembled inside the cryocooler.

6 Results and Discussion

Although in no way exhaustive, the results presented in this chapter show the most important findings with the Development Model (DM) and with the Engineering Model (EM). While the results presented for the DM focus in the preliminary testing to assess basic features such as liquid confinement and energy storage capabilities, it was extensively tested and cycled to ensure a good foundation or starting point to build the EM from. The results presented for the EM are the ones that best portray the capacity to answer the requirements established by ESA, including pre- and post-qualification test performance.

6.1 Development Model

The Development Model of the ESU was tested thoroughly using both a 56 ℓ expansion volume and the first metal hydride canister. The 56 ℓ experiments aimed to validate some of the basic features of the ESU as they allowed for independent testing of the cold part, without the influence of new phenomena that could arise from using the canister. These results are presented first as they were the basis for the more complex experiments that followed.

6.1.1 Preliminary testing

Before each experiment, the quantity of hydrogen gas stored in the expansion volume is measured and condensed inside the cold cell, and eventually adjusted until a desired liquid filling ratio is achieved at the targeted initial temperature: as explained in Section 4.3, as a rule the cell will not be filled above 90%. When the liquid hydrogen is completely condensed at 15 K, the heat absorption phase can begin. As a heat load is applied, the liquid hydrogen evaporates in the cell and the generated gas is stored in the expansion volume, with the resulting increase of pressure causing an increase in the temperature of the cold cell (cf. Section 3.4). ESA specifications do not require the cold cell to be thermally decoupled from its 15 mW cooling source at 15 K during the heat absorption mode: there was therefore no need for any special preparation of the system prior to the heat absorption mode or “ESU mode”. However, the cold finger temperature was

kept close to the initial cell temperature throughout the ESU mode; as such, the available cooling power at the Cold I/F can be considered negligible when compared to the heat load imposed by resistive heating during the experiments.

Figure 6.1 shows the two configurations (baseline and anti-gravity) used for testing the Development Model, as well as the placement of the thermometers and pressure sensors. These pressure sensors are located at room temperature and the measurements taken allow for the temperature of the liquid-vapour interface to be computed; P_{50L} is located in line with the expansion volume, and as such is not free of the pressure drop caused by the high hydrogen flow during heat absorption; P_{ESU} is located in a separate manifold with negligible volume, rendering it suitable for accurate measurements of the actual pressure in the cold cell since they are not affected by the pressure drop caused by hydrogen flow.

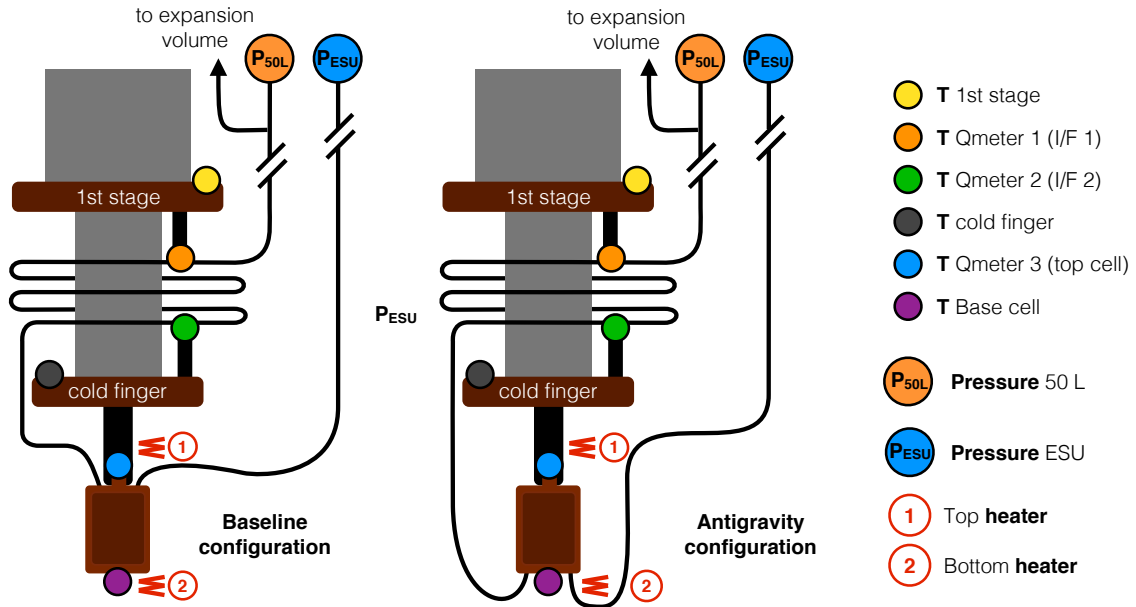


Figure 6.1: Configurations used during performance testing of the DM and thermometer placement. P_{50L} and P_{ESU} refer to pressure sensors at room temperature. The colours displayed for the thermometers match those found in the experimental result curves.

The porous material was installed in the cold cell for both configurations: although tests were performed with both the alumina foam and the vitreous carbon described in Section 4.4, the tests shown in this chapter were all produced using the alumina foam, as the carbon foam seemed to catalyse the ortho-to-para hydrogen conversion process without providing significant thermal homogeneity improvements when compared to the alumina foam.

Figure 6.2 shows an ESU mode with a constant load of 1 W applied with the cold cell in its baseline configuration.

The system was filled with 320 mbar at room temperature, then the hydrogen was

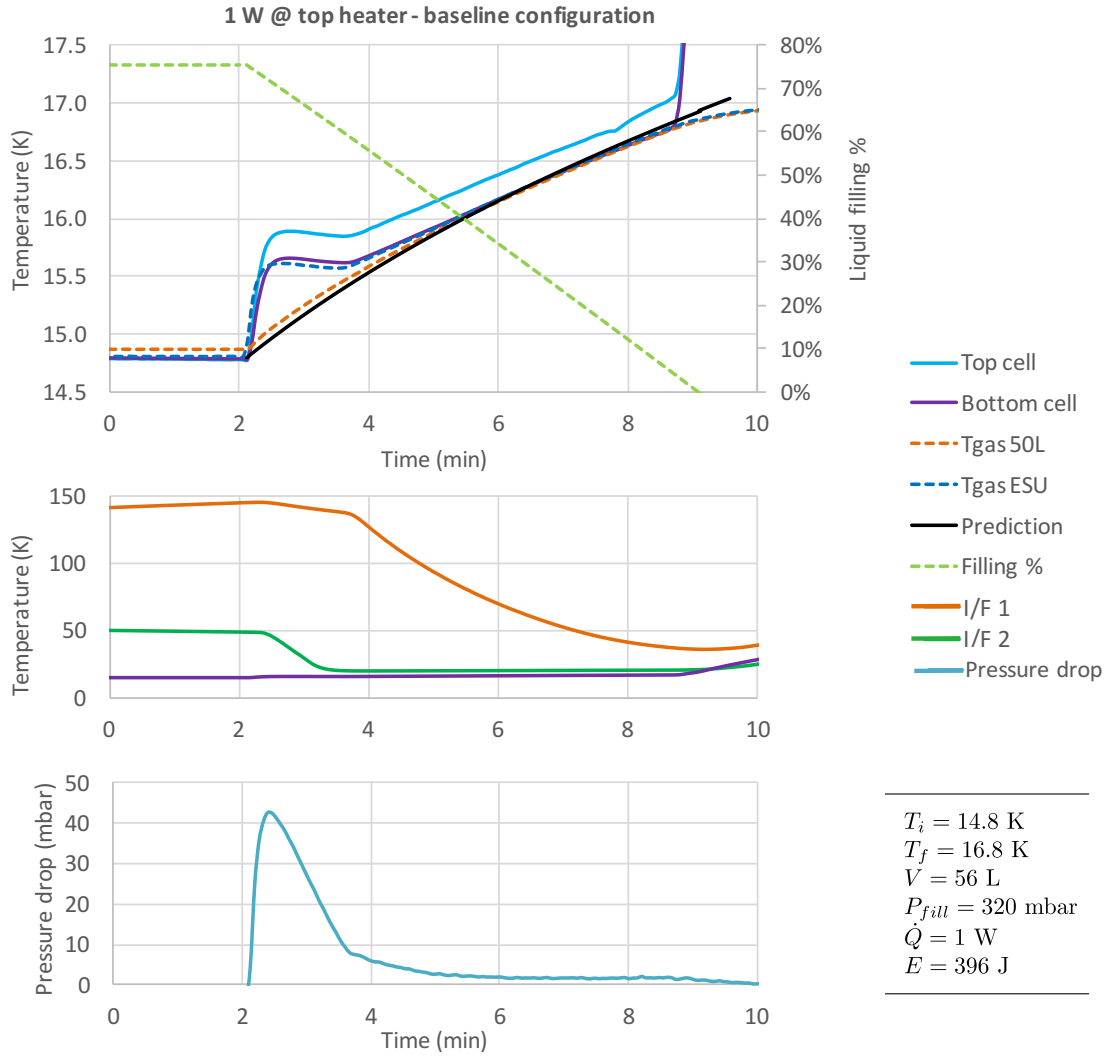


Figure 6.2: Experimental results for a 1 W constant-power heat absorption phase (“ESU mode”); temperatures are to be read on the left-hand side scale, while the liquid filling ratio is displayed on the right.

allowed to condense until a 76% liquid filling ratio was achieved at 14.8 K. At $t = 2 \text{ min}$, a constant heat load of 1 W is applied to the heater located at the top of the cell (capillary side), and the hydrogen starts to evaporate into the expansion volume. The cell wall temperature as measured by the thermometers increases rapidly during the first seconds of the experiment; for $t > 4 \text{ min}$ all the temperatures (including the ones derived from pressure measurements) are in rough agreement. Throughout the whole experiment, the evaporated hydrogen causes the pressure and hence the temperature to increase along the saturation curve from 14.8 K at $t = 2 \text{ min}$ to 16.8 K at $t = 9 \text{ min}$. At $t = 9 \text{ min}$, the temperature of the cell walls increases suddenly, indicating that no more energy can be efficiently stored. T_{gasESU} is the temperature deduced from pressure measurements free of the influence of hydrogen flow (P_{ESU}) and T_{gas50L} is the temperature deduced

from pressure measurements in line with the 56 ℓ expansion volume (P_{50L}). During the first 2 min of the ESU mode ($2\text{min} < t < 4\text{min}$ of the plot) it can be seen that these two temperatures do not match, and while T_{gas50L} is in agreement with the prediction computed from the thermal model (described in Section 3.3), T_{gasESU} matches the actual temperatures measured at both the top and bottom of the cold cell: this means that at the start of the ESU mode, there is indeed an observable pressure drop between the cold cell and the room temperature expansion volume due to the high hydrogen flow rate. This situation starts to improve at approximately $t = 2.5\text{min}$: this decrease in the original pressure drop is due to the fact that the high hydrogen flow being evaporated cools the capillary tube down (as can be seen from the temperature evolution of I/F 1 and I/F 2 in Figure 6.2), which in turn leads to a significant decrease of the pressure drop (bottom plot of Figure 6.2). Interfaces I/F 1 and I/F 2 were purposely heated (120 mW and 30 mW respectively) above their nominal temperature to force a “worst-case scenario” for pressure drop; although the heating in the interfaces was maintained throughout the whole experiment, it was not enough to counteract the cooling effect of the evaporated hydrogen gas.

At $t \approx 9\text{min}$, the sudden increase in the cell wall temperature is due to a decoupling between the temperature of the outside of the cell (measured by thermometers) and the temperature measured in its inside (deduced from pressure measurements): while there is still liquid hydrogen available inside the cell, it is thermally decoupled from the cell itself. This phenomenon (see Section 4.3) has been extensively discussed in previous works [36, 52] with different porous media and for different fluids and heat loads, and was interpreted as small droplets that remain trapped inside the alumina foam. This decoupling renders the liquid droplets unusable for energy absorption and hence the temperature of the cell starts to increase abruptly, whereas the increase of T_{gasESU} and T_{gas50L} is slower. However, for alumina foam with liquid hydrogen, the portion of liquid that remains trapped inside the foam is $\approx 5\%$, and this amount was accounted for when sizing the ESU (cf. Section 4.3), posing no unexpected issues.

The ESU mode shown in Figure 6.2 allowed for 396 J (1 W during 6.6 min) to be stored between 14.8 K and 16.8 K, *i.e.* along a temperature drift of 2 K. After the initial effects of pressure drop, which are not contemplated in the thermal model, there is a good agreement between the prediction and the actual experimental results; additional experiments were carried out where the I/Fs were heated to even higher temperatures leading to a similar result. One additional remark is the fact that there is a slight difference ($\approx 0.3\text{K}$) between the temperature measured at the top of the cell and the one measured at the bottom of the cell: this was found to be due to the two parts of the cell having been soft-soldered, and the resulting contact resistance hinders thermal homogeneity between the two parts of the cell. As will be seen further on, the EM cell was brazed using an Ag-based solder, and this effect is no longer observable.

6.1.2 Liquid confinement tests

The Development Model was tested under two different configurations, discussed earlier: in the “baseline” configuration the capillary exhaust is located at the top of the cell (left-hand side of Figure 6.1) and the liquid remains inside the cell whether or not there is a porous material inside it by the effect of gravity, whereas in the “anti-gravity” configuration the capillary exhaust is located at the bottom of the cell, and liquid confinement is achieved exclusively by capillary action with the aid of a porous material (right-hand side of Figure 6.1). These liquid confinement experiments were performed with both a 56 ℓ and a 6 ℓ expansion volumes: while using the 56 ℓ volume validates the experiments within the temperature range of the ESU, using the 6 ℓ allows for liquid confinement to be studied along a broader temperature range. This is of interest because the further away from the triple point, the lower the surface tension and as such the worse the capillary action: if the alumina foam is capable of retaining liquid hydrogen up to 23 K (due to using a 6 ℓ volume), not only is it suitable for the 15 K to 17 K range but can also be used for slightly higher temperatures within a safety margin.

Figure 6.3 shows the experimental results for an ESU mode performed in the baseline configuration and an ESU mode in the anti-gravity configuration, where a constant heat load of 1 W was applied to the top of the cell at $t = 0$.

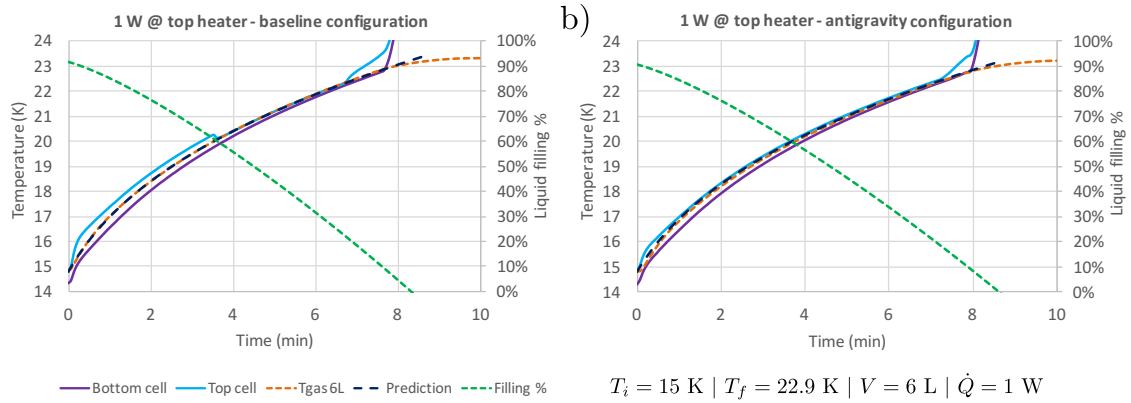


Figure 6.3: Liquid confinement experiments using a 6 ℓ expansion volume: a) cell in the baseline configuration and heating at the top of the cell (capillary side); b) cell in the anti-gravity configuration, heating at the top of the cell (opposite to capillary side). In both cases, a constant load of 1 W was applied.

Both experiments stored energy along the same temperature drift (7.9 K, from 15 K to 22.9 K), although the amount of energy stored differs slightly between experiments: for the baseline configuration the filling pressure was 2.18 bar (91.7% liquid filling ratio at 15 K) leading to 450 J stored and for the anti-gravity configuration the filling pressure was 2.15 bar leading to an initial liquid filling ratio of 90.4% and a total of 480 J stored. No significant differences can be observed between the two experiments, even though

these represent the best- and worst-case scenarios. In the baseline configuration, the cell is being heated close to the exhaust capillary, and as the gas forms it can exit the cell without obstructions; the anti-gravity experiment was performed under the worst possible conditions, *i.e.* the cell was being heated at the top while the capillary was at the bottom of the cell. This seems to be the worst possible scenario because the liquid begins to evaporate at the top of the cell, and the increase in pressure can push the remaining liquid through the capillary even if the porous foam is able to confine the liquid under normal conditions. Still, even with a 1 W load applied, results show that this was not the case and the expected amount of energy was stored in both experiments without any observable liquid spilling. This would have lead to an abrupt increase of the cell temperature at the start of the experiment due to the increase in pressure and also a sudden decrease of the amount of liquid in the cold cell. Experiments performed with lower heat loads corroborated the results obtained with 1 W. As in Figure 6.2, a small pressure drop was also observed at the beginning of the ESU mode, however this is not as readily seen in the results due to a higher slope of temperature as a function of time due to the 6 ℓ volume being used.

The same type of experiment was performed for all four heater/capillary configurations using the 56 ℓ expansion volume, although with slightly different filling pressures for each configuration, and with different starting temperatures as well. The data for each experiment is presented in Table 6.1 and the results are displayed in Figure 6.4: for the sake of clarity, for each configuration only the temperatures inferred from pressure measurements in the cell (T_{gasESU}) are displayed.

Table 6.1: Conditions of each liquid confinement experiment using the 56 ℓ volume. In all cases, a heat load of 1 W was applied.

	T_i	T_f	Filling P	Stored Energy
Baseline, top heater	14.8 K	16.8 K	320 mbar	395 J
Baseline, bottom heater	14.75 K	16.8 K	320 mbar	400 J
Anti-gravity, top heater	15 K	17.2 K	370 mbar	468 J
Anti-gravity, bottom heater	15.1 K	17.15 K	370 mbar	474 J

It can be seen that, within a 1% margin, the position of the heater does not influence the results, as the experiments performed under the same conditions show the same behaviour without any observable liquid spilling. All of these experiments were compared against the thermal model and a good agreement was found between the prediction and the effective amount of energy stored. Since it has been shown that the cold cell filled with alumina foam was capable of proper liquid confinement when heat loads as high as 1 W were applied, the results that follow are only going to be shown for the worst case, *i.e.* anti-gravity configuration with heating at the top of the cell.

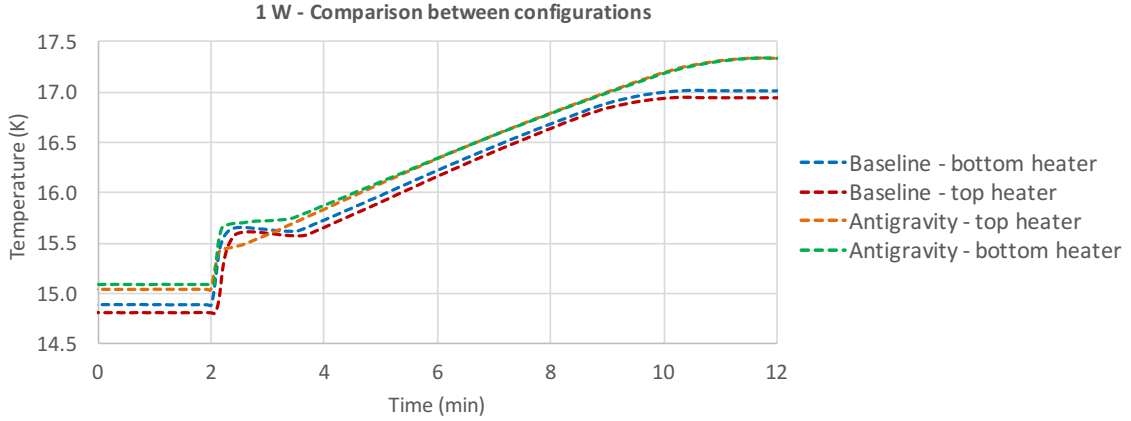


Figure 6.4: Liquid confinement experiments using a 56 ℓ expansion volume when a constant load of 1 W is applied. The temperature shown for each case is the temperature inferred from pressure measurements free of pressure drop (T_{gasESU}).

6.1.3 Heat Load Profile using a 56-litre volume

After the constant power experiments confirmed proper liquid confinement and the basic operation of the system, the Heat Load Profile (HLP) specified by ESA was applied in order to assess its performance under this specific profile that features a variable heat load that reaches up to 1 W. Figure 6.5 shows one of these experiments, carried out in the anti-gravity configuration and with heating at the top of the cell.

The HLP starts at $t = 2.5$ min with a liquid filling ratio of 90%, and the temperatures in the cold cell start to increase due to the heat load. An observable departure from what was shown in the 1 W experiment in Figure 6.2 is that both temperatures derived from pressure (T_{gasESU} and T_{gas50L}) are in close agreement (and with the temperatures measured by the thermometers) throughout the whole experiment (within ≈ 50 mK). This is due to the slowly increasing heat load at the start of the HLP, which causes the capillary tube to be cooled down by the evaporating hydrogen before the effects of pressure drop can be felt. The thermal model for a variable heat load is also in good agreement with the experimental results; the small discrepancy (≈ 0.2 K) at the end of the experiment can be due to an error in the number of moles calculated in the 56 ℓ volume. Also, because during the HLP experiment the liquid filling ratio in the cell remained between 90% and 20%, there is no decoupling between the cell wall temperature and the liquid temperature as seen previously when the liquid ratio inside the cell reached roughly 5%: this is in agreement with the calculation for the cell capacity discussed in Section 4.3 that aimed for the 400 J heat load (and even 440 J) to be absorbed without reaching a liquid filling ratio lower than 8%. Similar experiments where a 440 J heat load was applied confirmed that the decoupling was not observed.

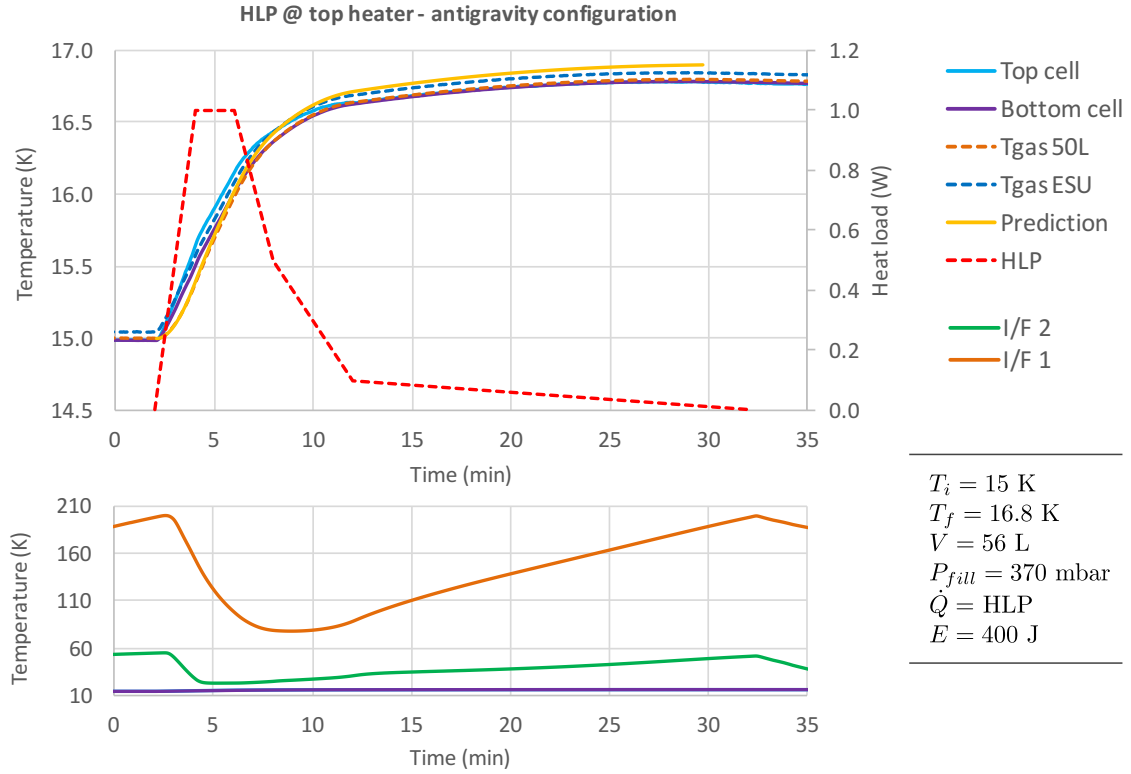


Figure 6.5: Temperature evolution when the Heat Load Profile is applied to the top of the cold cell in its anti-gravity configuration; the applied power can be read on the right-hand side of the plot. Experiment performed using a 56 ℓ expansion volume.

The system was able to absorb the required 400 J that make up the **HLP** with a temperature increase of 1.8 K, from 15 K to 16.8 K, while the liquid filling ratio varied from 90% to 20% at the end of the **HLP**; although this complies with the specifications for the temperature to remain below 17 K, the temperature measured in the cold cell is higher than 16 K during most of the **HLP**, which does not comply with requirement **FPR 5** which states that the cell should not have a temperature above 16 K for longer than 10 min. This was already discussed during the sizing process, and for the system to remain below 16 K an expansion volume of at least 100 ℓ would be required, rendering it unsuitable for space applications. While the 56 ℓ volume is also not suitable for space, it allowed for the cold cell to be tested in the 15 K to 17 K temperature range of interest, before moving on to the metal hydride canister.

6.1.4 Condensation using a 56-litre volume

In the framework of **ESA** requirements, the regeneration phase of the **ESU** should last less than 24 h while remaining below the cooling power budget at the three available interfaces (**FPR 2** and **IR 1**). To assess compliance with these requirements, the condensation process needs to be monitored to ensure that the heat load at each interface does not

exceed the budget; this was discussed in [Section 4.6](#). When using an expansion volume, the condensation rate and hence the heat load at a determined interface can be obtained by means of the variation in pressure in the expansion volume:

$$\dot{n}_{flow} = \frac{V_{exp}}{RT_{exp}} \frac{\delta P}{\delta t} \quad (6.1)$$

where $\delta P/\delta t$ is the variation in pressure measured at room temperature. The heat load can then be calculated by knowing the variation in enthalpy that occurs at the various interfaces. For example, for I/F 1 the heat load is given by:

$$\dot{Q}_{I/F\ 1} = (H(300K) - H(T_{I/F1})) \times \dot{n}_{flow} \quad (6.2)$$

It has been discussed in [Section 4.10](#) that this direct determination of the flow rate (using [Eq. 6.1](#)) will not be possible when using the metal hydride canister; instead one needs to rely on the calibrated Qmeters in order to know the heat load at the interface that gives access to the condensation rate through [Eq. 6.2](#), which in turn allows for the determination of the liquid filling ratio in the cell.

While still using the expansion volume, the condensation process was analysed in order to verify compliance with the requirements but also to validate the Qmeter calibrations and assess whether, within a margin for error, the results obtained by both methods were similar. [Figure 6.6](#) shows a typical condensation phase using the 56 ℓ expansion volume, where a total of 0.52 mol was condensed (cell \approx 88% full).

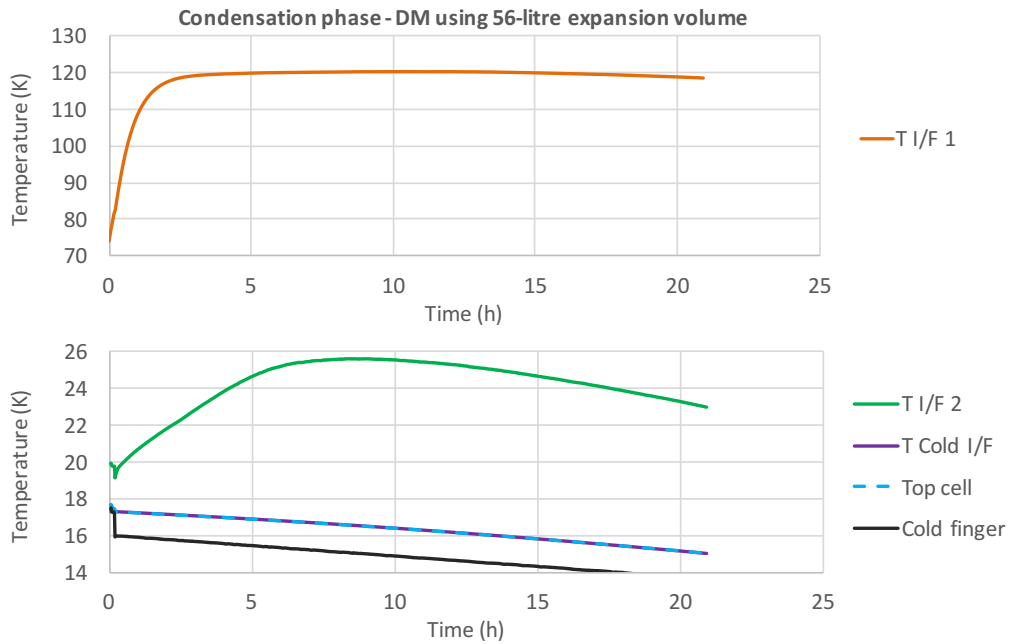


Figure 6.6: Temperature evolution during a regeneration phase of the ESU, where liquid hydrogen is condensed from the gas stored in a 56 ℓ expansion volume over a period of 21 h.

For a condensation phase to be carried out within the parameters requested by ESA, I/F 1 must be kept at ≈ 120 K while I/F 2 must be kept at ≈ 25 K throughout the entire duration of the condensation so that the cooling power available at each interface is 40 mW and 15 mW, respectively. In our system, and because the interfaces cannot be considered as heat sinks, their temperature depends on the condensation rate \dot{n} (since $\dot{Q} = \dot{n}\Delta H$), which in turn depends on the temperature difference between the cold finger of the cryocooler and that of the Cold I/F, *i.e.* the cell: this temperature difference determines the cooling power available for condensation and hence \dot{n} . For this particular condensation, the cooling power at the Cold I/F was limited to ≈ 7 mW so that the cooling power available at the other interfaces would not be exceeded (namely of I/F 2): this cooling power was obtained by maintaining a fairly constant temperature difference between the cold finger and the cell of about 1.5 K (bottom plot of Figure 6.6).

Figure 6.7 shows the heat load at each of the interfaces during the condensation period, calculated using both methods described at the beginning of this section. It should be noted that the results presented for calculations using the flow rate involved heating I/F 1 with an “artificial” heat load of 30 mW to compensate for the cooling effects of radiation in the capillary section that runs from 300 K to 120 K. During other experiments, a thermometer was placed between the 300 K and the 120 K stage, 2 cm before I/F 1: temperature measurements showed that the gas was effectively pre-cooled by radiation and solid conduction before reaching the 120 K interface, and as such was not at 300 K (which was used to calculate the heat load at I/F 1 using Eq. 6.2). It can be observed that, disregarding the transient period at the start of the condensation for I/Fs 1 and 2, the results obtained with both methods are in good agreement. The heat load dissipated at I/F 1 is under 35 mW (against the maximum allowed 40 mW), and the heat load at I/F 2 remains just below the allowed 15 mW. For this heat load to remain below the allowed maximum, the cooling power at the Cold I/F was kept below 9 mW (not far from the predicted 7 mW): this way, the condensation rate is controlled and the power dissipated at the three interfaces is kept below the budget. Figure 6.8 shows the amount of hydrogen that was condensed during this period using both the expansion volume method (flow rate) as well as by integration of the flow rate derived from the calibration curves for both Qmeters 2 and 3 along the whole condensation period.

It is observed that the results obtained with the calibration curve for Qmeter 3 are in agreement with the more reliable flow rate measurements, with a deviation of less than 5% in the liquid filling ratio: these results allows us to conclude that the energy spent at Qmeter 3 was the one needed to cool the gas from 25 K to 15 K and to condense it, and as such there was no observable heat load due to ortho-to-para conversion; even in this highly porous system, this process seems much slower than the 20 h time-scale of a normal condensation. The discrepancy of the results obtained with Qmeter 2 is due to the beginning of the condensation process, where the I/F temperature has yet to stabilise; under steady-state conditions ($t > 5$ h in Figure 6.7) the three curves are roughly parallel and a reduction of the transient period should eliminate this discrepancy.

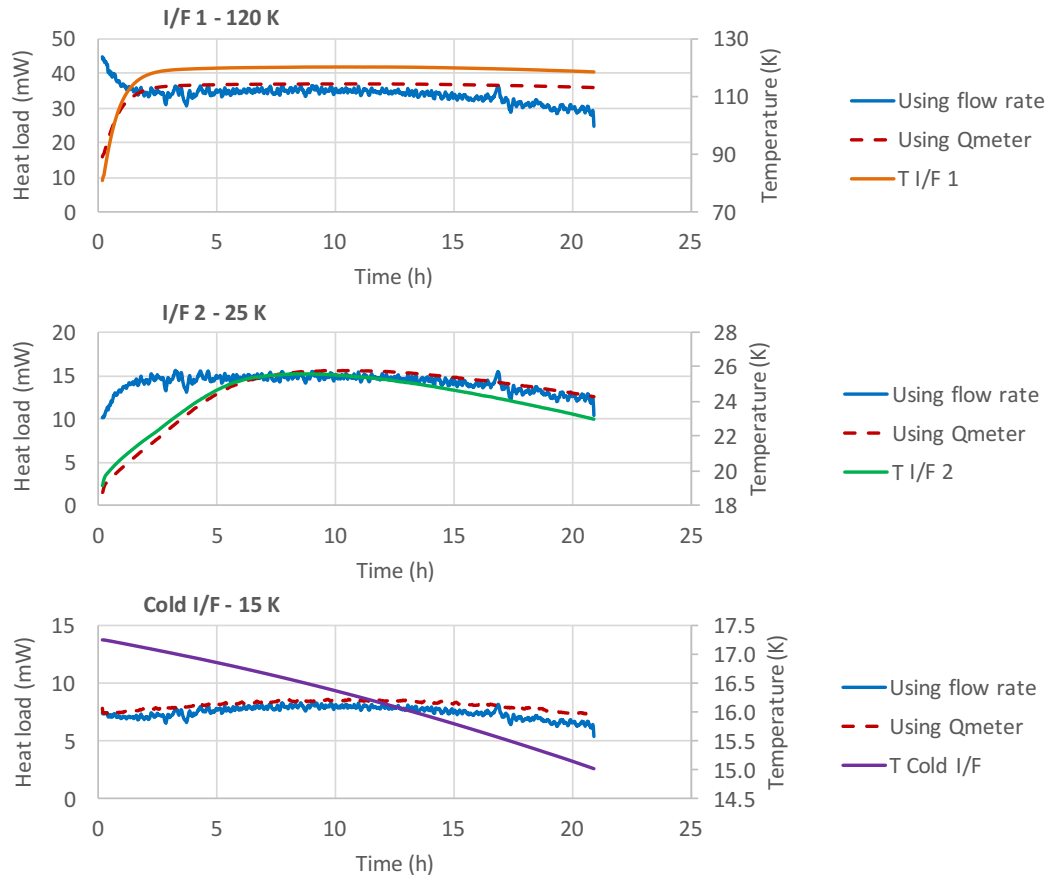


Figure 6.7: Heat load at each interface as calculated by means of flow rate and using Qmeter calibration. The temperature of the interface can be read on the right-hand side of each plot.

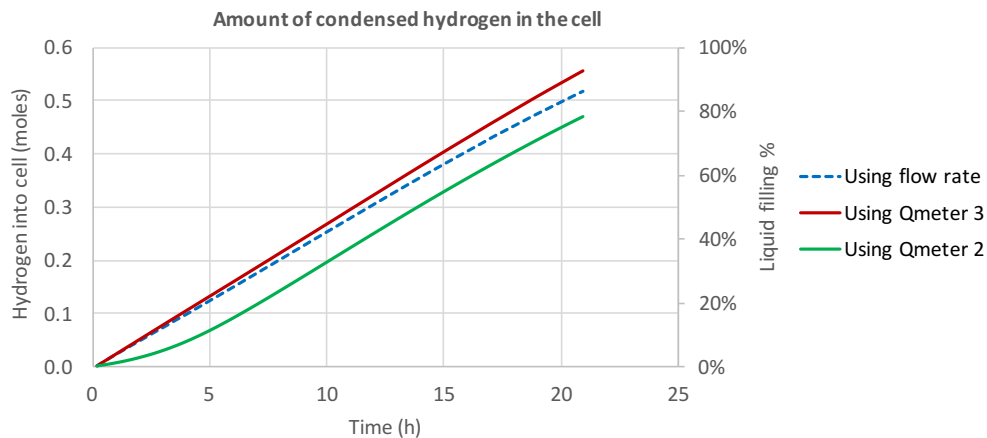


Figure 6.8: Amount of hydrogen condensed in the cold cell over the 21 hour regeneration phase, using three different methods: calculations using the flow rate inferred from the variation in the pressure and using the calibration of both Qmeters 2 and 3.

6.1.5 Heat Load Profile using metal hydrides

After the preliminary experiments using the expansion volume at room temperature, the cold part of the DM was well characterised and ready for the next step, which consisted in replacing the expansion volume with the metal hydride canister for storing hydrogen gas at near-room temperature. The canister was filled with 1 mol of hydrogen gas, although less than 0.5 mol are condensed during normal operation: this extra amount of hydrogen that acts as a buffer inside the canister allows for system to operate in a flatter part of the PCT curves of the metal hydride, *i.e.* the amount of hydrogen that is absorbed or desorbed each cycle is not the total amount of hydrogen inside the canister, but rather half of it (Figure 6.9).

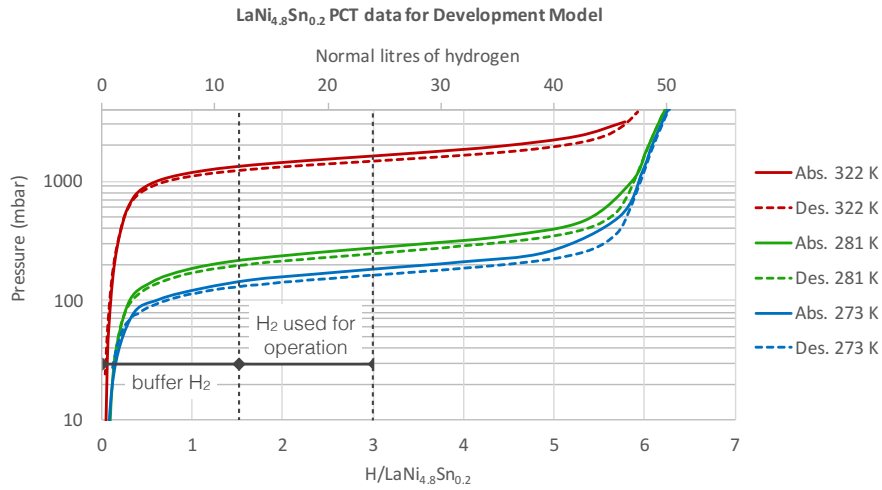


Figure 6.9: PCT curves for the DM canister, and explanation for the total amount of hydrogen inside the canister. Roughly 0.5 mol remain in the canister at all times acting as a buffer, so that the system can operate in the flat part of the pressure plateaus.

The rest of the experimental set-up was kept unchanged with the exception that it was no longer thought necessary to record measurements from both pressure sensors: the results obtained in previous experiments determined that the pressure drop was not an issue since the temperature inferred from pressure measurements was in agreement with the temperature measured by the thermometers; as such only the pressure sensor in line with the metal hydride canister (formerly P_{50L}) was kept; the temperature inferred from this measurement is T_{gas} . The metal hydride canister was coupled to the heat exchanger and cooling bath described in Section 5.1.7 and the whole assembly was thermally insulated from ambient conditions. Figure 6.10 shows the results obtained with the metal hydride canister when the HLP is applied to the cold cell; the condensation phase needed to reach the initial state displayed in the results will be described in Section 6.1.6.

The immediate observation is that the temperature profile is significantly different from what happened with the expansion volume (cf. Figure 6.5): as the HLP is applied to the cold cell, the temperature starts to rise up to a maximum of 16.7 K on the side

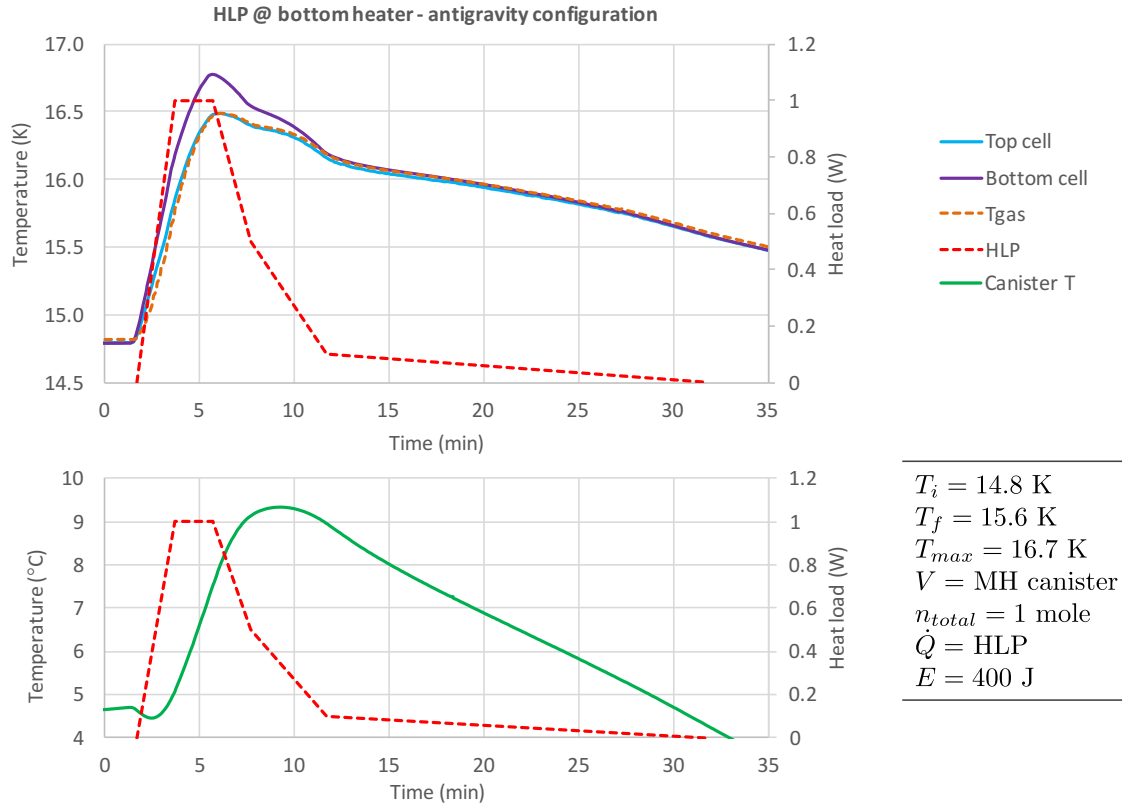


Figure 6.10: Temperature evolution when the Heat Load Profile is applied to the bottom of the cold cell in its anti-gravity configuration; experiment performed using the metal hydride canister for hydrogen gas storage.

that is being heated, and then starts to slowly decrease as the heat load decreases. A similar profile was predicted using the model for the canister described in [Section 4.10.2](#). As discussed previously, the first 4 minutes of the [HLP](#) are critical, as almost half of the hydrogen (the equivalent to 180 J) is evaporated during this period: when the metal hydride absorbs this amount of hydrogen it releases a significant amount of heat (≈ 6.6 kJ), causing the canister temperature to rise despite the available cooling power and the heat capacity of the canister itself. Even so, during this period the cold cell remains at a temperature below 17 K, which complies with the specifications. Moreover, the canister slowly cools down when the heat load becomes more manageable due to the decrease of the evaporation rate of hydrogen (from $t = 6$ min onwards). This cooling leads to a decrease in the equilibrium pressure of the metal hydride, and it starts to behave as a sorption pump for the cold cell: at the end of the [HLP](#) the cell temperature is ≈ 15.5 K even after 400 J have been absorbed. [Figure 6.10](#) shows that, due to this cooling phenomenon, the cell is above 16 K for a period shorter than 10 min: this complies with [FPR 5](#). As previously mentioned, maintaining the cold cell temperature below 16 K for an extended period of time would otherwise only be possible using a 100 ℓ expansion volume, whereas

in our system the total volume of the canister is less than 1ℓ , counting the stainless steel vessel. This is a major improvement and a significant result that allows for this configuration to satisfy all of the requirements established by ESA during the absorption of the heat peak.

Figure 6.10 also displays the temperature evolution of the canister during the heat absorption phase. At the beginning of the experiment ($t = 1 \text{ min}$) and before the start of the ESU mode, the heating power used to keep the canister at a constant temperature is cut which leads to a small temperature decrease (up to $t = 2.5 \text{ min}$). After this period, the pressure inside the canister increases due to the fast hydrogen evaporation in the cell: absorption starts to take place and the associated heat of absorption causes the canister temperature to increase. For $t > 9 \text{ min}$, the heat load released by the absorption process decreases due to the lower evaporation rate and becomes lower than the available cooling power and the canister starts to cool down.

Unlike with the expansion volume, the metal hydride canister needs some preparations before being ready for use: Figure 6.11 shows the period before the HLP was applied to the cell.

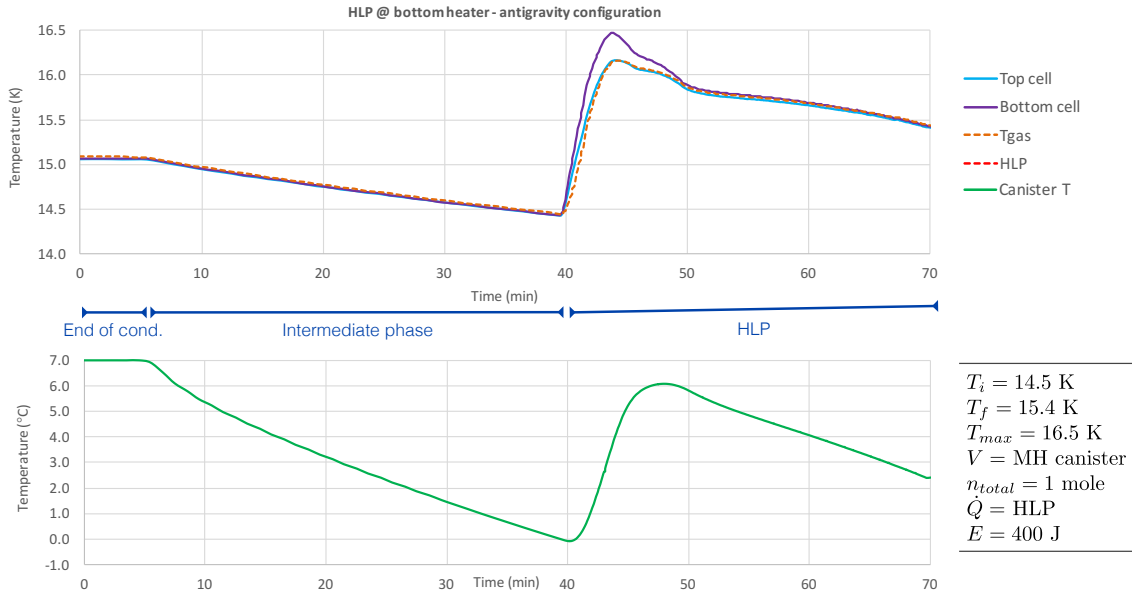


Figure 6.11: Typical preparation period before a heat absorption phase using the metal hydride canister. After condensation, the heating in the canister is cut and it is allowed to cool down, pumping on the liquid hydrogen and decreasing the cold cell temperature.

During the condensation phase, the canister needs to be artificially heated to aid desorption, for two reasons: the first one is that by raising the canister temperature the equilibrium pressure is also being raised, which in turn rises the temperature of the cold cell aiding the condensation process; the second one is that extra energy needs to be

provided to the canister during desorption, to compensate for the heat that is being used to desorb hydrogen. After the condensation period which ends at ≈ 6 min, the artificial heating on the canister is cut, and the canister begins to cool down. As it does so, the equilibrium pressure starts to decrease and the canister starts pumping on the liquid hydrogen in the cold cell, effectively decreasing its temperature: this is what happens during the so-called “intermediate phase”. The canister can be cooled down so that the cell temperature sits below 15 K, which is the case of the [HLP](#) displayed in the figure. This can further decrease the amount of time the cold cell is above 16 K, providing the same heat absorption at lower temperatures.

6.1.6 Condensation using the metal hydride canister

The condensation or regeneration phase while using the metal hydride canister is slightly different when compared to the experiments with the 56 ℓ volume. As previously mentioned, the canister needs to be artificially heated in order to both increase the equilibrium pressure and to compensate for the energy spent for hydrogen desorption. The temperature at which the canister is heated up to dictates the pressure in the whole system, and hence the temperature at which hydrogen starts to condense in the cell; as already explained, the temperature difference between this cell temperature and the cold finger of the cryocooler determines the available cooling power and hence the speed at which condensation takes place. Adjusting these two parameters is not always a straightforward process and some trial and error was needed to find the right combination. Figure [6.12](#) shows a condensation phase with the metal hydride canister.

The condensation took place during 25 h, to test if such a slow process would be feasible with the canister. A total of 0.5 mol was condensed (corresponding to an 83% liquid filling ratio) and the heat load at each interface remained well below the allowed limits, even though the condensation only exceeded the allowed time limit by one hour. The liquid filling ratio in the cell was calculated using the calibration curves of the Qmeters that were previously validated with the expansion volume. After the condensation, a constant heat load was applied to verify that the amount of stored energy corresponded to what was calculated with the Qmeters, and a good agreement was found between reality and the calculations of liquid amount. During this condensation, [I/F 2](#) remains at a temperature below 20 K indicating that the heat load at this interface is well below the 15 mW limit.

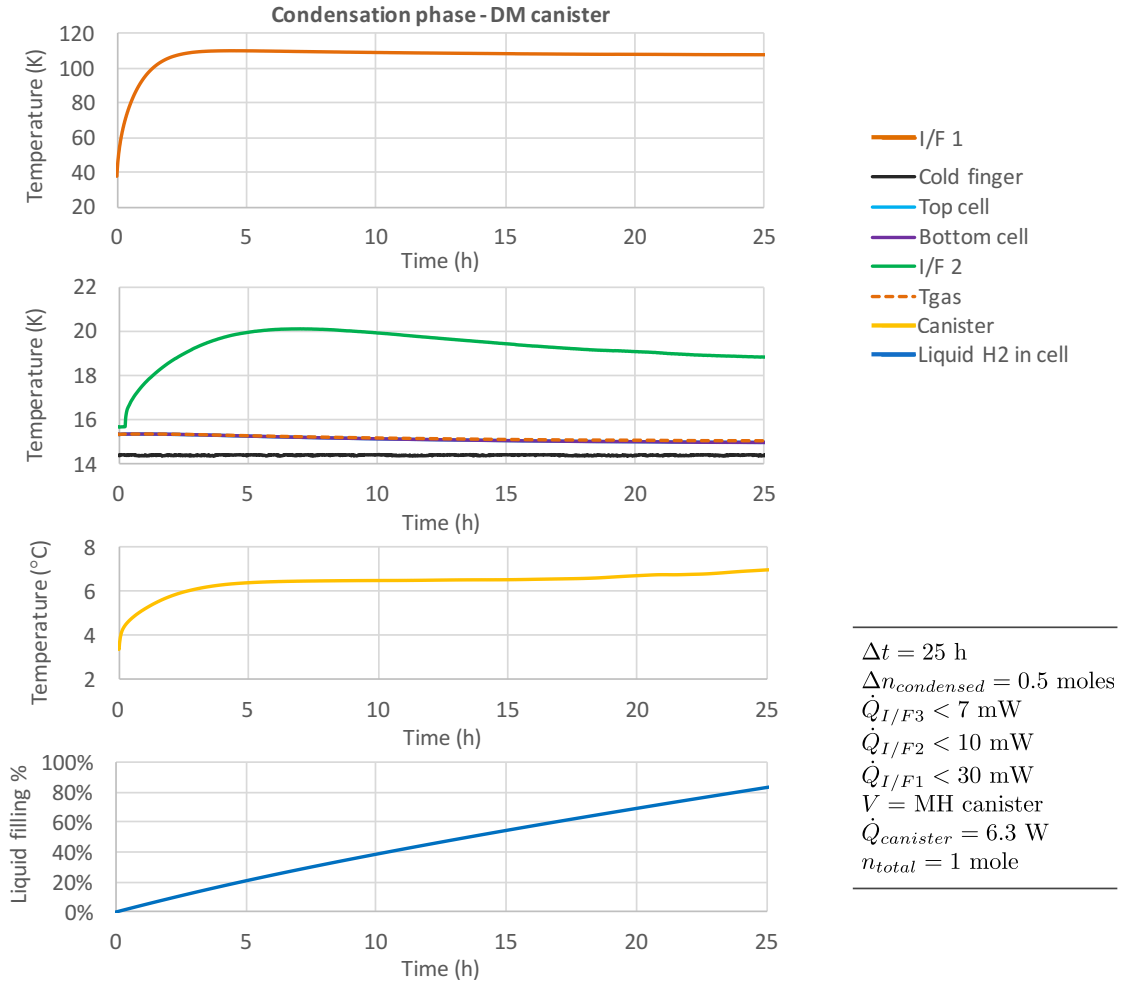


Figure 6.12: Condensation phase with the metal hydride canister for hydrogen storage. The temperature evolution of the cold cell and intermediate interfaces, as well as the canister, can be seen. The bottom plot shows the amount of condensed hydrogen, calculated using the flow rate obtained by the Qmeters calibration curves (cf. [Section 6.1.4](#)).

6.1.7 Effects of an additional heat load

One of the specifications given by ESA is that, during the design stage, a 10% margin in energy storage capacity should be considered (DR 1), which means that the cell should be designed for storing 440 J instead of 400 J. With this in mind, we decided to test the ability of the system to not only store an extra 40 J, but to withstand a heat load that was 10% higher than the specified HLP. An experiment was carried out by applying this “HLP+10%”. The results are shown in Figure 6.13, along with the results for a normal HLP for comparison.

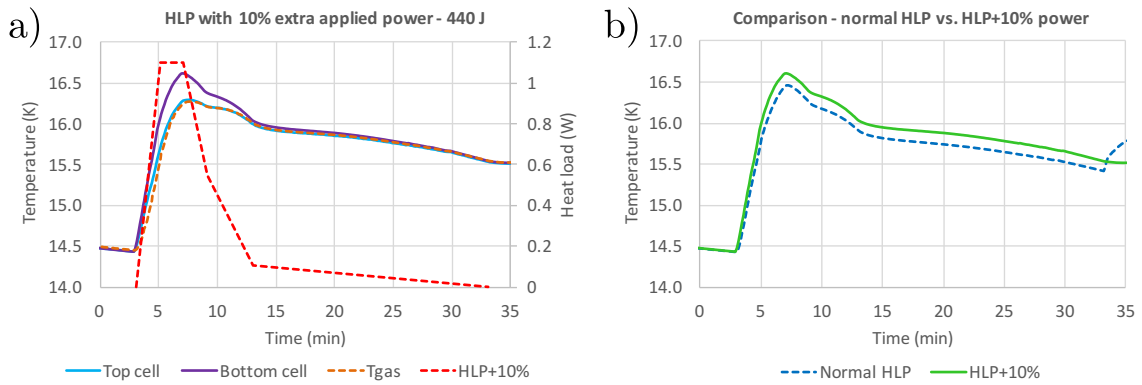


Figure 6.13: Heat load profile with an extra 10% applied power to the cold cell over 30 min: a) Temperature profile in the cold cell during the “HLP+10%”; b) Comparison of this experiment with one where the regular HLP is applied. For ease of comparison, only the highest temperature (Bottom cell) is displayed in this plot.

Although the temperature of the cell is naturally higher than when the normal HLP is applied, this effect is not dramatic: for a normal HLP the maximum temperature in the bottom of the cell is slightly below 16.5 K whereas it reaches 16.6 K with the additional heat load. The cold cell is still able to remain below 17 K for the whole duration of the experiment, and above 16 K for less than 10 min (8 min against 6 min for the normal HLP). This provides the system with some safety margins if the heat load that is supposed to be absorbed by the cold cell turns out to be slightly higher than expected. Let it be noted that there was no noticeable sign of thermal decoupling between the cell walls and the liquid, and as such the safety margins calculated during the cell sizing seems to be adequate; other experiments where a constant heat load was applied showed that the system is capable of storing about 480 J before decoupling can be seen.

6.1.8 Discussion and Summary

The Development Model of the ESU was thoroughly tested in a number of different configurations, using both an expansion volume and the metal hydride canister. These tests aimed to assess whether the ESU could operate while respecting the requirements established by ESA, both during the heat absorption phase when the HLP was applied and during the regeneration phase. Tests showed that the ESU could function both in the base-line and the anti-gravity configurations with no changes in performance. It was shown that a full regeneration of the ESU can be achieved in under 24 h while staying below the cooling power available at each interface, using both an expansion volume and the metal hydride canister. Experiments using the metal hydride canister showed that it worked remarkably well, confirming that this alternative allows for a better performance than the large expansion volume solution: despite its increased complexity, the metal hydride's ability to absorb hydrogen at near-constant pressure is a significant improvement. For instance, while the 17 K threshold is never exceeded in both cases during a HLP, the canister enables the heat load to be absorbed in the cold cell without ever going above 17 K, with a total time spent above 16 K of less than 10 min. The cold cell can be pre-cooled below 15 K before the heat absorption phase by tuning the temperature of the metal hydride canister, which can further reduce the temperature increase during the HLP. The battery of tests carried out with the Development Model validated its operation and the lessons learned were applied into improving the system for the Engineering Model.

6.2 ESU as a Cold Source

Beyond its original purpose, this system should be able to provide additional cooling power at the 15 K stage for a limited period of time using the metal hydride canister, and even to do so at a lower temperature. The aim of this experiment is to provide the system, and hence the 15 K stage, with additional cooling power during the non-HLP phase of operation: this can be achieved by using the metal hydride canister absorption properties so that the canister can act as a sorption pump. This mode is similar to pumping on a cryogenic bath to lower its temperature: in this case the cryogenic bath is the liquid hydrogen cell and the pump is the metal hydride canister. As the temperature of the metal hydrides is lowered, its equilibrium absorption pressure will decrease, and it will effectively pump on the liquid hydrogen bath, evaporating it slowly and providing additional cooling power to the cold stage.

The ESU could be used as a cold source and its cooling power measured in the following scenario: after a heat absorption phase, the system is allowed to re-condense all of the liquid hydrogen that had been spent up to a 90% filling ratio; as usual during this stage, the metal hydride canister is being heated to aid hydrogen desorption. When the cell is 90% full of liquid, the ESU as a Cold Source (EACS) mode can start. When the condensation is finished, the cold cell is at a temperature T_i (usually around 15 K) and the canister is kept at a constant temperature. The cold cell can be set to be controlled at a certain temperature T_{EACS} below T_i , and the heating in the canister is shut down, which causes the canister to cool down slowly, pumping liquid hydrogen from the cell and causing it to evaporate; this hydrogen is then absorbed into the canister at a ratio proportional to the heat input. This evaporative process at constant temperature provides additional cooling power to the cold cell interface: the temperature at which this cooling power is provided, T_{EACS} , can be controlled to an extent, and so can the duration of the process by controlling the cooling rate of the canister.

Figure 6.14 shows an EACS experiment carried out with the Development Model, for a controlled temperature of 14.2 K. At $t = 0.3$ h the canister starts to cool down and the EACS mode starts just before the one-hour mark, when the cell starts to be controlled at 14.2 K. The cold finger was set at the same temperature so that no cooling power would be provided by the cryocooler: the effective cooling power is then given by the heating power provided by resistive heating, which can in turn be measured via the voltage supplied by the temperature controller needed to maintain a stable temperature in the cell. During the 4.5 h period that follows, the canister was cooled down slowly, pumping on the liquid hydrogen in the cell and providing cooling power that averaged 30 mW throughout the experiment; integration of the heating power during this period leads to a stored energy of 480 J. If the ESU is to be used in ATHENA's cooling chain, this 2-fold increase in the cooling power at a temperature close to 14 K could be useful to boost the Joule-Thomson pre-cooling stage.

During the EACS mode the pressure inside the system is rather low, which could cause

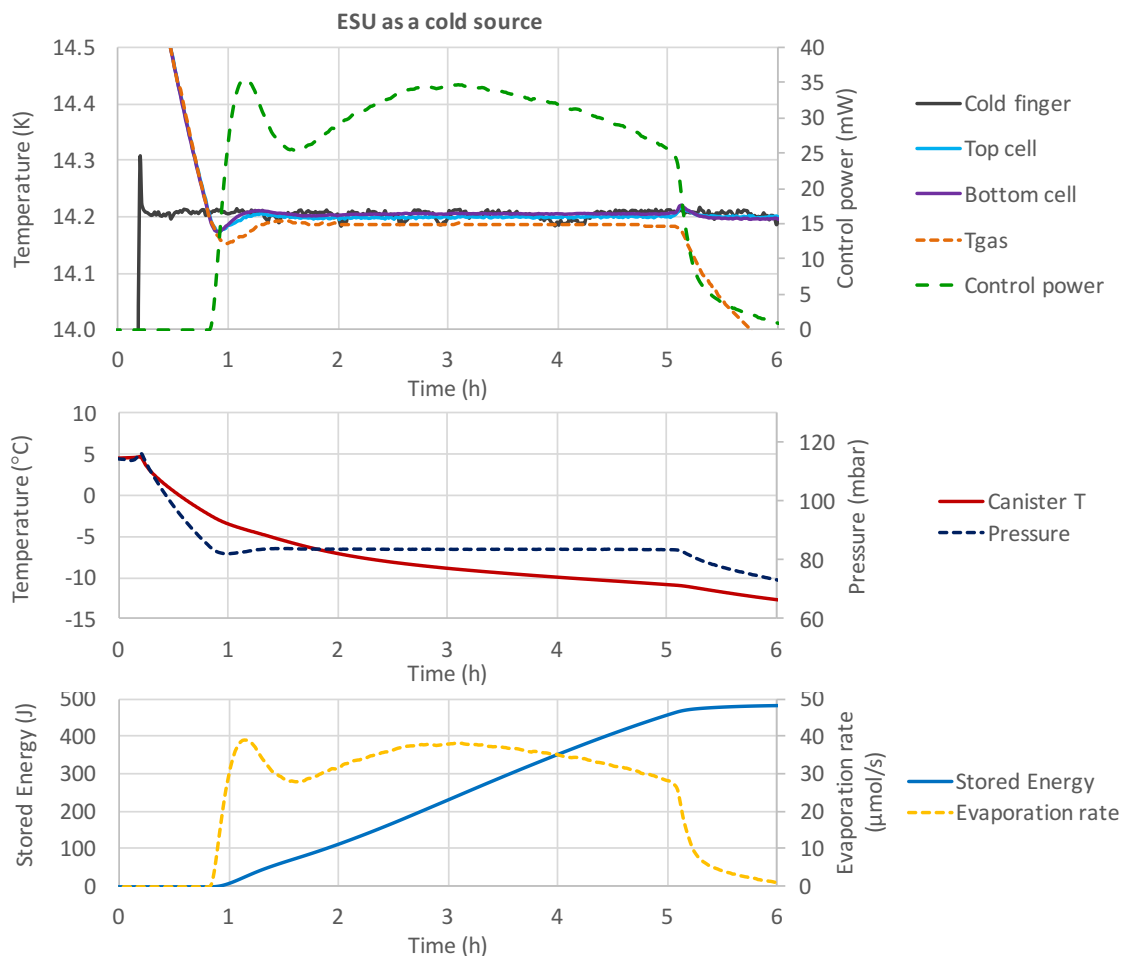


Figure 6.14: ESU as a Cold Source experiment performed at 14.2 K, which was able to provide an average extra cooling power of ≈ 30 mW during 4 h, absorbing a total of 480 J.

pressure drop issues that could limit operation. Preliminary calculations for the 75 mbar to 85 mbar range show that the maximum pressure drop is ≈ 2 mbar for a 2 mm inner diameter capillary with a length of 1 m. As such, pressure drop does not seem to be the limiting factor, but rather the poor absorption properties of the metal hydride at such low pressures and increasingly low temperatures: this fact might limit the operating temperature range. It remains to be seen whether performing an EACS when the hydrogen is in the solid phase would bring the same results, as the lack of liquid convection might hinder the performance of the ESU.

6.3 Engineering Model

The Engineering Model of the ESU was tested using both an expansion volume and the metal hydride canister, although the experiments carried out with the expansion volume were solely for verification purposes, and are not reported in this work unless necessary. Results with the Development Model showed that there was no observable difference between the baseline and the anti-gravity configurations, and as such the system was only tested in the anti-gravity configuration which is the relevant one for validation in a micro-gravity environment. The cold cell was filled with the same alumina foam as the DM cell, as it was able to confine the liquid properly under any orientation, and two Pt-100 thermometers were installed in the EM metal hydride canister, one at each end of the canister body. Figure 6.15 illustrates the Engineering Model as assembled in the refurbished cryocooler (cf. Section 5.2.4) along with thermometer placement. There are three pressure sensors in the system: one in the canister manifold (needed for when the canister is removed from the main manifold) and two in the wall manifold that connects the canister to the cold cell: as they are redundant in this configuration, P_{gas} indicates the pressure read by one of these sensors; it was not deemed necessary to install a pressure sensor for pressure drop measurements, as the results with the DM proved that it was not necessary and the capillary tube in the EM is shorter and wider (2 mm inner diameter), further reducing the effects of pressure drop.

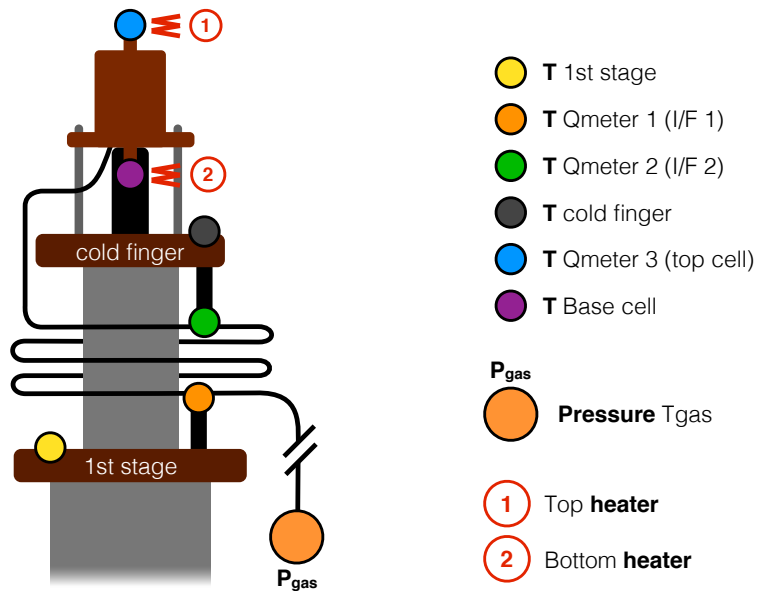


Figure 6.15: Anti-gravity configuration used during performance testing of the EM and thermometer placement. P_{gas} refers to the pressure sensor at room temperature. The colours displayed for the thermometers match those found in the experimental result curves.

6.3.1 Performance tests with constant heat load

The experiments shown over the course of this section aim to assess compliance with the several aspects requested by [ESA](#) that concern maximum allowed temperatures in the cold cell as a function of the applied heat load. Namely, the cold cell temperature should remain (cf. [Appendix A](#)):

- Lower than 17 K when a heat load of 1 W is applied;
- Lower than 15.5 K when a heat load of 100 mW is applied;
- Lower than 15 K when a heat load of less than 10 mW is applied.

The tests were carried out using the configuration described in [Figure 6.15](#), and the metal hydride canister for gas storage. In all cases, the canister was filled with 1 mol of hydrogen gas, but less than 0.5 mol are condensed; although this was explained for the Development Model, the effect is more advantageous for the [EM](#) due to the pressure plateaus of the [PCT](#) curves being flatter: by having a “buffer” amount of hydrogen, the absorption/desorption cycles are carried out in the even flatter part of the curve, as illustrated in [Figure 6.16](#) (the extra amount of hydrogen “pushes” the cycles to the right part of the plot).

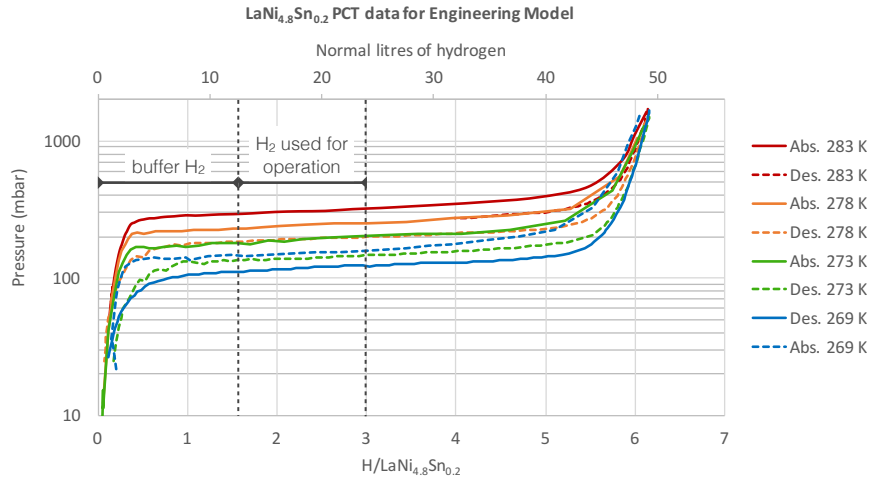


Figure 6.16: [PCT](#) curves for the [EM](#) canister, and explanation for the total amount of hydrogen inside the canister. Adding an additional amount of hydrogen allows the sorption cycles to be performed in the flat part of the pressure plateaus.

Figure 6.17 shows an [ESU](#) mode where 1 W was applied to the bottom of the cold cell. During absorption of the heat load, that lasted 6.5 min, the temperature of the cold cell rose from 14.7 K to 16.7 K, absorbing a total of 390 J and the mean canister temperature increased from -4°C to 3°C due to hydrogen absorption. This experiment confirms that the [ESU](#) is able to absorb a 1 W heat load with a temperature increase of less than 2 K, *i.e.*

without the cold cell temperature rising above 17 K if the heat load is applied at 15 K. The fact that only 390 J were stored instead of 400 J (or even 440 J) is due to an insufficient initial liquid filling, as will be shown later on. The temperatures measured in the cold cell by both the thermometers and T_{gas} are in close agreement throughout the experiment: it is noteworthy that there is no discernible temperature difference between both parts of the cell (in the DM cell a temperature difference of up to 0.6 K could be observed between the body and the lid of the cold cell). We attribute this to the fact that this cell was brazed with a silver-based alloy, significantly reducing contact resistance and improving homogeneity in the cell, and to the fact that it is made upon OFHC copper, further increasing heat transfer; the DM cell could not be brazed as it needed to be disassembled a number of times, rendering soft-soldering a more practical solution.

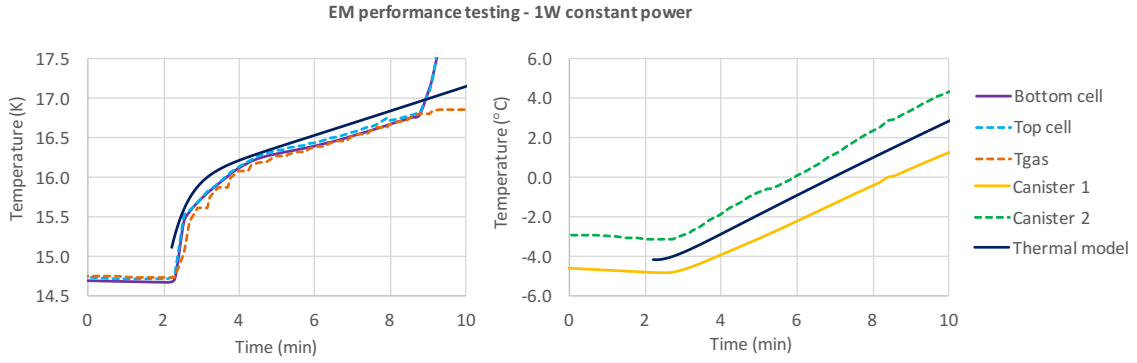


Figure 6.17: Evolution of system temperatures when a constant heat load of 1 W is applied to the bottom of the cell. Experiment carried out with the Engineering Model using the metal hydride canister for hydrogen storage; the cold finger was kept at 13 K during the experiment.

The thermal model for the metal hydride canister (described in Section 4.10.2) was computed considering the canister as an RC system in which the resistor is the thermal resistance caused by a 700 μm gas gap and the capacitor is the heat capacity of the canister and heat exchanger, with a total mass of 3.8 kg. The result of these thermal calculations is shown in Figure 6.17 under the “Thermal model” curve, and adequately fits the experimental data. However, for the cold cell temperature range from 14.7 K to 15.2 K, at the start of the ESU mode, the thermal model fails to correctly predict the cold cell temperature which rises faster than what was expected. It must be noted that the 700 μm gas gap that best describes the results seems exaggerated: as discussed in Section 4.9, the poor diffusivity of the stainless steel container and absorption dynamics can play a part in this initial phase. This handicap of the model is observed for other sets of data, as will be shown later on. We attribute this to the initial absorption dynamics of the metal hydride, which are not contemplated by the thermal model; when hydrogen absorption is well established (*i.e.* for $t > 4$ min), the experimental data is well described by the model.

Another experiment performed in similar conditions to the 1 W experiment discussed

above consisted of applying 0.5 W to the cold cell: the result is shown in Figure 6.18. However, more hydrogen was allowed to condense, resulting in a total of 450 J absorbed at the cold cell during approximately 14 min, satisfying DR 1; during this ESU mode, the temperature rose from 14.7 K to 16.5 K. Again, the model fits the experimental data quite well, with the exception of the onset of hydrogen absorption. In this experiment more than 10% extra energy was absorbed by the cold cell, and even then the temperature in the cold cell remained lower than 16.5 K.

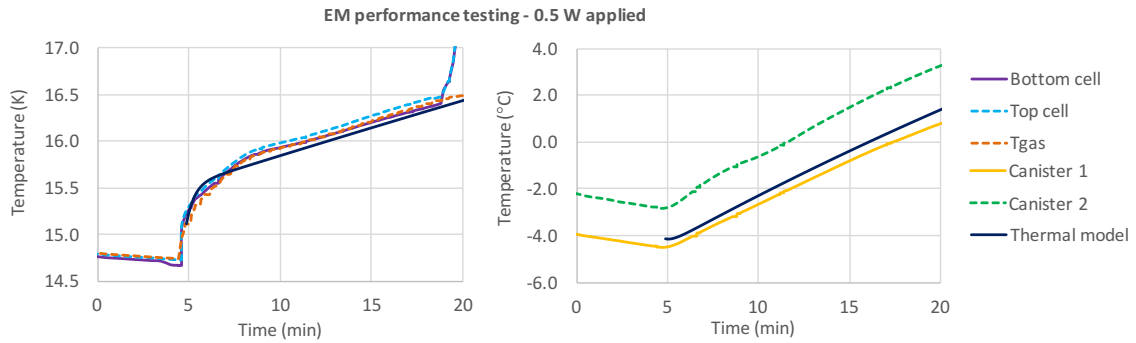


Figure 6.18: Evolution of system temperatures when a constant heat load of 0.5 W is applied to the bottom of the cell. Experiment carried out with the Engineering Model using the metal hydride canister for hydrogen storage; the cold finger was kept at 13 K during the experiment.

The last experiment carried out by applying a constant heat load of 100 mW to the cold cell, whose results are shown in Figure 6.19.

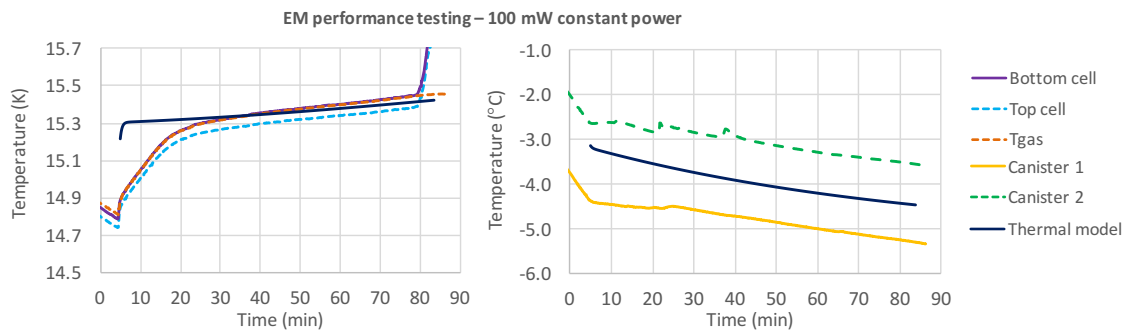


Figure 6.19: Evolution of system temperatures when a constant heat load of 100 mW is applied to the bottom of the cell. Experiment carried out with the Engineering Model using the metal hydride canister for hydrogen storage; the cold finger was kept at 13 K during the experiment.

The heat load of 100 mW was absorbed during ≈ 75 min, resulting in a total of 456 J of thermal energy stored. During this period the temperature of the cold cell increased from 14.8 K to 15.4 K, confirming the requirement not to exceed 15.5 K. This last experiment

shows that the ESU can be used as a cooling power booster, increasing the cooling power at the Cold I/F from 15 mW to 100 mW for over 70 min. With the exception of the first 20 min of the ESU mode, the temperature profile in the cold cell remained fairly flat, which is an indicator that the pressure remained somewhat constant throughout the whole absorption process. Looking at the canister temperature profile, it can be seen that not only its temperature did not increase but it effectively decreased during the ESU mode, indicating that the heat load released by the metal hydrides was lower than the available cooling power. Even though the canister temperature decreased slightly during the experiment, the temperature of the cold cell increased over time: this is due to the fact that the pressure plateaus are not perfectly flat. As the amount of hydrogen absorbed inside the canister increases, the pressure of the system can still increase: this is best explained in Figure 6.20.

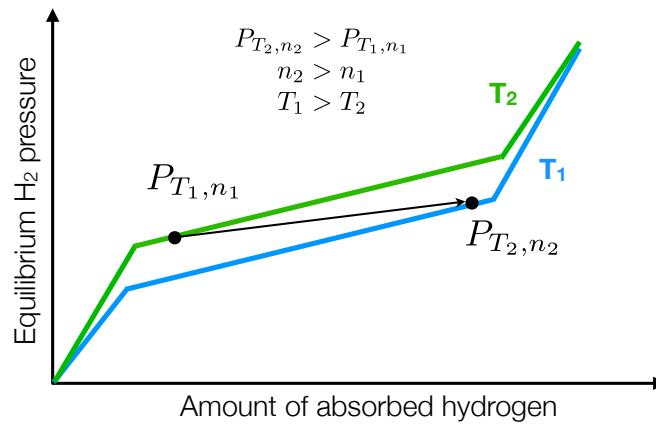


Figure 6.20: Increasing system pressure in a metal hydride canister with decreasing temperature: because the plateaus are not flat, the global pressure can increase with increased hydrogen absorption even as the metal hydride temperature decreases.

In this case it is notorious that the thermal model does not adequately describe the first 25 min of the experiment shown in Figure 6.19; again, we attribute this phenomenon to the absorption dynamics of the metal hydride: because the heat load was fairly low, so was the rate of hydrogen absorption by the canister, leading to a longer time before homogenisation and stabilisation of the dynamics inside the metal hydride.

6.3.2 Operational cycle tests

The ESU is intended for continuous use during a minimum period of 5 years. To test the system's reproducibility and ability to operate cyclically, a 4-day continuous operation experiment was carried out, during which 5 complete regeneration and heat absorption cycles were completed. Figure 6.21 shows the temperature profiles of the cell, intermediate interfaces and metal hydride canister that resulted from this experiment.

Prior to the cycling tests, the cell was completely depleted of liquid hydrogen; during the first condensation period, hydrogen was allowed to condense until the cell was 90%

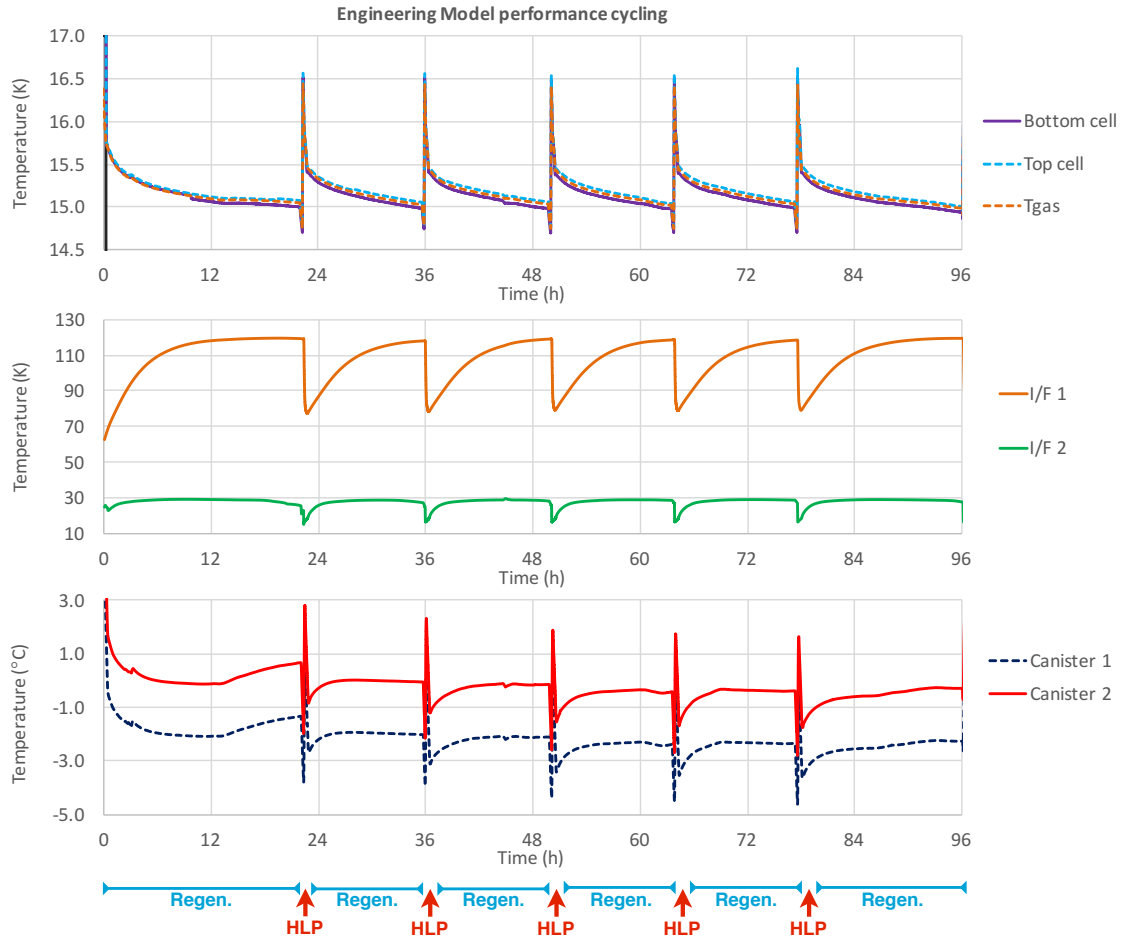


Figure 6.21: Cycling tests with the Engineering Model. The temperature evolution of the cold cell, interfaces and canister are shown as a function of time for a period of 96 h that encompasses 5 complete regeneration and heat absorption cycles.

full of liquid (which corresponds to $\approx 500\text{J}$). In the condensation phases that followed only the amount of liquid that had been used up during the HLP (the equivalent of 400 J) was re-condensed, hence the shorter duration. It can be observed that the cycles seem to be highly reproducible, with similar condensation times and temperature profiles in both the cold cell, intermediate interfaces and canister, despite the relative complexity of the whole regeneration cycle (due to maintaining the canister temperature, controlling the rate of condensation and so on). During the whole experiment, the temperature of the cold cell never exceeded 16.6 K and the mean canister temperature varied between $-5\text{ }^{\circ}\text{C}$ and $3\text{ }^{\circ}\text{C}$; the progressive decrease in the canister temperature is due to ambient conditions that slightly altered the temperature of the cooling bath that is part of the canister heat exchanger. The temperature of I/F 2 is higher than 25 K during the condensation periods, however this is not due to an excessive heat load on the interface, but rather due to an artificial 7 mW heating provided throughout the experiments. This was to prevent the

interface from cooling down too much during condensation, which could cause unwanted liquid formation at I/F 2. I/F 1 was also artificially heated with 35 mW to compensate for the cooling effects of its 50 K radiative environment.

For ease of comparison, the result of the 5 heat absorption phases (by application of the HLP) is superimposed in Figure 6.22 for both the cold cell and canister temperatures. Only the temperature as inferred from pressure measurements, T_{gas} , is represented. The results show to be highly reproducible, with no remarkable differences between each experiment: after condensation, the cold cell was pre-cooled down to 14.8 K (which corresponds to a canister temperature of $\approx -4^\circ\text{C}$), and then the HLP was applied to the bottom of the cold cell, at $t = 13$ min in Figure 6.22. The heat absorption phase went as expected, with a maximum temperature of 16.4 K reached right after the end of the 1 W plateau. For the duration of the HLP, the cold cell was at a temperature above 16 K for only 8 min; again, this can be further reduced by pre-cooling the cold cell down to a lower temperature before the HLP.

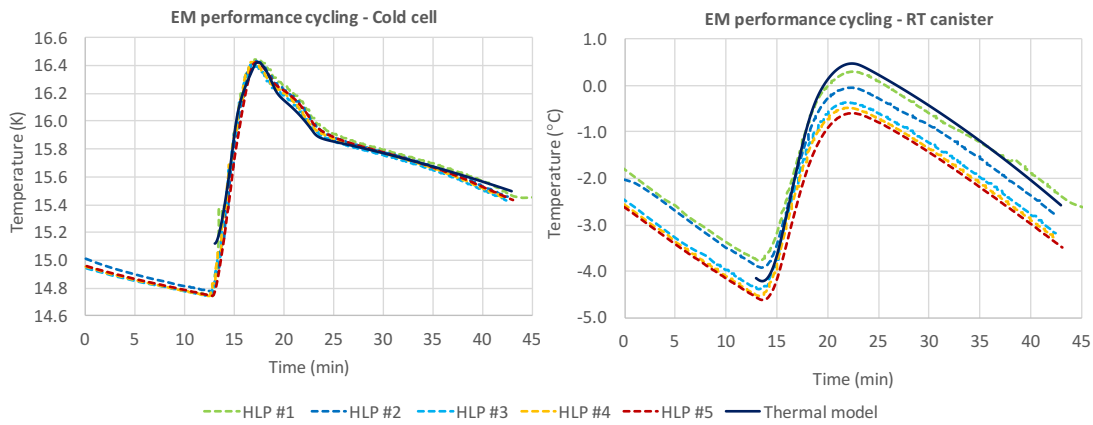


Figure 6.22: Evolution of cold cell and canister temperatures when the HLP is applied to the bottom of the cell; results shown for the 5 HLP cycles performed continuously during a 96 h period.

The temperature profile of the metal hydride canister, also pictured in Figure 6.22, shows that the results for the 5 cycles are slightly shifted in temperature: the temperature measured during the HLP was not exactly the same for every cycle, and the dispersion of the curves can reach 1.5°C . It was commented that this was due to the changing temperature of the canister bath during the 96 h period that the experiments took place, as environmental conditions affected its base temperature. However, it should be noted that although the temperature of the canister, and hence of the metal hydride, were not kept exactly the same, this is not noticeable in the cold cell temperature, whose results showed to be almost perfectly superimposed. This means that the canister does not need an extremely rigorous control in temperature for the system to operate correctly and produce satisfactory results. In short, this experiment yielded very positive results that proved the

ability of the developed system to work uninterrupted in a continuous regeneration/heat absorption cycle, producing reproducible results that are within specifications.

The regeneration phases for each cycle are also worth discussing. As shown in Figure 6.21, the temperatures at each of the interfaces are quite reproducible for each cycle; the heat load at I/F 1, I/F 2 and Cold I/F were calculated using the calibration curves of the respective Qmeters and are presented in Figure 6.23. To help maintain the temperature of I/F 1 and 2 close to their nominal value during condensation, an additional heat load of 35 mW was applied to I/F 1 and of 7 mW to I/F 2.

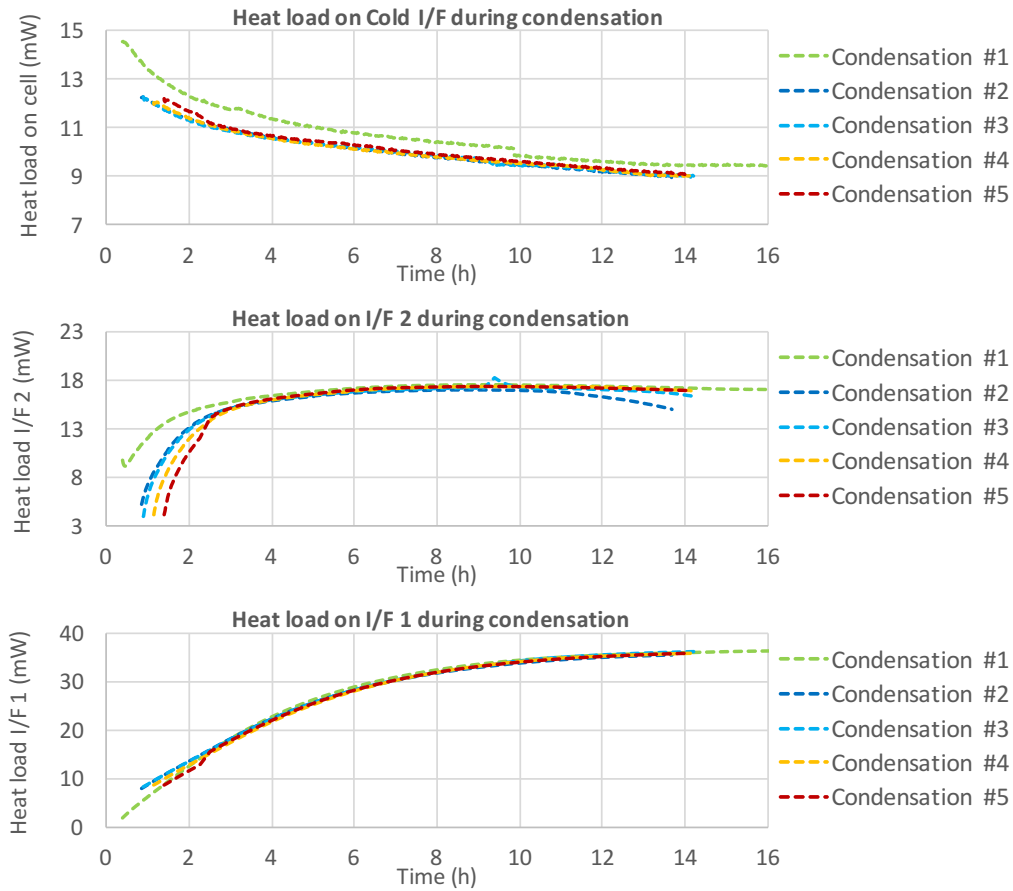


Figure 6.23: Heat load at each of the three interfaces during the condensation phase for each of the 5 cycles. During this experiment, an artificial heat load of 7 mW was being constantly applied to I/F 2 and of 35 mW to I/F 1.

Each condensation period lasted approximately 14 h with the exception of the first condensation where more hydrogen was allowed to liquefy, which lasted 16 h. During this phase, the heat load at the Cold I/F (*i.e.* the cell) did not exceed 15 mW, averaging ≈ 10 mW, which is compatible with a 14 h condensation as calculated in Section 4.6. The results for I/F 2 show that the maximum heat load during condensation reached 18 mW; however, this heat load is the sum of the heat load due to the pre-cooling of hydrogen at the interface and the 7 mW that were artificially applied at I/F 2 with a resistive heater. As

such, the heat load released due to the condensation only reached a maximum of 11 mW. This value is considerably below the heat load calculations presented in [Section 4.6](#) which indicate that for a 14 h condensation the heat load should be around 20 mW; an explanation for this discrepancy has not yet been found. The same phenomenon is observed when analysing the results of I/F 1. Although [Figure 6.23](#) shows that the heat load slowly increases until a maximum of 37 mW, 35 mW were being artificially applied to the interface, which would mean that the heat load due to hydrogen pre-cooling, would be, at best, 2 mW, when calculations say it should be around 50 mW; this issue was already discussed in [Section 6.1.4](#). However, there is an hypothesis as to why this happens on I/F 1: its nominal temperature is around 120 K whereas its thermal environment is approximately 50 K due to the radiation shield inside the cryocooler: this might cause the filling capillary tube and the I/F 1 copper part itself to be cooled by radiation, partially explaining the “missing” heat load. For example, considering a surface area of 8 cm² for the copper piece that makes up I/F 1, and considering a thermal environment where this part is at 120 K and the radiation shield is at 50 K, even with an emissivity of 1 this would only account for 9 mW.

6.3.3 Discussion and summary of Operational tests

The Engineering Model was extensively tested for its thermal performance and compliance with the imposed requirements. Unlike the Development Model, which was intended to be a more experimental device where configurations could be changed to assess different issues, the EM design is a result from the lessons learned with the DM, and is therefore a much more mature device in terms of performance and integrity. Using the metal hydride canister, the ESU was able to successfully absorb constant heat loads up to 1 W without a cold cell temperature rise above 17 K; absorption of the HLP was achieved with a maximum temperature increase of 16.4 K, with only 8 min spent above the 16 K mark. The ESU was also run continuously for 96 h in what consisted of 5 complete regeneration and heat absorption cycles: the results were found to be highly reproducible for both phases; the specifications were met for the heat absorption phase and condensation was achieved within the time limit while the heat loads remained below the budget for each interface. [Table 6.2](#) summarises the results, not only for the Engineering Model but also for the Development Model, where more extensive testing was performed.

Table 6.2: Checklist for ESA requirements and achieved results.

Req.	Description	Result
FPR 1	Ability to absorb 400 J at 15 K according to the specified HLP.	HLP was successfully absorbed with both the expansion volume and the metal hydride canister.
FPR 2	Ability to regenerate within 24 h.	Full regeneration of 0.5 mol is achieved in under 24 h without exceeding heat loads.
FPR 3	During heat absorption, the temperature of the cold cell shall be lower than 17 K with 1 W applied, 15.5 K with 100 mW applied and 15 K with less than 10 mW applied.	The maximum temperatures of the cold cell remained within the specifications for the aforementioned heat loads.
FPR 4	As a goal, the ESU shall be able to provide a temperature below 15 K during absorption of the peak.	The ESU can be used as a cold source for lower heat loads in which more than 400 J can be absorbed entirely below 15 K.
FPR 5	A temperature increase above 16 K is acceptable for a duration shorter than 10 min.	This can be achieved with an expansion volume of 100 ℓ or higher, or with the metal hydride canister for a more compact solution.
ER 1	The ESU shall demonstrate its performance in a 50 K radiative thermal environment.	The ESU was tested in a redesigned cryocooler that provided the desired radiative environment.
PRR 1	The overall ESU mass shall be less than 5 kg, excluding electronics.	The mass of the system was kept below 4.5 kg, including instrumentation.
PRR 2	The cryogenic mass of the ESU shall be less than 500 g.	The mass of the cold part does not exceed 240 g considering a 20% margin.
PRR 3	The cold volume of the ESU shall be less than 0.2 ℓ at intermediate I/F 1, 0.1 ℓ at intermediate I/F 2 and 0.1 ℓ at Cold I/F.	The requirements were met for each interface.
PRR 4	The ambient volume of the ESU shall be less than 5 ℓ.	The total volume of the canister is ≈ 4ℓ, including instrumentation and manifold.
PRR 5	The average power consumption of the ESU shall be less than 15 W.	The maximum power consumption of the ESU is lower than 10 W applied on the metal hydride canister during the regeneration phase.
OR 2	The ESU shall be able to operate on ground under any orientation and in micro-g environment.	The ESU was tested in both the baseline and the anti-gravity configurations and was able to maintain the expected performance.

6.4 Qualification Tests

In order to achieve a Technology Readiness Level (TRL) of 5, meaning that the device should be able to demonstrate its performance in a relevant environment, a number of “qualification” tests were carried out. These consist mainly of mechanical and thermal shock tests to assess the structural stability of the ESU and its components, so that it can be demonstrated that the whole system could survive launch conditions. The various tests took place in different locations and required the system to be flushed and filled with different gases (such as helium and hydrogen), especially the metal hydride canister which had to travel back and forth: one of the main concerns throughout the whole test campaign was not to contaminate the $\text{LaNi}_{4.8}\text{Sn}_{0.2}$ alloy. This section summarises the most important tests and the obtained results.

6.4.1 Proof pressure tests

Proof pressure tests consisted of exposing the whole system to a constant pressure, register the results and perform posterior leak tests to verify that there was no damage to the ESU. For practical reasons, the cold part (cell and filling capillary with heat exchangers) was tested separately from the metal hydride canister, although under the same conditions. Purified helium gas was used to fill both parts, increasing the pressure in 1 bar increments until the proof pressure of 6 bar was reached. After spending 10 min at the proof pressure, the system was de-pressurised and leak tests were performed; both parts were tested at room temperature and the cold part was also tested at 10 K. The experimental set-up is shown in Figure 6.24: the cold cell was tested inside the vacuum jacket of the cryocooler, and the canister inside its thermal insulation housing for safety reasons should the parts not resist the proof pressure test.

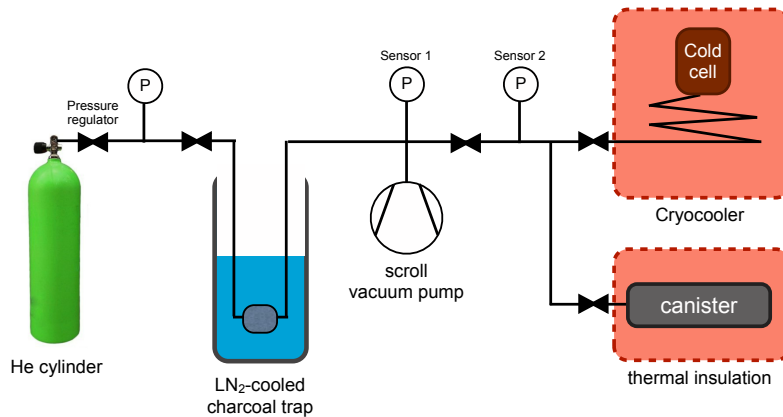


Figure 6.24: Illustration of the manifold used for helium purification and proof pressure tests.

Both parts were exposed to 6 bar during at least 10 min, after which a visual inspection and leak tests were carried out. Both parts were found to be in good condition and the

measured helium leak rate was below 1×10^{-9} mbar \cdot l \cdot s $^{-1}$.

6.4.2 Burst test of cold cell

A dedicated model of the cold cell (Figure 6.25, left-hand side) with the same structural features but without the outer support features, was built for a burst test. This test was found necessary to determine at what pressure the cell would structurally burst should there be a blockage in the capillary tube and liquid hydrogen started to evaporate: this would dramatically increase the pressure inside the cell and could cause a system failure.

A manual hydraulic pump using water as the working fluid was used for the test, coupled to a pressure sensor and connected to the dummy cell via a long capillary tube. The cell itself was placed in a protected area to protect nearby equipment and personnel, and pressure was increased incrementally until it reached 110 bar: due to technical restrictions, this pressure was not exceeded. The right-hand side of Figure 6.25 shows the cell after the test, and it can be seen that the cell suffered significant deformation during the tests, although no burst occurred for pressure lower than 110 bar.

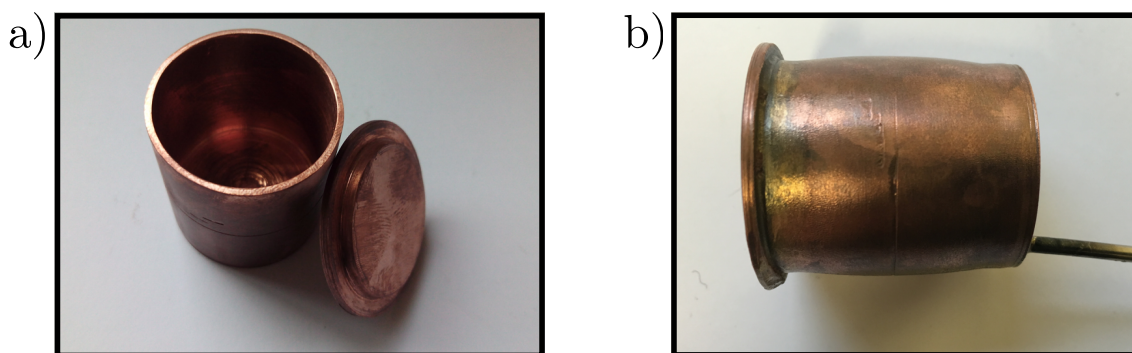


Figure 6.25: Dedicated model of the cold cell for the burst test: a) after machining, before the tests; b) after the burst test.

6.4.3 Thermal shock to cold cell

Thermal shock tests on the cold part (including the CFRP tubes) were performed by completely dipping it in liquid nitrogen at 77 K: complete submersion was achieved in 10 s. After thermal stabilisation of the entire cold part, it was removed from the liquid nitrogen dewar and allowed to warm up back to room temperature. To minimize condensation of water vapour inside the cell and capillaries, the system was filled with 1 bar of helium gas and then sealed. Figure 6.26 shows the cold cell being immersed in nitrogen and immediately after the test, before warming up to room temperature.

The main objective of the thermal shock was to verify the integrity of the CFRP tubes when exposed to violent temperature variations. To further assess the behaviour of the tubes, a dummy model of the CFRP tubes was built exclusively for this test: the tube was

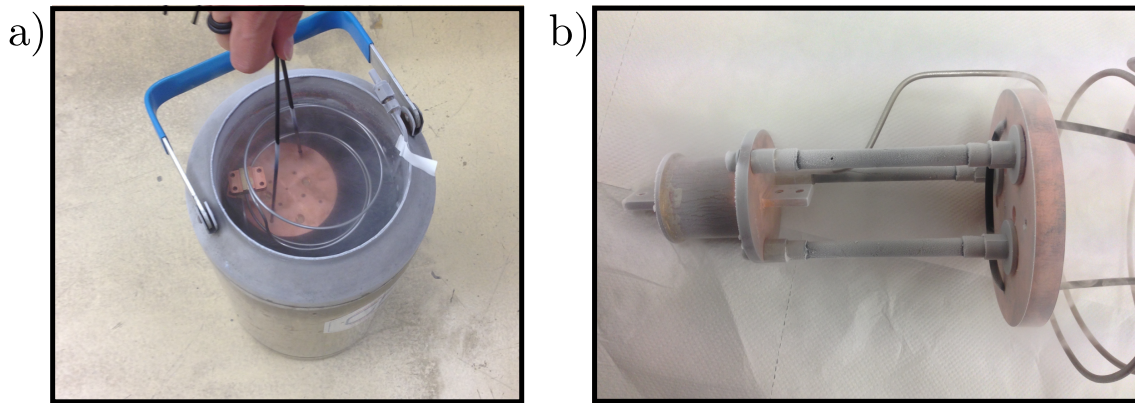


Figure 6.26: Thermal shock tests: a) cold part being dipped in liquid nitrogen; b) cold part immediately after the tests before thawing back to room temperature.

subjected to 300 K down to 77 K and back to 300 K for 20 complete cycles. Figure 6.27 shows this model during one of the tests.

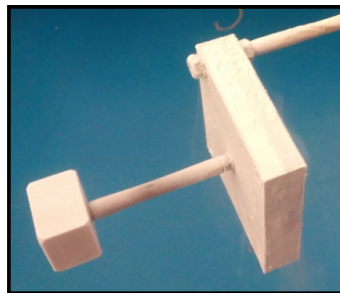


Figure 6.27: Dedicated CFRP tube dummy for thermal shock tests.

After visual inspection, both the cold part and the dummy model showed no cracks or faults, indicating the CFRP tubes are able to withstand thermal shock without visible losses in structural integrity.

6.4.4 Thermal cycling of RT canister

The metal hydride canister was subjected to thermal cycling tests, carried out at the LABET laboratory at Instituto de Soldadura e Qualidade (ISQ) in Castelo Branco. The test was performed with the canister charged with the same amount (1 mol) of hydrogen used for the ESU performance tests, to verify if the hydrogen pressure remained below the proof pressure when the canister temperature was raised to 60 °C, and also because this helps protect the metal hydride against contamination. Prior to the thermal cycling at ISQ, pressure measurements were performed on the canister (with hydrogen inside) for different temperatures: the results are shown in Figure 6.28. For the temperature range of the thermal cycling tests the hydrogen pressure remains well below the proof pressure, and as such the tests were considered safe to perform.

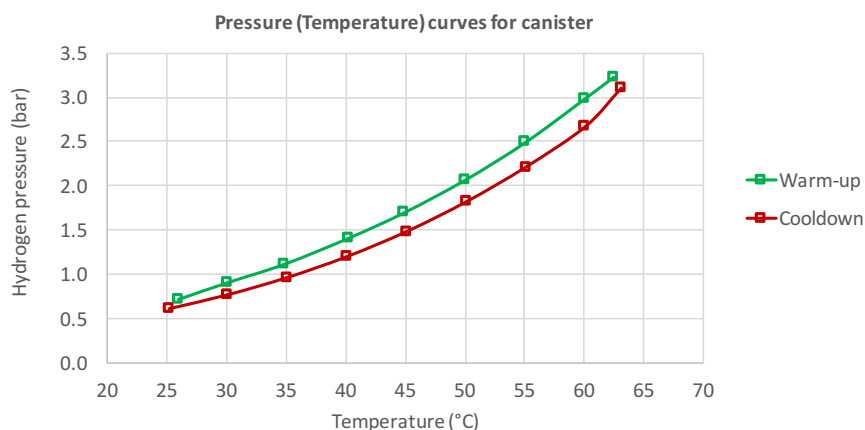


Figure 6.28: Measurements of the hydrogen pressure inside the canister as a function of temperature, for a content of 1 mol of hydrogen.

The canister, along with the resistive heaters, wiring and dedicated pressure sensor (cf. Figure 5.26), was placed inside ISQ's thermal chamber filled with pure nitrogen gas to prevent oxidation on the exterior parts of the device. Then, over a period of 72 h, the canister was cycled 20 times between -20°C and 60°C , with a minimum stabilisation time of 1 h at each temperature extreme. After the test, both a visual inspection and a leak test showed no issues. Posterior tests with the canister also showed that the performance of the metal hydride was not hindered by the thermal cycling.

6.4.5 Thermal vacuum cycling of cold cell

Thermal vacuum tests consisted of cycling the cell between 270 K and 10 K for a total of 8 cycles; tests were performed with the cell assembled in the cryocooler under vacuum conditions. Figure 6.29 shows the results for this cycling test.

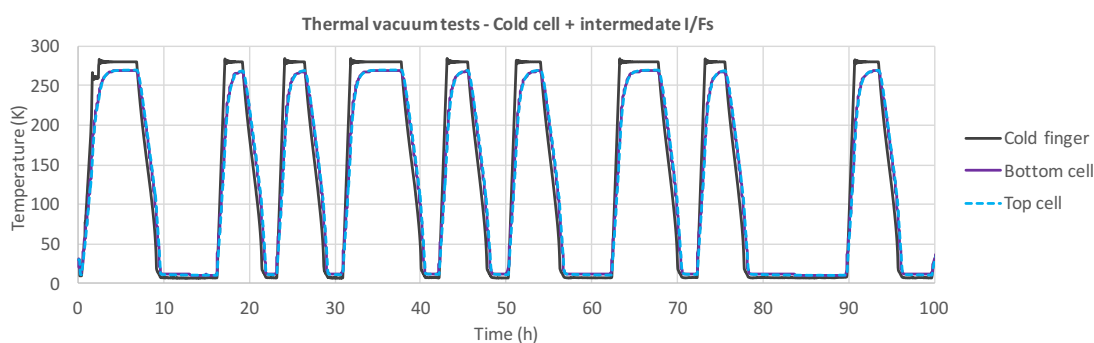


Figure 6.29: Thermal vacuum tests performed in the cold part of the system.

For the last 4 cycles, a leak test using helium as tracer gas was carried out at the same time; results are displayed in Figure 6.30.

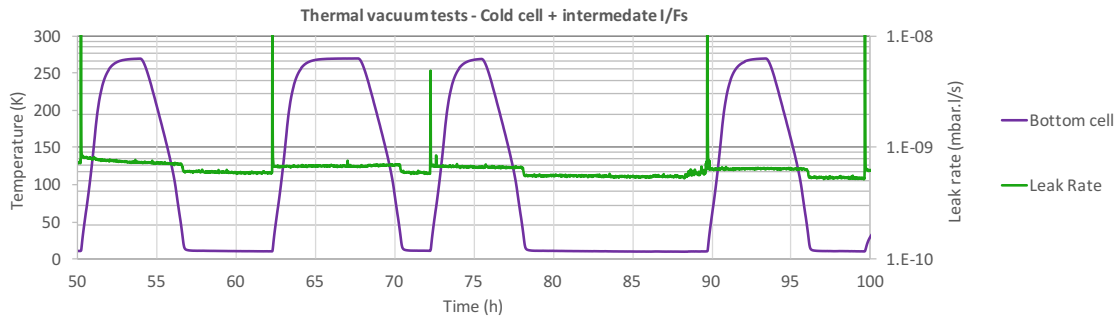


Figure 6.30: Last half of the thermal vacuum tests performed in the cold part of the system where a leak test was performed simultaneously.

Results showed a helium leak rate lower than $1 \times 10^{-9} \text{ mbar l s}^{-1}$ at both ends of the temperature range of interest; posterior visual inspection showed no discernible problems.

6.4.6 Vibrational tests

The whole system underwent a series of vibrational tests in order to test its mechanical integrity and ability to survive conditions similar to those of a satellite launch. The cold part and canister were tested separately, and they were mounted into a shaker at [AST](#) facilities. The tests consisted of a Sine Survey test to identify the frequencies of the system, followed by a Qualification Sine test and a Random Vibration test; between each one, the Sine survey was repeated to check for deviations in the resonant frequencies. The sine vibration and random vibration test levels employed are the ones specified by [ESA](#) in [ER 2 \(Appendix A\)](#); acceptance criteria was defined as follows:

- The first resonance frequency of each part shall be lower than 140 Hz;
- After the post-random sine test, the resonance frequencies shall match those detected in the pre-Random sine test within an acceptable deviation of 10%;
- After the post-random sine test, the resonance peaks shall match those detected in the pre-Random sine test within an acceptable deviation of 20%.

Figure 6.31 shows both parts of the [ESU](#) assembled and ready for testing in the shaker unit, and the results of these tests are summarised from Table 6.3 through Table 6.6.

Results show that the first resonance frequency is always above 140 Hz for either of the components, and that after both the Sine Qualification and Random Vibration tests the deviations in the resonant frequencies were below well 10%. However, measurements on the cold cell revealed a significant amplification of the shaker excitation of around 100. This leads to high acceleration peaks on the cell which could disintegrate the alumina

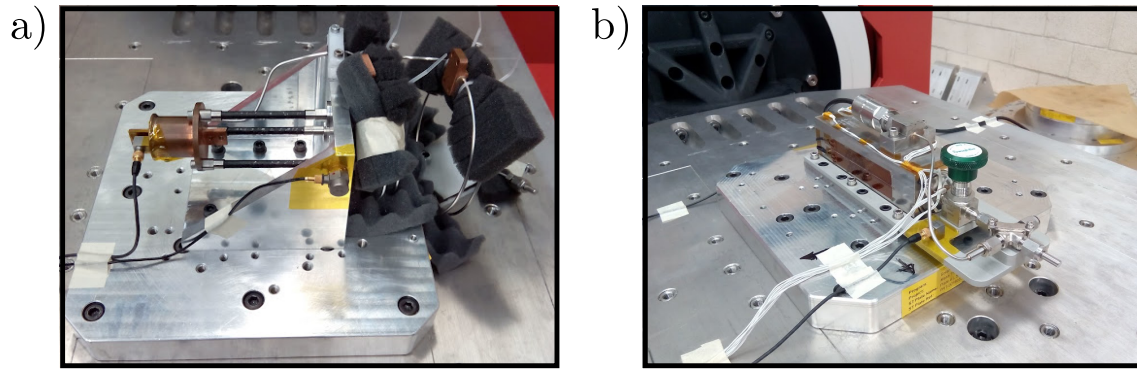


Figure 6.31: ESU ready for the vibrational tests, assembled in the shaker unit at AST: a) Cold part; b) RT canister.

Table 6.3: Vibrational test results for the cold part: Sine qualification tests.

Sine qualification tests			
Axis	Test	1 st Resonance Freq. (Hz)	Deviation (%)
X	Pre-sine	217.92	0.15
	Post-sine	217.60	
Y	Pre-sine	228.03	2.74
	Post-sine	221.78	
Z	Pre-sine	218.24	0.73
	Post-sine	219.84	

Table 6.4: Vibrational test results for the cold part: Random vibration tests.

Random vibration tests			
Axis	Test	1 st Resonance Freq. (Hz)	Deviation (%)
X	Pre-sine	217.60	0.44
	Post-sine	216.65	
Y	Pre-sine	221.78	3.73
	Post-sine	213.50	
Z	Pre-sine	219.84	0.00
	Post-sine	219.84	

Table 6.5: Vibrational test results for the canister: Sine qualification tests.

Sine qualification tests			
Axis	Test	1 st Resonance Freq. (Hz)	Deviation (%)
X	Pre-sine	675.24	0.00
	Post-sine	675.24	
Y	Pre-sine	593.67	0.00
	Post-sine	593.67	
Z	Pre-sine	585.05	0.15
	Post-sine	585.90	

Table 6.6: Vibrational test results for the canister: random vibration tests.

Random vibration tests			
Axis	Test	1 st Resonance Freq. (Hz)	Deviation (%)
X	Pre-sine	675.24	0.73
	Post-sine	670.32	
Y	Pre-sine	593.67	0.15
	Post-sine	594.54	
Z	Pre-sine	585.90	0.29
	Post-sine	585.62	

foam if its is not tightly fit to the cell walls; these results will be further discussed in the next section.

After the vibrational tests, which were considered the most critical to both parts of the system, a leak test was carried out. Figure 6.32 shows the results for the cold part and Figure 6.33 shows the results obtained for the canister. In both cases, helium was used as the tracer gas, and for the cold part the temperature was varied between 300 K and 10 K.

In both cases, the measured helium leak rate was between $1 \times 10^{-8} \text{ mbar l s}^{-1}$ and $1 \times 10^{-9} \text{ mbar l s}^{-1}$, which was considered acceptable and in line with previous leak tests.

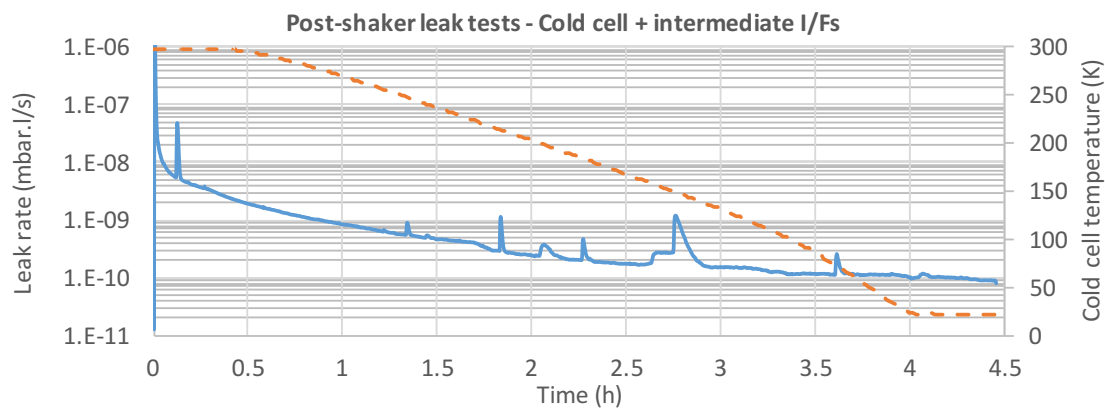


Figure 6.32: Leak test in the cold part of the ESU, using helium as tracer gas; the right-hand side of the plot shows the cell temperature (orange dashed line) during the leak test.

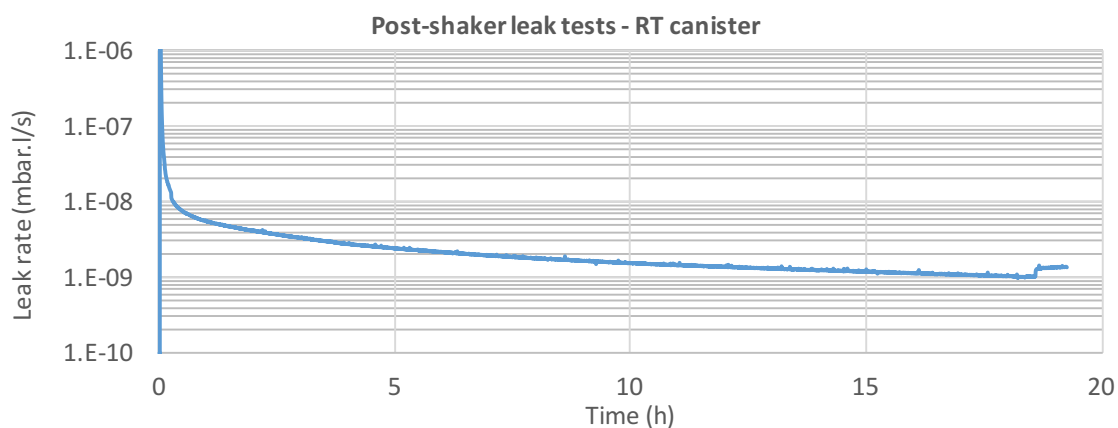


Figure 6.33: Leak test in the room temperature canister using helium as tracer gas; the test was performed at room temperature.

6.5 Functional tests

After the qualification test campaign the Engineering Model was assembled again in the cryocooler for functional testing. These tests have the objective of assessing whether the mechanical and thermal tests carried out during the qualification tests have in any way altered the performance of the ESU: experiments performed under the same conditions before and after the qualification test campaign should yield similar results. Although there was no indication of problems when first inspected, the cold part of the system was affected by the shaker tests. The ESU was set up using a 6 ℓ expansion volume, and hydrogen was allowed to condense until a 85% liquid filling ratio was achieved. The condensation process went as expected without any noticeable issues. Then a 0.5 W heat load was applied to the cold cell: results are shown in Figure 6.34.

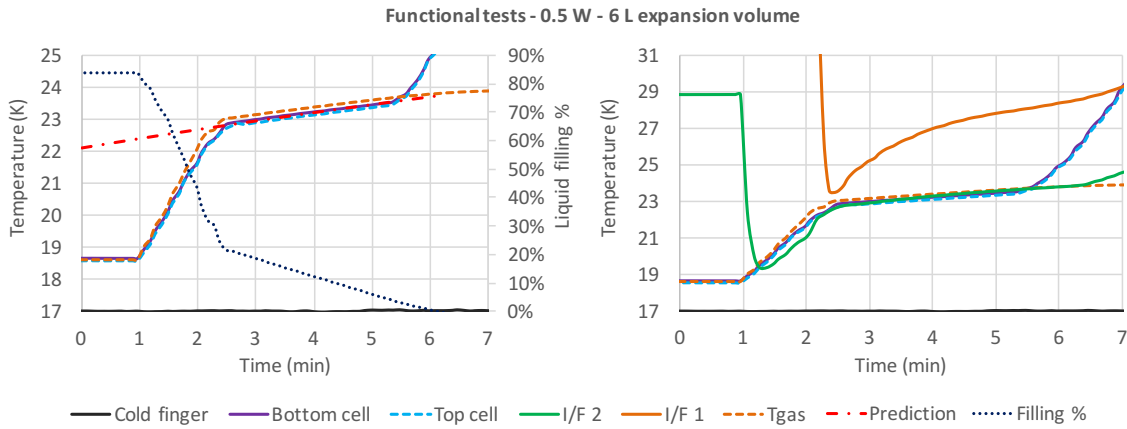


Figure 6.34: Functional test performed after the qualification test campaign using a 6 ℓ expansion volume, with an applied heat load of 0.5 W.

For this experiment only a total amount of 130 J was stored. Results show that the temperature increased abruptly from $t = 1$ min to 2.5 min, and that during this time the liquid level in the cell decreases rapidly: this means that during this period of time the liquid hydrogen was spilled out of the cell, a hypothesis that is corroborated by the fast and pronounced drop in temperature of I/Fs 1 and 2 which does not occur during a normal evaporation phase. From $t = 2.5$ min onwards, the cold cell temperature profile starts to behave as expected, but the model indicates that this only happened for a liquid filling ratio lower than $\approx 22\%$. This could mean that the porous material inside the cell is no longer confining the same amount of liquid. Posterior analysis of the results led to the cold cell being opened to check for issues with the alumina foam: Figure 6.35 shows what was observed.

The alumina foam inside the cell suffered quite some damage, disintegrating and collapsing on itself in the process: the cold cell was filled with a single block of alumina, originally filling it to the top; as shown in Figure 6.35, this is no longer the case. This

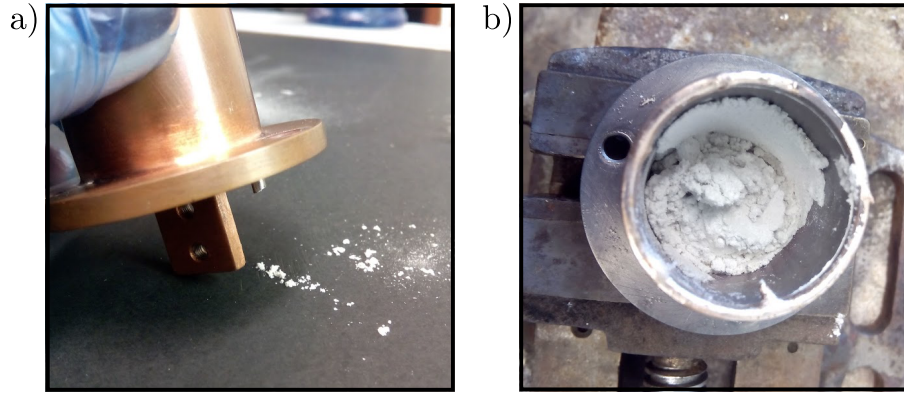


Figure 6.35: EM cold cell after preliminary functional tests: a) exhaust capillary was cut and alumina powder can be seen exiting the cell; b) open cell, where what is left of the alumina foam can be seen as powder.

lead, among loss of liquid confinement capacity, to the formation of alumina powder that formed an obstruction in the capillary. Because of the low mass of the alumina foam (≈ 2 g), this phenomenon was not detected during the shaker tests as it did not lead to a significant change in the system's resonance frequency.

A different alumina foam with greater mechanical integrity, KVR 174-402, was fitted inside the cell to test whether it could withstand the vibrational tests without significant loss of performance: Figure 6.36 depicts SEM images of the porous ceramic's structure. The mean pore size is $\approx 50\mu\text{m}$, rendering it suitable for liquid hydrogen confinement.

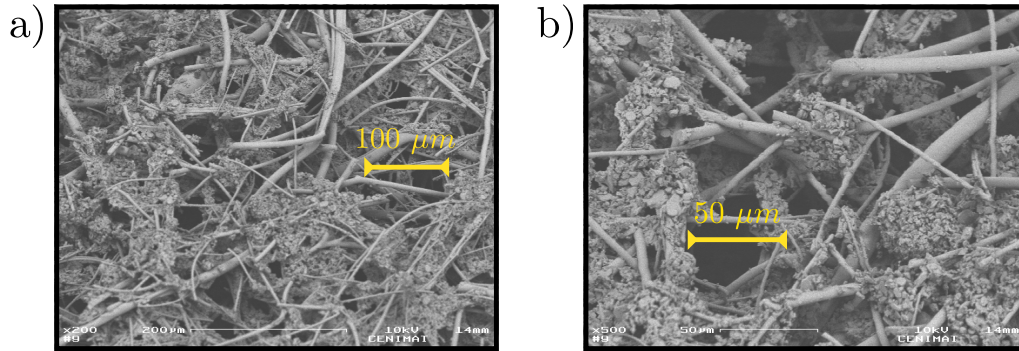


Figure 6.36: SEM images of alumina foam KVR 174-402; its structure can be seen as well as the mean “pore” size; a) scale: $200\mu\text{m}$; b) scale: $50\mu\text{m}$.

Due to timing constraints on the project, this “new” cell + alumina foam set-up was not tested regarding its thermal performance (*i.e.* no ESU mode experiments were carried out) prior to the vibrational tests. As a matter of fact, this type of ceramic has always been found to adequately retain cryogenic liquids considering its mean pore size of $50\mu\text{m}$ to $100\mu\text{m}$; as such, this configuration was *a priori* apt for being used regarding expected thermal performance. The cold part of the system (cell, CFRP tubes and filling capillary) underwent vibrational tests again, and the “new” cell + alumina foam set-up was tested

both with the 6 ℓ expansion volume and the metal hydride canister; Figure 6.37 illustrates an experiment with the 6 ℓ volume where a constant heat load of 0.5 W was applied, with a liquid filling ratio of 86%.

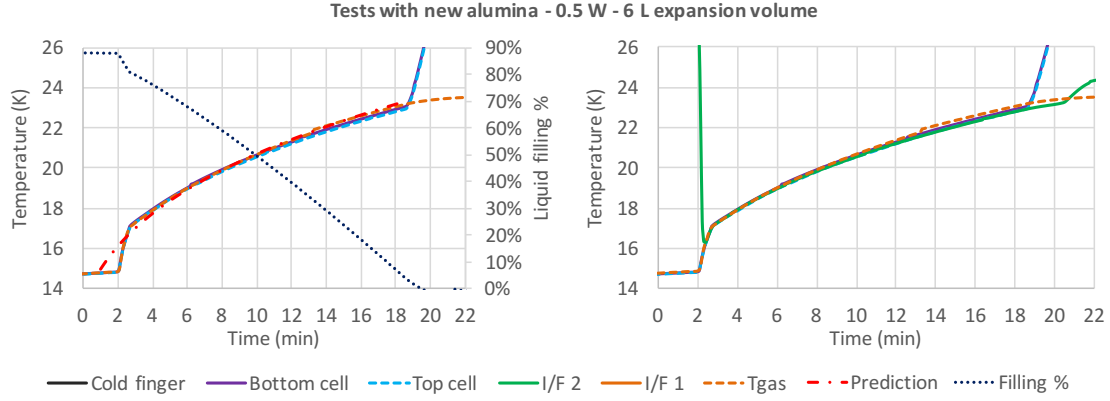


Figure 6.37: Post-shaker experiment with 0.5 W constant heat load applied, using the EM cold cell with new alumina foam and a 6 ℓ expansion volume.

During this experiment 500 J were stored. Results show that the temperature increased abruptly at the beginning of the experiment along with a fast liquid filling ratio decrease, meaning that there was still some liquid that was spilled out of the cell; however, the amount of liquid spilled (less than 10%) is far smaller what was observed in Figure 6.34 with the other foam ($\approx 70\%$): the new alumina foam was able to confine liquid starting from an 85% filling ratio. Although the temperature of I/F 2 dropped suddenly as a consequence of the initial spill, the amount of liquid was not large enough to cause the temperature of I/F 1 to drop, as had happened during testing with the other alumina foam. The rest of the experiment went as predicted, showing a good agreement with the model: this was considered a good enough result and testing proceeded with the metal hydride canister.

Figure 6.38 shows an experiment where the HLP was applied to the cold cell with the new alumina foam, using the canister for storing hydrogen gas. After the HLP ended, an additional 200 mW were applied to assess the amount of liquid left inside the cell; during this experiment a total of 440 J was stored. An initial spill (from 14.5 K to 15 K) can still be seen, but had very to little impact on the overall performance of the ESU: it successfully absorbed over 400 J during the HLP as requested within specifications. The amount of time spent above 16 K was less than 6 min, even less than previously shown: this is due to the fact that the canister, and hence the cell, were pre-cooled to a lower starting temperature.

The experiments with the new alumina foam are a major result since they demonstrate that the ESU can perform as expected even after the vibrational tests. The first attempts with the KVR 164-242 ceramic foam proved that, although it worked well during the operational tests, it was heavily damaged after the test campaign, namely by the shaker

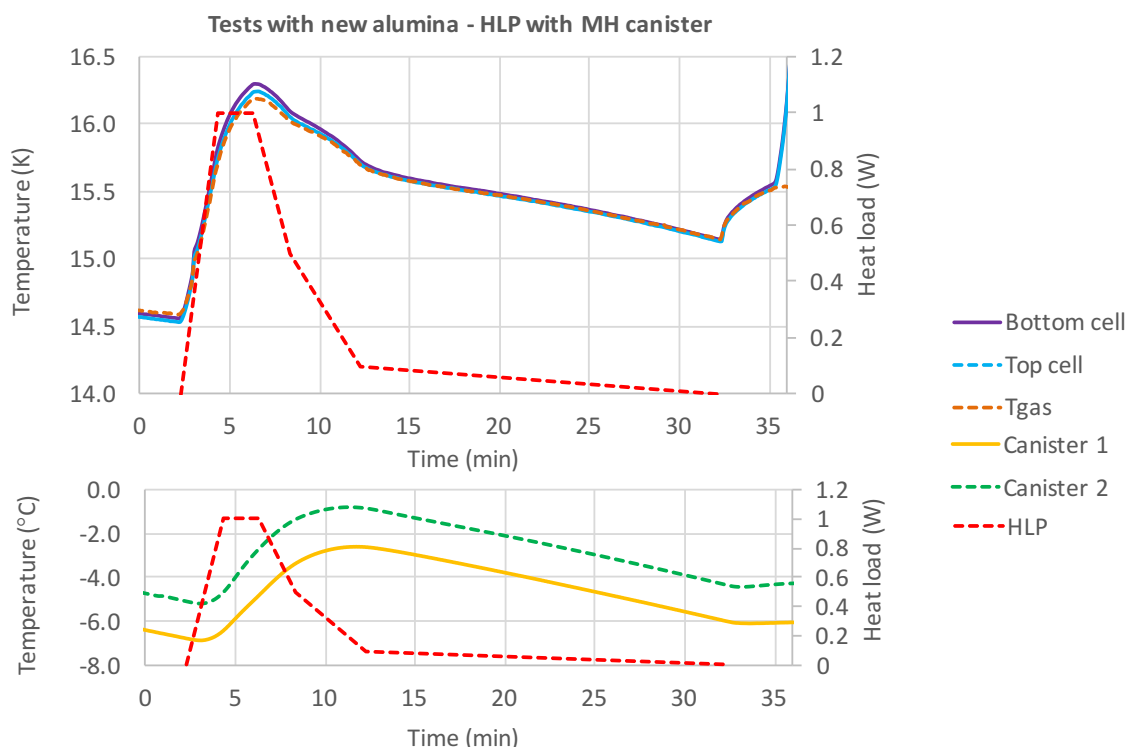


Figure 6.38: Post-shaker experiment with the HLP applied to the cold cell, using the EM cold cell with new alumina foam and the metal hydride canister.

tests: these tests hindered the performance of the ESU in such a way that operation was not possible as not enough energy was stored during a heat absorption phase due to the fact that most of the liquid was spilled from the cell. Tests with the new KVR 174-402 ceramic foam show that it was “only” a matter of structural integrity of the foam itself, and using a denser and rigid foam proved sufficient for the ESU to pass the qualification tests successfully with a performance that complies with every specification.

As a remark, it should be noted that similar ceramic foams have already gone through more severe qualification tests: as a matter of fact, the sorption evaporator used in the ^3He cooler on-board Herschel relied on this type of ceramic for liquid confinement, and the cooler was able to pass all kinds of tests, including the actual launch, without failure. In our opinion, the most important (and sensitive) step when using these materials is to devise a procedure for fitting the ceramic inside the cold cell that avoids any movement of the ceramic during the vibrational tests. If movement is restricted to an absolute minimum, the mechanical resistance of the material itself should be enough to avoid any structural degradation; however, if the ceramic material is allowed to move inside the cell, the friction between the cell walls and the ceramic during vibration is enough to provoke a catastrophic process that leads to the complete destruction of the material, as shown in Figure 6.35. This problem was solved due to the use of a sturdier ceramic coupled to a better fit inside the cell, and the results shown throughout this chapter demonstrate that

this ESU using a small liquid hydrogen cell at low temperature and a canister filled with $\text{LaNi}_{4.8}\text{Sn}_{0.2}$ to chemically absorb hydrogen is very effective in its objective of absorbing heat bursts and that it can be used even in an environment as severe as a satellite.

7 Final Remarks

This project set out to develop a liquid hydrogen Energy Storage Unit operating at 15 K that was able to absorb a 400 J heat load originated during the recycling phase of a 300 mK sorption cooler to be integrated into the projected cryogenic chain of X-IFU in ESA's new satellite, ATHENA. The ESU would allow for the sorption/ADR cooler to regenerate faster, leading to an improved duty cycle and hence for an extension of the operational time of X-IFU's detectors, and would also provide a more stable temperature to the Joule-Thomson stage of the cryogenic chain. This was a challenging undertaking, as the ESU needed to comply with several thermal and mechanical requirements from ESA in order to be considered for space applications. These included a limited and rather low cooling power at each of the available interfaces, the ability to operate under micro-gravity conditions, a strict mass and volume budget and severe mechanical tests to assess its ability to survive launch conditions.

Two complete and separate systems were developed: the Development Model, a highly customisable device designed for preliminary testing and validation of separate components, and the Engineering Model, a finely-tuned version of the previous model that was designed taking the lessons learnt from preliminary testing with the DM into account. Experimental results showed that the ESU was able to absorb a heat load of 400 J over a variable heating power with peaks that reached 1 W over a baseline cooling power of 15 mW. With the metal hydride canister, the cold cell temperature reached a maximum temperature of ≈ 16.5 K during the HLP and where less than 10 min were spent above 16 K. This significantly helps reduce the impact of the regeneration of the sorption/ADR cooler on the other stages of the cryogenic chain, namely the JT cooler. The regeneration process was closely monitored regarding heat loads and duration, and it has been shown that full condensation can be achieved in under 24 h without exceeding the allowed heat loads at the three thermal interfaces of the ESU. Testing with both models proved the desired performance respecting all of the given requirements, as well as much needed reproducibility for a system that is expected to work in space conditions for at least 5 years. Although the tests were not extensive in the number of cycles performed, the effects of ageing and degradation on the most sensitive part of this system, the metal hydride

canister, have already been studied for the sorption cryocooler on board Planck.

A metal hydride canister was developed to answer the need for a compact solution for hydrogen gas storage at room temperature, replacing the usual expansion volumes that have traditionally been used in dual-volume liquid-to-vapour enthalpy reservoirs. For the heat load at low temperature to be absorbed with a maximum temperature increase from 15 K to 17 K with no more than 10 min spent above 16 K an expansion volume of over 100 ℓ would be necessary, rendering this a rather cumbersome solution not viable for space applications. This expansion volume was one of the major drawbacks of liquid-to-vapour Energy Storage Units, and to our knowledge this is the first time that a compact metal hydride canister has been employed for gas storage in such a type of device. The price to pay for this otherwise elegant solution is the increased complexity of the system at room temperature: this includes thermometry, a cooling source (that in space could be a 20 cm \times 20 cm radiator) and ON/OFF control of the canister heaters that would need to be included. While manageable, it is a significant step towards compactness when compared to a simple and completely passive expansion volume. Despite this, the metal hydride canister passed all performance and mechanical tests in a relevant environment, and this type of configuration has already been flown on-board Planck to successful results under much worse conditions, such as heating up to 470 K in cycles that lasted only 700 s. Thanks to the use of metal hydrides, the pressure can be controlled by controlling the canister temperature, meaning that there are no moving parts; this is a departure from previous works at the laboratory that employed pressure control valves to achieve pressure/temperature control. Metal hydrides also enable the ESU to be used as a temporary cold source by pumping the liquid hydrogen bath down to temperatures slightly above 14 K: this can be useful for the Joule-Thomson pre-cooling stage, as even a small temperature decrease in the JT stage can significantly help the performance of the cryogenic chain.

It has been the first time that the Energy Storage Units developed at the laboratory underwent relevant qualification testing in order to achieve a TRL 5, namely relevant mechanical environment testing such as the vibration tests and continuous cycling. The system was also tested in an anti-gravity configuration throughout all the main experiments in order to prove operation in a micro-gravity environment. This type of system using hydrogen in alumina foams for liquid confinement needed to be slightly tilted by some degrees in order for it to work in previous experiments such as in the sorption cooler developed at CEA/SBT, while the hydrogen ESU was able to show its performance in a situation of complete anti-gravity.

Further improvements could be made to the system for an eventual flight model. These include an optimisation of the canister geometry to promote better heat transfer between the metallic alloy and the canister body: any improvement in maintaining the metal hydride temperature near or slightly below 273 K during the heat absorption phase would reduce the pressure and hence the temperature increase of the cold cell. Taken to a case of extremely efficient heat transfer, the metal hydride temperature could be

kept constant which would lead to a liquid hydrogen cell capable of absorbing 400 J at an almost constant temperature of 15 K, the limiting factor being only the flatness of the pressure plateaus of the metallic alloy. While the addition of aluminium foam to the inside of the canister aimed to uniformise the temperature of the metal hydride, other options might yield better results such as using expanded graphite mixed with the metal hydride powder. This expanded graphite method has been used by the [CNRS](#) group and produced satisfactory results. New and more structurally sound porous materials with pores in the 100 μm to 200 μm range with a high void volume percentage should also be investigated for liquid confinement, since the alumina foam can be considered too fragile when simulating launch conditions. A material with a more defined pore structure would also allow for capillary action calculations that could better describe the real behaviour of the porous matrix. These improvements, along with more specific and severe testing, are needed if the [ESU](#) is expected to reach higher [TRLs](#) up to [TRL 8](#) where it can be deemed “flight qualified” and have a chance of integrating [X-IFU](#)’s cryogenic chain.

Space observation and science missions will continue to exist and will be increasingly more exigent on the requirements for their payload. As new and better detectors are developed, cryogenics will continue to be a part of the solution (again, a “necessary evil”) for these missions that require lower and more stable temperatures: the tendency will be for more complex and intricate cryogenic chains. We hope that the work described throughout this thesis is a step towards helping solve some of these issues by providing a stabilising “block” in these ever more sophisticated systems.

References

- [1] G. Ventura and L. Risegari. *The Art of Cryogenics: Low-Temperature Experimental Techniques*. Elsevier Science, 2010. ISBN: 978-0-08-044479-6.
- [2] Yale News. *Yale system are key to coldest cubic meter experiment*. [online; accessed 20-11-2015]. URL: <http://news.yale.edu/2014/10/20/yale-systems-are-key-coldest-cubic-meter-experiment>.
- [3] Aalto University - O.V. Lounasmaa Laboratory. *World Record in Low Temperatures*. [online; accessed 20-11-2015]. URL: http://ltl.tkk.fi/wiki/LTL/World_record_in_low_temperatures.
- [4] P. Shirron. “50 years of progress in space cryogenics”. In: *Cold Facts vol. 30 number 1* (2014), pp. 20–22.
- [5] M. Linder, N. Rando, A. Peacock, and B. Collaudin. “Cryogenics in space: a review of the missions and of the technologies”. In: *ESA Bulletin 107* 40.12 (2001), pp. 797–819.
- [6] L. Duband. “Space Cryocooler Developments”. In: *Physics Procedia* 67 (2015). Proceedings of the 25th International Cryogenic Engineering Conference and International Cryogenic Materials Conference 2014, pp. 1–10. DOI: [10.1016/j.phpro.2015.06.003](https://doi.org/10.1016/j.phpro.2015.06.003).
- [7] P. Shirron. “Low temperature cooling for space missions: from mechanical coolers to sub-kelvin cooling”. In: *Proc. ICEC 24, 2012, Fukuoka, Japan*. 2012, pp. 9–16.
- [8] European Space Agency. *Athena to study the hot and energetic universe*. [online; accessed 06-11-2015]. URL: <http://sci.esa.int/cosmic-vision/54241-athena-to-study-the-hot-and-energetic-universe/>.
- [9] N. Luchier, J. Duval, L. Duband, and T. Tirolien. “Performances of the 50 mK ADR/sorption cooler”. In: *Cryogenics* 52.4–6 (2012). 2011 Space Cryogenics Workshop, pp. 152–157. DOI: [10.1016/j.cryogenics.2012.01.029](https://doi.org/10.1016/j.cryogenics.2012.01.029).
- [10] European Space Agency. *ESA Science & Technology: ATHENA*. [online; accessed 26-11-2015]. URL: <http://sci.esa.int/cosmic-vision/54517-athena/>.

- [11] L. Ravera et al. “The X-ray Integral Field Unit (X-IFU) for Athena”. In: vol. 9144. 2014, pp. 91442L–91442L–13. DOI: [10.1117/12.2055884](https://doi.org/10.1117/12.2055884).
- [12] K. Nandra, X. Barcons, J.-W. den Herder, M. Watson, D. Barret, A. Fabian, and L. Piro. *The Advanced Telescope for High-Energy Astrophysics*. Mission Proposal. 2012. URL: http://userpages.irap.omp.eu/~dbarret/ATHENA/The_Athena_Mission_Proposal.pdf.
- [13] ATHENA. *ATHENA+ X-Ray Observatory: INSTRUMENTS*. [online; accessed 10-01-2016]. URL: <http://athena2.irap.omp.eu/spip.php?rubrique2>.
- [14] B. Collaudin and N. Rando. “Cryogenics in space: a review of the missions and of the technologies”. In: *Cryogenics* 40.12 (2000), pp. 797–819. DOI: [10.1016/S0011-2275\(01\)00035-2](https://doi.org/10.1016/S0011-2275(01)00035-2).
- [15] S. Triqueneaux, L. Sentis, P. Camus, A. Benoit, and G. Guyot. “Design and performance of the dilution cooler system for the Planck mission”. In: *Cryogenics* 46.4 (2006), pp. 288–297. DOI: [10.1016/j.cryogenics.2005.12.004](https://doi.org/10.1016/j.cryogenics.2005.12.004).
- [16] P. Camus, G. Vermeulen, A. Volpe, S. Triqueneaux, A. Benoit, J. Butterworth, S. D’Escrivan, and T. Tirolien. “Status of the Closed-Cycle Dilution Refrigerator Development for Space Astrophysics”. In: *Journal of Low Temperature Physics* 176.5-6 (2013), pp. 1069–1074. DOI: [10.1007/s10909-013-1001-8](https://doi.org/10.1007/s10909-013-1001-8).
- [17] L. Duband, L. Clerc, E. Ercolani, L. Guillemet, and R. Vallcorba. “Herschel flight models sorption coolers”. In: *Cryogenics* 48.3-4 (2008), pp. 95–105. DOI: [10.1016/j.cryogenics.2008.03.016](https://doi.org/10.1016/j.cryogenics.2008.03.016).
- [18] L. Duband, J. Duval, and N. Luchier. “SAFARI engineering model 50mK cooler”. In: *Cryogenics* 64 (2014), pp. 213–219. DOI: [10.1016/j.cryogenics.2014.02.008](https://doi.org/10.1016/j.cryogenics.2014.02.008).
- [19] N. Luchier, J. Duval, L. Duband, P. Camus, G. Donnier-Valentin, and M. Linder. “50 mK cooling solution with an {ADR} precooled by a sorption cooler”. In: *Cryogenics* 50.9 (2010). 2009 Space Cryogenic Workshop, pp. 591–596. DOI: [10.1016/j.cryogenics.2010.02.022](https://doi.org/10.1016/j.cryogenics.2010.02.022).
- [20] J. Duval, N. Luchier, L. Duband, and T. Tirolien. “Progress in the Development of the IXO 50 mK Sorption-ADR stage”. In: *16th International Cryocooler Conference*. Boulder, CO, 2011, pp. 537–546. URL: <http://hdl.handle.net/1853/39673>.
- [21] D. Bugby and B. Marland. “Cryogenic Thermal Storage Units”. In: *Spacecraft Thermal Control Handbook, Volume II: Cryogenics*. 2nd. The Aerospace Press, 2003. Chap. 17, pp. 409–432. ISBN: 1-884989-14-4.
- [22] E. Gopal. *Specific Heats at Low Temperatures*. 1st ed. Springer US, 1966. ISBN: 978-1-4684-9081-7.
- [23] C. Kittel. *Introduction to solid state physics*. 8th. New York, 2005. ISBN: 978-0-471-41526-8.

-
- [24] G. Bonfait, I. Catarino, J. Afonso, D. Martins, M. Linder, and L. Duband. “20K Energy storage unit”. In: *Cryogenics* 49.7 (2009), pp. 326–333. DOI: [10.1016/j.cryogenics.2009.03.003](https://doi.org/10.1016/j.cryogenics.2009.03.003).
- [25] I. Catarino, J. Afonso, D. Martins, M. Linder, L. Duband, and G. Bonfait. “6K solid state Energy Storage Unit”. In: *Cryogenics* 50.2 (2010), pp. 102–110. DOI: [10.1016/j.cryogenics.2009.12.002](https://doi.org/10.1016/j.cryogenics.2009.12.002).
- [26] E. Marquardt, J. Le, and R. Radebaugh. “Cryogenic Material Properties Database”. In: *11th International Cryocooler Conference* 12.6 (2000), pp. 1–7. DOI: [10.1016/0142-1123\(90\)90249-E](https://doi.org/10.1016/0142-1123(90)90249-E).
- [27] National Institute of Standards and Technology. *Regenerator Materials Properties*. [online; accessed 17-11-2015]. URL: <http://www.cryogenics.nist.gov/MPPropsMAY/RegeneratorMaterials/RegenPlot.htm>.
- [28] K. A. Gschneidner Jr., A. O. Pecharsky, V. K. Pecharsky, K. A. Gschneidner, A. O. Pecharsky, and V. K. Pecharsky. “Development of New Cryocooler Regenerator Materials — Ductile Intermetallic Compounds”. In: *Cryocoolers 13 SE - 47*. Ed. by R. Ross Jr. Springer US, 2005, pp. 363–371. DOI: [10.1007/0-387-27533-9{_}47](https://doi.org/10.1007/0-387-27533-9{_}47).
- [29] B. G. Williams and I. E. Spradley. “Test Results of a Nitrogen Triple-Point Thermal Storage Unit”. In: *Cryocoolers 10 SE - 82*. Ed. by R. G. Ross Jr. Springer US, 2002, pp. 697–706. DOI: [10.1007/0-306-47090-X{_}82](https://doi.org/10.1007/0-306-47090-X{_}82).
- [30] I. Charles, A. Coynel, and C. Daniel. “Thermal Storage Unit Using the Triple Point of Hydrogen”. In: *16th International Cryocooler Conference*. 2008, pp. 575–582. URL: <http://hdl.handle.net/1853/39677>.
- [31] E. Lemmon, M. Huber, and M. McLinden. *NIST Standard Reference Database 23: Reference Fluid Thermodynamic and Transport Properties - REFPROP, version 9.1*. Gaithersburg, 2013.
- [32] T. M. Flynn. *Cryogenic Engineering, Second Edition, Revised and Expanded*. CRC Press, 2004. ISBN: 978-0-8247-5367-2.
- [33] J. Afonso, I. Catarino, R. Patrício, A. Rocaboy, M. Linder, and G. Bonfait. “Liquid nitrogen energy storage unit”. In: *Cryogenics* 51.11-12 (2011), pp. 621–629. DOI: [10.1016/j.cryogenics.2011.09.008](https://doi.org/10.1016/j.cryogenics.2011.09.008).
- [34] J. Afonso, D. Martins, I. Catarino, R. Patrício, A. Rocaboy, T. Tirolen, and G. Bonfait. “Liquid–gas cryogenic energy storage units operating at constant temperature”. In: *Applied Thermal Engineering* 95 (2016), pp. 178 –185. DOI: [10.1016/j.applthermaleng.2015.11.059](https://doi.org/10.1016/j.applthermaleng.2015.11.059).
- [35] D. Martins, P. Borges de Sousa, I. Catarino, and G. Bonfait. “40 K Liquid Neon Energy Storage Unit”. In: *Physics Procedia* 67 (2015), pp. 1193–1198. DOI: [10.1016/j.phpro.2015.06.188](https://doi.org/10.1016/j.phpro.2015.06.188).

REFERENCES

- [36] D. Martins. “40 K Neon Liquid Energy Storage Unit”. PhD thesis. Universidade Nova de Lisboa, 2014. URL: <http://hdl.handle.net/10362/14565>.
- [37] Y. Milenko, R. Sibileva, and M. Strzhemechny. “Natural ortho-para conversion rate in liquid and gaseous hydrogen”. In: *Journal of Low Temperature Physics* 107.1 (1997), pp. 77–92. DOI: [10.1007/BF02396837](https://doi.org/10.1007/BF02396837).
- [38] D. Martins, L. Ribeiro, D. Lopes, I. Catarino, I. Esteves, J. Mota, and G. Bonfait. “Sorption characterization and actuation of a gas-gap heat switch”. In: *Sensors and Actuators A: Physical* 171.2 (2011), pp. 324–331. DOI: [10.1016/j.sna.2011.08.017](https://doi.org/10.1016/j.sna.2011.08.017).
- [39] L. Vasiliev, L. Kanonchik, A. Kulakov, and D. Mishkinis. In: *Hydrogen Materials Science and Chemistry of Carbon Nanomaterials*. Springer Netherlands, 2007, pp. 633–651. DOI: [10.1007/978-1-4020-5514-0_80](https://doi.org/10.1007/978-1-4020-5514-0_80).
- [40] J. Mota. private communication, October 2013.
- [41] B. Sakintuna, F. Lamari-Darkrim, and M. Hirscher. “Metal hydride materials for solid hydrogen storage: A review”. In: *International Journal of Hydrogen Energy* 32.9 (2007), pp. 1121–1140. DOI: [10.1016/j.ijhydene.2006.11.022](https://doi.org/10.1016/j.ijhydene.2006.11.022).
- [42] S. F. Matar. “Intermetallic hydrides: A review with ab initio aspects”. In: *Progress in Solid State Chemistry* 38.1-4 (2010), pp. 1–37. DOI: [10.1016/j.progsolidstchem.2010.08.003](https://doi.org/10.1016/j.progsolidstchem.2010.08.003).
- [43] J. Reilly. “Chemistry of intermetallic hydrides”. In: *180th meeting of the Electrochemical Society*. 1991. URL: <http://www.osti.gov/scitech/servlets/purl/6084207>.
- [44] M. Lototsky, V. Yartys, B. Pollet, and R. Bowman. “Metal hydride hydrogen compressors: A review”. In: *International Journal of Hydrogen Energy* 39.11 (2014), pp. 5818–5851. DOI: [10.1016/j.ijhydene.2014.01.158](https://doi.org/10.1016/j.ijhydene.2014.01.158).
- [45] D. Pearson, R. Bowman, M. Prina, and P. Wilson. “The Planck sorption cooler: Using metal hydrides to produce 20 K”. In: *Journal of Alloys and Compounds* 446–447 (2007). Proceedings of the International Symposium on Metal-Hydrogen Systems, Fundamentals and Applications (MH2006), pp. 718 –722. DOI: [10.1016/j.jallcom.2006.11.202](https://doi.org/10.1016/j.jallcom.2006.11.202).
- [46] G. Morgante, D. Barber, P. Bhandari, R. C. Bowman Jr., P. Cowgill, D. Crumb, T. Loc, A. Nash, D. Pearson, M. Prina, A. Sirbi, M. Schemlzel, R. Sugimura, and L. A. Wade. “Two hydrogen sorption cryocoolers for the Planck mission”. In: *AIP Conference Proceedings* 616.1 (2002), pp. 298–302. DOI: [10.1063/1.1475648](https://doi.org/10.1063/1.1475648).
- [47] R. Bowman Jr., C. Luo, C. Ahn, C. Witham, and B. Fultz. “The effect of tin on the degradation of LaNi₅-ySn metal hydrides during thermal cycling”. In: *Journal of Alloys and Compounds* 217.2 (1995), pp. 185 –192. DOI: [10.1016/0925-8388\(94\)01337-3](https://doi.org/10.1016/0925-8388(94)01337-3).

- [48] F. Laurencelle, Z. Dehouche, and J. Goyette. "Hydrogen sorption cycling performance of $\text{LaNi}_{4.8}\text{Sn}_{0.2}$ ". In: *Journal of Alloys and Compounds* 424.1-2 (2006), pp. 266–271. DOI: [10.1016/j.jallcom.2005.11.085](https://doi.org/10.1016/j.jallcom.2005.11.085).
- [49] P. Bhandari, R. Bowman, R. Chave, C. Lindensmith, G. Morgante, C. Paine, M. Prina, and L. Wade. "Sorption Cryocooler Development for the Planck Surveyor Mission". In: *Astrophysical Letters and Communications* 37 (2000), p. 227. URL: <http://adsabs.harvard.edu/full/2000ApL%26C..37..227B>.
- [50] G. Sandrock. "A panoramic overview of hydrogen storage alloys from a gas reaction point of view". In: *Journal of Alloys and Compounds* 293–295 (1999), pp. 877–888. DOI: [10.1016/S0925-8388\(99\)00384-9](https://doi.org/10.1016/S0925-8388(99)00384-9).
- [51] European Space Agency. *Statement of Work: Hydrogen liquid-gas-phase Energy Storage Unit operating between 15-20 K*. ESA contract 4000108532/NL/E. 2012.
- [52] J. Afonso. "Unidade criogénica de armazenamento de energia com mudança de fase". MSc thesis. Universidade Nova de Lisboa, 2009. URL: <http://hdl.handle.net/10362/2298>.
- [53] MatWeb - Material Property Database. *Oxygen-free electronic Copper*. [online; accessed 12-01-2016]. URL: <http://www.matweb.com/search/DataSheet.aspx?MatGUID=25cdd9bd3ebb4941be91cb0bee4cc661>.
- [54] MatWeb - Material Property Database. *Copper, Cu; Annealed*. [online; accessed 12-01-2016]. URL: <http://www.matweb.com/search/datasheettext.aspx?matguid=9aebe83845c04c1db5126fada6f76f7e>.
- [55] S. H. Castles and M. E. Schein. "Development of a Space Qualified Surface Tension Confined Liquid Cryogen Cooler (STCLCC)". In: *Advances in Cryogenic Engineering SE - 99*. Ed. by R. Fast. Vol. 33. A Cryogenic Engineering Conference Publication. Springer US, 1988, pp. 819–826. DOI: [10.1007/978-1-4613-9874-5_{99}](https://doi.org/10.1007/978-1-4613-9874-5_{99}).
- [56] R. Nussle, E. Otto, and D. Petrash. *Effect of contact angle and tank geometry on the configuration of the liquid-vapor interface during weightlessness*. Technical report NASA-TN-D-2075. 1963. URL: <http://ntrs.nasa.gov/search.jsp?R=19630013804>.
- [57] C. Siegert, D. Petrash, and E. Otto. *Behavior of Liquid-vapor Interface of Cryogenic Liquids During Weightlessness*. NASA technical note D-2658. National Aeronautics and Space Administration, 1965. URL: <https://searchworks.stanford.edu/view/8599487>.
- [58] National Institute of Standards and Technology. *Cryogenics Materials Properties*. [online; accessed 12-01-2016]. URL: <http://cryogenics.nist.gov/MPropsMAY/material%20properties.htm>.
- [59] Lakeshore Cryotronics. *Appendix I: Cryogenic Reference Tables*. [online; accessed 12-01-2016]. URL: http://www.lakeshore.com/Documents/LSTC_{appendixI}_{1}.pdf.

REFERENCES

- [60] Z. S. Spakovszky. *Unified Thermodynamics and Propulsion*. [lecture notes; accessed 05-02-2016]. URL: <http://web.mit.edu/16.unified/www/FALL/thermodynamics/notes/node131.html>.
- [61] F. Incropera. *Fundamentals of heat and mass transfer*. 6th. John Wiley, 2007. ISBN: 9780471457282.
- [62] Wolfram Mathworld. *Sphere Packing*. [online; accessed 14-01-2016]. URL: <http://mathworld.wolfram.com/SpherePacking.html>.
- [63] I. Catarino, G. Bonfait, and L. Duband. “Neon gas-gap heat switch”. In: *Cryogenics* 48.1–2 (2008), pp. 17–25. DOI: 10.1016/j.cryogenics.2007.09.002.
- [64] R. Bowman Jr. “Development of metal hydride beds for sorption cryocoolers in space applications”. In: *Journal of Alloys and Compounds* 356–357 (2003). Proceedings of the Eighth International Symposium on Metal-Hydrogen Systems, Fundamentals and Applications (MH2002), pp. 789–793. DOI: 10.1016/S0925-8388(03)00089-6.
- [65] MatWeb - Material Property Database. *Aluminum 6061-T6; 6061-T651*. [online; accessed 05-02-2016]. URL: <http://www.matweb.com/search/DataSheet.aspx?MatGUID=25cdd9bd3ebb4941be91cb0bee4cc661>.
- [66] MatWeb - Material Property Database. *304 Stainless Steel*. [online; accessed 05-02-2016]. URL: <http://www.matweb.com/search/DataSheet.aspx?MatGUID=25cdd9bd3ebb4941be91cb0bee4cc661>.
- [67] W. Giauque and J. Stout. “The Entropy of Water and the Third Law of Thermodynamics: The Heat Capacity of Ice from 15 to 273 K”. In: *Journal of the American Chemical Society* 58.7 (1936), pp. 1144–1150. DOI: 10.1021/ja01298a023.
- [68] R. Reed, F. Fickett, L. T. Summers, and M. Stieg. *Advances in Cryogenic Engineering Materials: Volume 40 Part A*. Springer US, 1994. DOI: 10.1007/978-1-4757-9053-5.

A Requirements

The following information was retrieved from “Statement of Work: Hydrogen liquid-gas-phase Energy Storage Unit operating between 15-20 K” [51], a document prepared by [ESA](#) in the framework of the project. It describes the various requirements that need to be observed when designing the [ESU](#) as well as some specifications for compliance with space-borne applications.

Table A.1: Functional & Performance Requirements.

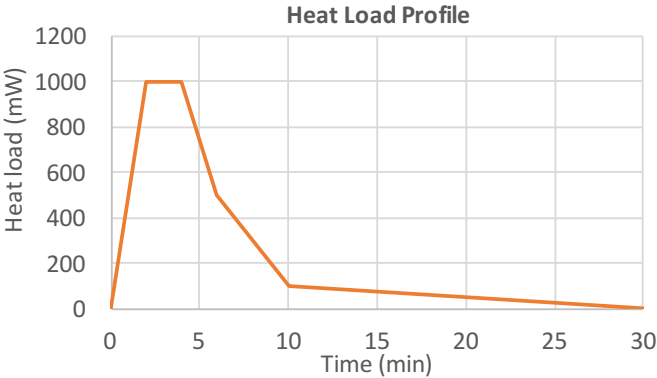
Requirement	Description														
FPR 1	<p>The ESU shall be able to absorb a heat peak of 400 J at 15 K during 30 min according to the following heat load profile:</p> <div data-bbox="568 817 1227 1193"><table border="1"><caption>Heat Load Profile Data</caption><thead><tr><th>Time (min)</th><th>Heat load (mW)</th></tr></thead><tbody><tr><td>0</td><td>0</td></tr><tr><td>2.5</td><td>1000</td></tr><tr><td>5</td><td>1000</td></tr><tr><td>6</td><td>500</td></tr><tr><td>10</td><td>200</td></tr><tr><td>30</td><td>0</td></tr></tbody></table></div>	Time (min)	Heat load (mW)	0	0	2.5	1000	5	1000	6	500	10	200	30	0
Time (min)	Heat load (mW)														
0	0														
2.5	1000														
5	1000														
6	500														
10	200														
30	0														
FPR 2	<p>The ESU shall be able to regenerate within 24 h.</p>														
FPR 3	<p>During absorption of the heat peak, the I/F temperature of the ESU shall be lower than:</p> <ul style="list-style-type: none">• 17 K with 1 W applied;• 15.5 K with 100 mW applied;• 15 K with less than 10 mW applied.														
FPR 4	<p>As a goal, the ESU shall be able to provide a temperature below 15 K during absorption of the peak</p>														
FPR 5	<p>A temperature increase above 16 K is acceptable for a duration shorter than 10 min.</p>														

Table A.2: Interface Requirements.

Requirement	Description
IR 1	Four thermal interfaces are available for the ESU , as follows: <ul style="list-style-type: none"> • Ambient I/F: 10 W at 270 K; • Intermediate I/F 1: 40 mW at 120 K; • Intermediate I/F 2: 15 mW at 25 K; • Cold I/F: 15 mW at 15 K.
IR 2	The cold I/F shall be compatible with a direct mounting on a Al or Cu thermal bus.
IR 3	Any connection between the ambient I/F and intermediate I/F 1 must be disconnect-able and routed via a vacuum-tight feed-through to enable integration into a vacuum-tight vessel at a later stage.

Table A.3: Environmental Requirements.

Requirement	Description
ER 1	The ESU shall demonstrate its performance in a 50 K radiative thermal environment.
ER 2	Mechanical environment: the ESU shall be capable of surviving the mechanical environment (Qualification Level) as follows (duration 2.5 min/axis); tying down of interconnection pipes shall be allowed.

Sine vibration			
Frequency (Hz)		Level (minimum)	Level (goal)
5 - 25 Hz		5 mm out of plane 7 mm in plane	10 mm (all directions)
25 Hz -		15 g out of plane 25 g in plane	25 g (all directions)
Sweep Rate		2 octaves/min, 1 sweep up	
Random vibration (minimum)			
	Frequency (Hz)	Level	g RMS
Normal to fixation plane	20 - 100	+3 dB/oct.	12
	100 - 200	0.4 g ² /Hz	
	200 - 300	0.2 g ² /Hz	
	300 - 2000	-5 dB/oct.	
Other axes	20 - 100	+3 dB/oct.	11.20
	100 - 200	0.1 g ² /Hz	
	200 - 300	0.25 g ² /Hz	
	300 - 2000	-5 dB/oct.	

Table A.4: Physical & Resource Requirements.

Requirement	Description
PRR 1	The overall ESU mass shall be less than 5 kg, excluding electronics.
PRR 2	The cryogenic mass of the ESU (cold reservoir and pipe/heat exchanger) shall be less than 500 g.
PRR 3	The cold volume of the ESU shall be less than: <ul style="list-style-type: none">• 0.2 ℓ at intermediate I/F 1;• 0.1 ℓ at intermediate I/F 2;• 0.1 ℓ at Cold I/F.
PRR 4	The ambient volume of the ESU shall be less than 5 ℓ.
PRR 5	The average power consumption of the ESU shall be less than 15 W.

Table A.5: Operational Requirements.

Requirement	Description
OR 1	The ESU shall be designed for a lifetime of minimum 6 years (10 year goal) in orbit, continuous operation plus 1 year for ground testing, plus 2 years storage.
OR 2	The ESU shall be able to operate on ground under any orientation and in micro-g environment.
OR 3	The ESU shall be leak tight at operating temperatures (<i>i.e.</i> the leak rate shall be less than 1×10^{-9} mbar l s ⁻¹).

Table A.6: Design Requirements.

Requirement	Description
DR 1	10% margins in energy storage capabilities shall be applied when design phase to reduce the risks.
DR 2	The ESU shall be designed to withstand an external pressure between 1 atm air and vacuum $< 10^{-4}$ Pa.
DR 3	The ESU shall be able to withstand a depressurisation profile compatible with Soyuz.
DR 4	The ESU shall not be sensitive to radiation (average value 20 K rad.).
DR 5	The contractor shall comply with national and international safety regulations of pressurised vessels and hydrogen utilisation.
DR 6	All materials used in the manufacturing of the ESU shall be compatible with hydrogen and shall be flight approved in the ECSS.
DR 7	Resonance: the ESU elements, at the exclusion of moving parts and pipework, shall be designed such that the first resonance frequency is higher than 140 Hz.
DR 8	Pressures: the ESU shall comply to ECSS-E-ST-32-02C Rev. 1.

B Useful data

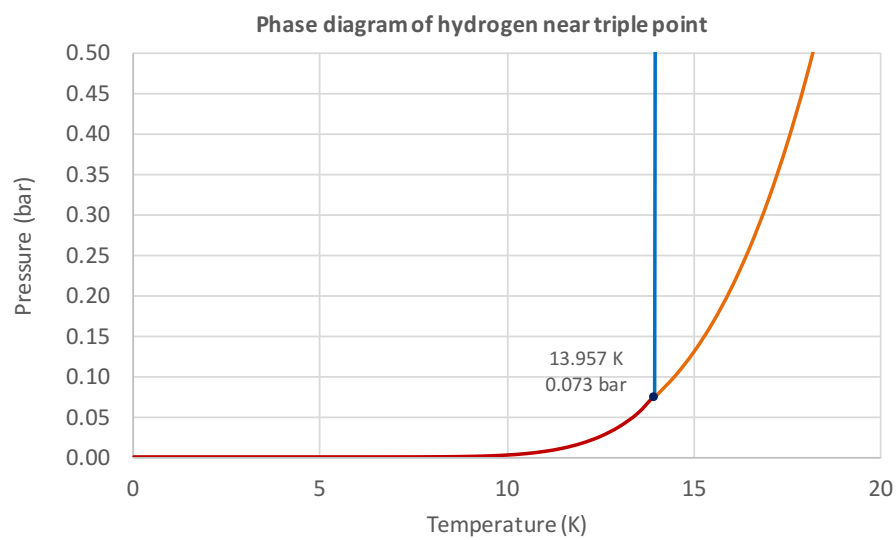


Figure B.1: Phase diagram of hydrogen near the triple point; data obtained using [REFPROP](#) [31].

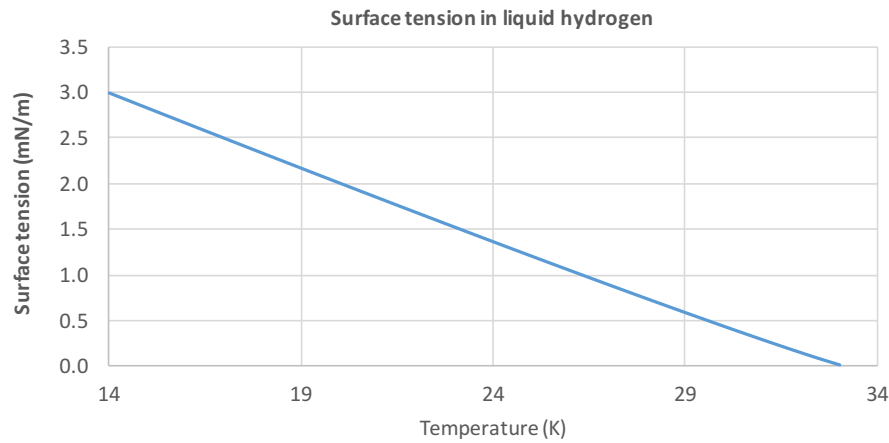


Figure B.2: Surface tension of liquid hydrogen at saturation conditions as a function of temperature; data obtained using REFPROP [31].

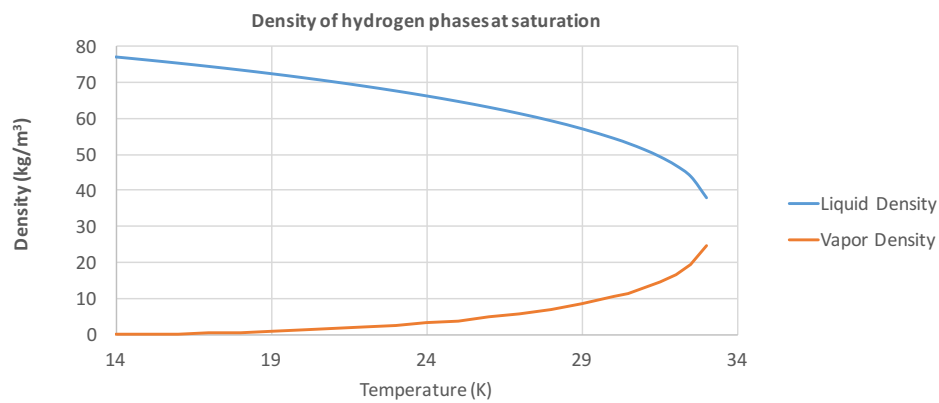


Figure B.3: Density of liquid and vapour hydrogen under saturation conditions as a function of temperature; data obtained using REFPROP [31].

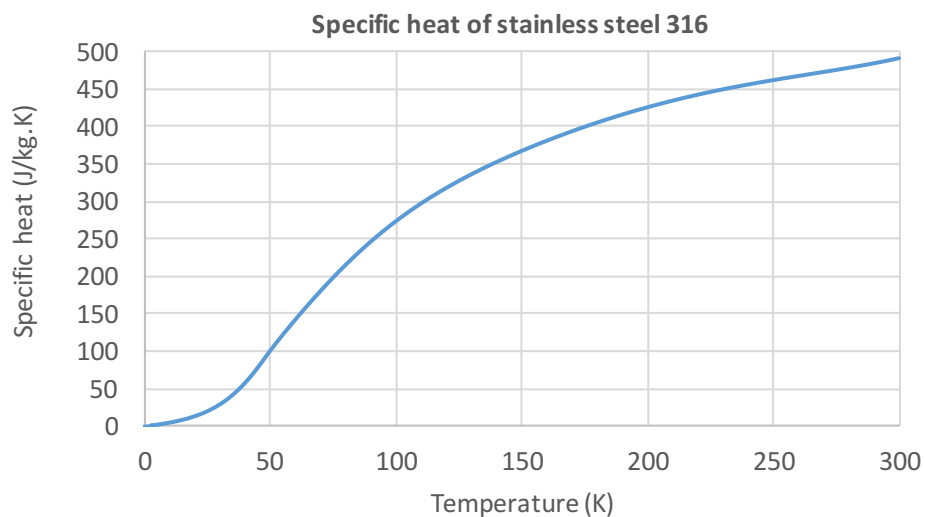


Figure B.4: Specific heat of stainless steel 316 as a function of temperature; data obtained from NIST [58].

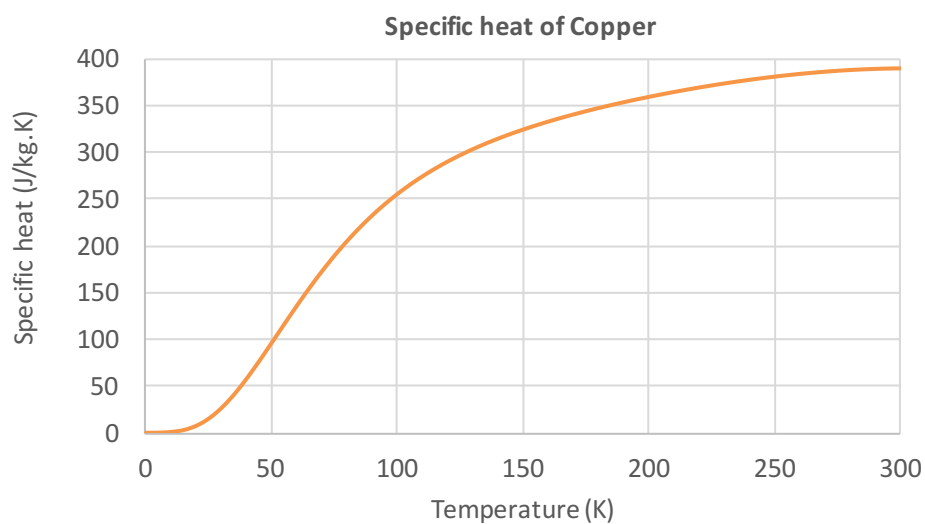


Figure B.5: Specific heat of copper as a function of temperature; data obtained from NIST [58].

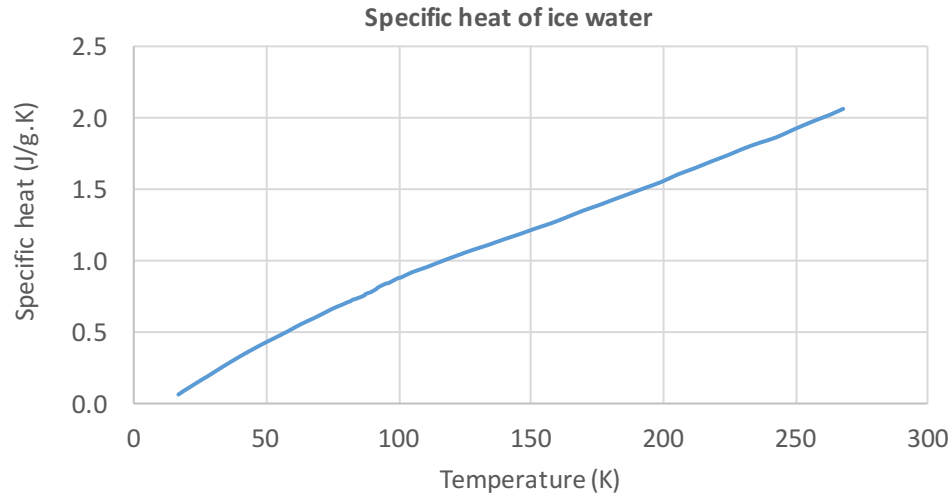


Figure B.6: Specific heat of ice water as a function of temperature; data taken from [67].

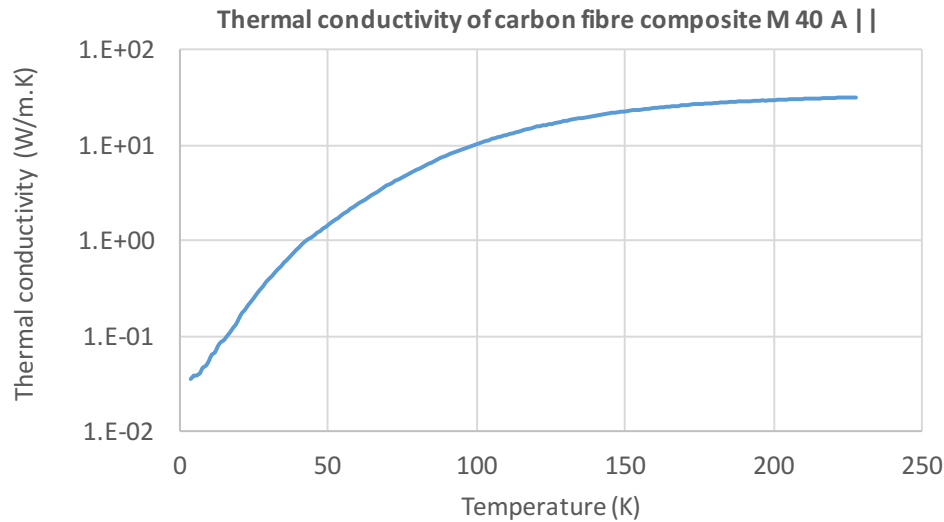
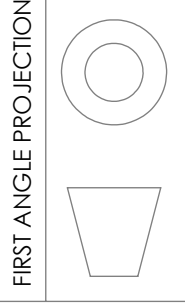
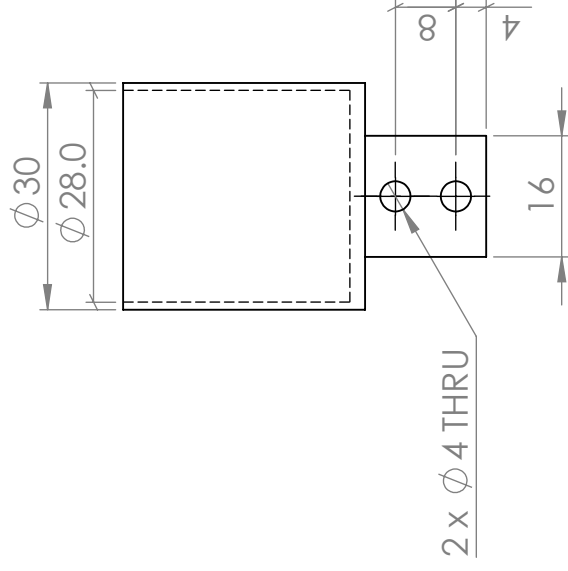


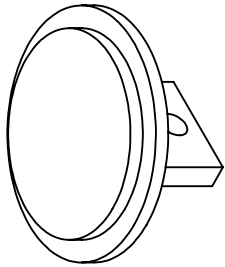
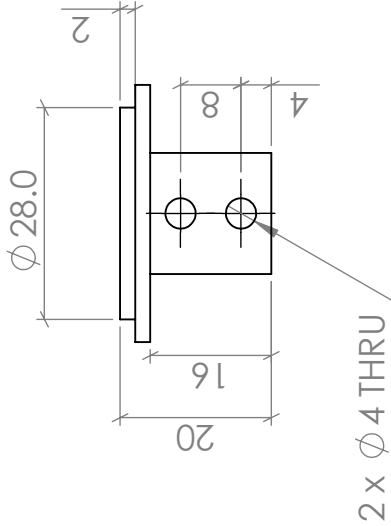
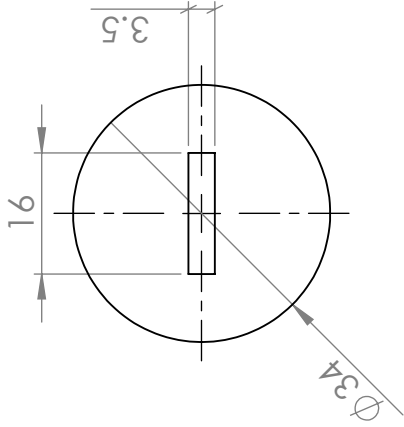
Figure B.7: Thermal conductivity of carbon fibre composite M 40 A || [68].

C Technical Drawings

- Development Model cold cell body
- Development Model cold cell cover
- Development Model metal hydride canister body
- Development Model metal hydride front cover
- Development Model metal hydride back cover

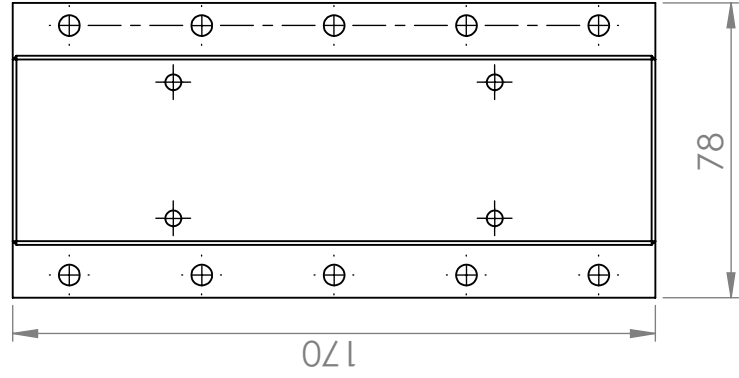
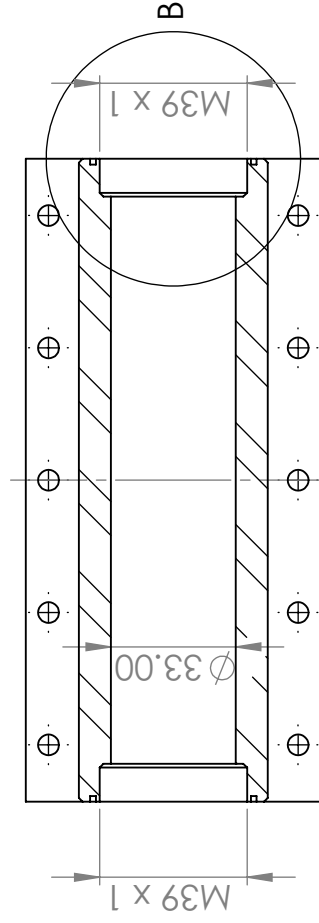
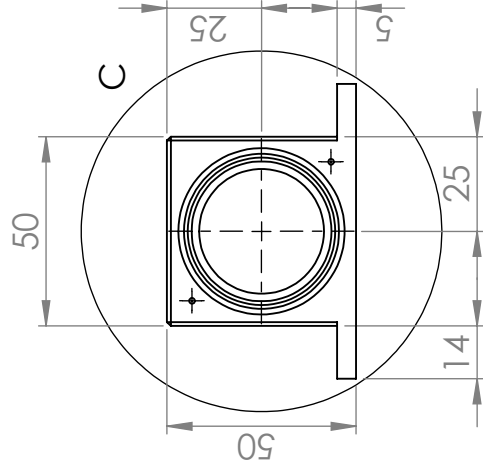


Name		Date	<p>Cold cell - body</p>	<p>Part:</p>	<p>Lab. Criogenia FCT-UNL</p>
Drawn by	PBS	22/01/14			
Checked by	GB	22/01/14			
MATERIAL:			<p>Copper</p>	<p>ESU DM cold cell</p>	<p>1 part</p>
Size: A4					
<p>Tolerances: X: +0.1 X.X: +0.05</p>					
Scale: 1 : 1					



FIRST ANGLE PROJECTION

Name	Date	Part:	Cold cell - cover		Lab. Criogenia FCT-UNL	
Drawn by	PBS	22/01/14	MATERIAL: Copper			
Checked by	GB	22/01/14				
Size: A4		Tolerances:	Drawing name:			
Scale: 1 : 1		X:±0.1 X.X:±0.05				
			ESU DM cold cell			
					1 part	

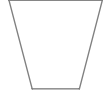


DETAIL B
SCALE 1:1

Lab. Criogenia FCT-UNL

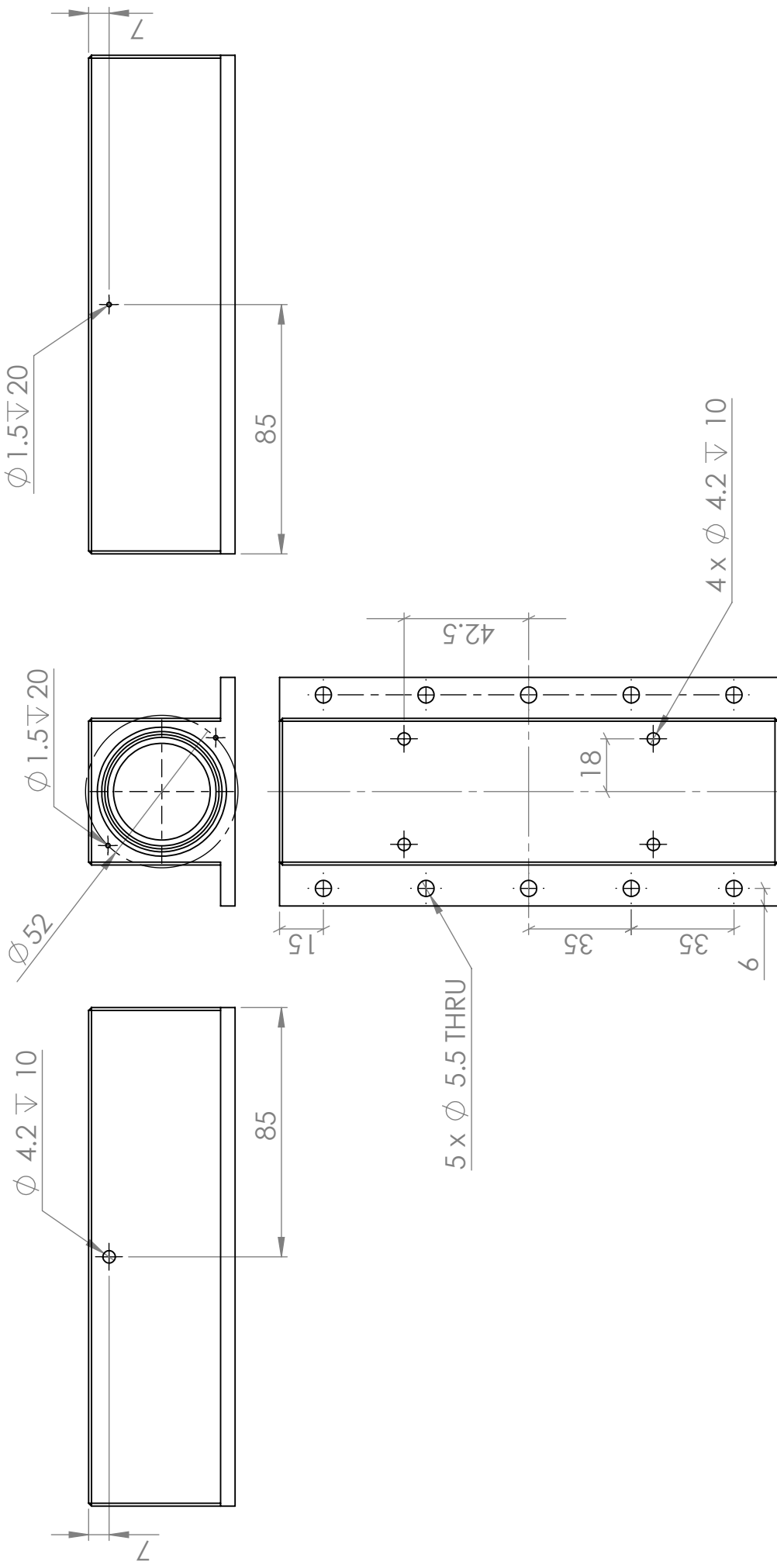
Part:			
Name	Date		
Drawn by	PBS	30/09/14	
Checked by	GB	30/09/14	
MATERIAL:		SS 316	
Size: A4	Tolerances: XX:±0.1 XX.X:±0.05 XX.XX:±0.01		
Scale: 1 : 2		Drawing	

FIRST ANGLE PROJECTION



me:
Canister for DM ESU - page 1 of 2

1 part	
--------	--

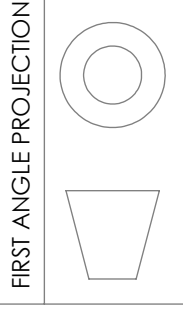
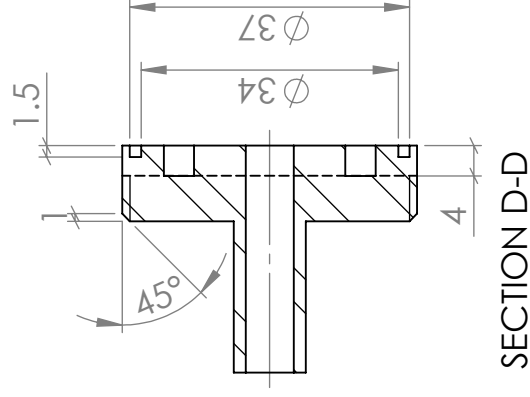


Name		Part		Part:	
Drawn by	PBS	30/09/14			
Checked by	GB	30/09/14			
MATERIAL:		SS 316			
Size: A4		Tolerances:		Drawing name:	
Scale 2 : 1		XX:±0.1		Canister for DM ESU - page 2 of 2	
		XX:±0.05		1 part	
		XX:XX:±0.01			

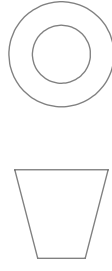
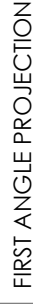
FIRST ANGLE PROJECTION

Canister body with flaps

Lab. Criogenia FCT-UNL



Canister for DM ESU - front cover



Closing lid with thread

	Name	Date
Drawn by	PBS	26/09/14
Checked by	GB	26/09/14
<p>MATERIAL:</p> <p>SS 316</p>		
Size: A4		<p>Tolerances:</p> <p>XX:±0.1</p> <p>XX X:±0.05</p> <p>XX XX:±0.01</p>
Scale: 1 : 1		